Fabrication of atomic force microscope probes with high aspect ratio silicon tips, silicon/silicon nitride cantilevers and stair-shaped handles

by

Aixi Pan

A thesis

presented to the University of Waterloo

in fulfillment of the

thesis requirement for the degree of

Doctor of Philosophy

in

Electrical and Computer Engineering (Nanotechnology)

Waterloo, Ontario, Canada, 2024

© Aixi Pan 2024

Examining Committee Membership

The following served on the Examining Committee for this thesis. The decision of the Examining Committee is by majority vote.

External Examiner: Prof. Qiying Chen
Professor
Department of Physics and Physical Oceanography
Memorial University of Newfoundland

Supervisor: Prof. Dayan Ban
Professor
Department of Electrical and Computer Engineering
University of Waterloo

Co-supervisor: Prof. Bo Cui
Professor
Department of Electrical and Computer Engineering
University of Waterloo

Internal Member: Prof. Guo-Xing Miao
Associate professor
Department of Electrical and Computer Engineering
University of Waterloo

Internal-External Member: Prof. Eihab Abdel-Rahman

Professor

Department of Systems Design Engineering

University of Waterloo

Internal-External Member: Prof. Vivek Maheshwari

Associate Professor

Department of Chemistry

University of Waterloo

Author's Declaration

This thesis consists of material all of which I authored or co-authored: see Statement of Contributions included in the thesis. This is a true copy of the thesis, including any required final revisions, as accepted by my examiners.

I understand that my thesis may be made electronically available to the public.

Statement of Contributions

A part of this thesis is based on a combination of published works. Several sections were adapted from the following list of published work, specifically referring to the published work provided within the chapter.

Chapter 3, Section 3.1

Pan, A., Samaan, M., Yan, Z., Hu, W. & Cui, B. Fabrication of ultrahigh aspect ratio Si nanopillar and nanocone arrays. (2023). Journal of Vacuum Science & Technology B 41 (2).

I am the first author of this paper and was responsible for all experimental planning, methodology, data collection and analysis, and draft writing and editing. Medhat Samaan assisted in performing initial experiments, and Zheng Yan and Wenhan Hu assisted in the data supplement (measurements of etching rates). Prof. Bo Cui assisted in supervision, experiment planning, and manuscript review and editing. Copyright © 2023, American Vacuum Society.

Chapter 3, Section 3.2

Pan, A., Zhu, C., Yan, Z., Zhu, X., Liu, Z., Cui, B. Fabrication of the highly ordered silicon nanocone array with sub-5 nm tip apex by tapered silicon oxide mask. (2024). IEEE Transactions on Semiconductor Manufacturing, vol 37, No. 2 doi:10.1109/TSM.2024.3372521.

I am the first author of this paper and was responsible for all experimental planning, methodology, data collection and analysis, and draft writing and editing. Chenxu Zhu and Zheng Yan performed experiments on the etching recipe for Table 1 in the manuscript, and Dr. Xiaoli Zhu assisted in editing the manuscript. Dr. Zhongyi Liu provided the EVENHEAT artisan 688 stp

and did the oxidation sharpening. Prof. Bo Cui assisted in supervision, experiment planning, and manuscript review and editing. Copyright © 2024, IEEE.

Chapter 3, Section 3.3

Zhu, X., **Pan, A.**, Cui, B. Cryogenic etching of positively tapered silicon pillars with controllable profiles. (2024). Journal of Vacuum Science & Technology B 42, 032206.

This project primarily involves Dr. Zhu's work, and I carried out parts of the experiments with several characterizations (Section III. A and B). Dr Xiaoli Zhu performed all the rest of the experiments and wrote the manuscript. I helped with the editing the manuscript. Prof. Bo Cui assisted in supervision, experiment planning, and manuscript review and editing. Copyright © 2024, American Vacuum Society.

Chapter 3, Section 3.4

Kang, R., **Pan, A.**, Cui, B. Fabrication of silicon sharp nanocones using dry etch with periodic oxygen plasma shrinking and wet etch. (2024). Journal of Vacuum Science & Technology B 42, 033002.

I am the co-first author of this paper and was responsible for all experimental planning and methodology, half of the data collection and analysis and the first half part (Section II and Section III. A) draft writing and editing. Renqiang Kang was responsible for half of the data collection and analysis and the latter part (Section I and Section III. B-C) draft writing and editing. Prof. Bo Cui assisted in supervision, experiment planning, and manuscript review and editing. Copyright © 2024, American Vacuum Society.

Other published works beyond the scope of this thesis:

Wu, H., **Pan, A.,** Zhu, C., Cui, B. Fabrication of slanted gratings by using glancing angle deposition. (2024). Journal of Vacuum Science & Technology B 42, 023002. (Co-first author).

Wang, Y., **Pan, A.**, Zhu, X., Cui, B. Fabrication of blazed gratings by tilted reactive ion beam etching with the side mask for augmented reality applications. (2024). Journal of Vacuum Science & Technology B 42, 013001. (Co-first author).

Zhu, C., Ekinci, H., **Pan, A.**, Cui, B. & Zhu, X. Electron beam lithography on nonplanar and irregular surfaces. (2024). Microsystems and Nanoengineering 10 (52).

Yan, Z., Ekinci, H., **Pan, A.**, Cui, B. Ordered silicon nanocone fabrication by using a pseudo-Bosch process and maskless etching. (2024). Journal of Vacuum Science & Technology B 42, 032802.

Zhu, C., **Pan, A.,** Zhu, X., Zheng, S., Cui, B. Edge lithography based on aluminum dry etching. (2024). Micro and Nano Engineering 22, 100233.

Hu, W., Wang, Z., **Pan, A.,** Cui, B. High aspect ratio silicon ring-shaped micropillars fabricated by deep reactive ion etching with sacrificial structures. (2024). Micro and Nano Engineering 22, 100234.

Aydinoglu, F., **Pan, A.,** Zhu, C., Cui, B. Effect of oxygen plasma cleaning on the nonswitching pseudo-Bosch etching of high aspect ratio silicon pillars. (2020). Journal of Vacuum Science & Technology B, 012804.

Abstract

The atomic force microscope (AFM) is a versatile tool with promising applications in biomedical detection, optical spectroscopy, and material characterization. However, its widespread utilization faces challenges due to limitations in conventional fabrication methods of commercially available probes. Specifically, the standard tips may not meet the requirements for scanning deep or narrow structures accurately, and the rectangular handle design can block a portion of the reflected laser signal, leading to inconsistent feedback. Overcoming these limitations is crucial for expanding the utility and unlocking the full potential of AFM in diverse scientific and technological applications. In this thesis, we propose innovative strategies to enhance the scanning performance of AFM probes with high aspect ratio (HAR) tips and stair-shaped handles.

Chapter 3 explores four distinct silicon (Si) AFM tip fabrication methods, each offering unique advantages and contributions to the field. The first method (Section 3.1) integrates non-switching pseudo-Bosch etching with wet sharpening techniques to achieve an exceptional aspect ratio of 1:135, marking a significant advancement in tip fabrication. The second method (Section 3.2) introduces an innovative approach utilizing tapered silicon oxide (SiO_2) masks to fabricate Si nanocones with extraordinary apex measuring just 3.54 nm. The third method (Section 3.3) explores a novel two-step cryogenic etching process to yield a controllable tip profile with a slight taper angle of 2.2°. The fourth method (Section 3.4) combines the Bosch process with the pseudo-Bosch process, incorporating periodic oxygen (O_2) shrinking steps. This approach achieves a remarkable tip apex sharpness of 20 nm, pushing the boundaries of nanofabrication capabilities.

Chapter 4 details the fabrication of a stair-shaped Si handle to mitigate laser blocking. Two techniques are described: one leveraging the loading effect and RIE-lag to attain stage heights of 71 μm, 151 μm, 168 μm, and 287 μm, while the other employs pseudo-grayscale lithography with

a titanium (Ti) mask, yielding final stages of 52 μm, 83 μm, 161 μm, and 211 μm. Both these methods are applicable for practical AFM probe fabrication without laser blocking.

Chapter 5 delves into the mass fabrication of all-Si HAR AFM probes, merging tips fabricated by the O_2 shrinking method with handles fabricated using the loading effect and RIE-lag. Furthermore, Chapter 6 explores the adoption of silicon nitride (SiN_x) as an alternative to Si for cantilevers. Amorphous low-pressure chemical vapor deposition (LPCVD) SiN_x offers benefits such as low spring constants and precise deposition control, resulting in thin and low-spring constant cantilevers. This configuration minimizes damage to the sample and tip, making it ideal for delicate samples. By combining a SiN_x cantilever with a Si tip, the probe capitalizes on both tip apex and thin cantilever advantages, facilitating accurate AFM imaging with high resolution while preventing false images on fragile samples.

Keywords: atomic force microscope probe; high aspect ratio tip; stair-shaped handle; nitride cantilevers.

Acknowledgements

First and foremost, I am deeply indebted to my supervisors, Prof. Dayan Ban and Prof. Bo Cui. I extend my heartfelt gratitude to Prof. Bo Cui, whose profound knowledge and selfless mentorship have profoundly influenced my journey in semiconductor research. From guiding the inception of my master's and doctoral theses to refining experiments and manuscripts, your unwavering support has been instrumental in shaping my academic prowess and personal growth over the past eight years. Your dedication to my academic skills and genuine concern for my overall well-being have left an indelible mark on my life. I wish you continued success and fulfillment in your academic pursuits.

At the close of 2023, I had the privilege of becoming a student under the tutelage of Prof. Dayan Ban. Your unwavering dedication and meticulous guidance have been a beacon of light during challenging moments in my academic endeavors. I am profoundly grateful for your steadfast support and mentorship, which have significantly contributed to my academic journey. I extend my sincerest wishes for Prof. Dayan Ban's continued success and fulfillment, both personally and professionally.

I want to extend my gratitude to my committee members, Prof. Guo-Xing Miao, Prof. Eihab Abdel-Rahman, Prof. Vivek Maheshwari, and Prof. Qiying Chen, for dedicating their time to review my thesis and offering valuable feedback. Your critical insights and thoughtful suggestions not only helped clarify complex aspects of the research but also provided a new perspective. The encouragement and guidance from each of you have been instrumental in navigating the complexities of my study, fostering a deeper and more nuanced understanding of the subject matter.

I also want to thank Dr. Nathan Nelson-Fitzpatrick, Dr. Lino Eugene, Dr. Greg Holloway, Dr. Richard Barber, Dr. Czang-Ho Lee, Rodello Salandanan, Matt Scott, Ken Speirs for their invaluable assistance in the cleanroom throughout my Ph.D. studies.

The accomplishments presented in this thesis are a testament to the invaluable collaborations I've been fortunate to have over the recent years. I extend my sincere thanks to my colleagues Dr. Xiaoli Zhu, Dr. Ferhat Aydinoglu, Dr. Ripon Kumar Dey, Dr. Medhat Samaan, Dr. Mohammad Soltani, Dr. Navid MS Jahed, Dr. Huseyin Ekinci, Dr. Asif Abdullah Khan, Dr. Chenxu Zhu, Dr. Zheng Yan, Dr. Farheen Aurangzeb, Dr. Jian Yin, Dr. Zihao Wang, Dr. Wenhan Hu, Yunchenxin Wang, Hongwen Wu, Renqiang Kang, and all the other current and former members at Prof. Dayan Ban and Prof. Bo Cui’s research groups for your support and collaboration.

To my family, especially my mom Pan Pan and my dad Min Ai, your unwavering love and constant support have been my greatest source of strength and motivation, helping me persevere through the toughest times. To my friends Mei Han and Miao He, thank you for being my pillars of support, for the countless moments of laughter, and for the understanding and companionship that have made this journey not only bearable but enjoyable.

Dedication

To my parents,

For introducing me to the idea of home.

And to Zhongyi Liu,

For joining me in the adventure of creating our own.

Table of Contents

Author's Declaration iv

Statement of Contributions v

Abstract viii

Acknowledgements x

List of Figures xix

List of Tables xxx

List of Abbreviations xxxi

Chapter 1 Introduction to the AFM System 1

1.1 Background 1

1.2 Overview of AFM Systems 3

1.2.1 Working mechanism 3

1.2.2 Scanning modes 5

1.2.2.1 Contact mode AFM 5

1.2.2.2 Non-contact mode AFM 6

1.2.2.3 Tapping (intermittent contact) mode AFM 7

1.3 Critical Parameters and Recent Advances 8

1.3.1 Peak force tapping AFM (PFT-AFM) 10

1.3.2 Multi-head AFM (MH-AFM) 13

1.3.3 High-speed AFM (HS-AFM) 14
1.3.4 Critical dimension AFM (CD-AFM) 16
1.4 Applications *18*
1.5 Motivations and Research Objectives *20*
Chapter 2 Traditional Fabrication Process of AFM Probe 23
2.1 Batch Fabrication of Commercial All-Si AFM Probes *23*
2.2 Commercially Available Batch Fabrication of All-Si_3N_4 AFM Probes *25*
2.3 Traditional Techniques for Fabricating HAR AFM Tip *28*
2.3.1 Focus ion beam (FIB) milling technique 29
2.3.2 Electron/ion beam-induced deposition (EBID/IBID) techniques 31
2.3.3 Carbon nanotube (CNT) attachment technique 32
2.3.4 NaugaNeedles self-assembly technique 33
2.3.5 Thermal oxidation sharpening technique 34
2.4 Specific Techniques in Probe Fabrication *35*
2.4.1 Electron beam lithography (EBL) 35
2.4.2 Lift-off process 36
2.4.3 Reactive ion etching (RIE) 38
2.4.3.1 Inductively coupled plasma-RIE (ICP-RIE) 38
2.4.3.2 Bosch process 40
2.4.3.3 Non-switching pseudo-Bosch process 41
2.4.3.4 Cryogenic etching process 42

Chapter 3 HAR AFM Tip Fabrication 43

3.1 Fabrication of Ultra-high Aspect Ratio Si Nanopillar and Nanocone Arrays 44

3.1.1 Introduction 44

3.1.2 Experiment 46

3.1.3 Results and discussion 48

3.1.3.1 Wet etching using a mixture of HF and HNO_3 48

3.1.3.2 Fabrication of HAR nano-pillars for sparse pillar array 50

3.1.3.3 Fabrication of nano-cones for dense pillar array 51

3.1.4 Summary and conclusions 53

3.2 Fabrication of the Highly Ordered Si Nanocone Array with sub-5 nm Tip Apex by Tapered SiO_2 Mask 54

3.2.1 Introduction 54

3.2.2 Experiment 57

3.2.3 Results and discussion 58

3.2.3.1 SiO_2 Mask Patterning with Cr Mask 58

3.2.3.2 Si Etching with 1.1 μm Design 61

3.2.3.3 Si Etching with 1.0 μm Design 64

3.2.4 Summary and conclusions 65

3.3 Cryogenic Etching of Positively Tapered Si Pillars with Controllable Profiles 65

3.3.1 Introduction 65

3.3.2 Experiment 67

3.3.3 Results and discussion 69

3.3.3.1 Effect of O_2 content 70

3.3.3.2 Effect of RF bias voltage 72

3.3.3.3 Two-step etching 74

3.3.3.4 Summary and conclusions 78

3.4 Fabrication of Si Sharp Nanocones using Dry Etch with Periodic Oxygen Plasma Shrinking and Wet Etch 79

3.4.1 Introduction to etching recipe 79

3.4.2 Introduction 80

3.4.3 Experiment 82

3.4.4 Results and discussion 84

3.4.4.1 Dry etching using the standard Bosch process and the non-switch pseudo-Bosch with oxygen plasma resist shrinking 84

3.4.4.2 Anisotropic wet etching using KOH 85

3.4.4.3 Isotropic wet etching using HNO_3 and HF 87

3.4.4.4 Oxidation sharpening of Si nanocones 88

3.4.5 Summary and conclusions 88

3.5 Summary 89

Chapter 4 AFM Stair-shaped Handle Fabrication 91

4.1 Stair-shaped Handle Fabrication using RIE Loading Effect and RIE-lag 91

4.1.1 Introduction 91

4.1.2 Results and discussion 94

4.2 Stair-shaped Handle Fabrication by Pseudo-grayscale Lithography with a Titanium Photomask 95

4.2.1 Introduction 95
4.2.2 Experiment 96
4.2.3 Results and discussion 98
4.3 Summary 99
Chapter 5 Cost-effective Mass Fabrication of High-performance All-Si AFM Probes with HAR Tips and Stair-shaped Handles 101
5.1 Simulation and Design 101
5.1.1 Direct calculation by MATLAB 102
5.1.2 Finite element simulation by COMSOL 104
5.1.3 Calculation of spring constant using Sader's method 108
5.2 Fabrication Process 109
5.3 Results and Discussion 113
5.3.1 Probes fabrication with 120 μm cantilever length 113
5.3.1.1 Experiment results 113
5.3.1.2 Performance test on AFM system 117
5.3.2 Probes fabrication with 140 μm cantilever length 121
5.3.2.1 Experiment results 121
5.3.2.2 Performance test on AFM system 123
5.4 Summary 124
Chapter 6 Mass Fabrication of Low-spring-constant AFM Probes with HAR Si Tips, SiN_x Cantilevers and Stair-shaped Handles 126

6.1 Simulation and Design 126

6.1.1 Direct calculation by MATLAB 126

6.1.2 Finite element simulation by COMSOL 127

6.2 Fabrication Process 129

6.3 Results and Discussion 131

6.4 Performance Test of Fabricated AFM Probe 134

6.5 Summary 135

Chapter 7 Conclusions and Future Work 137

References 140

Appendix: Supplementary Information for Chapter 3.2 170

List of Figures

Figure 1.1 The working mechanism of the AFM system. 3

Figure 1.2 Force curve of interatomic force versus distance in different scanning modes..... 4

Figure 1.3 The profile of (a) Au-coated tip[33], (b) polycrystalline diamond-coated tip[34], (c) magnetic-coated tip[35]. 8

Figure 1.4 (a) Standard tip[33] (b) Rotated AFM tip[33] (c) HAR AFM tip[36]. 9

Figure 1.5 Experimental data of force (dotted line) and probe z-position (dashed line) versus time curve for a cantilever oscillated in PFT mode. (Reproduced with permission from Ref. [44]). .. 11

Figure 1.6 Different biological samples with PFT mode. (A) AFM images of Caenorhabditis elegans epicuticle cell at different processes of growth, (B) The images of the microvilli structure on a Madin-Darby Canine Kidney (MDCK) C11 cell with a vertical force of 100–130 pN setting, (C) The images of the microvilli structure on an MDCK C11 cell with a vertical force of 80–100 pN setting, (D) The image of the M immunoglobulin antibodies absorbed on mica in liquid environment, (E) High-resolution AFM topography of a single-molecule DNA. (Reproduced with permission from Ref. [47]). 12

Figure 1.7 Overview of parallel SPM. (a) schematic illustration of parallel miniaturized SPM (MSPM) to image simultaneously several locations (here 11) on a wafer or mask. (b) detail with a wafer stage in the middle, up to 2×50 positioning arms (here 2×7) on two sides of the wafer stage, each capable of moving an MSPM scan head onto the 450 mm wafer. (Reproduced with permission from Ref. [53]). 13

Figure 1.8 Cantilever, tip, and relative arrangement of cantilever and sample stage. (a) Scanning electron microscope (SEM) image of a small cantilever. (b) SEM image of an electron-beam-deposited (EBD) tip grown on an original bird-beak-shaped tip. (c) The relative arrangement between the sample stage and cantilever circumvents the disturbance by hydrodynamic pressure produced by quick displacement of the z-scanner. (Reproduced with permission from Ref. [63]). 15

Figure 1.9 HS-AFM images of B. subtilis were captured using the wide-area scanner. (a) Topographic image of B. subtilis in a culture medium solution before adding lysozyme (imaging rate, 15 s/frame, pixels, 200 200). (b) Successive HS-AFM images showing the bacteriolysis process of B. subtilis subjected to lysozyme (imaging rate, 20s / frame; pixels 256). (Reproduced with permission from Ref. [65]). 16

Figure 1.10 An SEM image was taken of the used CDR120 tip after the AFM measurements. (Reproduced with permission from Ref. [67]). 17

Figure 1.11 Profile of a line structure of a photomask measured in vertical oscillation mode, shown as eight profiles taken at different positions within one measurement (a) and a profile after first-order levelling (b). The middle CD is evaluated as the width of the structure at the half-height of the profile. (Reproduced with permission from Ref. [67]). 18

Figure 1.12 Projected distribution of AFM probe applications by 2032. 20

Figure 1.13 Research objectives for AFM probes. 21

Figure 2.1 Batch fabrication of commercial all-Si AFM probes[83] 24

Figure 2.2 The profile of the standard tapping probe, and the probe type is NanoWorld Pointprobe NCH[84]. 25

Figure 2.3 Batch fabrication of commercial all-Si_3N_4 AFM probes[83]. 26

Figure 2.4 Batch fabrication of commercial all-Si_3N_4 AFM probes[83]. (continued)..... 27

Figure 2.5 The profile of the standard nitride probe, and the probe type is NanoWorld PNP-DB[85]. 28

Figure 2.6 Schematic representation of AFM scanning process using standard tips..... 29

Figure 2.7 (a) Top view after bilayer metal deposition of Al (30 nm) and Cr (10 nm), (b) top view after FIB milling of Cr (10 nm), (c) tilted view (70º) after plasma etching of Al (30 nm), and (d) tilted view (70º) after plasma etching of Si. (Reproduced with permission from Ref. [90]).... 30

Figure 2.8 SEM images of (A) a commercial OMCL-TR800PB-1 cantilever and (B) the same cantilever following modification by EBID of Pt; scale bars: 200 nm. In both images, the axis of the probe is tilted at 52° to the electron beam. The magnified probe tips (shown inset) show calibrated circles drawn in the SEM software to measure radius-of-curvature; circles of radius∼21 nm and∼4 nm for the commercial and modified probe, respectively. (Reproduced with permission from Ref. [94]). 32

Figure 2.9 Electron micrograph of an epitaxially grown SiNW on an AFM cantilever. (Reproduced with permission from Ref. [97]). 33

Figure 2.10 Time-lapse SEM images that show the growth of an Ag_2Ga nanoneedle on an AFM tip. The images show the cantilever tip (a) first inserted into the droplet, then retracted (b) 10 μm, (c) 43 μm, and (d) 67 μm. (Reproduced with permission from Ref. [98]). 34

Figure 2.11 Schematic drawing of the oxidation sharpening process. (Reproduced with permission from Ref. [102]). 35

Figure 2.12 The fabrication process of the lift-off process. 37

Figure 2.13 The schematic of the ICP-RIE system. (Reproduced with permission from Ref. [111]). 39

Figure 2.14 Schematic representation of the standard Bosch process (a) passivation step, (b) etching step. 40

Figure 3.1 Schematic of the fabrication process for very thin and HAR nano-pillars: (a) prepare a silicon wafer, (b) spin coat a bilayer of PMMA and ZEP-520A, (c) lithography, (d) development, (e) Cr deposition, (f) resist removal, (g) etch silicon, (h) Cr mask removal, (i) wet sharpening. (The fabrication process is the same for the nano-cone array except that those structures before wet etching are very dense) 47

Figure 3.2 Plots of average lateral and vertical etching rate as a function of the weight percentage of nitric acid in the mixture. 49

Figure 3.3 SEM images of nanopillar array with 1 μm dots and 8 μm spacing (a) before wet thinning (b) after wet thinning. 51

Figure 3.4 SEM images of nanopillar array with 500 nm dots and 700 nm spacing (a) before wet sharpening (b) after wet sharpening. 53

Figure 3.5 Schematic of the fabrication process for Si nanocone array: (a) prepare and clean a Si wafer (b) wet thermal oxidation and spin coat a bilayer of PMGI and S1811 resists (c)

photolithography (d) development (e) Cr deposition and lift-off (f) etch SiO_2 by RIE (g) etch SiO_2 by BOE (h) Si etching (i) oxidation sharpening. 58

Figure 3.6 SEM images of (a) Cr mask array with 1.0 μm diameter and 10 μm period, (b) SiO_2 array after 20 minutes of pure wet etching by BOE, (c) the enlarged view of the single Cr mask pattern, (d) the enlarged view of the single SiO_2 pattern. All structures in this work were examined using JOEL JSM-7200F SEM with the samples on a 70° tilted stage. 59

Figure 3.7 SEM images of SiO_2 array after 80 seconds of a dry etching by RIE and 10 min wet etching by BOE, and the designed diameter of MLA is (a) 1.0 μm (b) 1.1 μm (c) 1.2 μm (d) 1.3 μm. 61

Figure 3.8 SEM images of (a) the Si nanocone with 1.1 μm design after 10 minutes of etching using Recipe 1, (b) the cylindrical Si structure after thermal oxidation, (c) the enlarged view of the Si apex. 63

Figure 3.9 SEM images of (a) the Si array with 1.0 μm design after 5-minute etching, (b) the enlarged view of the Si apex, (c) the Si array after oxidation sharpening, (d) the enlarged view of the Si apex after oxidation sharpening. 64

Figure 3.10 Schematic process flow for fabricating cone-shaped silicon nanopillars using cryogenic silicon etching. It consists of (a) thermal oxide deposition and PS resist coating, (b) e-beam exposure and development, (c) oxide etching, (d) cryogenic etching with a higher O_2 flow, and (e) cryogenic etching with a lower O_2 flow. 68

Figure 3.11 Patterned oxide dot array as a hard mask for cryogenic etching. 69

Figure 3.12 The dependence of silicon etching rates and taper angles on O_2 concentration. 72

Figure 3.13 SEM images of silicon pillars etched using different O_2 gas flows of (a) 9 sccm, (b) 12 sccm and (c) 10 sccm for the lower portion and 13 sccm for the upper portion. 72

Figure 3.14 Taper angle variation with RF bias voltages of (a) 71 V, (b) 84 V, (c) 93 V and (d) 119 V. The SEM images were captured at 45 degrees tilt. 74

Figure 3.15 The dependence of silicon and SiO_2 etching rates (a), as well as taper angle and selectivity (b) on the bias voltage. 74

Figure 3.16 High aspect-ratio silicon pillars were etched using a two-step cryogenic etching process with SiO_2 masks having (a) 82 nm diameter and (b) 194 nm diameter. 76

Figure 3.17 Cone-shaped silicon pillars with 10.3 μm height and different tapered parts with (a) 10 μm period and (b) 2 μm period. The embedded image depicts the top of the pillars. 77

Figure 3.18 Schematic representation of Bosch etching to form a cylinder-shaped base (lower portion) in silicon. 80

Figure 3.19 Schematic representation of pseudo-Bosch process with periodic O_2 shrinking, and the profile of etched pillar after (a) Bosch process, (b) 1 cycle of pseudo-Bosch plus O_2 shrinking of the resist, (c) 2 cycles of pseudo-Bosch plus shrinking, (d) 30 cycles of pseudo-Bosch plus shrinking (the number of steps should be 30, but here we draw fewer steps just to show the concept of the process). 80

Figure 3.20 Schematic of the fabrication process for nanocones. (a) Prepare a Si wafer, (b) spin-coat nLof 2035 photoresist, (c) photolithography, (d) develop, (e) etch Si using the standard Bosch process, (f) alternatively etch Si by C_4F_8/SF_6 and shrink resist mask using O_2 plasma, (g) remove resist, (h) wet etch, (i) thermal oxidation sharpening. 83

Figure 3.21 Si nanocones were created using the standard Bosch process and the non-switch pseudo-Bosch with O_2 plasma shrinking. 85

Figure 3.22 35% KOH etching at room temperature for 8 minutes with ultrasonication. 86

Figure 3.23 Nanocones after isotropic wet etching by 100:1 HNO_3: HF for 3 minutes. 87

Figure 3.24 SEM image of tips after oxidation sharpening at 950 ℃ for 2 hours. 88

Figure 4.1 Schematic representation of tilted AFM probes with (a) rectangular cross-section handle, and (b) stair-shaped handle. 91

Figure 4.2 Partial CAD pattern design of the AFM handle part. 93

Figure 4.3 The expected 3D shape of the handle part using the CAD pattern design shown above. 94

Figure 4.4 The cross-sectional profile of the handle part after (a) 250 cycles of standard anisotropic Bosch etching, (b) 550 additional cycles of standard anisotropic Bosch etching, followed by SF_6 isotropic etching and 50 more cycles of Bosch etching. 95

Figure 4.5 Schematic of the fabrication process for grayscale lithography mask with titanium. (a) prepare a quartz wafer, (b) photoresist coating and lithography, (c) development, (d) 4 nm Ti evaporation, (e) resist removal, (f) photoresist coating and aligned lithography, (g) development, (h) 4 nm Ti evaporation, (i) resist removal, (j) one more round of lift-off process with 4 nm Ti, (k) one more round of lift-off process with 4 nm Ti, (l) top view of fabricated grayscale mask. 97

Figure 4.6 Schematic of the fabrication process for Si stair-shaped handle by the exposure with a Ti mask. (a) prepare a Si wafer, (b) photoresist coating, (c) lithography with the photomask, (d) development, (e) etch the Si substrate by Bosch process, (f) resist removal. 98

Figure 4.7 (a) the optical microscope image of the grayscale photomask, (b) the heights of resist stages after photolithography (Figure 4.6d) by using the BRUKER-Dektak XT system. 98

Figure 4.8 The SEM image of a fabricated stair-shaped handle. 99

Figure 5.1 The 4D plot of spring constant k (unit N/m) and dimensions w,t,l. 103

Figure 5.2 The resonance frequency was simulated for a rectangular cantilever with 30 μm in width, 3 μm in thickness and 120 μm in length. 105

Figure 5.3 The plot of the displacement of a rectangular cantilever with 30 μm in width, 3 μm in thickness and 120 μm in length. 106

Figure 5.4 The resonance frequency and the spring constant were simulated for a rectangular cantilever with 30 μm in width, 3 μm in thickness and 140 μm in length. 107

Figure 5.5 Plot of the real (solid line) and imaginary (dashed line) components of the hydrodynamic function Γ. (Reproduced with permission from Ref. [246]). 109

Figure 5.6 Fabrication process of all-Si AFM probes on an SOI wafer. 110

Figure 5.7 The schematic profile of HAR AFM Si tip. The formation of such a structure is explained in Section 3.4. 111

Figure 5.8 The schematic profile of HAR AFM Si probe. 112

Figure 5.9 SEM images of (a) the etched tip and protective structure, (b) the enlarged view of the tip, (c) the etched tip and cantilever, and (d) the enlarged view of the tip on the cantilever. All images were captured using JOEL JSM-7200F SEM with the samples on a 20° tilted stage. ... 114

Figure 5.10 The actual product of AFM probes with dimensions of 5 cm × 5 cm. 114

Figure 5.11 SEM images of (a) the side view of the AFM probe with the cantilever length of 120 μm, and (b-d) the enlarged view of the cantilever and the tip. All images were captured using JOEL JSM-7200F SEM with the samples mounted on a 90° tilted stage. 115

Figure 5.12 SEM images of (a) the final product of the AFM probe with 120 μm cantilever after oxidation sharpening, and (b-d) the enlarged view of the cantilever and the tip. All images were captured using JOEL JSM-7200F SEM with the samples mounted on a 90° tilted stage. 116

Figure 5.13 (a) the interior structure of the FM-Nanoview1000AFM model, (b) the image of a probe mounted onto the AFM system, and (c) the frequency-root mean square (f-RMS) curve of the fabricated probe. 117

Figure 5.14 (a) The top view of the standard scanning sample, (b) the scanning result by using the commercially available Si probe bought from AppNano Company. 118

Figure 5.15 (a) The profile of an ACCESS-NC Si probe (the measured cone angle of the upper tip is 39.5°). 118

Figure 5.16 The AFM scanning image of (a) the first scan of the fabricated tip, (b) the fabricated tip used for 120 minutes, (c) the fabricated tip used for 180 minutes, (d) the SEM image of the used Si probe after 3-hour continuous scanning. 119

Figure 5.17 (a) The SEM image of a Si sample featuring trenches with a width of 350 nm and a depth of 270 nm. 120

Figure 5.18 (a) The profile and cone angle of our probe, (b-c) the AFM scanning result by using our fabricated Si probe, (d) the profile and cone angle of the AppNano probe, (e-f) the AFM scanning result by using the AppNano probe. 120

Figure 5.19 (a) The profile and apex diameter of our probe, (b) the AFM scanning result by using our fabricated Si probe, (c) the profile and apex diameter of the AppNano probe, (d) the AFM scanning result by using the AppNano probe. 121

Figure 5.20 SEM images of (a) the side view of the AFM probe with the cantilever length of 140 μm, and (b) the enlarged view of the cantilever and the tip before oxidation sharpening. All images were captured using JOEL JSM-7200F SEM with the samples mounted on a 90° tilted stage. 122

Figure 5.21 SEM images of (a) the final product of the AFM probe with 140 μm cantilever after oxidation sharpening, and (b-d) the enlarged view of the cantilever and the tip. All images were captured using JOEL JSM-7200F SEM with the samples mounted on a 90° tilted stage. 122

Figure 5.22 The resonance frequency curve of the fabricated probe, which was mounted on the Aist-NT SmartSPM 1000 in AFM mode. 123

Figure 5.23 (a) The AFM scanning image of the photoresist AZ3330 lines with positively tapered sidewall, (b) the 3D view image, and (c) the cross-sectional view..... 124

Figure 6.1 The 4D plot of spring constant k (unit N/m) and dimensions w,t,l. 127

Figure 6.2 The resonance frequency and the spring constant were simulated for a rectangular nitride cantilever with 30 μm in width, 600 nm in thickness and 140 μm in length. 128

Figure 6.3 Fabrication of AFM probe with SiN_x cantilever and stair-shaped handle..... 129

Figure 6.4 The schematic structure of the AFM probe with a handle has several steps. 130

Figure 6.5 The lateral and vertical etching of the nitride layer using Cr as a mask for the test sample. 131

Figure 6.6 SEM image of (a) the etched tip before oxidation, (b) the tip profile after thermal oxidation at 950℃ for 2 hours, (c) the tip after 600 nm LPCVD nitride deposition, (d) the overview of the tip and the cantilever. All images were captured using JOEL JSM-7200F SEM with the samples mounted on a 20° tilted stage. 132

Figure 6.7 (a) Overview SEM image of nitride probe, (b) the enlarged profile of the thin cantilever, (c) the tip profile before thermal oxidation sharpening, (d) the tip profile after thermal oxidation sharpening. All images were captured using JOEL JSM-7200F SEM with the samples mounted on a 90° tilted stage. 133

Figure 6.8 The measured resonance frequency of fabricated AFM probe after metal (30 nm Al) deposition on the cantilever backside. 134

Figure 6.9 (a) The SEM image of the new photoresist sample featuring trenches with a trench bottom width of 400 nm and a depth of 700 nm, (b-c) the AFM scanning result by using our fabricated probe with nitride cantilever, (d-e) the AFM scanning result by using the AppNano probe. 135

List of Tables

Table 2.1 The recipe for our standard Bosch process on the Oxford PlasmaLab 100 ICP 380 DRIE Si etching system. 41

Table 3.1 Lateral and vertical etching rate for different HNO_3 and HF volume ratios without solution agitation. 50

Table 3.2 Recipes for Si etching with SiO_2 mask and corresponding etching rates and selectivities 62

Table 3.3 Parameters for two-step cryogenic etching process I 75

Table 3.4 Parameters for two-step cryogenic etching process II 77

Table 3.5 Recipe of the standard Bosch process 85

Table 3.6 Recipe of the non-switch pseudo-Bosch with O_2 shrinking process 85

Table 3.7 Comparisons for the four methods for tip fabrication are listed above. 89

Table 7.1 A summary of the parameters of the fabricated probes and three commercially available Si probes from Nanoworld, Bruker, and AppNano. 138

List of Abbreviations

AFM	Atomic force microscope
Au	Gold
BOE	Buffered oxide etchant
C_4F_8	Octafluorocyclobutane
CD-AFM	Critical dimension AFM
CNT	Carbon nanotube
DRIE	Deep reactive ion etching
EBID	Electron beam-induced deposition
EBL	Electron beam lithography
FIB	Focus ion beam
HAR	High aspect ratio
HF	Hydrofluoric acid
HS-AFM	High-speed atomic force microscope
IBID	Ion beam-induced deposition
IC	Integrated circuit
IPA	Isopropanol
KOH	Potassium hydroxide
LPCVD	Low-pressure chemical vapor deposition
MACE	Metal-assisted chemical etching
MH-AFM	Multi-head atomic force microscope
MLA	Maskless aligner
MEMS	Microelectromechanical systems

NEMS	Nanoelectromechanical systems
O_2	Oxygen
OBD	Optical beam deflection
PECVD	Plasma enhanced chemical vapor deposition
PFT-AFM	Peak force tapping atomic force microscope
Pt	Platinum
Q-factor	Quality factor
RIE	Reactive ion etching
SEM	Scanning electron microscope
STM	Scanning tunneling microscope
SF_6	Sulfur hexafluoride
Si	Silicon
SiN_x	Silicon nitride
SiO_2	Silicon oxide
SOI	Silicon on insulator
TMAH	Tetramethylammonium hydroxide
UV	Ultraviolet
VLS	Vapor-liquid-solid

Chapter 1 Introduction to the AFM System

Chapter 1 serves as an introduction to the AFM system, including its background, working principles, critical parameters, recent advances and applications.

1.1 Background

Since the 1200s, humanity has sought to overcome the limitations of the human eye's resolution by developing optical tools like lenses and magnifying glasses[1]. In 1590, Hans and Zacharias Janssen created the first compound microscope[1], which allows the observation of samples through lens magnification using visible light with 0.2 μm resolution.

In 1924, Louis de Broglie[2] proposed the revolutionary concept of wave-particle duality, suggesting that microscopic particles exhibit both particle-like and wave-like behaviours, and this concept laid the groundwork for exploring the behavior of matter on a smaller scale. Researchers recognized the similarity between the movement of electrons in a magnetic field and the propagation of light in a medium, inspiring the development of electron lenses. In the 1930s, German physicist Ernst Ruska[3] invented the electron microscope by leveraging electron lenses to focus electron beams. Subsequent decades witnessed remarkable advancements in scanning electron microscopy technology, enabling magnifications of tens of thousands of times and resolutions as fine as 1-10 nm[4]. However, it requires a conductive sample surface and a vacuum environment.

In 1982, at IBM's Zurich Research Laboratory, Gerd Binnig and Heinrich Rohrer developed the scanning tunneling microscope (STM)[5], marking a milestone in surface analysis instrumentation. This innovative device utilized the quantum mechanical phenomenon of tunneling, empowering researchers to observe the atomic arrangement on material surfaces in real

time. Applying a bias voltage between the STM probe and the sample surface allows an exceptionally sharp metal tip to approach the surface closely enough for the tunneling current to pass through the barrier potential. As the probe scans across the sample surface, the tunneling current varies exponentially with changes in surface height. By maintaining a constant tunneling current through feedback control of the probe's displacement, the vertical movement of the probe accurately reflects the surface topography[6]. However, despite its remarkable capabilities, the STM system and its working principle have two main limitations that can impact usage and research outcomes. Firstly, both the tip and material surface must be conductive and exceptionally clean for effective operation. Secondly, the STM is highly sensitive to mechanical and electrical noise, which can introduce artifacts and affect the accuracy of measurements.

In 1986, in response to the limitations of the STM, Binnig and colleagues introduced the world's first AFM[7]. Unlike the STM, which was restricted to conducting samples for high-resolution imaging, it expanded the scope of materials that could be analyzed. Based on micro-cantilever detection of interaction forces, the AFM system has evolved rapidly from simple surface morphology measurements to applications in environmental detection, semiconductor analysis, and biology[8]. Its advantages lie in its straightforward sample preparation, requiring no special treatment and resulting in minimal sample damage compared to other techniques. Moreover, it demonstrates versatility by operating effectively in diverse environments, including air, liquid, and vacuum. In the field of biology, AFM enables real-time observation of living cells and manipulation of individual biomolecules. Furthermore, it offers nanoscale resolution for observing local charge density and physical properties, facilitating the measurement of interaction forces between molecules[9,10]. The information obtained by AFM complements that from other analytical and microscopy techniques, providing a powerful tool for scientific research and applications.

1.2 Overview of AFM Systems

1.2.1 Working mechanism

The AFM employs an elastic micro-cantilever with a fixed end and a tip at the other end and gathers the interaction force between the tip and the sample surface[11], as shown in Figure 1.1.

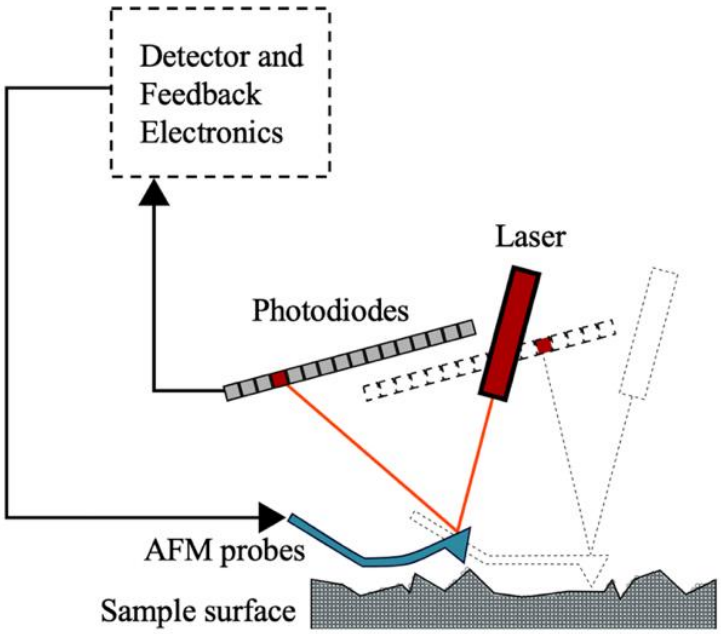


Figure 1.1 The working mechanism of the AFM system.

As the AFM tip scans, the interaction force between the tip and the sample surface induces deformation of the micro-cantilever, providing a direct measure of this force[12]. A laser beam shines on the cantilever and is reflected onto a photodetector with four quadrants. These quadrants accurately measure the change in location of the reflected laser beam resulting from cantilever deformation, which alters the differential output voltages from the photodetector. A feedback system compares the output signal to the preset oscillation amplitude of the system. It adjusts the piezo driver to maintain constant height/force between the sample and cantilever. This adjustment can be achieved by either moving the probe relative to the sample or by varying the sample surface's vertical (z-axis) position relative to the probe. By measuring the detector voltage change

corresponding to sample scanning positions, the AFM generates a surface morphology image of the sample[13].

In the AFM system, various interaction forces occur when the sample and the scanning probe approach each other[14,15]. In the far-field regime, where the tip-sample distance exceeds tens of angstroms, long-range forces such as van der Waals forces and electrostatic forces dominate. However, short-range forces become prominent as the tip and sample move closer, entering the near-field regime with distances smaller than tens of angstroms. These short-range forces arise from the distortion and overlap of the outer electron clouds. In Figure 1.2, as the tip and sample approach each other, the attractive forces increase due to the presence of both short-range and long-range forces[13,16]. However, when the tip-sample distance becomes very small, the electron clouds begin to repel each other, leading to an overall increase in the repulsive force between the AFM tip and the surface. At a distance of a few angstroms between atoms, the total force becomes zero, and upon contact, the force becomes repulsive[17].

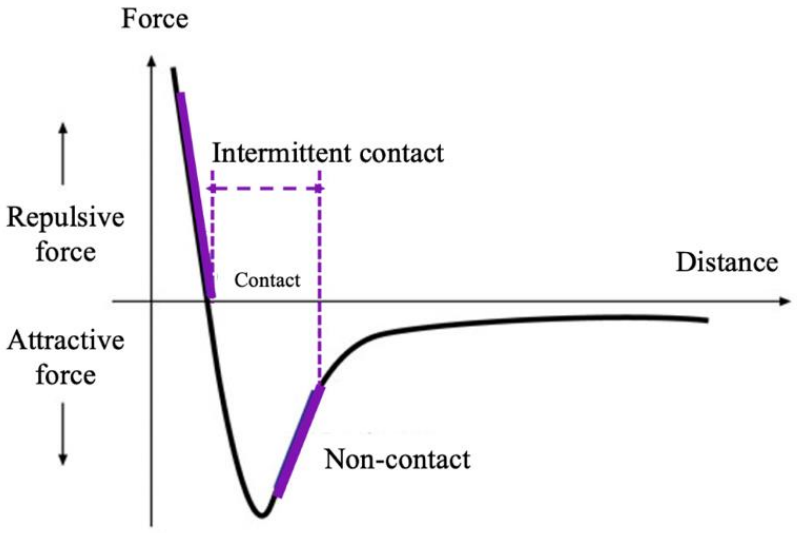


Figure 1.2 Force curve of interatomic force versus distance in different scanning modes.

1.2.2 Scanning modes

1.2.2.1 Contact mode AFM

In contact mode AFM, the probe maintains continuous contact with the sample surface while scanning. The primary interaction force between the tip and the sample is the Coulomb repulsion force, typically around 10^{-8}~10^{-11} N. This mode is commonly used for obtaining topographic images of sample surfaces, where the repulsive interaction force causes the cantilever to deflect upwards. The deflection can be converted into the interaction force magnitude by determining the cantilever's spring constant. Constant-force mode is the regular mode to measure the sample by fixing the interaction force in AFM. On the other hand, constant-height mode keeps the distance between the probe and the sample constant, allowing the probe-sample interaction force to reflect surface topography directly. This mode is beneficial for producing stable, high-resolution images on rigid samples with consistent atomic-scale features and relatively high scanning speed[18].

However, probe movement in contact mode AFM and adhesive forces between the tip and the surface can lead to sample deformation and tip damage, potentially resulting in image artifacts. This mode requires a soft cantilever with a low spring constant[19] to avoid damage.

In atmospheric conditions, sample surfaces often have water adsorbed layers, leading to concave surfaces due to capillary forces, further complicating imaging. Electrostatic charges on the probe tip and sample can also increase adhesion forces, while compressive and shear forces from the probe's movement may damage the sample (especially soft sample) surface, impacting image quality[20,21]. To mitigate these issues, immersing the sample in a liquid can help reduce capillary forces and shield electrostatic charges[22]. However, hydrated samples are typically softer and more prone to deformation during scanning, leading to reduced image quality and potential

sample damage. Additionally, some samples cannot be immersed in liquid, limiting the applicability of this approach.

1.2.2.2 Non-contact mode AFM

In non-contact mode AFM, the probe is scanned above the sample surface at a distance of 5~20 nm[23], without any physical contact. This mode prevents contamination or damage to the sample and the tip, addressing some of the issues encountered in contact mode. However, directly measuring force magnitude is challenging due to the significantly weaker long-range van der Waals attraction forces between the probe and the sample compared to contact mode. The operating principle involves driving the cantilever at a frequency slightly higher than its resonance frequency. As the probe approaches the sample surface, the amplitude of the cantilever decreases, indicating the force gradient acting on it, which correlates with the probe-sample distance. The feedback system adjusts this distance to maintain a constant cantilever amplitude during scanning, thereby generating the sample's surface topography image[24,25].

Non-contact mode offers advantages such as minimal influence from capillary and electrostatic forces, making it suitable for studying soft or elastic surfaces[26]. Furthermore, contamination is prevented since the probe never touches the sample surface. However, non-contact mode may have lower resolution and scanning speed than contact mode, particularly at longer probe-sample distances. Additionally, operational challenges arise, including instability caused by surface-adsorbed gas, making it unsuitable for imaging in liquids.

1.2.2.3 Tapping (intermittent contact) mode AFM

Tapping mode imaging is an intermediary between contact mode and non-contact mode in AFM. In this mode, the cantilever oscillates with an amplitude greater than that of non-contact mode (typically exceeding 20 nm), and the probe intermittently touches the sample surface. This approach combines the high resolution of contact mode with reduced sample damage, addressing the limitations of traditional scanning modes. The cantilever resonates slightly below its resonance frequency during atmospheric imaging in tapping mode through a piezoelectric probe holder. When the probe is away from the surface, the cantilever undergoes high-amplitude oscillations. As it approaches the surface, its amplitude decreases due to restricted space for oscillation, causing it to reverse direction upwards. The feedback system adjusts the tip-sample distance based on the measured amplitude, maintaining a constant force on the sample and capturing its surface topography[27].

The stable imaging force in the atmosphere is 10^{-9}~10^{-12} N with tapping mode, enabling imaging of soft, fragile, and adhesive samples without damage[27,28]. The probe overcomes adhesion forces upon contact by oscillating with sufficient amplitude, minimizing lateral friction and shear forces. Tapping mode offers a more extensive linear operating range, facilitating stable vertical feedback for repeated measurements than non-contact mode. In liquid environments, tapping mode operation provides similar benefits. The fluid medium reduces the cantilever's resonance frequency, and its oscillations drive the cantilever's motion, further reducing lateral friction and shear forces, ensuring minimal sample damage[29]. Static imaging force in liquid tapping mode can reach less than 100 pN.

1.3 Critical Parameters and Recent Advances

In recent AFM research, probe materials typically include Si or Si_3N_4. The probe can be coated with various materials to detect different interactions between the tip and the sample surface, as illustrated in Figure 1.3. For instance, a metal film, commonly platinum (Pt) or gold (Au), can be applied to enhance conductivity, and the Au layer may also be used to detect the covalent bonds of biological molecules and their interactions with surfaces[30]. Polycrystalline diamond (Figure 1.3 b) can extend the service life of the AFM probe due to its hardness[31]. Additionally, magnetic films can be coated to investigate the magnetic properties[32] of the sample (Figure 1.3 c).

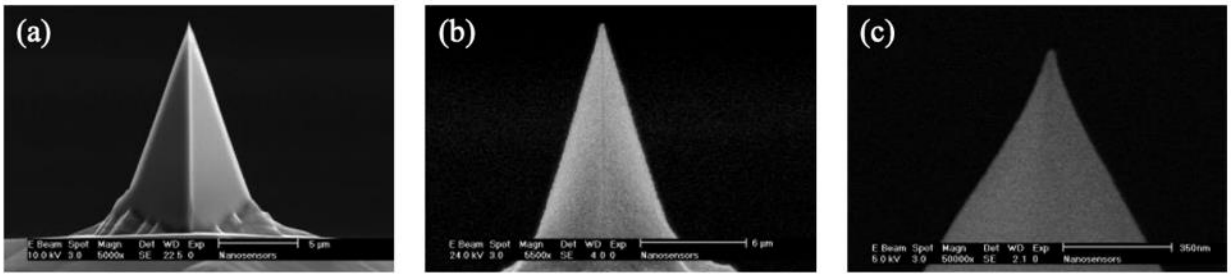


Figure 1.3 The profile of (a) Au-coated tip[33], (b) polycrystalline diamond-coated tip[34], (c) magnetic-coated tip[35].

In addition to coating materials, the profile of the AFM tip also significantly impacts imaging quality. A variety of tip designs are available, including the standard commercial tip shown in Figure 1.4 (a), the rotated tip, which is oriented 180° with respect to the center axis along the cantilever in Figure 1.4 (b) and the HAR tip in Figure 1.4 (c). Compared to a standard Si AFM tip, a HAR tip[36] offers higher resolution and clearer restoration, particularly for tiny/narrow structures and gaps. It also has an excellent performance in imaging tall structures due to its longer tip length, which is ~2 times longer than the tip base diameter. While the HAR tip demonstrates improved imaging properties for specific topographies, traditional fabrication processes are costly and time-consuming, a topic to be discussed in Section 2.3.

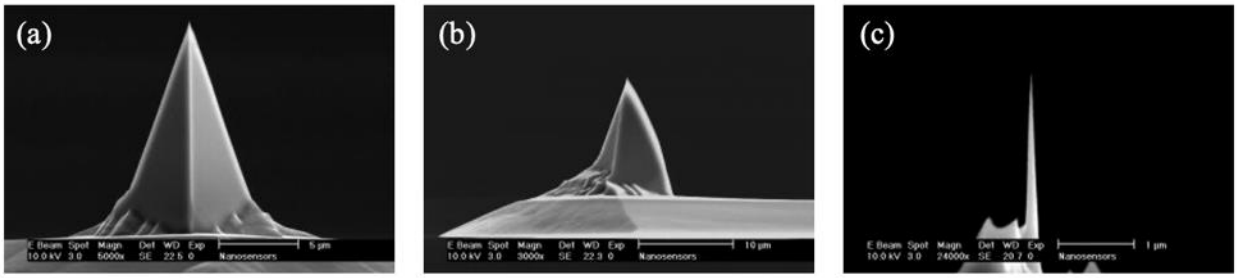


Figure 1.4 (a) Standard tip[33] (b) Rotated AFM tip[33] (c) HAR AFM tip[36].

In addition to tip characteristics, several essential factors of the cantilever significantly influence the performance and final scanning results of an AFM. These factors include the cantilever's resonance frequency, spring constant, and quality factor (Q-factor).

The resonance frequency of an AFM cantilever is the natural frequency at which it oscillates most efficiently when subjected to an external force, typically induced by methods like laser beam deflection or piezoelectric actuation. This frequency is primarily determined by the mechanical properties of the cantilever, such as stiffness and mass, and typically ranges from kilohertz to megahertz[37,38]. Cantilevers with higher resonance frequencies are more sensitive to weak tip-sample forces, making them capable of detecting subtle surface features. Additionally, they enable faster imaging speeds by facilitating rapid feedback adjustments, resulting in shorter scan times and increased throughput[39].

The spring constant of an AFM cantilever quantifies the force needed to deflect the cantilever by a given distance. It reflects the mechanical stiffness of the cantilever and is typically expressed in units of Newtons per meter (N/m). This constant is determined by the cantilever's geometry and material properties, including length, width, thickness, and Young's modulus. Cantilevers with lower spring constants are more flexible and exhibit more significant deflection in response to weak surface forces[40]. The spring constant also influences the stability and responsiveness of the AFM feedback control loop, which maintains a consistent interaction force

between the cantilever tip and the sample surface during scanning, so cantilevers with moderate spring constants facilitate stable feedback control and reduce imaging artifacts, resulting in more precise and reproducible outcomes.

The Q-factor of an AFM cantilever is a dimensionless parameter that gauges the ratio of the energy stored in the cantilever's oscillation to the energy dissipated per oscillation cycle. It measures the sharpness and stability of the cantilever's resonance peak and is inversely related to the damping and dissipation mechanisms within the system. The Q-factor is influenced by several factors, including the cantilever's geometry, material properties, environmental conditions, and interactions with the sample surface[41]. This parameter quantifies the energy dissipation and resonance behavior of the cantilever during oscillation, providing valuable insights into the dynamic response of the probe-sample interaction[42]. Cantilevers with higher Q-factors are more sensitive to weak tip-sample forces, such as van der Waals, electrostatic, and capillary forces. These cantilevers exhibit more stable oscillation amplitudes and reduced noise levels, improving feedback control and enhanced imaging stability, particularly in dynamic imaging modes like tapping mode and dynamic force microscopy. High-Q cantilevers enable precise control of oscillation amplitudes and minimize tip-sample interactions, resulting in artifact-free imaging and accurate characterization of surface morphology and properties[43].

1.3.1 Peak force tapping AFM (PFT-AFM)

PFT-AFM has emerged as a notable breakthrough in surface imaging, especially in addressing the limitations of traditional tapping mode AFM. Introduced by Bruker in 2009[44], PFT-AFM presents a novel approach that enhances imaging capabilities for soft samples in both air and liquid environments. Unlike tapping mode AFM, which operates near resonance, PFT-AFM

functions in a non-resonant mode, employing an oscillating frequency significantly lower than the cantilever resonance (0.5-8 kHz)[45,46]. This low-frequency operation gives the time for the acquisition of the force-distance curve for each pixel and thus the control of the interaction force at each pixel, making it suitable for delicate or soft samples. As illustrated by the tip trajectory indicated by the dashed line in Figure 1.5, the force curve (dotted line) remains continuous due to the modulation of the z-position by a sine wave rather than a triangular waveform. This method avoids undesirable resonances at contact turnaround points, thereby enhancing imaging quality and accuracy. However, the scanning speed is lower than the common tapping mode, since the probe oscillation frequency is roughly two orders (100 kHz versus 1 kHz) lower.

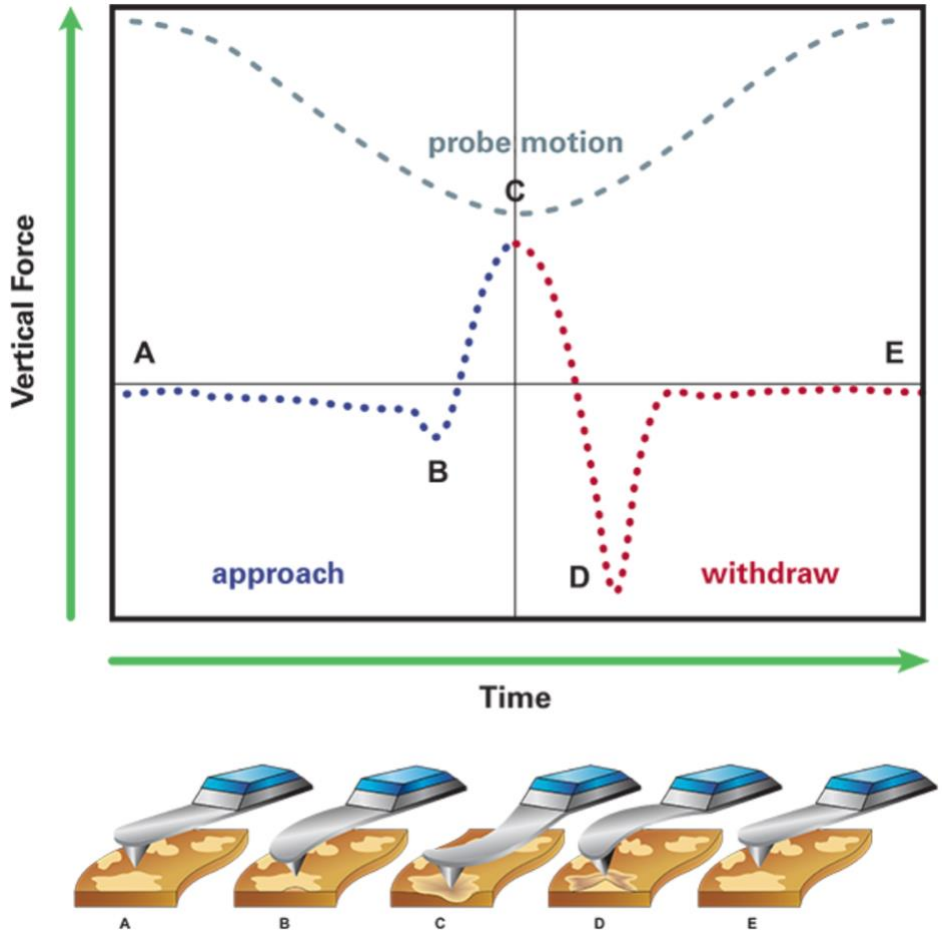


Figure 1.5 Experimental data of force (dotted line) and probe z-position (dashed line) versus time curve for a cantilever oscillated in PFT mode. (Reproduced with permission from Ref. [44]).

The primary advantage of PFT-AFM is its capability to operate at minimal forces, enabling the imaging of delicate and soft samples, such as cells in a liquid environment[45]. For instance, Xu *et al.*[47] presented the scanning results of four different biological samples[48–51] with PFT AFM, as depicted in Figure 1.6. The precise control of the peak interaction force at each distance point (pixel) eliminates the need for highly accurate cantilever tuning. Moreover, the force-distance curve generated by PFT-AFM provides valuable nanomechanical sample properties[52], offering deeper insights into the sample's characteristics that extend beyond surface topography.

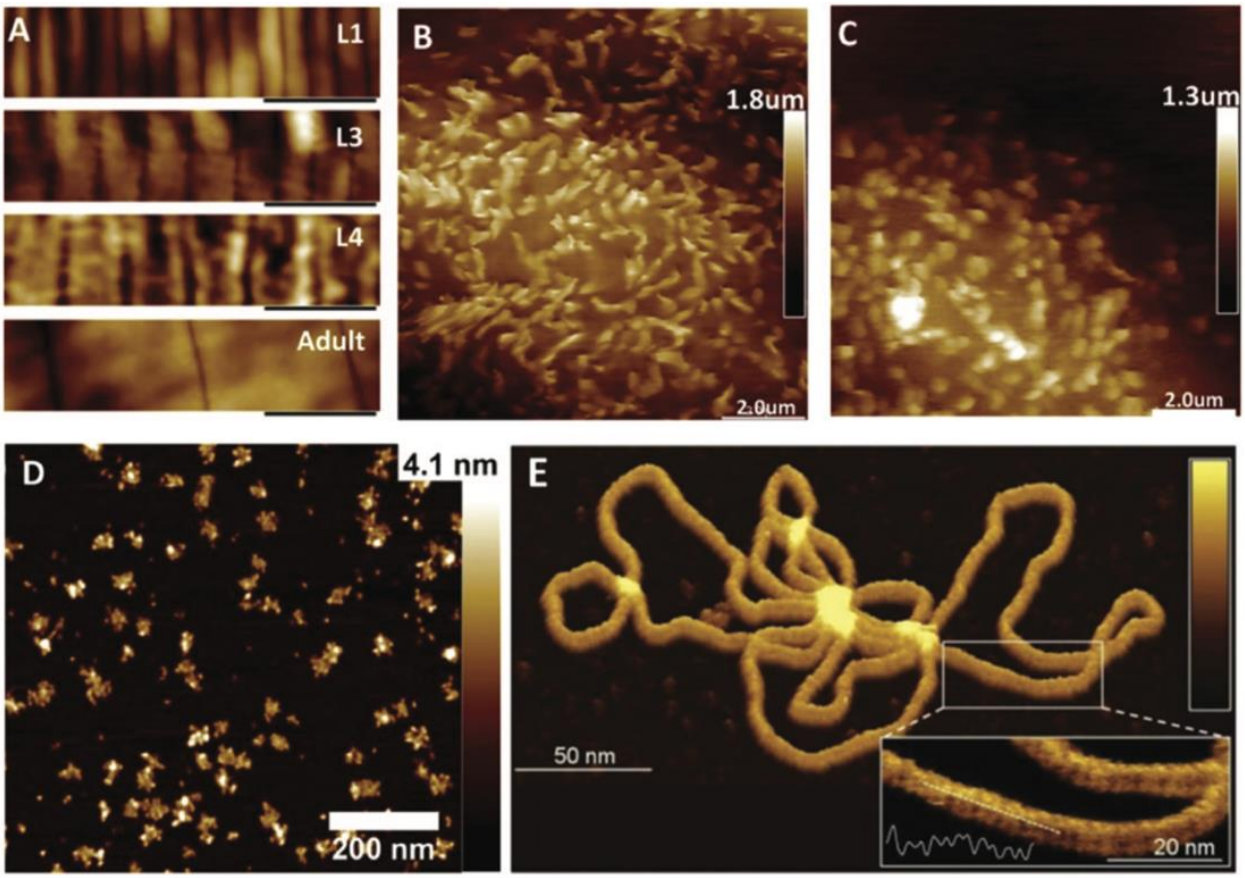


Figure 1.6 Different biological samples with PFT mode. (A) AFM images of Caenorhabditis elegans epicuticle cell at different processes of growth, (B) The images of the microvilli structure on a Madin-Darby Canine Kidney (MDCK) C11 cell with a vertical force of 100–130 pN setting, (C) The images of the microvilli structure on an MDCK C11 cell with a vertical force of 80–100 pN setting, (D) The image of the M immunoglobulin antibodies absorbed on mica in liquid environment, (E) High-resolution AFM topography of a single-molecule DNA. (Reproduced with permission from Ref. [47]).

1.3.2 Multi-head AFM (MH-AFM)

MH-AFM, referred to as parallel AFM[53], as illustrated in Figure 1.7, represents an advanced approach to surface imaging and characterization, offering unique capabilities for simultaneous and multifaceted nanoscale analysis. MH-AFM is commercialized by Nearfield Instrument Inc. and has been adopted by leading companies such as Samsung. Unlike conventional AFM systems that employ a single scanning probe, MH-AFM systems utilize multiple probes[54] arranged in a parallel configuration. This configuration enhances throughput, versatility, and efficiency in surface profiling and property mapping. This innovative technology shows significant potential for various applications across semiconductor manufacturing in-line inspection, materials science, nanotechnology, biology, and beyond[55]. One disadvantage of MH-AFM is the higher noise level, which results from the smaller mass of the positioning arms that place the scanning module onto the wafer at designated sites.

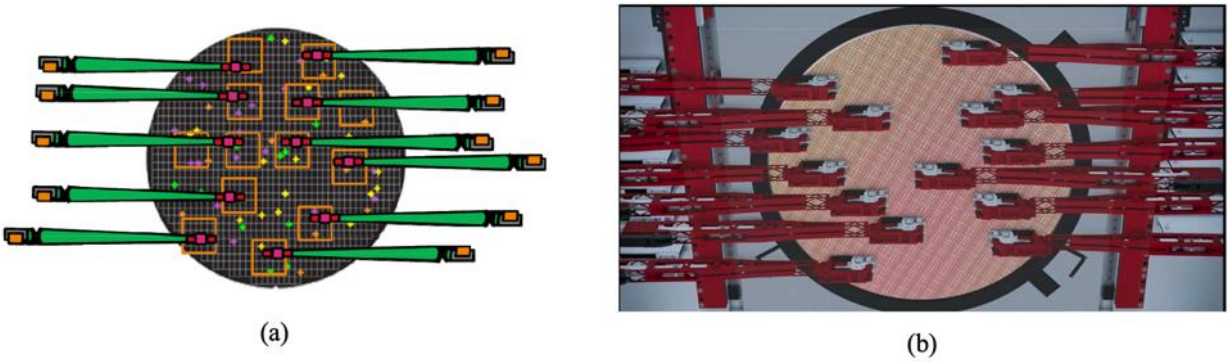


Figure 1.7 Overview of parallel SPM. (a) schematic illustration of parallel miniaturized SPM (MSPM) to image simultaneously several locations (here 11) on a wafer or mask. (b) detail with a wafer stage in the middle, up to 2×50 positioning arms (here 2×7) on two sides of the wafer stage, each capable of moving an MSPM scan head onto the 450 mm wafer. (Reproduced with permission from Ref. [53]).

Developed through a collaborative effort by researchers in nanoscience and microscopy, MH-AFM signifies a major advancement in surface measurement techniques, heralding a paradigm shift in the field[56]. By employing multiple scanning probes simultaneously, MH-AFM enhances imaging speed, throughput, and data acquisition efficiency, enabling the study of

complex surface phenomena with unprecedented detail and precision[57,58]. The concept of MH-AFM arose from recognizing limitations inherent in traditional single-probe AFM systems, such as the trade-off between imaging speed and resolution and the inability to perform multiple measurements concurrently.

1.3.3 High-speed AFM (HS-AFM)

HS-AFM represents a ground-breaking advancement in biological sensing, allowing researchers to observe rapidly changing biological phenomena in real time. Developed by Ando *et al.*, HS-AFM addresses the unique demands of imaging dynamic biological samples with exceptional temporal resolution, overcoming various challenges encountered in traditional AFM systems[59]. Ando's team emphasized using cantilevers with extremely high resonance frequencies and small spring constants, optimizing high-speed operation for biological samples. This combination facilitates high-speed scanning, allowing for the detection of rapid topographical changes with exceptional sensitivity.

Traditional Si and Si_3N_4 cantilevers face limitations in liquid environments due to their high Q-factors even with viscous damping. To address this, Adams's group explored alternative materials such as SU-8, which provide low Q-factors suitable for high-speed imaging of biological specimens[60]. Additionally, adopting small/short cantilevers (thus higher resonance frequency, $f \propto 1/L^2$) for high-frequency imaging poses challenges in conventional optical beam deflection (OBD) systems. Ando *et al.* developed modified beam detection methods to overcome this challenge, utilizing objective lenses with high working distances to effectively accommodate small cantilevers[61]. Furthermore, Schitter *et al.* redesigned the z-scanner for high-speed operation, introducing two types of z-scanners: one based on a comb-shaped flexure and another consisting

of several layers with interdependent motion between X, Y, and Z scanners[62]. These modifications enable precise and rapid sample movement while minimizing unwanted vibrations, thereby enhancing HS-AFM's performance for dynamic biological imaging.

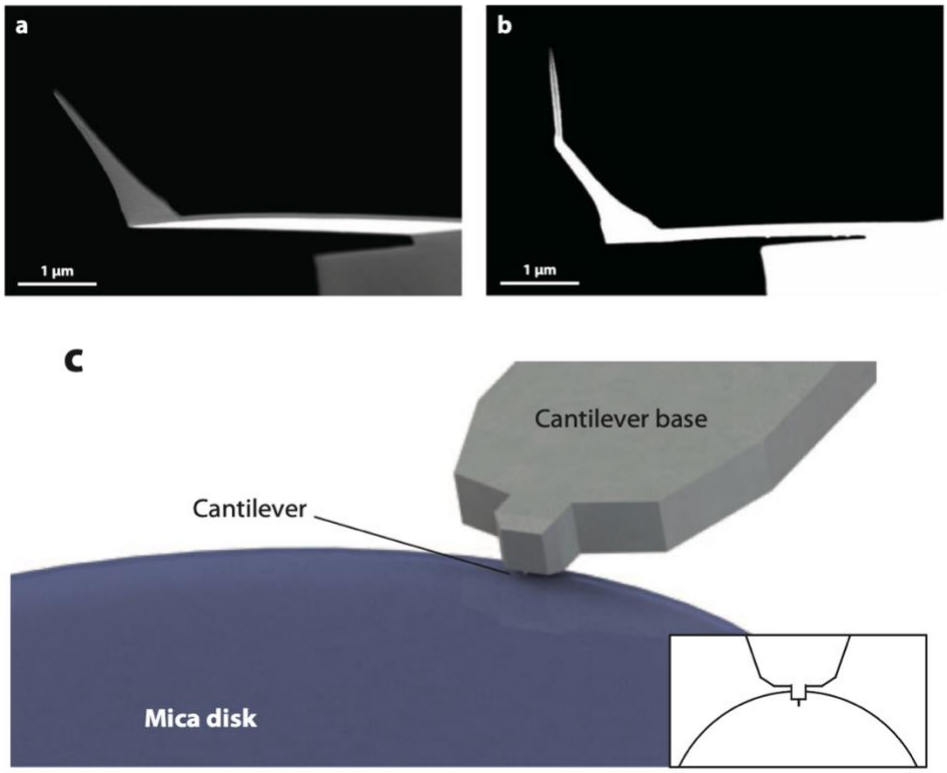


Figure 1.8 Cantilever, tip, and relative arrangement of cantilever and sample stage. (a) Scanning electron microscope (SEM) image of a small cantilever. (b) SEM image of an electron-beam-deposited (EBD) tip grown on an original bird-beak-shaped tip. (c) The relative arrangement between the sample stage and cantilever circumvents the disturbance by hydrodynamic pressure produced by quick displacement of the z-scanner. (Reproduced with permission from Ref. [63]).

The commercially available small cantilevers are primarily supplied by Olympus and NanoWorld. One particular model from Olympus[63], the BL-AC10DS-A2, is depicted in Figure 1.8. This cantilever measures 10 μm long, 2 μm width, and 130 nm in thickness, and it operates at a frequency of 0.6 MHz in water.

HS-AFM holds significant potential for investigating living cells. For instance, Payton *et al.*[64] have utilized HS-AFM in material science to study surface morphology and various properties of hydroxyapatite in different solvents. Uchihashi *et al.*[65] demonstrated the observation of the

bacteriolysis process of rod-shaped Bacillus subtilis subjected to lysozyme using a wide-area scanner in HS-AFM, as illustrated in Figure 1.9.

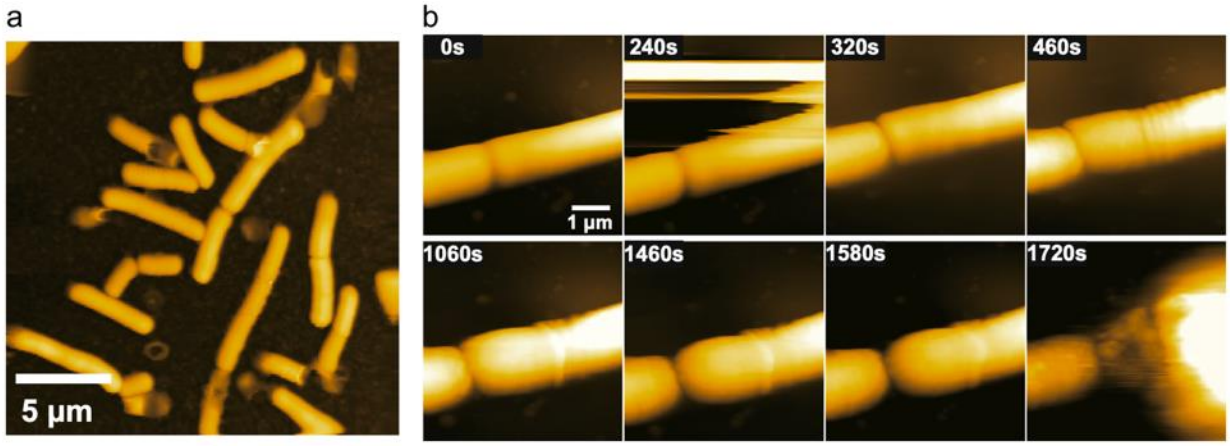


Figure 1.9 HS-AFM images of B. subtilis were captured using the wide-area scanner. (a) Topographic image of B. subtilis in a culture medium solution before adding lysozyme (imaging rate, 15 s/frame, pixels, 200 200). (b) Successive HS-AFM images showing the bacteriolysis process of B. subtilis subjected to lysozyme (imaging rate, 20s / frame; pixels 256). (Reproduced with permission from Ref. [65]).

1.3.4 Critical dimension AFM (CD-AFM)

Conventional AFMs, as mentioned above, gather information along a single axis (Z-axis) and are described as one-dimensional AFMs (1D-AFMs). These 1D-AFMs are limited in their ability to access and measure vertical features or profiles with negatively tapered sidewalls. Given the importance of controlling process variability in semiconductor manufacturing, there is a need for metrology capabilities beyond those of 1D-AFM. CD-AFM, also known as 3D-AFM, addresses this need by enabling force sensing and data acquisition in three axes. Developed in the early 1990s, CD-AFM is now the most commercially prevalent implementation of 3D-AFM[66]. This technique requires flared tips[67], as illustrated in Figure 1.10, allowing it to image vertical and reentrant sidewalls, which are crucial for quantifying 3D features.

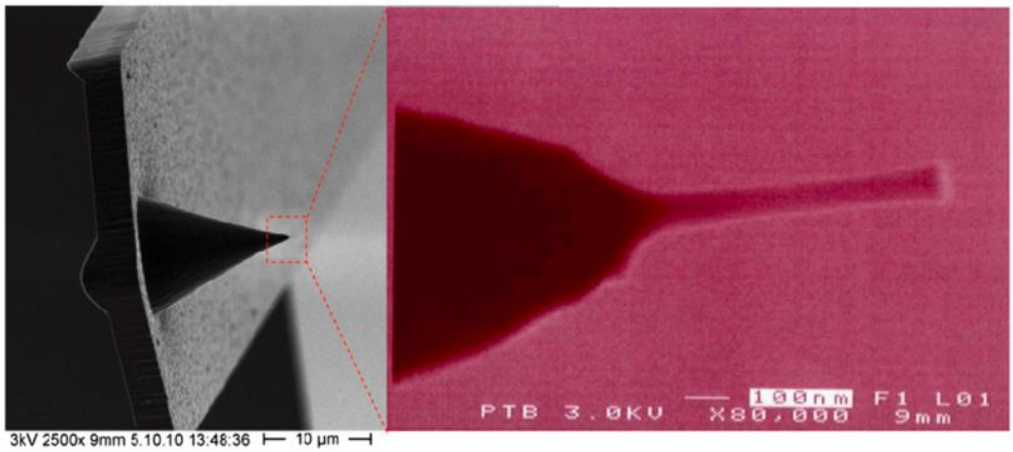


Figure 1.10 An SEM image was taken of the used CDR120 tip after the AFM measurements. (Reproduced with permission from Ref. [67]).

Incorporating a bidirectional servo and feedback system, CD-AFM captures data predicated on the sidewall topography rather than using fixed lateral spacing. Dai *et al.* have demonstrated the capability of CD-AFM in achieving 3D imaging of a line structure with a nominal width of 300 nm on a PTB photomask, with the middle CD evaluated by CD-AFM[67], as depicted in Figure 1.11. A more recent competing technique involves the controlled and measured tilting of the AFM head during imaging. This method obviates the need for flared tips, as its accuracy is derived from the decoupling of lateral and vertical scanner axes and the precision of data stitching at varying tilt angles. However, this technique is currently not commercially available. CD-AFM combines the high-resolution imaging capabilities of traditional AFM with enhanced metrological precision, enabling the accurate measurement of features such as line widths, trench depths, and other nanoscale geometries critical to the performance of semiconductor devices. This technique leverages a sharp probe tip that scans the surface of the sample, detecting interactions between the tip and the sample to produce detailed topographical maps. The key advantage of CD-AFM lies in its ability to provide three-dimensional measurements with sub-nanometer accuracy, making it indispensable for process control and quality assurance in

semiconductor manufacturing. Many companies such as Bruker[68] and Infinitesma[69] launched CD-AFM for commercial use in the semiconductor industry.

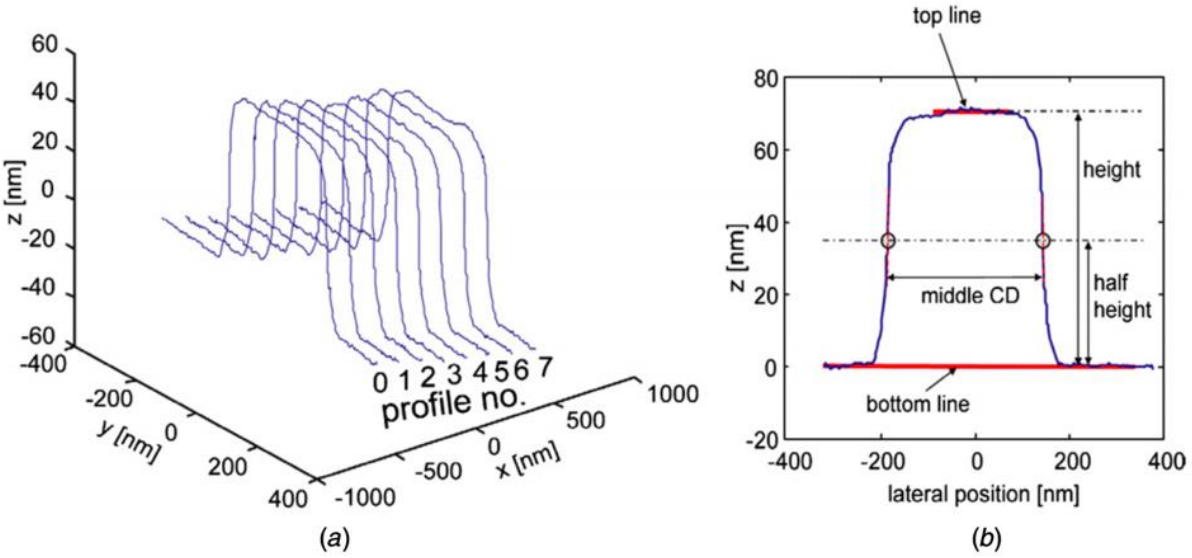


Figure 1.11 Profile of a line structure of a photomask measured in vertical oscillation mode, shown as eight profiles taken at different positions within one measurement (a) and a profile after first-order levelling (b). The middle CD is evaluated as the width of the structure at the half-height of the profile. (Reproduced with permission from Ref. [67]).

1.4 Applications

AFM is vital for characterizing micro/nanostructures and finds applications in diverse fields such as material science, medicine, and the semiconductor industry. It further offers valuable insights into the 3D morphology of chips for the integrated circuit (IC) industry with recent advances. According to a comprehensive report on AFM probe market size, share, growth and industry analysis, by type (Si AFM probes, SiN_x AFM probes, diamond AFM probes), by application (life sciences and biology, materials, semiconductors and electronics, others) and regional forecast to 2032[70], the global market for AFM probe was valued at USD 193 million in 2019. It is projected to reach USD 496.94 million by 2032, reflecting a compound annual growth rate (CAGR) of 7.5% over the forecast period. The anticipated distribution of AFM probe applications by 2032 is shown in Figure 1.12.

In material science, AFM is a versatile tool capable of capturing the three-dimensional topography and revealing variations in physical property distributions such as friction, piezoelectric characteristics, and magnetic properties. Xing *et al.*[71] introduced a method to analyze the topography of ferromagnetic 2D materials using AFM. In biomedicine, AFM finds extensive application in the in-situ imaging and research of various biological entities such as proteins, cells, viruses, and other biomolecules. For instance, Deng *et al.*[72] introduced a novel protocol for studying living cancer cells. Efremov *et al.*[73] proposed a method to investigate anisotropy and isotropy in living cells leveraging AFM. Yvanoff *et al.*[74] utilized AFM to investigate the osteocyte's dendrites penetrating the osteoblast's cell membrane in 2022, providing insights into Young's modulus stiffness map of the cell-cell contacts.

The International Technology Roadmap for Semiconductors (ITRS) predicts that the control of printed physical gate length variability will need to be within 0.7 nm by 2025[75]. Additionally, global semiconductor sales in 2023 have reached $515 billion[76], underscoring the increased demand (50% of total market size) for AFM characterization in semiconductor 3D characterization, as illustrated in Figure 1.12. In the semiconductor industry, AFM plays a crucial role in detecting substrate surface defects, surface topography, and roughness while further identifying critical parameters like leakage current, structural defects, and lattice mismatch. For instance, Lee *et al.*[77] showcased the advantages of AFM in the context of 45 nm node and beyond technologies. Since the 21st century, AFM has demonstrated the potential to meet the demands of 3D capabilities in the IC industry[78–80]. Murugesan *et al.*[81], for example, employed AFM to scan low-resistance copper-tin (Cu-Sn) micro-bumps for 3D chip stacking applications in 2012. With advancements in chip fabrication across various fields, the scope of application for AFM in 3D scenarios has expanded significantly. Ma *et al.*[82] developed a non-magnetic heating chip for a spin-

exchange relaxation-free (SERF) atomic magnetometer in 2022, utilizing AFM to characterize the nichrome film inside the chip.

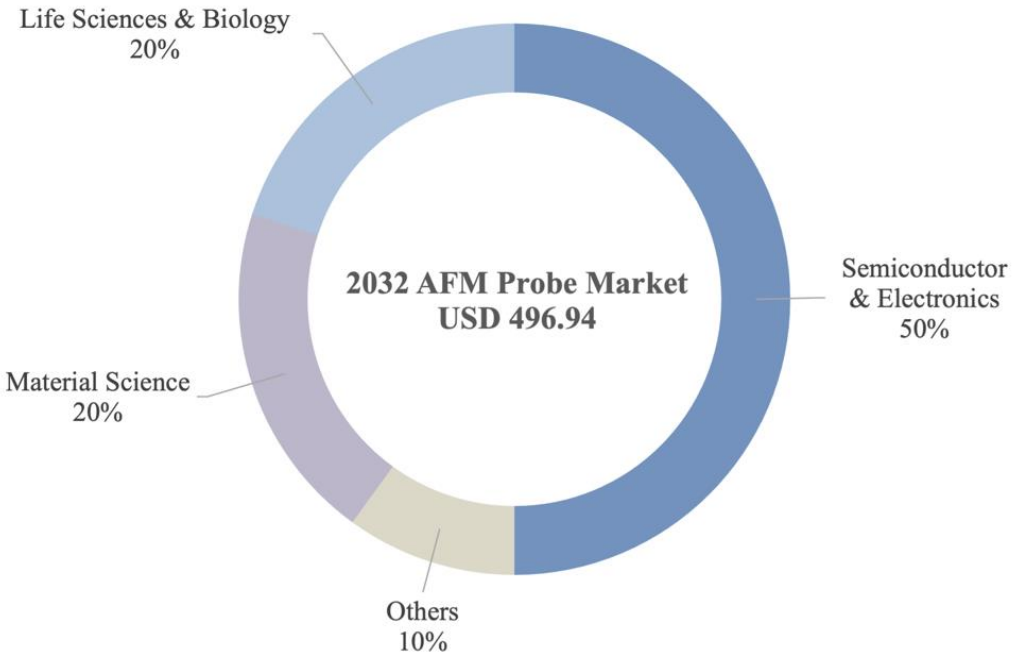


Figure 1.12 Projected distribution of AFM probe applications by 2032.

1.5 Motivations and Research Objectives

This thesis focuses on the fabrication techniques of the HAR AFM probe, including the fabrication of HAR Si nanocones and nanopillars with potential applications in diverse fields. The first objective is to fabricate Si tip/cone structures with high aspect ratios, applicable in field emission X-rays, solar cells, and various types of sensors. Current methods to fabricate such structures encompass bottom-up and top-down techniques. The bottom-up self-assembly approach, primarily vapor-liquid-solid (VLS) growth, struggles to achieve ordered Si nanocone arrays. Top-down approaches include wet and dry etching. Due to the poor uniformity and lack of tunability for the tip shape for wet etching, this thesis primarily employs dry etching, proposing four distinct methods. The innovations and advantages of each method are illustrated in Figure 1.13.

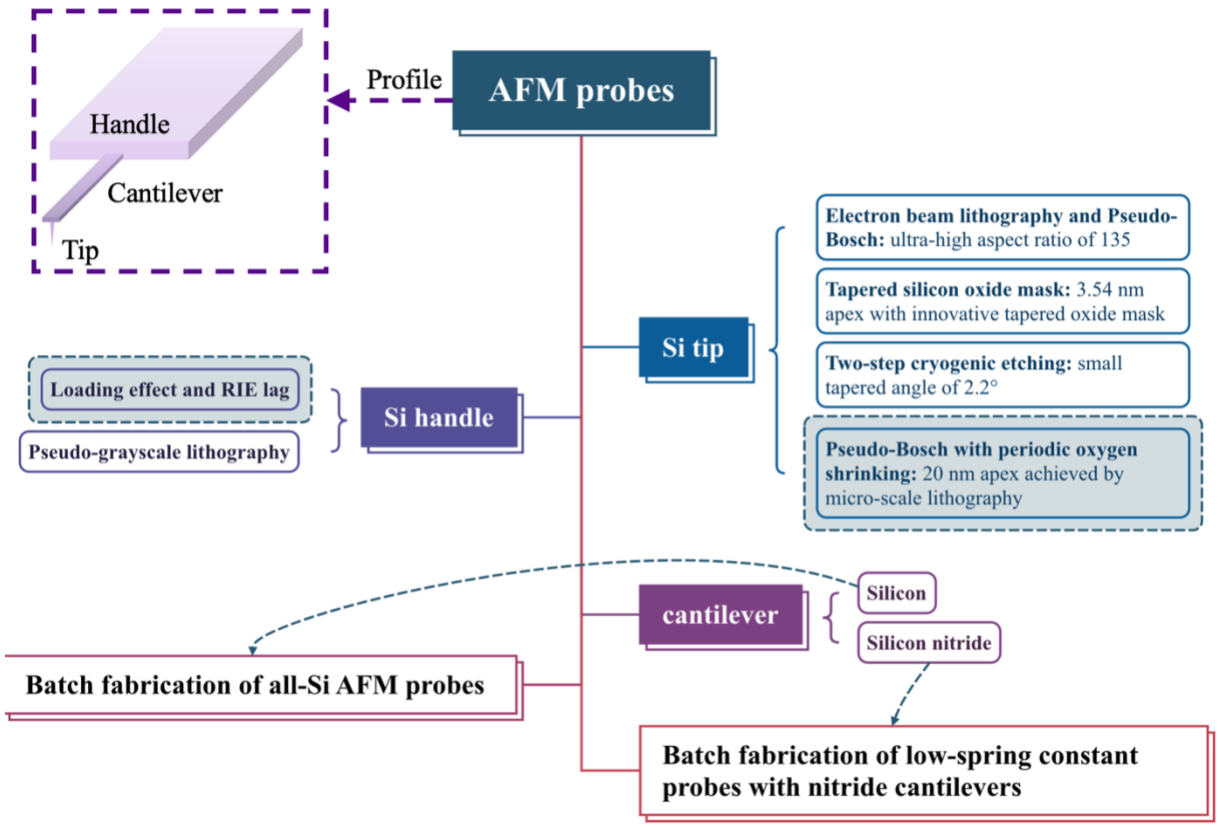


Figure 1.13 Research objectives for AFM probes.

For the tip handle fabrication, we also employed dry etching, notably deep silicon etching which is becoming more and more efficient. However, deep Si etching gives vertical sidewalls, which may block the laser light by the vertical wall at the handle-cantilever joining point. To address this issue, a novel stair-shaped handle has been proposed and developed using two methods. These methods are straightforward without adding more process steps (lithography and etching), as detailed in Figure 1.13.

The third objective of this thesis is the mass production of HAR probes for different imaging conditions. By combining HAR tips with the stair-shaped handle, two different probes were simulated and fabricated using Si and SiN_x for the cantilever. This mass production method is cost-effective and controllable. Given the rapid development of semiconductor devices and the

swift reduction in critical dimensions, this approach significantly broadens the range and applications of AFM probes.

Chapter 2 Traditional Fabrication Process of AFM Probe

Chapter 2 outlines the conventional batch fabrication techniques for two distinct AFM probes: all-Si and all-nitride probes. The resulting tip profiles in both cases are pyramids with modest aspect ratios. To enhance the aspect ratio of these tips, five traditional techniques for fabricating HAR tips, including FIB milling, EBID/IBID, carbon nanotube attachment, NaugaNeedles self-assembly and thermal oxidation sharpening techniques are presented, along with their respective advantages and disadvantages. The following section introduces the specific techniques employed for probe fabrication in this work.

2.1 Batch Fabrication of Commercial All-Si AFM Probes

The batch fabrication steps for standard and commercial all-Si AFM probes are depicted in Figure 2.1, and this batch fabrication process is provided by NanoWorld[83]. Initially, a double-side polished <100> Si wafer is utilized (Figure 2.1a), which undergoes cleaning with acetone, isopropanol (IPA), and a deionized water rinse. Thermal oxidation of both sides of the wafer results in forming SiO_2 layers (Figure 2.1b), enhancing selectivity to etching solutions in subsequent steps. Then, a layer of photoresist is spin-coated on the backside of the wafer, followed by photolithography (Figure 2.1c) and development (Figure 2.1d) to define the tip patterns. Similarly, a new round of resist spin-coating, baking, photolithography, and development is carried out on the front side of the wafer to define the cantilever patterns (Figure 2.1e and 2.1f). The pattern transferred from the photoresist to the SiO_2 layer is done by wet isotropic etching, commonly immersed in hydrofluoric acid (HF) or buffered oxide etchant (BOE) (Figure 2.1g). The remaining photoresist is then removed by immersing the sample in acetone and using ultrasonication to assist

the resist strip (Figure 2.1h). The successful transfer of the mask to the oxide layer and the adequate resist removal is crucial to prevent micro-masking in subsequent wet anisotropic etching of Si.

Subsequently, anisotropic Si etching using potassium hydroxide (KOH) is performed until the oxide mask at the apex of the pyramid falls off (Figure 2.1i). Further Si etching needs to be done on the backside of the wafer to obtain a cantilever with the desired thickness and release the AFM probe. However, the newly formed tip needs protection from subsequent KOH etching. For this reason, the front side of the sample is coated by the Si_3N_4 protective layer (Figure 2.1j). Anisotropic wet etching is done on the backside until the desired cantilever thickness is achieved (Figure 2.1k). Finally, the remaining Si_3N_4 is removed in an HF/BOE solution to expose the AFM probes (Figure 2.1l). Notably, the handle is omitted from the fabrication steps for clarity.

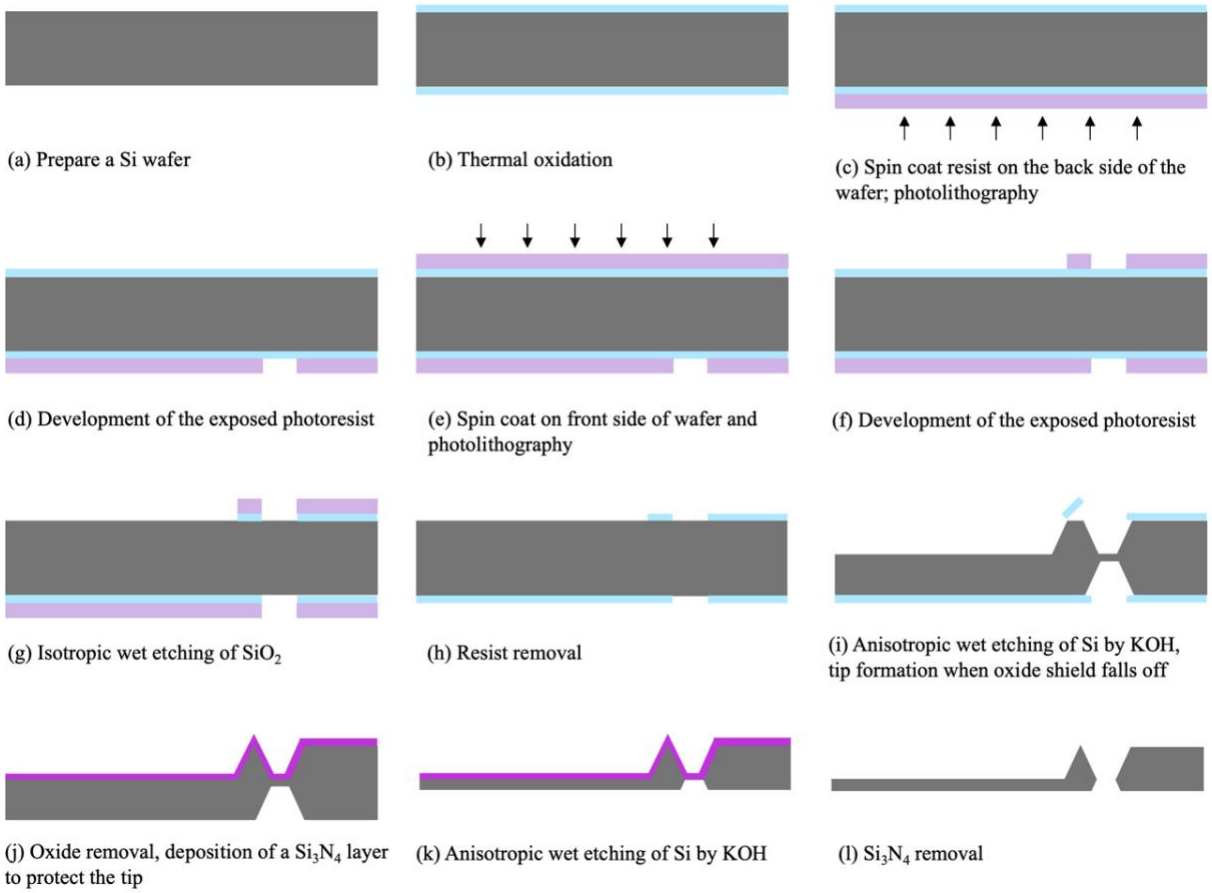


Figure 2.1 Batch fabrication of commercial all-Si AFM probes[83].

Figure 2.2 illustrates the profile of the standard tapping probe[84] (Non-contact/Tapping mode, high resonance frequency, NanoWorld Pointprobe NCH). This pyramidal probe features a resonance frequency ranging from 250 to 390 kHz, coupled with a force constant spanning from 21 to 78 N/m. Its dimensions include a cantilever length of 120 to 130 μm, a width ranging from 25 to 35 μm, and a thickness of 3.5 to 4.5 μm.

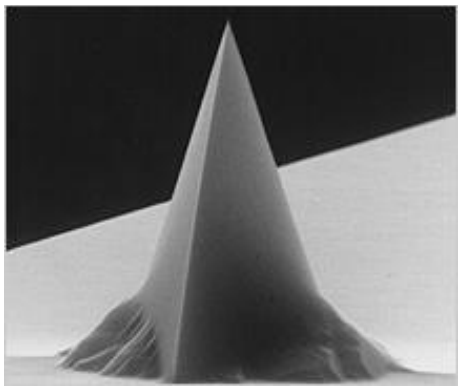


Figure 2.2 The profile of the standard tapping probe, and the probe type is NanoWorld Pointprobe NCH[84].

2.2 Commercially Available Batch Fabrication of All-Si_3N_4 AFM Probes

The batch fabrication steps of all-Si_3N_4 AFM probes[83] are depicted in Figure 2.3, and this batch fabrication process is provided by NanoWorld. Similar to the all-Si probe fabrication outlined in Chapter 2.1, cleaning and thermal oxidation are applied on the double-side polished <100> bare Si wafer (Figure 2.3a-b). After coating and exposing the imaging photoresist on the front side of the wafer (Figure 2.3c), the subsequent development determines the tip patterns (Figure 2.3d). Despite SiO_2 being present on the backside, a protective resist is spin-coated to prevent backside oxide etching (Figure 2.3e). The tip pattern is transferred to the oxide layer on the front side using HF/BOE, and the remaining photoresist is stripped using acetone (Figure 2.3f). The following Si etching in KOH forms an inverse pyramid gap, which is later filled by Si_3N_4 to be the tip structure (Figure 2.3g). After the oxide masks on both sides are removed, the sample undergoes oxidation again to sharpen the pyramid gap/tip profile (Figure 2.3h), and a layer of low-

stress amorphous nitride is deposited via the LPCVD process (Figure 2.3i). A resist layer is spin-coated on the front side to protect the gap (Figure 2.3j), and the oxide and nitride layers on the backside of the wafer are removed using BOE (Figure 2.3k). After resist removal, the imaging photoresist for probe separating is coated, followed by exposure (Figure 2.3l).

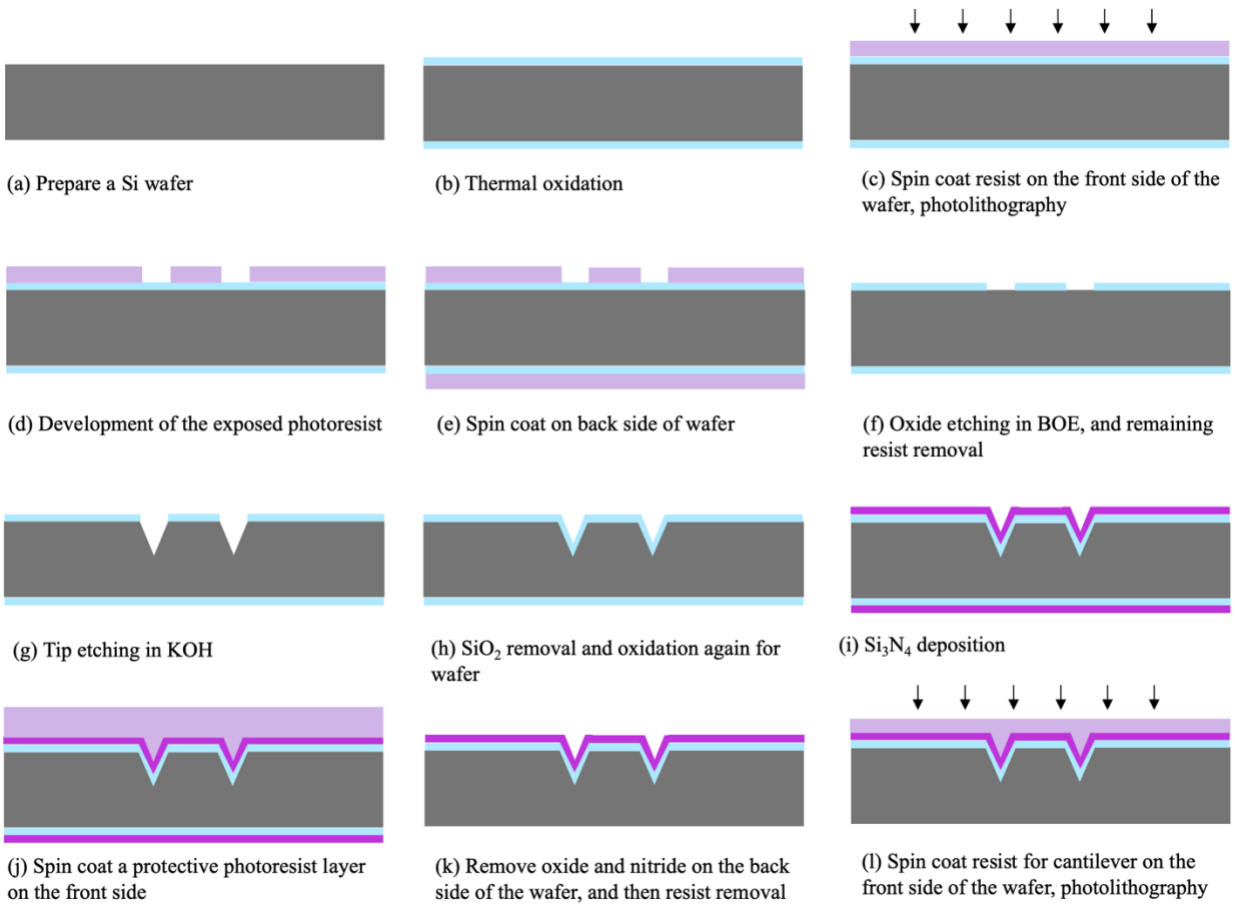


Figure 2.3 Batch fabrication of commercial all-Si_3N_4 AFM probes[83].

After development (Figure 2.4m), the Si_3N_4 layer is etched using DRIE (Figure 2.4n), which separates the probes from each other, and the remaining resist is removed via acetone ultrasonication or O_2 plasma (Figure 2.4o). A Pyrex wafer is prepared and cleaned for anodic bonding (Figure 2.4p), and it is then diced away from the regions covering both the tip and the cantilever (Figure 2.4q-r). Finally, the backside Si and SiO_2 are etched away by KOH and BOE

(Figure 2.4s-t). Optionally, a layer of aluminum or Au is coated on the backside to enhance the reflection signal (Figure 2.4u).

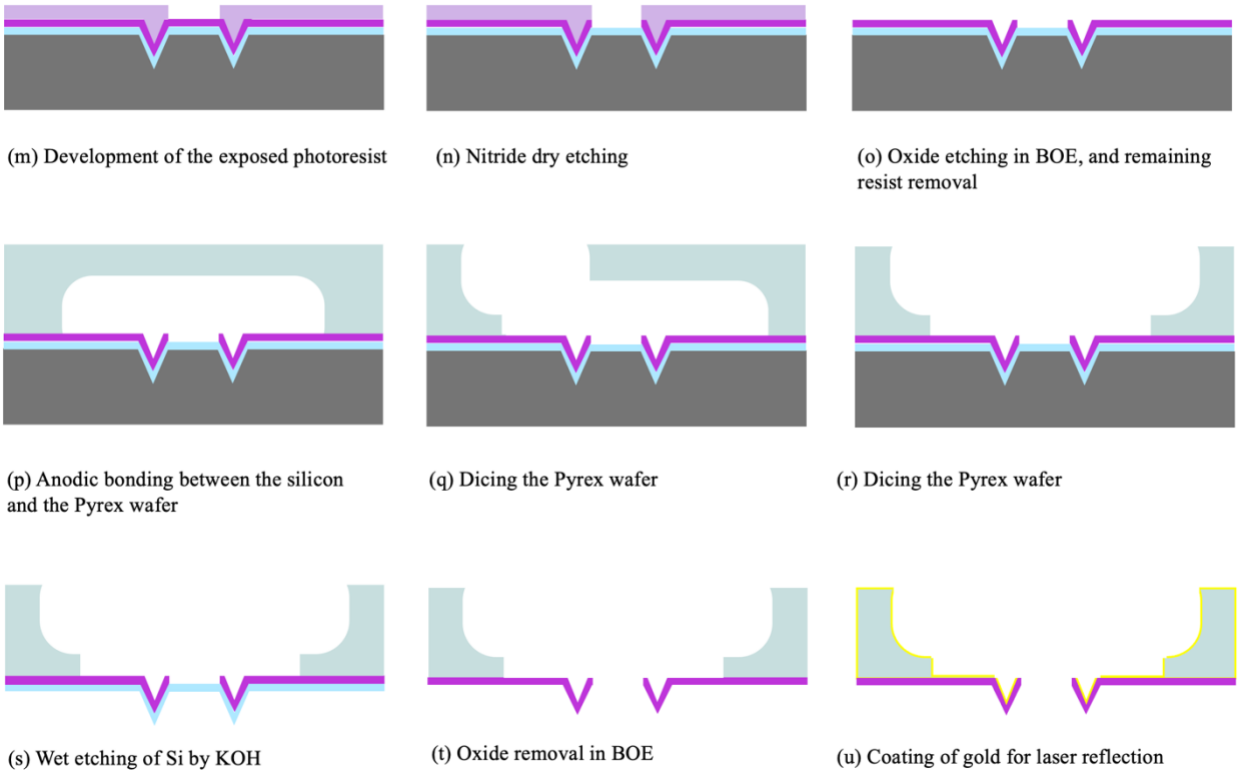


Figure 2.4 Batch fabrication of commercial all-Si_3N_4 AFM probes[83]. (continued)

Figure 2.5 presents the profile of the standard nitride probe, specifically the Pyrex-Nitride Probe-Diving Board AFM cantilevers[85] (NanoWorld PNP-DB). This particular probe boasts a resonance frequency of 67 kHz and a force constant of 0.48 N/m. Its dimensions comprise a length of 100 μm, a width ranging from 30 μm to 40 μm, and a thickness of 500 nm. The nitride layer is applied using thin-film technology, specifically LPCVD, allowing for precise control over the thickness of the cantilever. In contrast, the thickness of Si probes is less predictable due to the wet process involved in their production. Additionally, nitride is inherently harder than Si, resulting in increased durability, making it a preferred choice for contact mode measurements where repeated

contact with the sample surface occurs. However, Si probes can achieve finer tips than nitride tips, consequently offering higher resolution in the former case.

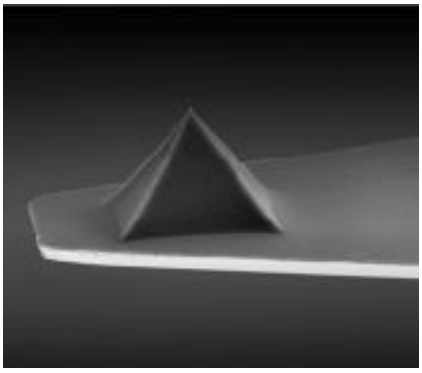


Figure 2.5 The profile of the standard nitride probe, and the probe type is NanoWorld PNP-DB[85].

2.3 Traditional Techniques for Fabricating HAR AFM Tip

In comparison to standard commercial Si AFM tips, high aspect ratio tips significantly enhance imaging resolution and clarity. As illustrated in Figure 2.6, standard AFM tips with low aspect ratio fails to reach the bottom of deep trenches, leading to distorted and inaccurate images. High aspect ratio tips, which typically have a length at least two times greater than the diameter of the tip base, are essential for accessing narrow gaps and intricate topographies. This design improvement ensures more precise and accurate scanning results, thereby providing higher-quality images during the AFM scanning process. In this work, the aspect ratio for cylindrical tip profiles is defined as the ratio of height to diameter, while for conical tip profiles, it is defined as the reciprocal of the tangent of the internal half angle ($\tan\theta$), where the internal half angle is the measured angle as depicted in Figure 2.6.

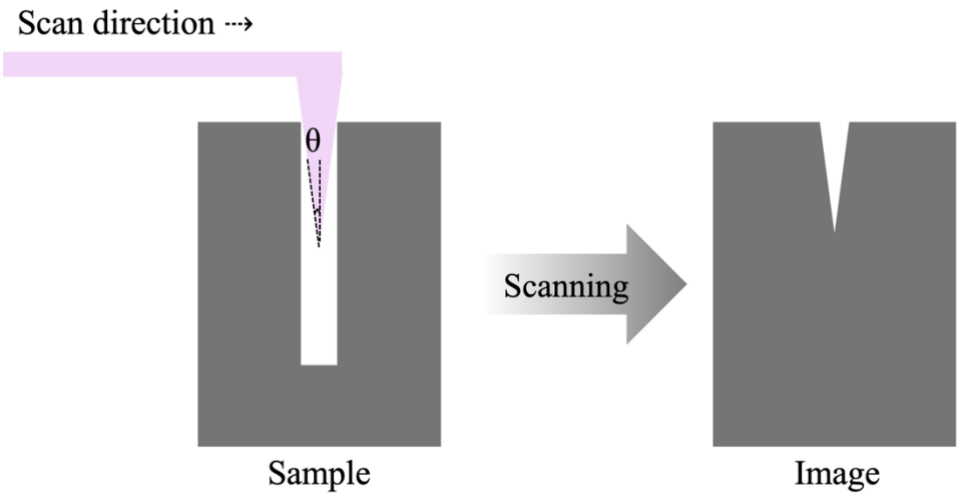


Figure 2.6 Schematic representation of AFM scanning process using standard tips.

2.3.1 Focus ion beam (FIB) milling technique

The concept of FIB originated from the intersection of ion beam technology and SEM, with the pioneering work of Albert Crewe and Charles Fiori in the 1970s[86]. However, it was not until the late 1980s and early 1990s that commercial FIB systems became available, thanks to efforts by companies like FEI Company[87] (now Thermo Fisher Scientific) and their development of sophisticated instruments capable of delivering tightly focused beams of ions with exceptional precision. At its core, FIB milling technology utilizes a focused beam of ions, typically gallium ions (Ga^+), to mill away material on a sample surface with nanometer-scale resolution. This enables the creation of intricate patterns, the removal of material for cross-sectional analysis, and the modification of device structures at the micro- and nanoscale levels.

The first HAR SPM metal probe was made by Vasile *et al.* in 1991[88], featuring a final tungsten (W) / iridium (Ir) tip apex sharpened to 3-4 nm using FIB milling. Building upon this achievement, Rodriguez *et al.* (2021)[89] applied FIB techniques to mill Si tips on commercial AFM probes. In a subsequent effort to enhance efficiency and reduce costs, Samaan *et al.*[90] employed

FIB to mill a metal mask layer, which was then transferred onto a Si commercial probe in 2023 (Figure 2.7). A novel FIB-based "lift-off" method, introduced by Tan *et al.* in 2016[91], enabled the milling of Si HAR nanowires to create commercial probes, allowing for easy adjustment of the tilt angle of the nanowire tip relative to the cantilever axis by tilting the sample stage. Additionally, Fu *et al.*[92] demonstrated in 2006 the feasibility of milling nitride using FIB techniques.

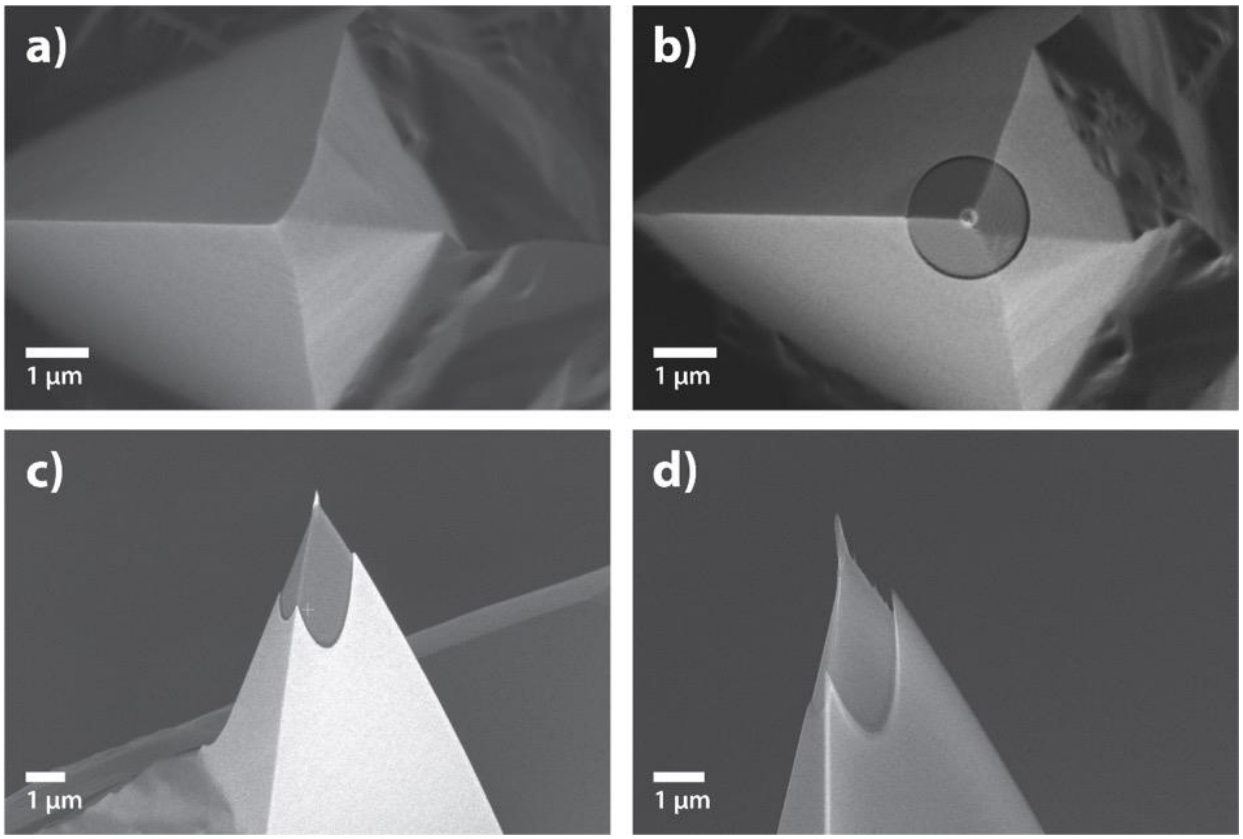


Figure 2.7 (a) Top view after bilayer metal deposition of Al (30 nm) and Cr (10 nm), (b) top view after FIB milling of Cr (10 nm), (c) tilted view (70º) after plasma etching of Al (30 nm), and (d) tilted view (70º) after plasma etching of Si. (Reproduced with permission from Ref. [90]).

Indeed, the current FIB milling process for fabricating probe tips suffers from low throughput and high costs. Each tip must be processed individually, requiring the operator to meticulously focus and adjust the electron and ion beams before milling. Consequently, the entire milling process for a single tip can take tens of minutes, leading to poor overall throughput and significantly inflated costs.

2.3.2 Electron/ion beam-induced deposition (EBID/IBID) techniques

In the 1980s and 1990s, researchers began exploring FIB and EB's potential for deposition instead of imaging and milling. By precisely controlling the beam position and intensity, they demonstrated the ability to deposit materials onto substrates at the nanoscale, effectively laying the groundwork for IBID and EBID. These early experiments laid the foundation for subsequent advancements in the field.

A crucial step involves introducing gaseous precursors into a vacuum chamber. As the electron or ion beam traverses the substrate surface, these gaseous materials undergo decomposition, resulting in two distinct product types: volatile and non-volatile species. Volatile species comprise molecules that readily vaporize under vacuum conditions within the chamber, and non-volatile species undergo chemical transformations or breakdown upon interaction with the electron or ion beam. These reactions lead to the formation of solid or semi-solid deposits, which adhere to the scanning area.

During the same timeframe as the fabrication of HAR probes through FIB milling, Keller *et al.*[93] pioneered using EBID by depositing a thin carbon pillar onto the tip of a commercially available nitride cantilever. This approach was subsequently adopted by Brown *et al.*[94], who utilized EBID to fabricate a HAR Pt tip apex, achieving a remarkable final tip diameter of only 4 nm in Figure 2.8. Similarly, Nanda *et al.*[95] demonstrated the fabrication of a HAR PtC AFM tip with a final diameter of 13 nm, employing the IBID technique to modify the tip apex.

Compared to FIB milling, EBID and IBID techniques offer the advantage of creating higher aspect ratio structures, reaching ratios as high as 1000:1. Although EBID and IBID techniques offer precise control over electron or ion beam deposition, allowing for the creation of

perfectly profiled structures, these methods are also associated with high costs and time-consuming processes.

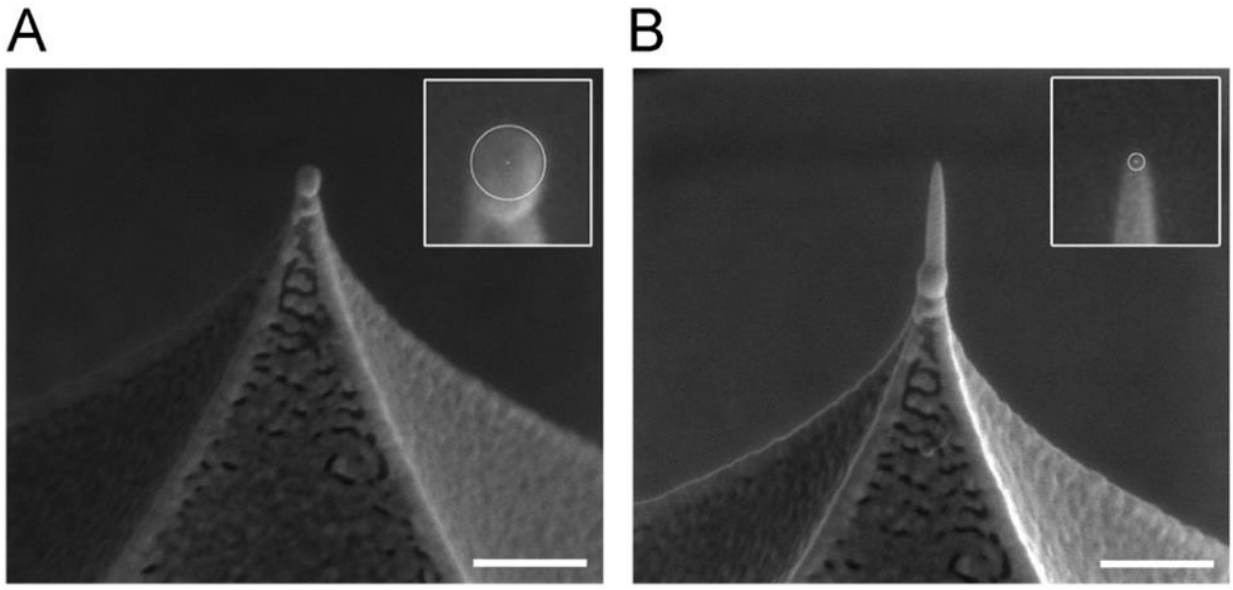


Figure 2.8 SEM images of (A) a commercial OMCL-TR800PB-1 cantilever and (B) the same cantilever following modification by EBID of Pt; scale bars: 200 nm. In both images, the axis of the probe is tilted at 52° to the electron beam. The magnified probe tips (shown inset) show calibrated circles drawn in the SEM software to measure radius-of-curvature; circles of radius~21 nm and~4 nm for the commercial and modified probe, respectively. (Reproduced with permission from Ref. [94]).

2.3.3 Carbon nanotube (CNT) attachment technique

CNTs are cylindrical nanostructures composed of carbon atoms arranged in a hexagonal lattice, reminiscent of rolled-up graphene sheets, and they represent a remarkable class of nanomaterials with extraordinary properties. Discovered in 1991 by Sumio Iijima[96], CNTs have since captured the imagination of scientists and engineers worldwide, sparking intense research efforts aimed at unlocking their unique properties and harnessing them for diverse applications. As depicted in Figure 2.9, the fabrication of wafer-scale CNT AFM tips was reported by Engstrom *et al.*[97], and they demonstrate an apex diameter of around 2 nm using PECVD. These tips offer a smaller apex diameter and more extended pillar height than those fabricated using EBID/IBID

techniques. However, a significant challenge lies in attaching or growing CNTs directly onto the tip apex with precise control over position, orientation, and length.

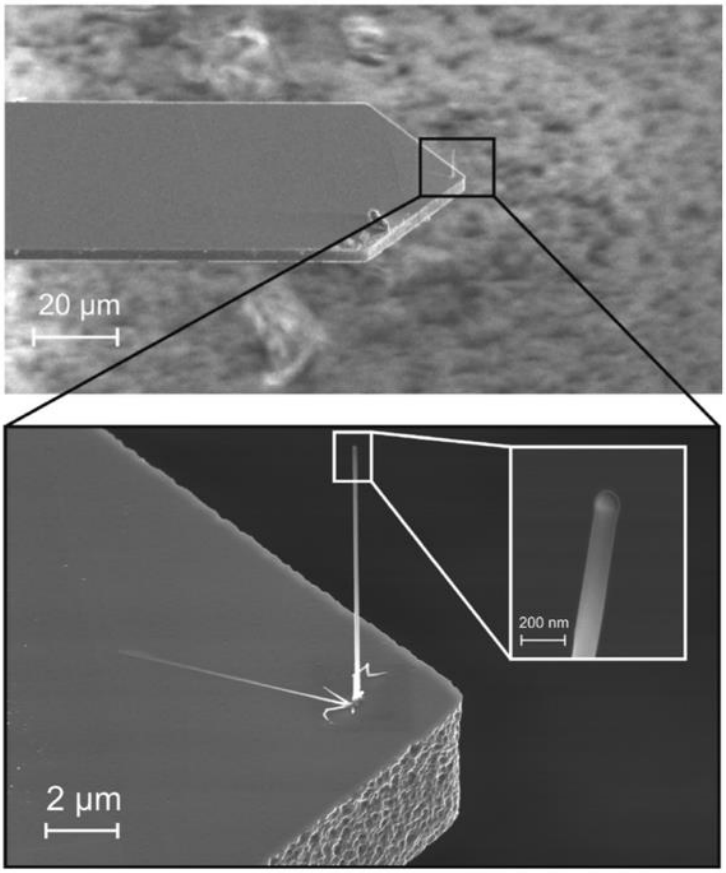


Figure 2.9 Electron micrograph of an epitaxially grown SiNW on an AFM cantilever. (Reproduced with permission from Ref. [97]).

2.3.4 NaugaNeedles self-assembly technique

Yazdanpanah *et al.*[98] introduced a novel method in 2008, based on the self-assembly of silver-gallium alloy (Ag_2Ga) at room temperature. This innovative approach, later commercialized by NaugaNeedles company[99], involved inserting a silver (Ag)-coated AFM probe into a freshly melted drop of gallium (Ga). As a result, the Ag_2Ga alloy self-assembled into structures extending to hundreds of µm, as illustrated in Figure 2.10, featuring long heights and needle tips with extremely high aspect ratios. However, controlling the length of these needle tips posed a challenge

due to the statistical nature of crystallization. Additionally, achieving volume production of needle-shaped HAR AFM tips using this method has not yet been realized.

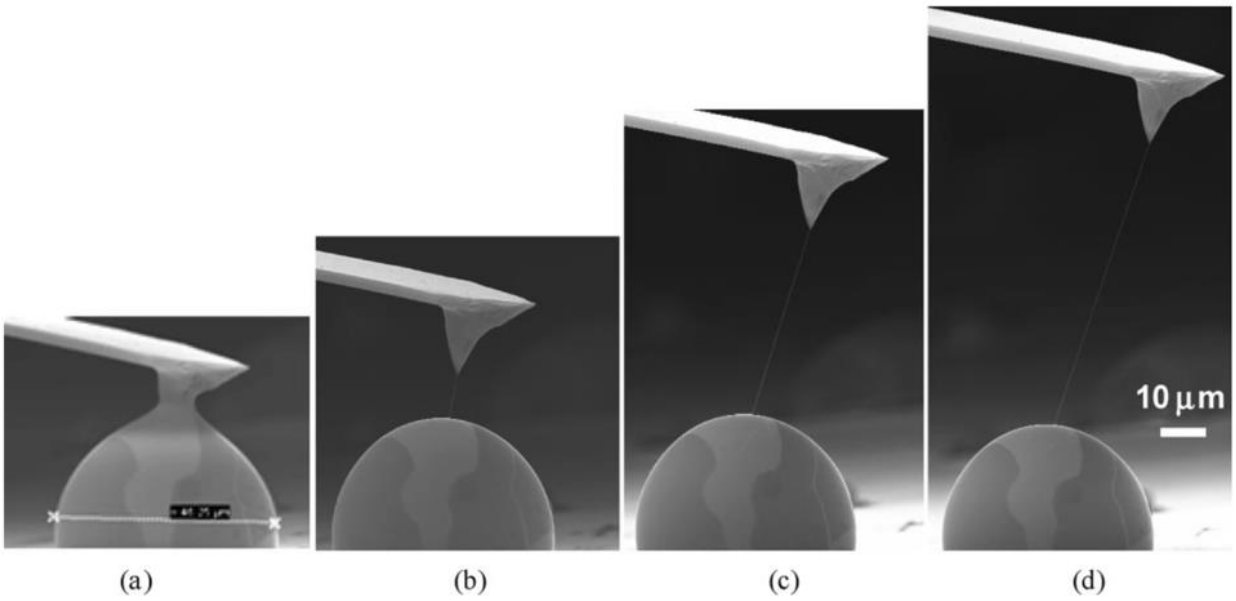


Figure 2.10 Time-lapse SEM images that show the growth of an Ag_2Ga nanoneedle on an AFM tip. The images show the cantilever tip (a) first inserted into the droplet, then retracted (b) 10 μm, (c) 43 μm, and (d) 67 μm. (Reproduced with permission from Ref. [98]).

2.3.5 Thermal oxidation sharpening technique

Bruce Deal and Andrew Grove[100] established a model for the thermal oxidation of Si, offering a comprehensive explanation of the one-dimensional (1D) growth of SiO_2. The model simplifies the process by illustrating that SiO_2 grows rapidly on the planar surface during the initial thermal oxidation stage, following a near-linear relationship. Subsequently, oxygen (O) atoms diffuse through the existing SiO_2 layer and react with Si, forming new oxide layers. However, as the oxide thickness increases, the diffusion slows down, limiting the growth rate of SiO_2 and establishing a parabolic model for long-term 1D SiO_2 growth[101].

In this study, the profile under consideration is a 3D nanocone with a convex apex, as shown in Figure 2.11[102], and the nanocone can be sharpened through thermal oxidation followed

by HF wet etching. This is due to the fact that the oxidation process depends on stress, and thermal oxidation always induces compressive stress owing to the insertion of O into the Si lattice. Slower oxidation occurs on curved (concave or convex corner) surfaces where stress is higher[102,103]; since the tip apex has the smallest radius of curvature, the oxide growth rate is correspondingly slower at these points.

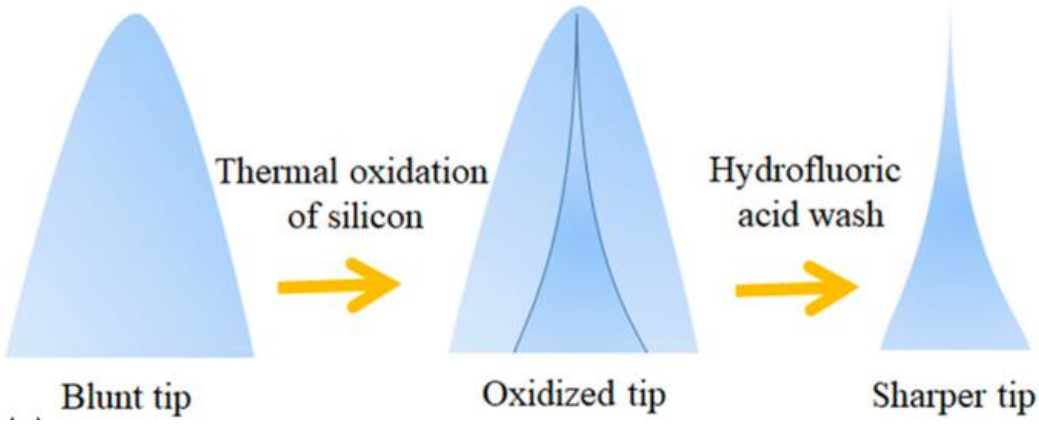


Figure 2.11 Schematic drawing of the oxidation sharpening process. (Reproduced with permission from Ref. [102]).

The oxidation sharpening technique described here requires an initial cone shape for effective sharpening. Without this prerequisite shape, the method may not achieve the desired results. This approach holds promise for further refining our nanocone structures in the context of our work. Higher temperatures contribute to stress reduction in SiO_2, which may not be conducive to achieving the desired sharpening effects when exceeding 1050 °C. Thus, a thermal oxidation temperature close to 950 °C is generally preferred to optimize results.

2.4 Specific Techniques in Probe Fabrication

2.4.1 Electron beam lithography (EBL)

EBL has undergone significant advancements, with ongoing research aimed at improving resolution, throughput, and scalability. Today, EBL remains a leading technique for nanoscale

patterning (less than 5 nm) in semiconductor fabrication. Electron beams are focused using electron optics, offering superior resolution to photon-based techniques due to their much smaller associated DeBroglie wavelength. The electron flow, generated by an electron emission gun, is accelerated to high kinetic energy before being focused onto a spot by a series of condenser lenses, achieving a final focused spot size of around 1 nm. Deflection coils then scan the surface coated with electron beam resist. The entire process is conducted in a high vacuum to minimize electron scattering and ensure precise electron beam control. EBL utilizes electron beam resists, which exhibit either positive or negative tone. Commonly used positive tone resists include PMMA (poly-methyl methacrylate)[104] and ZEP520A[105], composed of long-chain polymers broken by low-energy secondary electrons when exposed to the electron beam. In this study, the Raith 150TWO system[106] served as the primary equipment, albeit at a high cost.

2.4.2 Lift-off process

In semiconductor manufacturing, the "lift-off process" is used to fabricate certain types of microstructures, such as thin-film devices, IC, and MEMS. The lift-off process is critical in patterning thin films (metals, oxides, poly-Si) to create high precision and resolution features. Traditionally, a negative photoresist was employed to pattern the deposited materials. In this method, negative photoresists undergo crosslinking in exposed areas, leading to gradual undercutting from the surface to the bottom due to decreasing dose levels. While the coating may not fully cover the bottom of the photoresist, issues arise when the deposited material is relatively thick.

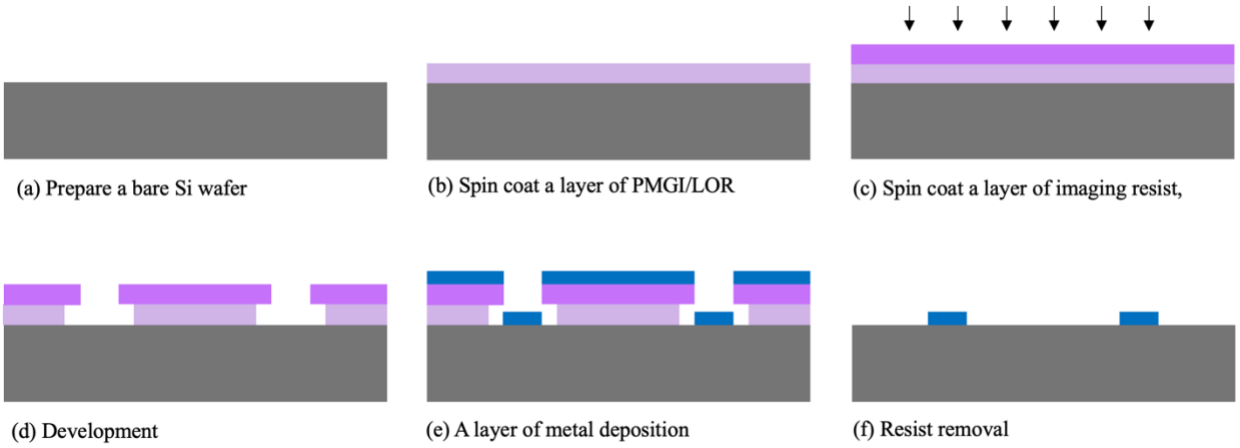


Figure 2.12 The fabrication process of the lift-off process.

To optimize the removal of the photoresist and prevent such issues, a lift-off resist like poly(dimethylglutarimide) (PMGI)/lift-off resist (LOR 3A)[107] is commonly used. The lift-off process involves resist coating and material deposition, as depicted in Figure 2.12. Initially, a bi-layer of PMGI/LOR and imaging resist is spin-coated onto the substrate and exposed. Upon exposure, the developer gradually dissolves the underlying PMGI layer, forming a lateral undercut beneath the imaging photoresist. With PMGI, this lift-off process generates a bilayer overhang structure, as shown in Figure, making it compatible with both positive and negative photoresists and enabling the creation of high-quality patterns even when the deposited material is thick (not to exceed one-third of the overall thickness of the bilayer resist).

Subsequently, after development, the desired coating material is deposited onto the patterned photoresist. Finally, the photoresist is removed using a PG remover, leaving behind the deposited material on the substrate and producing an inversely designed pattern. In this study, electron beam evaporation is employed for material deposition. This method offers directional deposition without leaving a film on the sidewalls of the photoresist, thereby facilitating the subsequent lift-off process.

2.4.3 Reactive ion etching (RIE)

The mid-1960s saw a significant breakthrough in IC manufacturing with the introduction of dry etching, and this technique exposed the target substrate to free radicals and ion bombardment within a plasma environment[108]. During the late 1960s and early 1970s[109], researchers delved into utilizing reactive gases in ion etching processes. Introducing gases such as fluorine or chlorine into the ion etching chamber, chemical reactions could occur at the substrate surface, enhancing the etching selectivity and enabling precise control over the etching process. The term "RIE" emerged in the early 1970s to describe a specific type of dry etching that combined physical ion bombardment with chemical reactions. RIE offered advantages over conventional ion etching techniques, including enhanced selectivity, higher etch rates, and better anisotropy[110] (the ability to etch vertically).

Effective etching in a traditional RIE system relies on capacitive coupled plasmas (CCP), where the voltage between parallel plate electrodes generates energy. By applying radio frequency (RF) voltage to these plates with a capacitor in between, negative charges accumulate on the plate, creating a potential difference known as the bias voltage (V_b). This V_b then attracts positive ions from the plasma towards the wafer, causing physical bombardment on the sample surface. Higher RF power, thus higher V_b, increased physical bombardment and reduces etching selectivity[111].

2.4.3.1 Inductively coupled plasma-RIE (ICP-RIE)

On top of the RIE parallel plate setup, an inductively coupled plasma (ICP) has been added[111], as shown in Figure 2.13.

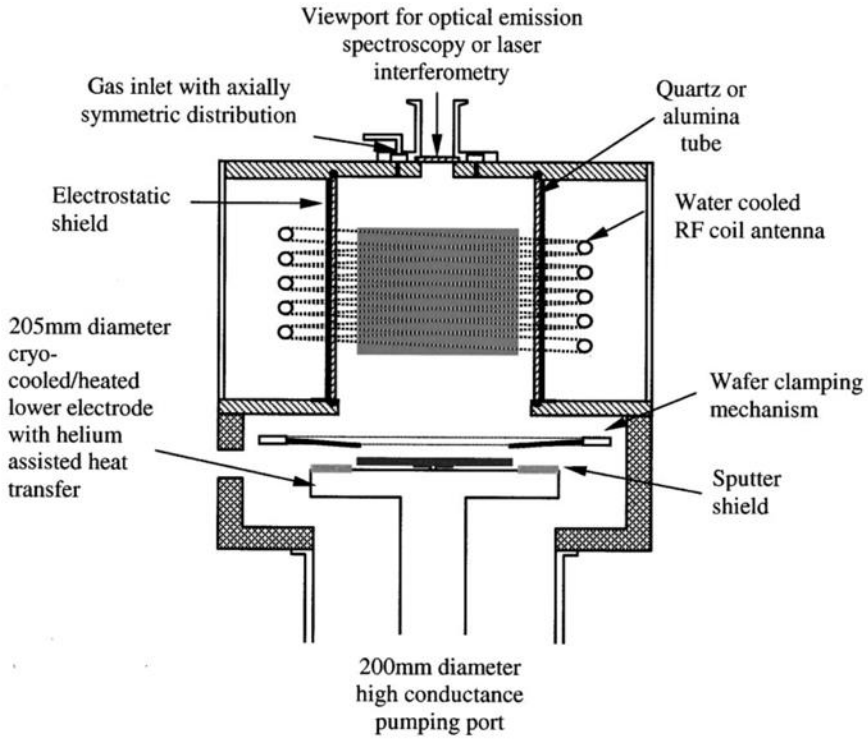


Figure 2.13 The schematic of the ICP-RIE system. (Reproduced with permission from Ref. [111]).

The inductive coil in the ICP component is excited by the RF power and converts the gas into an excited state plasma, including free radicals, ions, and electrons. Compared to an electrostatic field, a changing electric field is more effective at ionizing gas. When electrons move at a faster speed, a large number of ions find it difficult to synchronize their motion with the rapidly changing electric field, narrowing the ionization zone. Within the given ionization zone, electrons receive more energy than ions during the ionization process, making gas molecules more likely to ionize. The upper RF power source is called ICP power, and it directly influences the density of the plasma. Higher ICP power increases the density of the plasma, leading to more gas molecules being excited into the plasma state. With increased plasma density, there is an increase in the number of free radicals participating in reactions and the number of ions bombarding the sample, resulting in a significantly enhanced chemical etching process.

2.4.3.2 Bosch process

In 1996, Laermer Franz and Schilp Andrea[112] introduced a novel dry etching technique involving the sequentially introducing etching and protection gases. This innovative approach, patented by Robert Bosch GmbH[112], later became known as the Bosch Process. Renowned for its unique sidewall protection mechanism, this method revolutionized the fabrication of HAR Si structures. It gained recognition as deep reactive ion etching (DRIE)[113] and typically serves as the primary etching method in ICP-RIE systems.

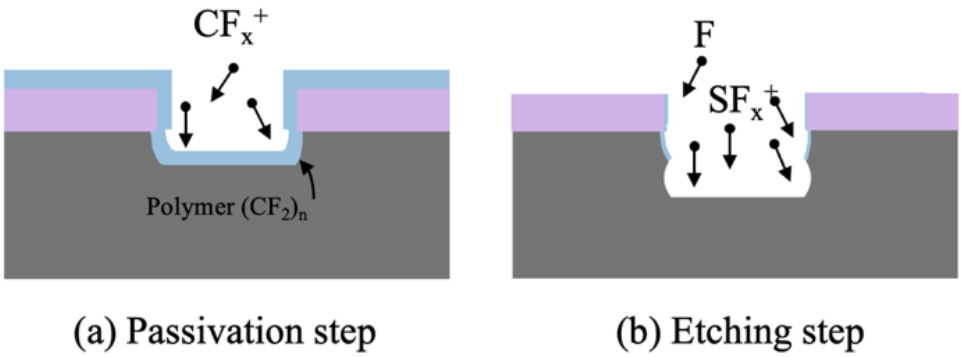


Figure 2.14 Schematic representation of the standard Bosch process (a) passivation step, (b) etching step.

The Bosch process primarily comprises two distinct steps. In the passivation step, as illustrated in Figure 2.14 (a), octafluorocyclobutane (C_4F_8) is introduced to safeguard the etched surface. When ionized, C_4F_8 gas decomposes into the CF_x group under the plasma state and forms polymer chains $(CF_2)_n$, protecting both the sidewalls and the surfaces from etching[114]. In the etching step, as illustrated in Figure 2.14 (b), a chemical reaction occurs between sulfur hexafluoride (SF_6) and Si, generating SiF_4 (a volatile byproduct) and then its removal. The physical bombardment is primarily induced by SF_6 ionization, generating SF_x^+ ions and F radicals.

Once the etching cycle is established, the polymer deposited on the flat surface can be physically removed, exposing the underlying Si. The intervals between the etching and passivation steps are short, as shown in Table 2.1, and the final etched sidewall is wavy[115]. In the etching step,

the gas flow of SF_6 is 160 sccm, with ICP power 1000W, RF power 20W, pressure 15 mTorr; and in the passivation step, the C_4F_8 gas flow is 160 sccm, with ICP power 1000W, RF power 5W, pressure 20 mTorr.

Table 2.1 The recipe for our standard Bosch process on the Oxford PlasmaLab 100 ICP 380 DRIE Si etching system.

Parameters		Etching step	Passivation step
Pressure (mTorr)		25	20
Temperature (°C)		15	15
RF power (W)		20	5
ICP power (W)		1000	1000
Gas flow (sccm)	C_4F_8	0	160
	SF_6	160	0
Time (s)		7	5

2.4.3.3 Non-switching pseudo-Bosch process

The non-switching pseudo-Bosch process represents a variation of the traditional Bosch technique, wherein both gases, SF_6 and C_4F_8, are simultaneously introduced into the chamber[116–119]. Unlike the sequential introduction in the standard Bosch process, here, SF_6 is utilized for etching Si, while C_4F_8 is employed to deposit a chemically inert passivation layer concurrently. This process allows for adjusting the sidewall taper angle to achieve a positively tapered tip profile by varying the gas flow ratio of SF_6 to C_4F_8. Parameters such as an ICP power of 1200 W, RF power of 20 W, and pressure of 10 mTorr are typically employed.

Compared to the standard Bosch process, the non-switching pseudo-Bosch offers significant advantages in controlling process parameters, improving sidewall profile accuracy, and

reducing equipment costs. This approach yields HAR nanostructures with smooth sidewalls, making it particularly suitable for fabricating HAR tips in AFM systems.

2.4.3.4 Cryogenic etching process

Cryogenic etching has garnered widespread attention for its exceptional anisotropy and ability to control sidewall angles effectively. In a cryogenic system, the temperature of the wafer is regulated by cooling it with liquid nitrogen. At the same time, helium (He) gas at the back of the electrode acts as a conductive medium to maintain the sample at a low temperature. During cryogenic etching, the etching products are less volatile, resulting in the formation of a passivation layer on the sample surface, and ion bombardment can selectively remove this passivation layer at the bottom while preserving it on the sidewalls, facilitating a vertically downward etching[120].

A well-established cryogenic etching process typically involves plasma etching of Si using a combination of SF_6 and O_2 gases. When introduced into the chamber simultaneously, the fluorine and oxygen radicals in the plasma react with exposed Si, and then polymer SiO_xF_y is produced[121]. This product would evaporate at room temperature, but at low temperatures (below -40°C), it accumulates on the sample surface to form a passivation layer. The gas ratio, ion bombardment, and temperature influence the thickness of the passivation layer. It is worth noting that when the temperature is too low (below -140°C), SF_6 gas liquefies and adheres to the sample surface, preventing the etching process from continuing.

Chapter 3 HAR AFM Tip Fabrication

Four distinct approaches are outlined in this chapter to overcome the low cost-efficiency and low throughput of four techniques (Section 2.3.1-2.3.4). The first method (Section 3.1) integrates non-switching pseudo-Bosch etching with wet sharpening techniques to achieve an exceptional aspect ratio of 1:135, marking a significant advancement in tip fabrication. The second method (Section 3.2) introduces an innovative approach utilizing tapered SiO_2 masks to fabricate Si nanocones with extraordinary apex measuring just 3.54 nm. The third method (Section 3.3) explores a novel two-step cryogenic etching process to yield a controllable tip profile with a slight taper angle of 2.2°. The fourth method (Section 3.4) combines the Bosch process with the pseudo-Bosch process, incorporating periodic O_2 shrinking steps to achieve a tip apex sharpness of 20 nm. All cross-sectional profiles were analyzed using a JOEL JSM-7200F scanning electron microscope with samples positioned on a 70° tilted stage. The planar dimensions, including width, length, and angle, were measured directly. The height dimension was then calculated from measurements, taking into account the 70° tilt angle of the stage.

The main body of Section 3.1 is reprinted with permission from Ref.[116] *Copyright © 2023, American Vacuum Society.*

Pan, A., Samaan, M., Yan, Z., Hu, W. & Cui, B. Fabrication of ultrahigh aspect ratio Si nanopillar and nanocone arrays. (2023). Journal of Vacuum Science & Technology B 41 (2).

The main body of Section 3.2 is reprinted with permission from Ref.[122] *Copyright © 2024, IEEE.*

Pan, A., Zhu, C., Yan, Z., Zhu, X., Liu, Z., Cui, B. Fabrication of the highly ordered silicon nanocone array with sub-5 nm tip apex by tapered silicon oxide mask. (2024). IEEE Transactions on Semiconductor Manufacturing, vol 37, No. 2 doi:10.1109/TSM.2024.3372521.

The main body of Section 3.3 is reprinted with permission from Ref.[121] *Copyright © 2024, American Vacuum Society.*

Zhu, X., Pan, A., Cui, B. Cryogenic etching of positively tapered silicon pillars with controllable profiles. (2024). Journal of Vacuum Science & Technology B 42, 032206.

The main body of Section 3.4 is reprinted with permission from Ref.[123] *Copyright © 2024, 2024, American Vacuum Society.*

Kang, R., Pan, A., Cui, B. Fabrication of silicon sharp nanocones using dry etch with periodic oxygen plasma shrinking and wet etch. (2024). Journal of Vacuum Science & Technology B 42, 033002.

3.1 Fabrication of Ultra-high Aspect Ratio Si Nanopillar and Nanocone Arrays

3.1.1 Introduction

HAR structures could find applications in electrical, optoelectronic or biomedical devices such as transistors[124], solar cells[125], photodetectors[126], biosensors[127], nano-needles, and probes[128–130]. For instance, nano-needles have been widely utilized for intracellular detection and extraction in biomedical and clinical research. Single solid Si nano-needle can penetrate the cell membrane to complete protein extraction by direct lysis of cells; it can detect bio-signals and avoid cell destruction with a few tens of nanometers-diameter, which is significantly smaller than the cell size. Hollow silicon nano-needles were reportedly used in drug delivery and extraction of intracellular proteins or mRNA[131,132]. The hollow structure can maintain cellular biological activity and reusability thereof with a diameter of hundreds of nanometers instead of lysing cells directly[133], but it adds a new level of complexity to the nanofabrication process. Compared to a single nano-

needle, a nano-needle array has excellent potential to massively parallelize the tunnel to enable high throughput applications including but not limited to stem cell monitoring, gene expression, and biological reaction catalysis; and HAR has always been pursued in these applications to obtain more intracellular information and more precise delivery.

HAR structures can be fabricated by both bottom-up self-assembly and top-down nanofabrication methods. For bottom-up self-assembly approaches, VLS growth[97,134] and metal-assisted chemical etching (MACE)[135,136] are well-developed for HAR structure fabrication. In the synthesis using VLS, silicon is integrated into a fluid eutectic Au-Si nanodroplet from the vapor phase precursor, then silicon nucleates into the solid phase when the concentration exceeds saturation for the eutectic phase. However, in addition to the high temperature needed, the presence of metal catalyst may lead to metal impurities. MACE of nanoneedles also requires metal structures. Metal nano-holes fabricated on top of silicon catalyze nanoneedle etching in a mixture of hydrogen peroxide and HF. Although low cost and large area capabilities are attractive in many nano-fabrications, MACE is not suitable for nanoneedle etching as the inter-needle spacing cannot be large such as well beyond 1μm. Overall, the main limit of the bottom-up method is the poor control of structure dimension, direction, density/spacing and location on the wafer surface.

The top-down method offers much better control, though usually with higher fabrication cost. It typically consists of nanolithography and plasma etching steps. For silicon, the popular Bosch deep etching with alternating deposition using C_4F_8 gas and etching using SF_6 gas can achieve a very high aspect ratio; but the sidewall is not smooth with scallops due to its switching nature[137]. To minimize the scallop, one can either greatly reduce the cycle time[138], or add a significant amount of O_2 gas to the etching half-cycle[139], at the cost of reduced etching rate and selectivity. Alternatively, to attain a very smooth sidewall, one can employ the mixed gas recipe,

also termed as non-switching pseudo-Bosch recipe[118,119], as it utilizes the same gases as the Bosch process but with the two gases introduced into the chamber simultaneously[119,137]. Compared to the Bosch process, the pseudo-Bosch process gives a slower etching rate because the reactive etching species and deposition species neutralize each other to form harmless CF_4, and lower selectivity to resist because the etching relies on constant physical bombardment. As a result, the pseudo-Bosch process is perfect only for not-so-deep etching, which is the case for nanoscale HAR structures.

In this paper, we fabricate nano-pillar and nano-cone arrays by an innovative combination of pseudo-Bosch etching followed by thinning or sharpening using wet isotropic etching in order to further increase the aspect ratio. We demonstrate nano-pillar fabrication with a very high height/width aspect ratio of 135. When the pillar array becomes very dense, the structure after wet etching becomes a nano-cone shape with an apex diameter of less than 20 nm (base diameter 1 μm).

3.1.2 Experiment

The fabrication procedure is shown in Figure 3.1. A 4-inch Si wafer with <100> surface orientation was pre-cleaned by rinsing in acetone and isopropyl alcohol (IPA), then cleaned with O_2 plasma to further remove organic contaminants. After the cleaning process, a double-layer resist was utilized to facilitate liftoff after EBL. The first layer of 250 nm ZEP-520A resist[140] was coated at 3000 rpm and baked at 180°C for 3 minutes, and the second layer of 220 nm PMMA resist was then coated at 4000 rpm and baked at 180°C for 5 minutes. EBL was followed using the Raith 150^{TWO} system at 20 kV with 500 μC/cm^2 dose to write a two-by-four array with identical 1 μm-

dots and 8 μm spacing for sparse HAR pillar fabrication, and 500 nm-dots and 700 nm spacing for dense sharp nano-cone fabrication.

For the lift-off process, different dissolution rates (since ZEP has 3-4 times higher sensitivity than PMMA) of different resists will create an overhang or undercut structure that is favourable for resist removal after metal deposition. The electron beam resist developer is xylene for both resists, and the development time is 2 minutes. Then, 150 nm Cr evaporation and liftoff in acetone were conducted. Next, a non-switching pseudo-Bosch process instead of standard Bosch was carried out to etch the Si substrate to a target height of 10 μm. In the etching process, we used a 22/38 gas ratio of SF_6 over C_4F_8 with 1200 W ICP power and 20 W RF power under 10 mTorr for 20 min. After Cr mask removal, the sample was thinned down (for sparse nano-pillars) or sharpened (for dense nano-cones) by a mixture of aqueous HF (49%) and HNO_3 (70%) with a ratio of 1:200 for 5 minutes under atmospheric conditions.

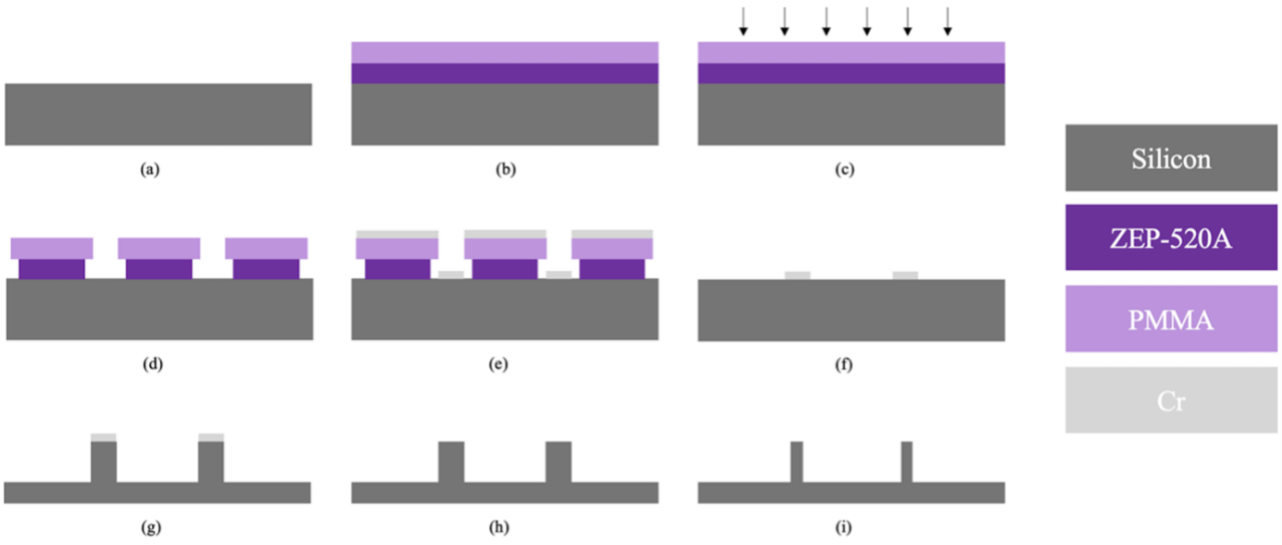


Figure 3.1 Schematic of the fabrication process for very thin and HAR nano-pillars: (a) prepare a silicon wafer, (b) spin coat a bilayer of PMMA and ZEP-520A, (c) lithography, (d) development, (e) Cr deposition, (f) resist removal, (g) etch silicon, (h) Cr mask removal, (i) wet sharpening. (The fabrication process is the same for the nano-cone array except that those structures before wet etching are very dense)

3.1.3 Results and discussion

3.1.3.1 Wet etching using a mixture of HF and HNO_3

In this work, the pillars were thinned down or sharpened using a mixture of HF and HNO_3, though sometimes diluent like water or acetic acid (CH_3COOH) (HNA system) can also be added to slow down the etching rate[141]. In the reaction, Si loses electrons and bonds with oxygen to form oxide by the effect of HNO_3, and then the oxide reacts with HF and dissolves in the solution. According to its reaction model that matches with the experimental results, the Si etching rate is fastest (a few hundred μm/min) for an undiluted system with 68% HF and 32% HNO_3. As expected, oxidation is rate-limiting in the HF-rich region, and oxide removal is rate-limiting in the HNO_3-rich region.

For our purpose of nanoscale fabrication, the overall etching rate should be sufficiently slow for precise process control, and the etched surface should be very smooth. According to a variety of experimental results for this etching system, a low etching rate can be obtained using both HF-rich solution and HNO_3-rich solution, but the etched surface would be quite rough with a high ratio of HF over HNO_3. In this etching system, HNO_2 is the catalyst, and there is always some trace amount of HNO_2 impurity in the HNO_3 solution. Once the etching starts at some random sites where HNO_2 exists, new HNO_2 will be produced by the oxidation reaction for which HNO_3 will be reduced. That is, the oxidation is auto-catalytic with a kind of positive feedback, leading to a rough surface unless the etching is limited by the oxide removal process. As a consequence, we have chosen a low HF concentration etchant. In addition, though adding water or acetic acid diluent can also reduce the etching rate, we decided not to add them for simplicity.

According to the analysis above, the ratio of HF and HNO_3 is a variable worth investigating. Six identical samples with very large inter-pillar spacing were prepared and etched in the mixture

with different ratios. To calculate the lateral and vertical etching rate, all samples were imaged and measured using SEM before and after the wet etching process. Here the Cr mask on top of the pillar is not removed, and thus the pillar will become taller after wet etching; the height difference is used to calculate the vertical etching rate. The lateral etching rate is calculated based on the average pillar radius shrinkage (the diameter shrinkage is apparently twice that of radius shrinkage). The average lateral and vertical etching rates at atmospheric temperature and pressure are shown in Table 3.1, as well as plotted in Figure 3.2 for different HNO_3 percentages. As expected, a higher nitric to HF ratio gives a lower etching rate; and the etching rate is dominated by the availability of HF that depends on its diffusion from bulk to the silicon surface to etch. Moreover, the apparent lateral etching rate is significantly faster than the vertical one, since here the lateral etching involves 2D (along x and y-direction) diffusion of etchant, whereas vertical etching involves 1D (along z-direction) diffusion.

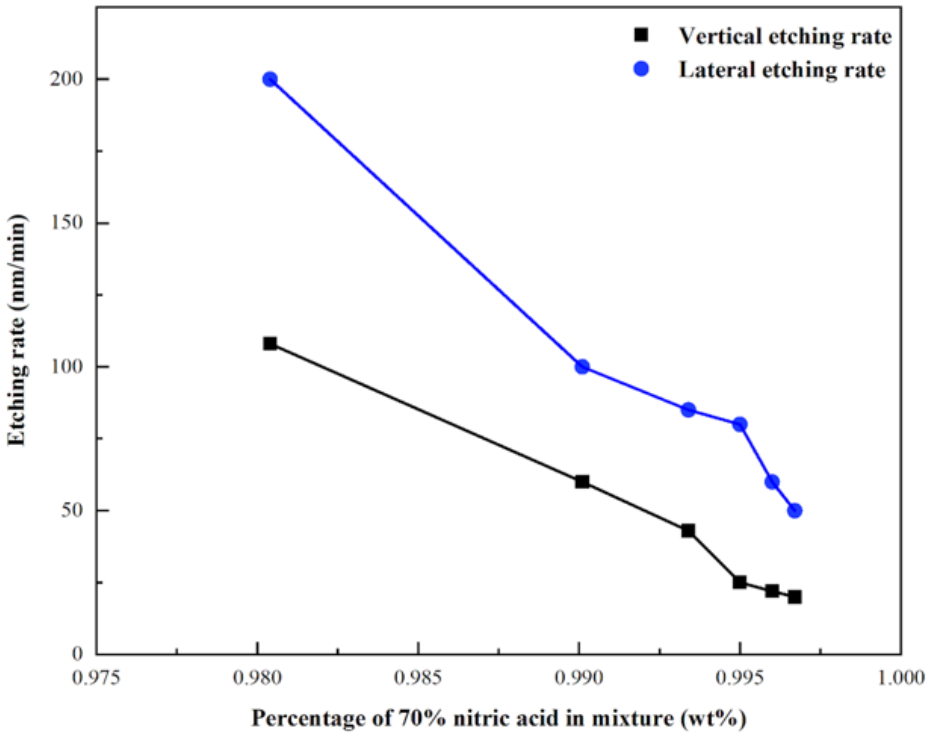


Figure 3.2 Plots of average lateral and vertical etching rate as a function of the weight percentage of nitric acid in the mixture.

Table 3.1 Lateral and vertical etching rate for different HNO_3 and HF volume ratios without solution agitation.

Ratio of 70% HNO_3 and 49% HF	Percentage of 70% HNO_3 (wt%)	Vertical etching rate (nm/min)	Lateral etching rate (nm/min)
50:1	0.9804	108	200
100:1	0.9901	60	100
150:1	0.9934	43	85
200:1	0.9950	25	80
250:1	0.9960	22	60
300:1	0.9967	20	50

3.1.3.2 Fabrication of HAR nano-pillars for sparse pillar array

After dry etching and wet thinning using 200:1 HNO_3:HF, the nanopillars were examined by scanning electron microscopy (SEM) as shown in Figure 3.3. The pillar before wet thinning has a pretty vertical sidewall profile with a diameter of 755 nm. After wet etching for 5 min without solution agitation, the pillar apex diameter shrank to 74 nm, and the base diameter to 129 nm. For those 10 μm-tall nanopillars, the aspect ratio is about 100 when the average diameter is taken as 100 nm. Those pillars could also be sharpened by thermal oxidation followed by oxide removal using HF, which would offer better control than wet etching, but it needs very high temperature and expensive equipment and is a lengthy process.

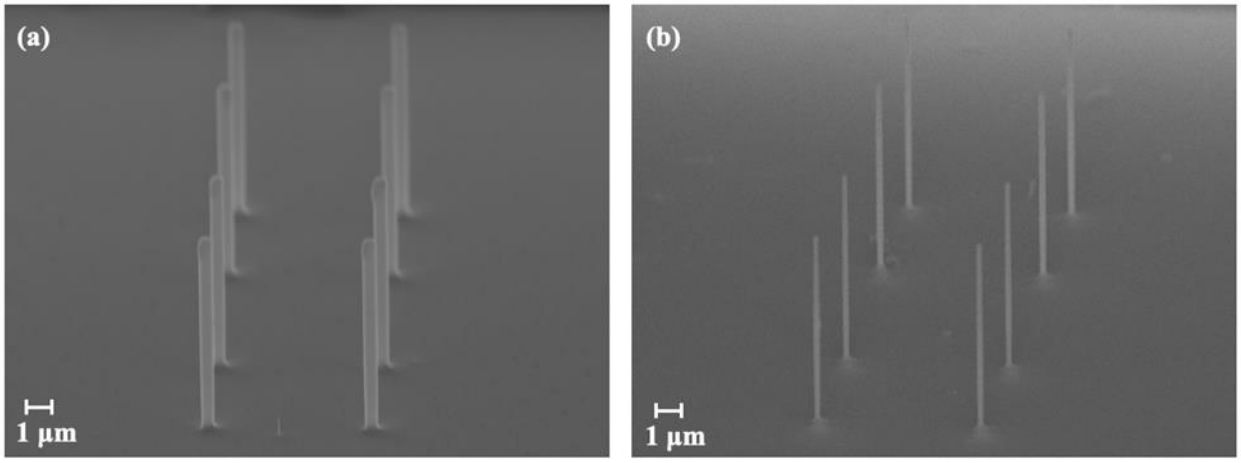


Figure 3.3 SEM images of nanopillar array with 1 µm dots and 8 µm spacing (a) before wet thinning (b) after wet thinning.

3.1.3.3 Fabrication of nano-cones for dense pillar array

To investigate the effect of pattern density, we also carried out the same fabrication procedure but with a much smaller array periodicity of 1.2 µm, as compared to 8 µm above. Figure 4a shows the pillars after pseudo-Bosch etching for 15 min. The pillar base (1.09 µm) is significantly larger than the pillar top (0.63 µm), or one can say that the inter-pillar gap becomes narrower with increasing etching depth. This is caused by the so-called aspect ratio dependent etching (ARDE) effect, which states that the etching of a hole, trench or gap becomes slower and more difficult with increasing aspect ratio, and the etching may even completely stop (pinch-off at feature bottom) at certain etching depth for a given hole or trench size[137].

ARDE effect can be explained by considering several factors, though it is still unclear which factor dominates. The first factor is neutral and ion shadowing. In the plasma, neutrals are non-directional, so they might hit the sidewall of the profile and will not be able to reach the bottom if they come in at a large angle relative to normal incidence. Although ions are directional and anisotropic, they can be scattered by gas molecules and then lose directionality. That is, both neutrals and ions can be "shadowed" by the structure sidewalls. The second factor is charging. The

feature sidewall accumulates a negative charge when electrons arrive, and it will deflect and thus attenuate etching. The third factor is etching species transportation. In the etching process, the transportation of etching species from the surface to target spots of the hole/gap bottom, and the etching product from bottom to surface, will become more difficult as lateral dimension decreases or feature depth increases.

Figure 3.4 (b) shows the structure after wet etching using an HNO_3 to HF ratio of 200:1 for 5 min at room temperature. Unlike the sparse pattern shown in the previous section, here the pillar became greatly sharpened with an apex diameter as small as 17 nm. Here the upper part of the pillar (pillar top shrank by 613 nm) was etched much more than the lower part (pillar base shrank by 380 nm), because the etching for very low HF concentration is limited by HF diffusion to the sample surface, and the mass transport is faster to the upper part of the structure and the etchant got gradually depleted toward the lower part of the structure. An alternative sharpening method for silicon pillars is oxidation sharpening which consists of silicon thermal oxidation followed by HF removal of the oxide. It works because the Si oxidation rate is slower on the curved surface due to stress, and the rate decreases with decreasing radius of curvature[142]. As a result, for a silicon structure with a sloped sidewall, the oxide thickness will be smaller near the apex than away from the apex, leading to a sharpened structure after oxide removal. For comparison, the current method using wet etching relies on dense patterns, but it does not need a sloped sidewall profile. In fact, as shown in Figure 3.4 (a), the upper portion of the silicon structure has rather a vertical sidewall, thus it cannot be sharpened (but can be thinned) by the thermal oxidation sharpening process. The fabricated sharp cone array would be very effective in cell lysis and penetration for protein extraction.

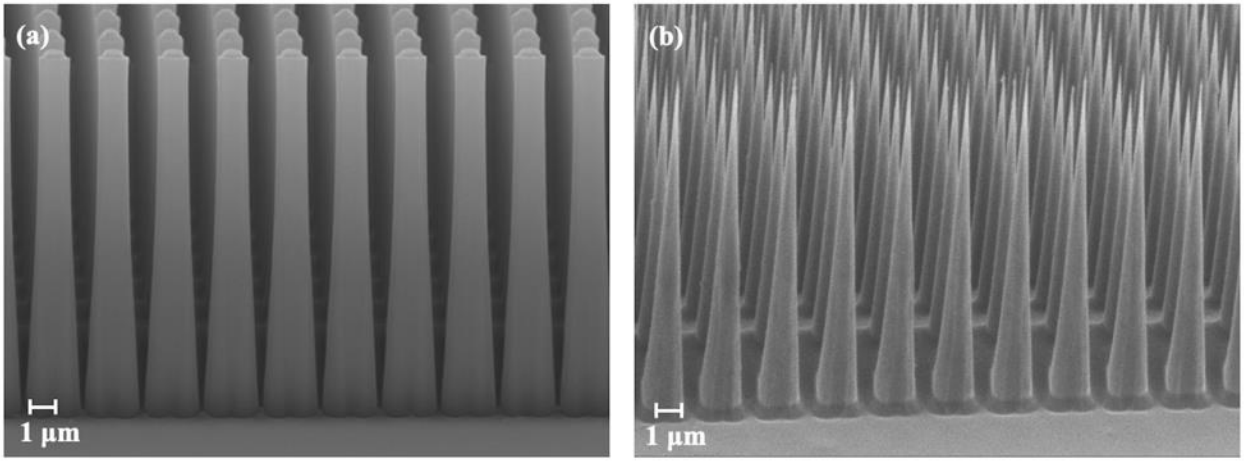


Figure 3.4 SEM images of nanopillar array with 500 nm dots and 700 nm spacing (a) before wet sharpening (b) after wet sharpening.

3.1.4 Summary and conclusions

Nano-pillar or cone array with a very HAR and/or very sharp apex have many applications, but it is difficult to fabricate. Here we developed a process combining pseudo-Bosch etching and wet isotropic etching. First, a pillar array with a nearly vertical sidewall angle is fabricated using pseudo-Bosch etching; and then the pillars are thinned or sharpened using a mixture of HF and HNO_3. The pseudo-Bosch etching process consists of a simultaneous etching by fluorine largely from SF_6 dissociation in the plasma, and passivation by fluorocarbon polymer from C_4F_8; and it was found that a gas flow ratio for SF_6/C_4F_8 of 22/38 can give a vertical etching profile. For the wet thinning/sharpening, a high HNO_3/HF ratio will drive the process to the HF diffusion-limited etching regime, which promotes smooth etching/polishing, and a higher ratio gives slower thus more controllable etching. Here a ratio of 200/1 HNO_3 and HF mixture is chosen to sharpen silicon structures with an appropriate etching rate of 160 nm/min in the lateral direction and 25 nm/min in the vertical direction. Since the diffusion of HF etchant depends on the local pattern arrangement, a sparse pillar array mainly resulted in pillar thinning, with an aspect ratio up to 135 attained; whereas a dense array leads to negligible etching near the pillar base as the etchant diffusion

through the narrow and deep gap between adjacent pillars is slow, thus giving a sharpened cone structure, with apex diameter down to only 17 nm.

3.2 Fabrication of the Highly Ordered Si Nanocone Array with sub-5 nm Tip Apex by Tapered SiO_2 Mask

3.2.1 Introduction

With the rapid development of the semiconductor industry, Si nanostructures have been one of the most widely researched areas in science, medicine, and engineering[143–147]. Among these structures, Si nanocones have emerged as a focal point in various research applications, including field emission X-rays[148], solar cells[149–151], optical sensors[152], nanoneedles[153] and nanoprobes[154] in characterization tools. These valuable contributions played a crucial role in advancing technology. For instance, carbon nanotubes (CNTs) and Si have emerged as prevalent materials used in field emission arrays for X-ray imaging. Compared to CNT-based X-ray cathodes[155–158], Si-based arrays can provide higher currents at lower voltages due to enhanced control of the tip geometry, such as height, tip radius of curvature, and spatial orientation of emission sites. Moreover, using semiconductor materials, especially p-type Si, enables precise and stable regulation of the emission current[159]. On the other hand, Si fabrication techniques have been well developed in IC, micro-electromechanical systems (MEMS) and nano-electromechanical systems (NEMS) fields[137,160]. In comparison to alternative materials such as germanium (Ge)[161], gallium arsenide (GaAs)[162], and metals[163], Si offers a straightforward and efficient fabrication process, as well as it can be easily oxidized and further sharpened. From this perspective, we have chosen Si as the preferred option for this study.

Si nanocone array can be fabricated using either bottom-up or top-down techniques. The

VLS method is the primary bottom-up self-assembly approach, where silicon is integrated into a fluid Au-Si nanodroplet and then nucleates into a solid phase. However, achieving a uniformly aligned array with consistent profiles in the desired direction is challenging [164,165]. Until the 1970s, anisotropic etching of Si to create cone structures was exclusively achieved using top-down wet techniques involving tetramethylammonium hydroxide (TMAH) or KOH[109,166]. While wet etching methods are cost-efficient and have high throughput, they have fixed sidewall tapered angles determined by the Si crystalline structure. MACE requires metal nanostructures to catalyze Si etching, which can introduce metal impurities and create porous structures[120]. Moreover, wet etching often suffers from poor uniformity and significant critical dimension loss due to over-etching. In contrast, top-down dry etching, especially DRIE, can create anisotropic structures with excellent depth and profile control[147,167,168]; but DRIE that consists of alternating etching and passivation steps creates a rough sidewall profile with scallops due to its switching nature[137,169]. Therefore, this work used a non-switching pseudo-Bosch process, also known as continuous-mode etching, where SF_6 and C_4F_8 gases are simultaneously introduced into the reaction chamber to prevent rough sidewall surfaces[165,170].

In previous studies, significant efforts have been dedicated to exploring the non-switching pseudo-Bosch process, specifically focusing on controlling the taper angle of the etched sidewall. It has been demonstrated that the ratio of SF_6 and C_4F_8 gases in the reaction chamber plays a dominant role in achieving this control. By increasing the percentage of C_4F_8 gas flow, a negatively tapered profile can be transformed into a positively tapered profile. Notably, Ayari-Kanoun *et al.* achieved a considerable negative taper angle of -9.7° using an SF_6/C_4F_8 ratio of 24/36[119], while Saffin *et al.* successfully fabricated an impressive taper angle of 39° with an SF_6/C_4F_8 ratio of 1/59[118]. Nevertheless, the reproducibility could be poor caused by chamber condition changes. The

introduction of argon (Ar)/O_2 can reduce the sidewall roughness[117,171] but does not significantly improve the tip sharpness, and it also deduces the etching rate and mask selectivity. Cryogenic etching at lower than -80 ℃ can also etch a Si nanocone array but is not cost-efficient[172].

The employment of a mask in the Si etching also plays a dominant role in fabricating nanocone, providing a more controlled and tunable approach[173,174]. The first candidate is the self-assembly polystyrene (PS) nanosphere[175,176]. Dip coating on H_2O is a cost-effective and convenient method to obtain a large area of PS monolayer mask in just a few seconds. However, achieving uniform coating is challenging, as some regions may lack PS spheres, while other regions may have multiple-layer sphere stacks. Metals such as chromium (Cr) and aluminum (Al) can be another mask candidate, and the lift-off or direct etching methods can achieve the mask structure. Costly EBL is required for both methods, and the resulting metal mask profile will be disk-like with a nearly vertical sidewall.

The third option for a mask material is SiO_2, which offers good selectivity to the Si substrate and can be patterned and etched using both dry and wet processes. The oxide mask can be shaped to have different sidewall profiles, providing an additional degree of freedom for the silicon nano-cone fabrication process compared to a hard metal mask. This study developed a novel approach for creating a SiO_2 mask with a tapered sidewall and sharp apex using a combination of dry and wet etching techniques. Next, the SiO_2 mask structure was transferred into the Si substrate using dry etching, resulting in a Si nanocone array with a sharp apex. After thermal oxidation sharpening, the Si nanocone was further sharpened to reach a sub-5 nm apex.

3.2.2 Experiment

The process of fabricating a Si nanocone array, as shown in Figure 3.5 starts with a p-type (boron dopant, 0.01 Ω·cm) prime Si wafer with <100> orientation. Prior to engaging in high-temperature processing steps, such as thermal oxidation, O_2 plasma treatment and RCA cleaning are conducted. 2-minute O_2 plasma cleaning with 20 W radio-frequency (RF) power, 20 sccm O_2 gas flow, and 20 mTorr using the YES CV200-RFS photoresist plasma asher was done to remove organic contamination. After 15-minute SC-1 (hydrogen peroxide (H_2O_2): ammonium hydroxide (NH_4OH): H_2O = 1:1:5, 80 ℃) to clean organic residues, 45-second BOE dip to remove the natural oxide and 15-minute SC-2 (H_2O_2: hydrogen chloride (HCl): H_2O = 1:1:5, 80 ℃) to remove alkali ions and cations (Figure 3.5a), wet thermal oxidation under a pressure of 0.92 atm at 1000 ℃ was carried out for 270 minutes to grow 1 μm SiO_2 on the top of the Si substrate. Then we coated a bilayer resist, consisting of PMGI, which was spin-coated at 5000 rpm and baked at 180 ℃ for 1 minute, and 1.7 μm Shipley positive resist (S1811), which was coated at 3000 rpm and baked at 120 ℃ for 90 seconds (Figure 3.5b). Standard mask-less photolithography using a direct write UV lithography system (MLA150, Heidelberg Instruments) was utilized with a 405 nm light source and 100 mJ/cm^2 to write a 1 cm × 1 cm array with identical dots with a 10 μm period (Figure 3.5c). After development, a 30 nm chromium (Cr) metal mask was deposited by e-beam evaporation (Figure 3.5d). As the profile of the bilayer resists gives an undercut structure, the lift-off process is straightforward by Remover PG (MicroChem Corporation) with ultrasonic agitation (Figure 3.5e).

Next, SiO_2 was first anisotropically dry-etched (40 sccm C_4F_8 and 15 sccm O_2 flow for 80 seconds in an RIE chamber with 200 W RF power, 2500 W inductively coupled plasma (ICP) power and 10 mTorr chamber pressure) using the Oxford PlasmaLab 100 ICP 380 III-V and metal

etching system (Figure 3.5f), and then isotropically wet-etched by BOE for 10 minutes, leading to a cone structure sitting atop a base (Figure 3.5g). To etch the silicon cone array, a non-switching pseudo-Bosch process (22/38 gas flow ratio of SF_6 over C_4F_8, 1200 W ICP power, 20 W RF power, 10 mTorr, 5 minutes) using the Oxford PlasmaLab 100 ICP 380 DRIE Si etching system was carried out to transfer the conical oxide mask structure to the Si substrate (Figure 3.5h). Finally, dry thermal oxidation at 950 ℃ for 30 minutes using a furnace (EVENHEAT artisan 688 stp) and oxide removal in HF was carried out to sharpen the nanocone (Figure 3.5i). The oxidation process is conducted within the ambient air environment, and the ramping rate is set at 15 ℃/minute.

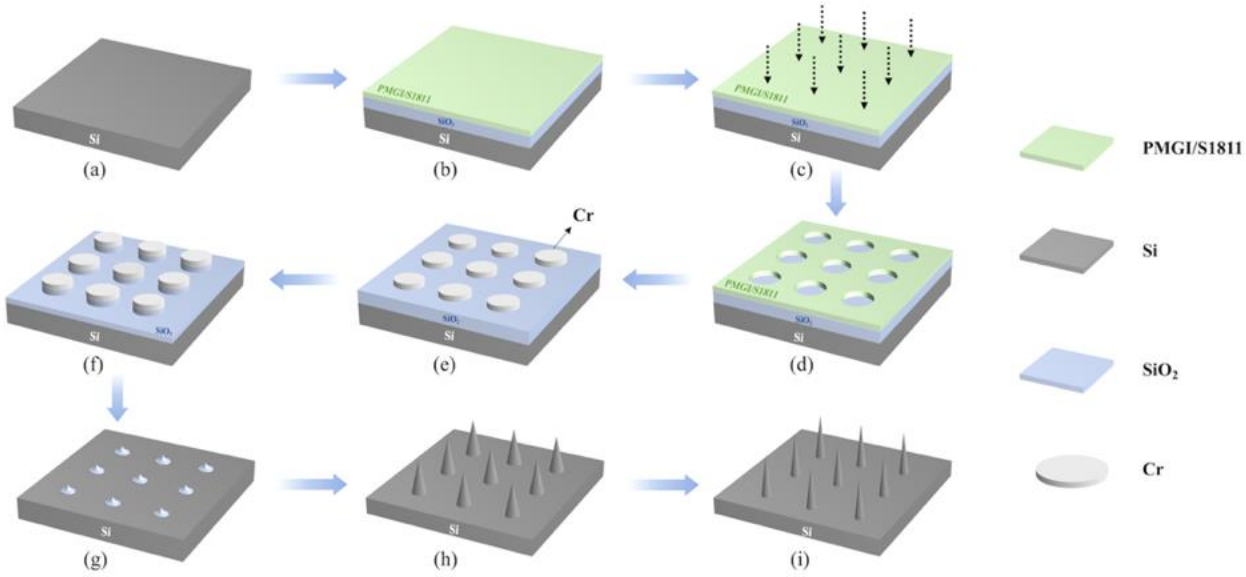


Figure 3.5 Schematic of the fabrication process for Si nanocone array: (a) prepare and clean a Si wafer (b) wet thermal oxidation and spin coat a bilayer of PMGI and S1811 resists (c) photolithography (d) development (e) Cr deposition and lift-off (f) etch SiO_2 by RIE (g) etch SiO_2 by BOE (h) Si etching (i) oxidation sharpening.

3.2.3 Results and discussion

3.2.3.1 SiO_2 Mask Patterning with Cr Mask

Dot arrays with identical periods of 10 μm and diameters of 1.0 μm, 1.1 μm, 1.2 μm and 1.3 μm were patterned using MLA. The pattern design is shown in Fig. SI-4 (a). The actual writing

time to expose a 1 cm × 1 cm array on MLA is only 1 minute, as illustrated in Fig. SI-1, which means MLA has much higher throughput and lower cost than EBL. However, it is still slower than traditional optical lithography using a photo mask.

Following the 30 nm Cr layer deposition and subsequent lift-off process, the resulting patterns were checked under a scanning electron microscope (SEM). Here we use a 1 μm dot array as an illustrative example, as shown in Figure 3.6 (a). It is worth mentioning that this photolithography approach ensures satisfactory feature sizes for our purpose.

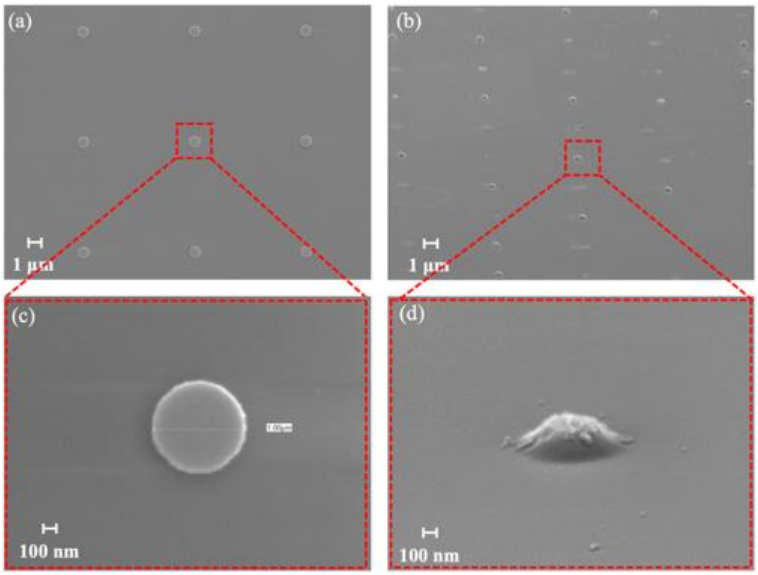


Figure 3.6 SEM images of (a) Cr mask array with 1.0 μm diameter and 10 μm period, (b) SiO_2 array after 20 minutes of pure wet etching by BOE, (c) the enlarged view of the single Cr mask pattern, (d) the enlarged view of the single SiO_2 pattern. All structures in this work were examined using JOEL JSM-7200F SEM with the samples on a 70° tilted stage.

To obtain the desired shape of the SiO_2 mask for fabricating Si nanocone structures, we compared the effectiveness of wet etching alone versus a combination of wet and dry etching. Firstly, wet etching was only used to pattern and shape the oxide mask structure. SiO_2 exhibits a lateral etching rate of 40 nm/min under the Cr mask in BOE, which is slightly slower than its vertical etching rate of 50 nm/min. After 20 minutes of pure wet etching, the 1 μm SiO_2 layer resulted in irregular and randomized profiles. 70% of the patterns were removed, while 30%

remained. The best profile, outlined in Figure 3.6 (b), displays a frustum cone shape due to progressive BOE lateral and over-etching. A larger diameter would prevent the mask from falling off, but wet etching alone couldn't achieve optimal sidewall profiles for silicon etching.

Secondly, the combination of wet and dry etching was utilized. We first etched the oxide with ICP-RIE for 80 sec using the same recipe as aforementioned which yielded a pillar structure with a slightly positively tapered sidewall of ~80°. Then, the dry-etched SiO_2 patterns were soaked in BOE for 10 minutes for wet isotropic etching to give the final profiles as shown in Figure 3.7 (a)-(d) for different dot sizes ranging from 1.0 μm to 1.3 μm diameter.

For the 1.0 μm design in Figure 3.7 (a), the measured height of the etched structure is 485 nm, with a diameter of the SiO_2 tip apex measuring 20 nm. For the design 1.1 μm in Figure 3.7 (b), the height is 626 nm, and the tip apex is 100 nm. Similarly, the height is 708 nm and the apex diameter is 200 nm in Figure 3.7 (c), and the height is 750 nm and the apex diameter is 320 nm in Figure 3.7 (d). Assuming that the pattern transfer from the mask to the Si substrate approximately follows the profile of the etching mask, this conical profile in Figure 3.7 (a) with smooth sidewalls is suitable for fabricating a final Si nanocone structure. In the last three subfigures of Figure 3.7, the top ends of the structure have approximated cylindrical shapes, and the shaped SiO_2 as a mask will result in the top structures of Si being cylindrical after etching. To confirm our hypothesis, we used the structures shown in Figure 3.7 (a) and (b) as masks to etch the Si substrate.

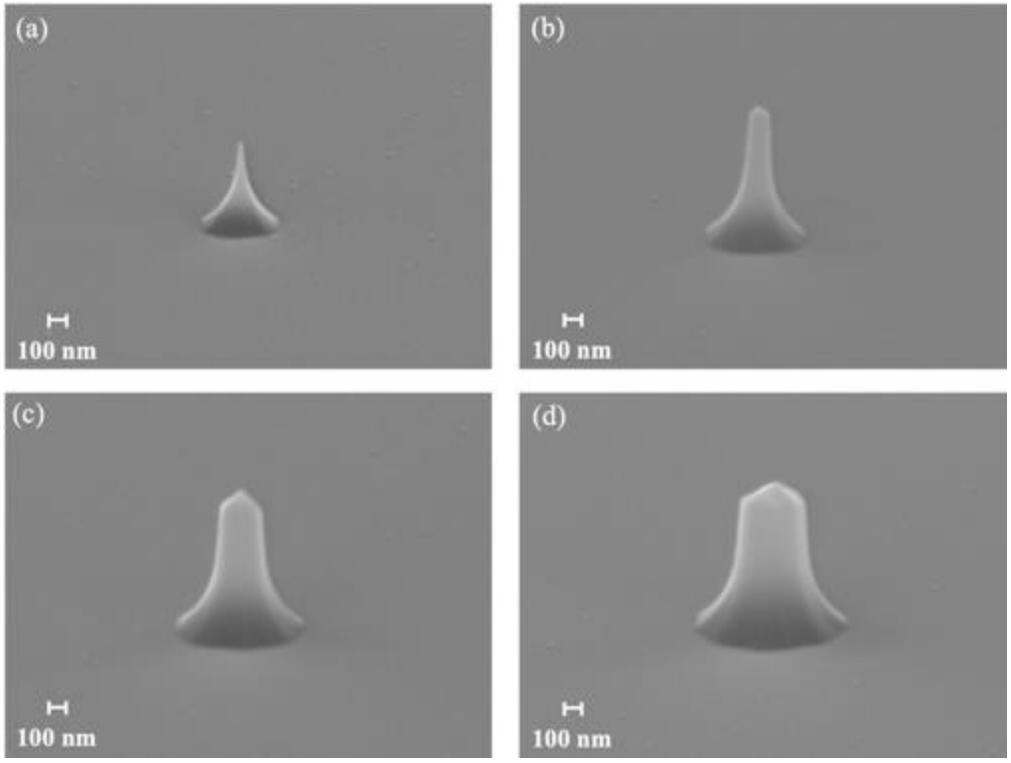


Figure 3.7 SEM images of SiO_2 array after 80 seconds of a dry etching by RIE and 10 min wet etching by BOE, and the designed diameter of MLA is (a) 1.0 μm (b) 1.1 μm (c) 1.2 μm (d) 1.3 μm.

3.2.3.2 Si Etching with 1.1 μm Design

To avoid the sidewall scallop for the Bosch process, the non-switching pseudo-Bosch process can be applied here to etch our Si nanocone array with C_4F_8 and SF_6 supplied continuously and simultaneously to the chamber. In this process, the ratio of SF_6 and C_4F_8 gases can be adjusted to change the tapered angle of the sidewall. Increasing the C_4F_8 gas flow gives a positively tapered profile, but the formation of black silicon was observed, as shown in Fig. SI-2 when the C_4F_8 gas flow is higher than 45 sccm. To avoid these drawbacks and transfer the profile of the SiO_2 mask to the Si substrate, several recipes were carried out to find the etching rate and selectivity between Si and SiO_2, which are listed in Table 3.2. Six sets of Si and SiO_2 pieces coated with photoresist masks are etched using six distinct recipes, and the etching depths were subsequently measured by the BRUKER-Dektak XT system.

The increase in C_4F_8 concentration in Recipes 4, 5, and 6 leads to a slower Si etching rate and smaller selectivity due to over-passivation. With 22 sccm SF_6 gas flow and 38 sccm C_4F_8 gas flow, the increasing ICP power to 2000 W results in increases in both Si and SiO_2 etching rates, but the selectivity decreases. Similarly, increased RF power will decrease the selectivity but enhance the etching rate. Recipe 1 has the highest selectivity and is the appropriate etching rate of Si.

Table 3.2 Recipes for Si etching with SiO_2 mask and corresponding etching rates and selectivities

Recipe #	SF_6 (sccm) / C_4F_8 (sccm)	RF power (W)	ICP power (W)	Si etching rate (nm/min)	SiO_2 etching rate (nm/min)	Selectivity between Si and SiO_2
1	22/38	20	1200	412	59	6.98
2	22/38	20	2000	510	149	3.42
3	22/38	10	1200	301	53	5.68
4	10/50	20	1200	126	95	1.33
5	10/50	20	2000	138	159	0.86
6	10/50	50	1200	185	150	1.23

The fabricated SiO_2 mask patterns in Figure 3.7 (b) were etched using Recipe 1 for 10 minutes, and the achieved Si nanocones are shown in Figure 3.8 (a). The height of the etched profile is 4.03 ± 0.04 μm, and the apex diameter is 63 ± 3.12 nm, as stated in Table SI-1. As we mentioned, the top end of the final etched profile under a circular mask will follow the mask shape, but such a cylinder-shaped apex could not be sharpened by thermal oxidation into a cone-shaped apex[102]. After 30 minutes of dry oxidation at 950 ℃ followed by 1-minute BOE removal of the grown oxide, the apex retained its cylinder shape as shown in Figure 3.8 (b) and (c). Additional SEM images of Si nanocones for the sample size of N = 9 cones are presented in Figure SI-3, and

the dimensions of these nanocones are illustrated in Table SI-2. Based on the diameter of 32.44 nm that was thinned down from 63 nm, further oxidation sharpening may be able to thin down the pillar to a sub-10 nm apex diameter.

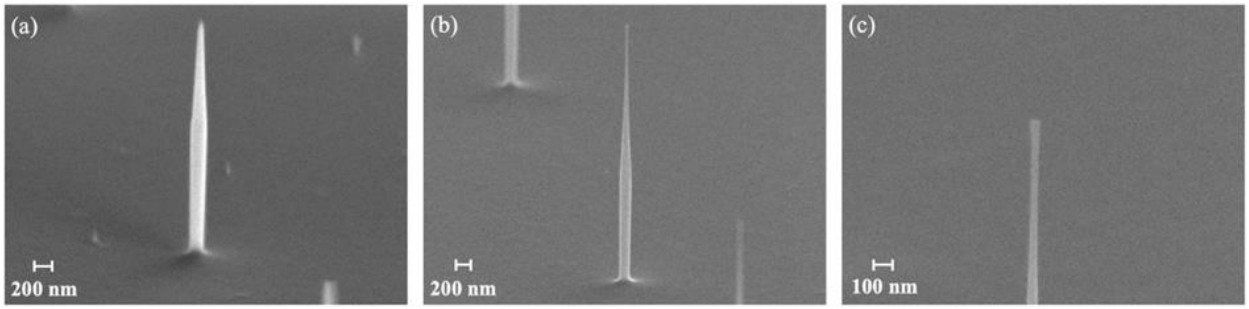


Figure 3.8 SEM images of (a) the Si nanocone with 1.1 μm design after 10 minutes of etching using Recipe 1, (b) the cylindrical Si structure after thermal oxidation, (c) the enlarged view of the Si apex.

While I. Obataya *et al.* reported that a cylindrical nanoneedle with a 200 nm apex diameter has advantages in penetrating the cell membrane with low force and a high success rate[177], M. Penedo *et al.* presented discrepancies in their work[178]. According to their findings, the 200 nm sharp conical nanoneedle exhibits a lower penetration force with a higher success rate than the 200 nm cylinder nanoneedle. They attribute this discrepancy to the sharper tips with smaller apex diameters, facilitating membrane rupture and subsequent perforation. Besides nanoneedles for cell penetration/lysis, Si cones with nano-scale apex have been adopted extensively to develop scanning probes in AFM or STM measurement to reduce the interaction forces and provide higher resolution[179,180], as the scanning results can be significantly influenced by the tip dimensions of the probe in use, as the convolution of the tip profile and the sample surface topography plays a crucial role[181]. Moreover, a nanoprobe with a flat-ended tip may introduce considerable measurement uncertainty owing to imperfect contact[182].

3.2.3.3 Si Etching with 1.0 μm Design

In Section 3.2.3.2, we previously discussed the advantages of using a sharp conical over a cylindrical structure. As a result, we have selected a design that features a 1.0 μm structure to fabricate a Si nanocone through profile transfer from the tapered oxide mask with a conical apex. After 5-minute etching with Recipe 1 in Table 1, the etched nanocones are shown in Figure 3.9 (a) and (b).

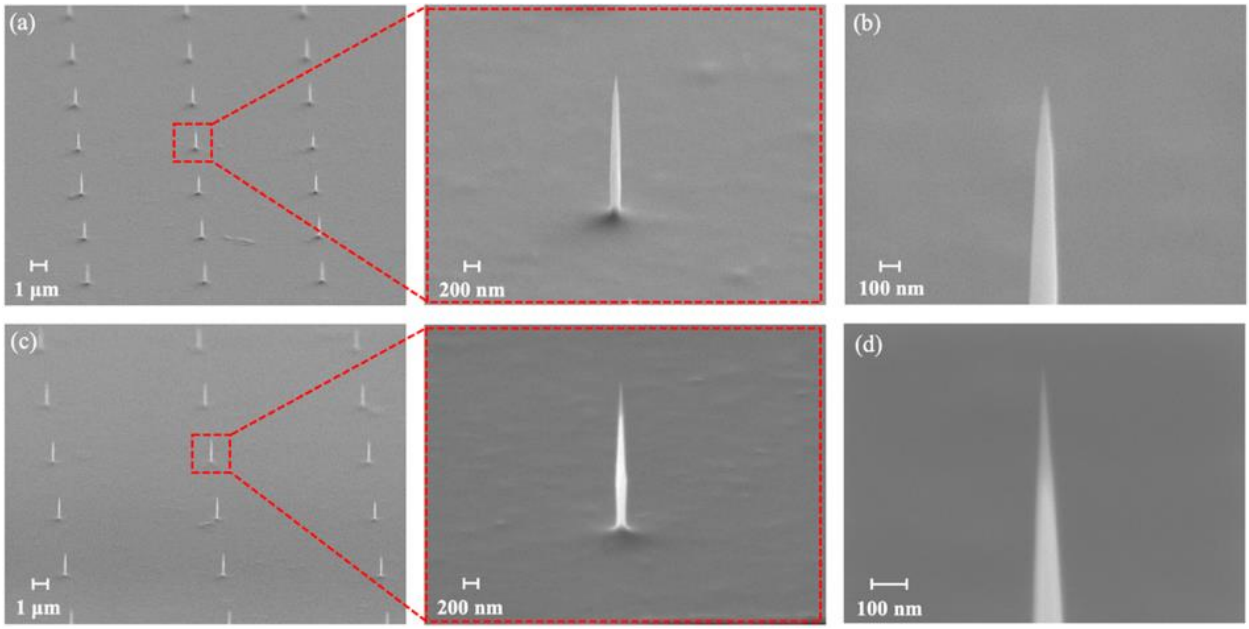


Figure 3.9 SEM images of (a) the Si array with 1.0 μm design after 5-minute etching, (b) the enlarged view of the Si apex, (c) the Si array after oxidation sharpening, (d) the enlarged view of the Si apex after oxidation sharpening.

The height is measured at 2.04 ± 0.03 μm, while the apex diameter reached 27.11 ± 1.17 nm, as stated in Table SI-3. According to our previous study, 950 ℃ is the most appropriate temperature to sharpen the nanostructures[102]. The nanocone array is further sharpened at 950 ℃ for 30 minutes, followed by oxide removal, and the final profiles of the Si nanocones are shown in Figure 3.9 (c) and (d). The nanocone apex is ultimately reduced to 3.54 nm ± 1.13 nm, while the height is measured at 2.01 ± 0.03 μm. The aspect ratio (here defined as the reciprocal of the tangent of the internal half angle, tanθ) is 12.4 ±1.0.

3.2.4 Summary and conclusions

In this study, we developed a novel and CMOS-compatible approach for fabricating the Si nanocone array with large aspect ratios of larger than 10 and sub-5 nm tip apex by using photolithography and then transferring the tapered oxide mask profile into Si. Without using expensive nano-lithography techniques, we employed maskless photolithography and obtained nano-cone structures with a 3.54 nm apex. In the process, a combination of dry and wet etching techniques produced an optimized SiO_2 etching mask with a tapered sidewall profile. Subsequently, the non-switching dry etching process was employed using this oxide mask to transfer the tapered mask shape to the Si substrate, forming the initial nanocone array with 27.11 ± 1.17 nm apex. Thermal oxidation sharpening was subsequently carried out to further sharpen the silicon cone apex to 3.54 ± 1.13 nm. This cheap and efficient process holds great potential for various applications, including X-ray field emission array, trapping array for optical sensors, Si nanoneedle for clinical use, and Si nanoprobes for AFM and STM.

3.3 Cryogenic Etching of Positively Tapered Si Pillars with Controllable Profiles

3.3.1 Introduction

HAR Si nanopillars with diverse profiles are crucial for various applications including solar cells[183], metasurfaces[184], and biosensors[185]. Positively tapered nanopillars with smaller tips are more suitable in applications of cell membrane disruption[186], HAR AFM probes[91] and field emitter arrays[187]. Plasma etching of silicon has been used for decades to create precise features in IC and MEMS devices[109]. One method for fabricating HAR silicon structures is the Bosch process. This

process typically alternates between etching with SF_6 gas and polymer passivation with C_4F_8 gas[188]. However, the intrinsic problem of this process is the scalloped pillar profile on the sidewalls. The fluorine plasma mixed process is another efficient way of fabricating HAR silicon pillars and trenches with smooth sidewalls and no scallops[137]. In this process, the etching gas of SF_6 and the passivation gases of C_4F_8, C_4F_6, or CHF_3 are fed together simultaneously under the inductively coupled plasma (ICP) power and the radio frequency (RF) bias power. In SF_6/C_4F_8 chemistry, the neutral fluorine atoms dissociated from SF_6 are reactive to remove Si atoms while the C_xF_y are dominant to deposit polymers for passivation[189]. By varying the gas ratio of SF_6/C_4F_8, one can obtain silicon structures with diverse profiles[118,119]. In this case, when producing positively tapered silicon pillars, an additional step involving O_2 plasma is necessary to clean the samples and reactor chamber and remove the fluorocarbon deposition.

To prevent fluorocarbon contamination during fabrication of positively tapered silicon nanopillars, cryogenic silicon etching using SF_6/O_2 gases at temperatures ranging from -130 to -90 ℃ can be employed as an alternative etching method. This process was introduced to obtain anisotropic etching, high etch rate and high selectivity[190]. In cryogenic SF_6/O_2 plasma, fluorine radicals react with silicon atoms to form volatile SiF_x byproducts. Meanwhile, the SiF_x molecules interact with oxygen to create a passivation layer of SiO_xF_y[191]. Due to the directionality of plasma ions, the SiO_xF_y layer-covered sidewalls are less exposed to ion bombardment compared to the bottom of the structures and thus the etching proceeds. After the process, upon transfer to the load lock at room temperature, the SiO_xF_y molecules dissociate, resulting in contamination-free silicon etching. By optimizing the balance between the etching and passivation, deep silicon trenches and gratings with 200 nm half-pitch and depth of approximately 10 μm were obtained[192,193]. To obtain cone-shaped nanopillars for back silicon applications, one can increase the O_2 flow to enhance the

passivation using cryogenic etching on a bare wafer[194,195]. During the process, parameters such as SF_6/O_2 gas flows, operation pressure, ICP power, RF bias power, and temperature must be optimized for desired structures. Additionally, loading effects and aspect ratio dependent effect (ARDE) occur in cryogenic etching[196]. The crystallographic orientation dependent effect (CODE) due to the difference in surface density of silicon atoms also modifies the pattern geometry[197]. The cryogenic silicon etch has a higher etching rate and easier profile control compared to room temperature SF_6/O_2 plasma etching[198,199].

Here we investigate the cryogenic etching process to create cone-shaped Si nanopillars with HAR and controllable taper angles by adjusting the passivation and etching in SF_6/O_2 plasma. A two-step etching process with varying O_2 flows is utilized to obtain distinct taper angles at different depths. In addition, this method is efficient and contamination-free[200,201], for fabricating HAR silicon nanopillars.

3.3.2 Experiment

Our etching experiments were performed using a PlasmaPro 100 Cobra ICP tool from Oxford Instrument. This system consists of two RF plasma sources, providing an ICP power at a frequency of 2 MHz and an RF bias power at a frequency of 13.56 MHz. The ICP power antenna rotates around a dielectric alumina tube on the upper part of the chamber. On the lower part, the RF bias power is applied to the chuck where a wafer is placed. During etching, a quartz clamping plate was used to hold the substrate while helium backside cooling maintained a constant cryogenic temperature.

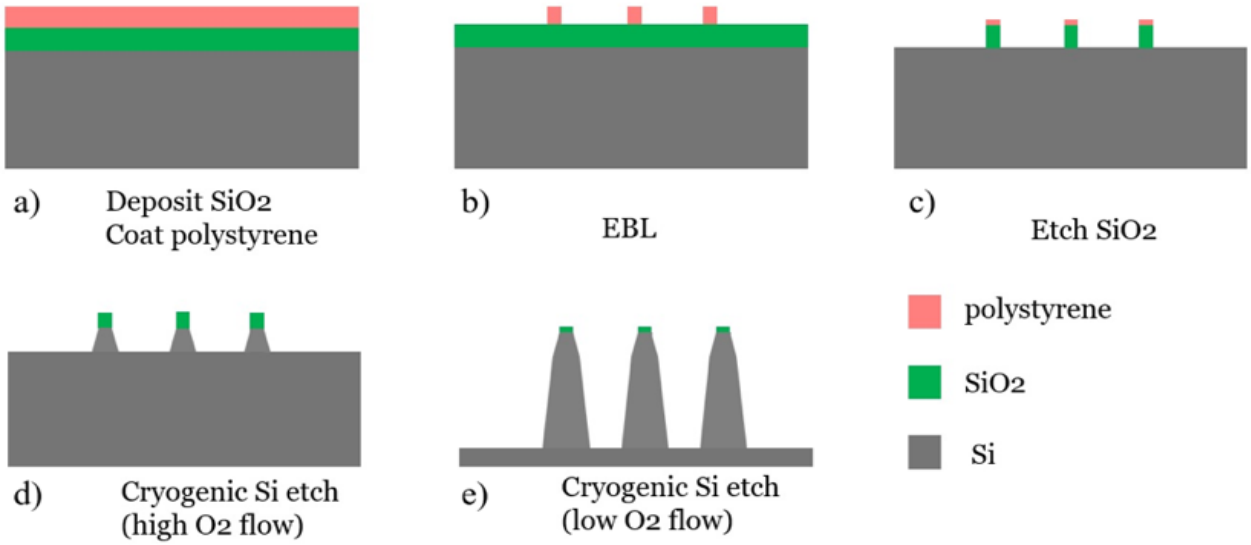


Figure 3.10 Schematic process flow for fabricating cone-shaped silicon nanopillars using cryogenic silicon etching. It consists of (a) thermal oxide deposition and PS resist coating, (b) e-beam exposure and development, (c) oxide etching, (d) cryogenic etching with a higher O_2 flow, and (e) cryogenic etching with a lower O_2 flow.

Figure 3.10 depicts the process flow for the cryogenic etch of cone-shaped silicon nanopillars. Firstly (Figure 3.10a), p-type boron-doped (100) silicon wafers were cleaned in acetone and isopropyl alcohol (IPA). The SiO_2 layer with a thickness of 210 nm was deposited by plasma-enhanced chemical vapor deposition (PECVD, Trion) with TEOS/O_2 gases at 300 ℃. Polystyrene (PS) (Mw= 190 kg/mol, Sigma-Aldrich) dissolved in anisole was spin-coated with a thickness of 320 nm. Secondly (Figure 3.10b), electron beam exposure was carried out using RAITH150 Two EBL System at 20 kV acceleration voltage with a 600 μC/cm^2 dose, and then the exposed PS was developed in methyl isobutyl ketone (MIBK) for 5 minutes and rinsed in IPA for 60 seconds. Thirdly (Figure 3.10c), the SiO_2 was etched using an etcher (RIE) (Trion) with 40 sccm CHF_3 and 5 sccm O_2 at 40 mTorr under 125 W RF power. The etching rates of PS and SiO_2 are 52 nm/min and 40 nm/min, respectively. Figure 3.11 shows the oxide dot array with 82 nm diameter, 2 μm or 10 μm period and 210 nm thickness after SiO_2 etching. The scanning electron microscopy (SEM) images were captured using RAITH150 Two EBL System. In the etch steps (d) and (e), The SF_6/O_2 plasma cryogenic etch was performed at -100 ℃ under 10 mTorr pressure

using a SiO_2 mask. The sample pieces were mounted on a 4-inch carrier wafer using Crystalbond 555 mounting adhesive. The varied O_2 gas flows were used to obtain different tapered angles in the first and second etch steps. The process parameters such as the gas ratio and the RF bias power were tuned with test samples consisting of a SiO_2 dot array with a thickness of 50 nm or 210 nm. The patterning parameters are the same as in step (b) but with a 160 nm PS thickness for 50 nm thick oxide.

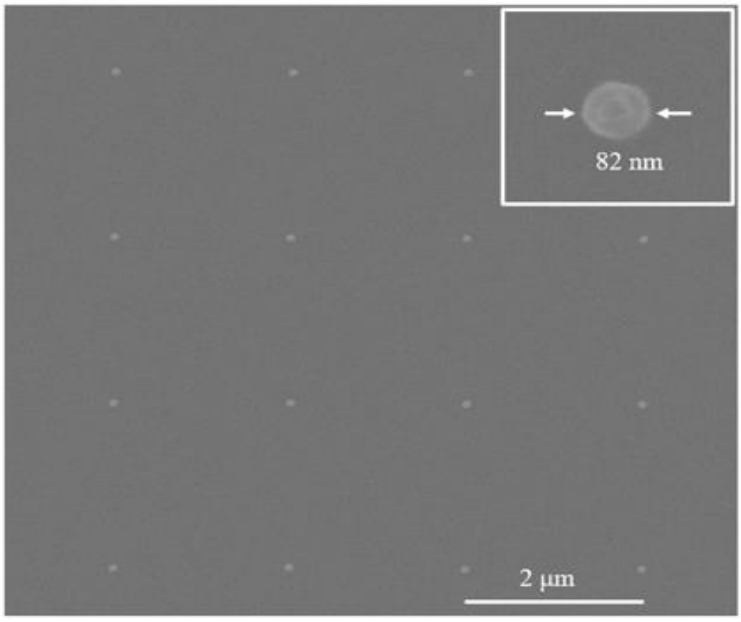


Figure 3.11 Patterned oxide dot array as a hard mask for cryogenic etching.

3.3.3 Results and discussion

In cryogenic silicon etching, fluorine radicals react with silicon atoms and release SiF_x byproduct. The SiO_xF_y film forms on the exposed silicon surface due to a reaction between oxygen atoms and SiF_x. With the ion bombardment accelerated by the RF bias power, the SiO_xF_y on the bottom is removed and the etching proceeds, leading to directional etching and specific profiles[202]. Increasing the O_2 content leads to a harder passivation layer on the sidewalls while a higher RF bias power/DC bias voltage (i.e. more ion energies) enhances the removal of the passivation layer.

To achieve nanopillars with a controllable positively-tapered profile and a 10 μm height and a HAR, a large O_2 gas flow for hard passivation to avoid lateral etching and high energy species for deep etching are required[202]. On the other hand, excessive O_2 gas flow leads to passivation islands as nano/micromask on the silicon surfaces, resulting in the formation of black silicon[195]. The high energy species lead to strong ion bombardment and deteriorate the mask erosion. When etching HAR structures, the ion angular distribution function (IADF) is an important plasma parameter which is determined by the reactor pressure and the DC bias voltage. Applying a higher DC bias on the chuck results in smaller IADF, which favours etching HAR structures[195,199]. This section explores the influence of O_2 content and RF forward power on pillar profile, etch rate and selectivity. A two-step etching process to obtain desired profiles is also presented.

3.3.3.1 Effect of O_2 content

In cryogenic silicon etching, the O_2 content is crucial for the formation of the passivation layer[203]. In SF_6/O_2 plasma in the temperature range of -70 ℃ to -140 ℃, the fluorine and oxygen radicals react with silicon atoms and create SiO_xF_y layers as the inhibitor on the silicon surface. The inhibitor on the bottom is removed by the bombardment of the incident ions driven by the RF bias voltage, and the silicon etching proceeds. The appropriate balance between passivation and lateral etching of inhibitors leads to various profiles[204]. Specifically, dominant passivation leads to a positive taper and vice versa. During the sample warm-up, the inhibitor of the SiO_xF_y layer desorbs and forms volatile byproducts, leaving a clean surface. The effects of O_2 content on the silicon etching rates and taper angles were investigated by varying the O_2 gas flow under the conditions of 71 sccm SF_6 gas flow, 9-13 sccm O_2 gas flow, 10 mTorr pressure, 3 W RF forward power (led to 78 V RF bias voltage), 600 W ICP power and -100 ℃ temperature. Figure 3.12

presents the changes in the silicon etch rate and the taper angle with the O_2 concentration. The etch rate of silicon remains constant at 2.7 μm/min, as the fixed SF_6 gas flow and operational pressure determine the reaction between fluorine radicals and silicon atoms. With the increase in O_2 gas concentration from 0.113 (9 sccm O_2 flow over 80 sccm total flow) to 0.155 (13 sccm O_2 flow over 84 sccm total flow), the taper angle increases steadily from 4.9° to 10.5°. To ensure the measurement accuracy, three measurements were conducted for each angle and then calculated their average. The taper angle is defined as the angle formed between the sidewall and the vertical direction. Figure 3.13 presents the SEM images of silicon profiles obtained with O_2 gas flows of 9 sccm (the main part in Figure 3.13a), 10 sccm (the lower part in Figure 3.13c), 12 sccm (Figure 3.13b) and 13 sccm (the upper part in Figure 3.13c). In Figure 3.13a, the mask with a thickness of 50 nm disappeared during the etching process, but the taper angle remained. For each O_2 gas flow, the taper angle is constant within 1 min to 4 min etching. Additionally, a relatively rough surface is observed on the upper portion of silicon pillars using a high O_2 gas flow of 12 sccm. Modifying the flow of O_2 gas can cause substantial variations in taper angles. More O_2 content leads to a thicker SiO_xF_y on the sidewalls, which is harder to remove. Consequent to this point, the lateral etching rate decreases, leading to larger positively tapered angles. The results are consistent with the previous studies. When the concentration of O_2 is increased, larger silicon features are created while etching HAR silicon grating structures using the same mask patterns[193]. Excessive addition of O_2 leads to the development of black silicon featuring a positively tapered profile[195].

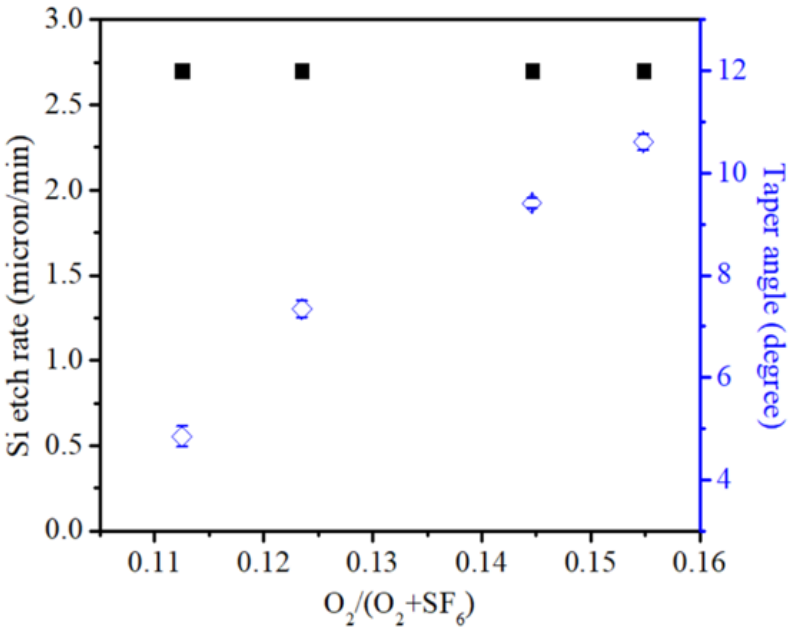


Figure 3.12 The dependence of silicon etching rates and taper angles on O_2 concentration.

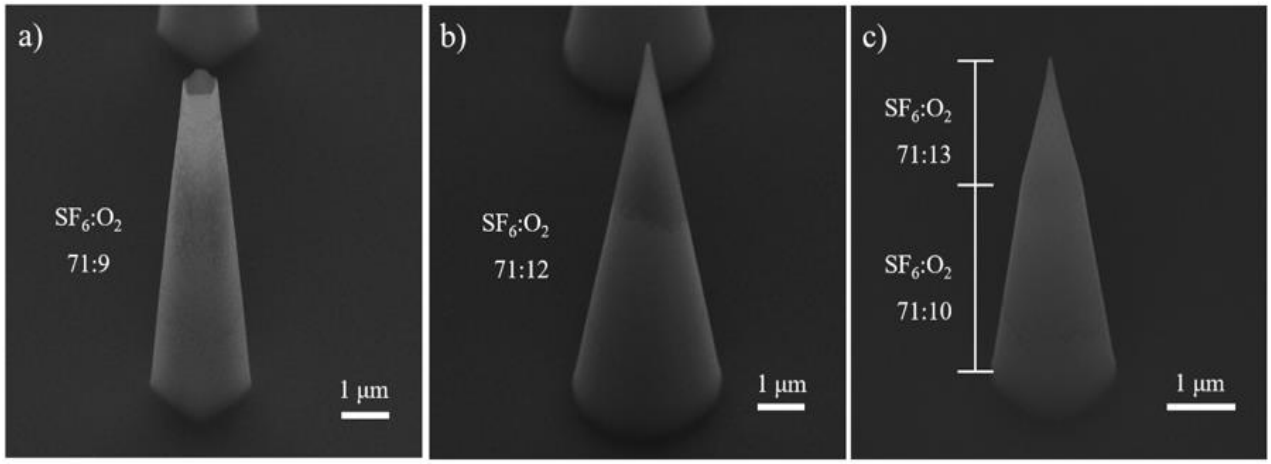


Figure 3.13 SEM images of silicon pillars etched using different O_2 gas flows of (a) 9 sccm, (b) 12 sccm and (c) 10 sccm for the lower portion and 13 sccm for the upper portion.
`

3.3.3.2 Effect of RF bias voltage

The RF bias voltage in silicon etching facilitates the anisotropic etching through the acceleration of positive ionic species across the plasma sheath[205]. With the same condition of SF_6/O_2 plasma density and passivation layer on the silicon sidewalls, higher RF bias voltage results in stronger bombardment and higher directional etching with increased verticality as well as the

deteriorated resistance of the mask. The patterned SiO_2 dot arrays with 82 nm diameter and 50 nm thickness were etched by varying the RF bias voltage from 74 V to 119 V under the conditions of 71 sccm SF_6 gas flow, 13 sccm O_2 gas flow, 10 mTorr pressure, 600 W ICP power, -100 ℃ temperature and 1-minute duration. Prior to etching, a 10-second strike step with a high O_2 flow of 15 sccm was inserted to avoid a noticeable undercut under the mask. This step goes beyond the over-passivation region, preventing significant silicon etching. Once a lower O_2 flow is injected, the fast etching begins. Figure 3.14 shows the SEM images of pillar profiles etched at RF bias voltages of 74 V, 83 V, 93 V and 119 V. The SEM images were captured at 45° tilt angle. Figure 3.15 presents the variations of Si/SiO_2 etch rates and the profile angles. In Figure 3.15a, the silicon etch rate remains nearly constant as the SF_6 gas flow was fixed as 71 sccm. With a variation of RF bias voltage, the etch rate of SiO_2 increases from 22.3 nm/min to 41 nm/min. The increasing RF bias voltage increases the SiO_2 etch rate and reduces the selectivity of SiO_2 to silicon, which is consistent with published literature[192,195]. In Figure 3.15b, the taper angle is around 10° at 74 V RF bias voltage and decreases to 6.3° at 119 V bias voltage. The value of each angle was calculated as the average of three measurements. When the RF bias voltage is 74 V, the surface of silicon structures is smooth, though nanoscale dots are found on the bottom surface due to insufficient bombardment. The increase in RF bias voltage up to 119 V, provides sufficient bombardment and enhances lateral etching, resulting in a smaller tapered angle and cleaner sidewalls and bottom surfaces. More importantly, the increase in RF bias voltage also decreases the IADF of the incident positively charged ions and their deflection on the etched sidewall[204]. Consequently, at higher RF bias voltages, the upper portions of silicon pillars are more vertical than the lower portions.

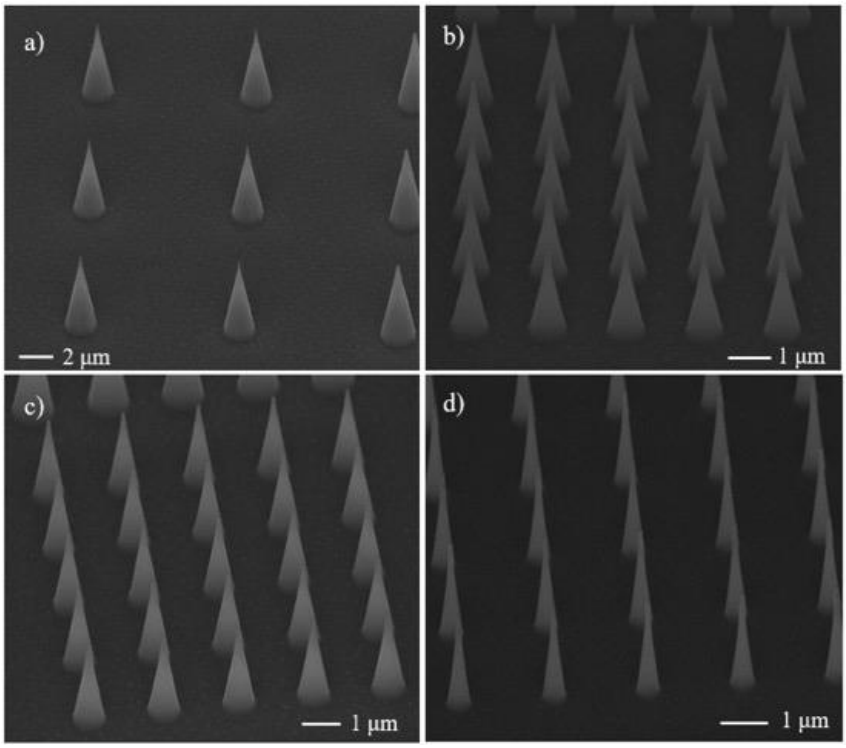


Figure 3.14 Taper angle variation with RF bias voltages of (a) 71 V, (b) 84 V, (c) 93 V and (d) 119 V. The SEM images were captured at 45 degrees tilt.

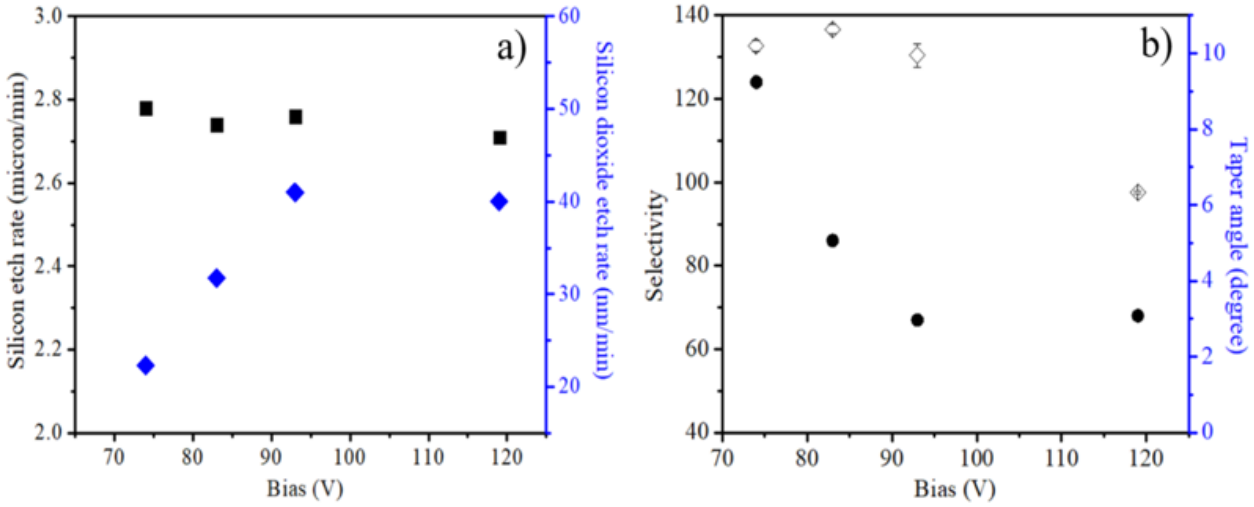


Figure 3.15 The dependence of silicon and SiO_2 etching rates (a), as well as taper angle and selectivity (b) on the bias voltage.

3.3.3.3 Two-step etching

By adjusting the O_2 content and RF bias voltage, the controllability of etched HAR profiles can be achieved, as discussed. HAR nanostructures with diverse portions along depth can be

obtained by combining different etching conditions. To achieve more vertical silicon pillars, two etch steps were combined with higher and lower O_2 contents. The two-step etching conditions are listed as Combination I in Table 3.3. The first etch step with 71/13 sccm SF_6 /O_2 flows leads to positively tapered profiles while the second one with 73/10 sccm SF_6 /O_2 flows results in relatively vertical profiles, as shown in Figure 3.16. In Figure 3.16a, with the 82 nm features of SiO_2 mask, the height of all pillars is 3 μm and the diameter of the middle part is 47 nm. The aspect ratio is around 63. With the 194 nm diameter SiO_2 mask, as shown in Figure 3.16b, both the top and base portions of silicon pillars are larger than the middle part. With different diameters and aspect ratios, the profiles appear slightly bowed. The reduced passivation at the middle portion may be due to factors such as Knudsen transport of neutrals, ion shadowing, neutral shadowing, and differential insulating charging charging[206–208].

Table 3.3 Parameters for two-step cryogenic etching process I

	Step 1	Step 2
SF_6 gas flow (sccm)	71	71
O_2 gas flow (sccm)	13	10
Pressure (mTorr)	10	10
ICP power (W)	600	600
RF bias power (W)	10	10
DC bias (V)	120	120
Duration (sec)	10	60
Temperature (°C)	-100	-100

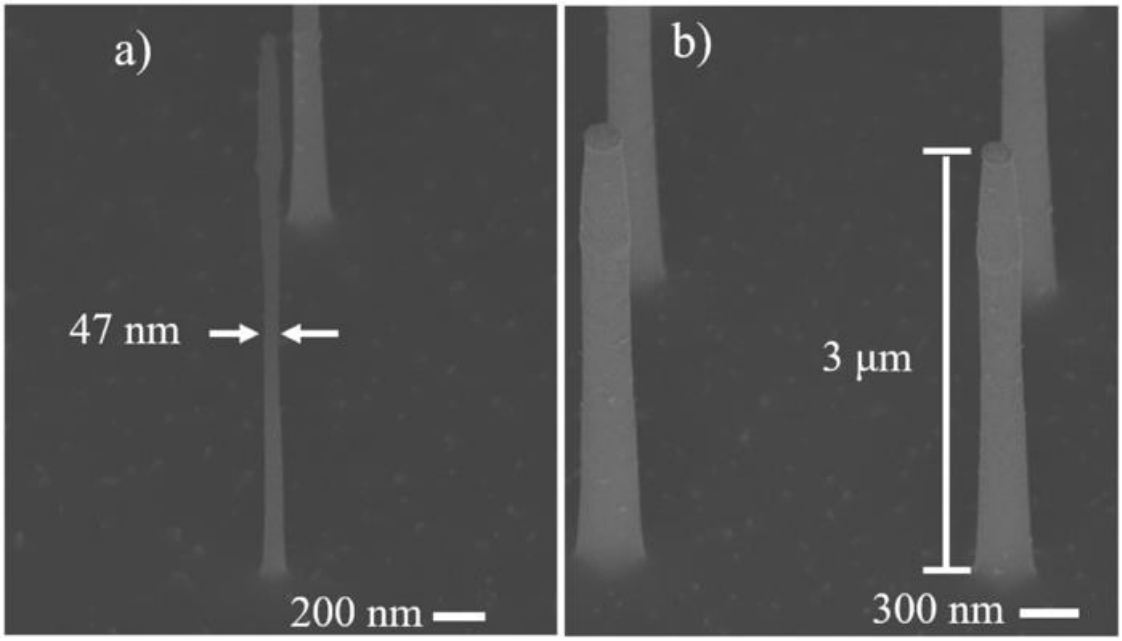


Figure 3.16 High aspect-ratio silicon pillars were etched using a two-step cryogenic etching process with SiO_2 masks having (a) 82 nm diameter and (b) 194 nm diameter.

In the above two-step process, 10 W RF bias power and corresponding 120 V bias voltage result in a low selectivity of SiO_2 during etching. To increase the selectivity and obtain a desired profile, 3 W RF bias power (led to 83 V bias voltage) were employed, and correspondingly, the O_2 gas in two steps decreased from 12 sccm and 10 sccm to 12 sccm and 9 sccm, respectively, as Combination II listed in Table 3.4. The reduction in bias voltage leads to less bombardment though the less O_2 content results in the decrease in passivation. Consequently, the profiles were pronounced to be more positively tapered as presented in Figure 3.17. It means that the reduction of bombardment is more significant than the decrease in passivation. In the etching process, the SF_6 gas flow was kept constant to maintain the Si etching rate of 2.7 μm/min. With 210 nm thick SiO_2 mask patterns, 10.3 μm high and positively tapered silicon pillars were achieved. The diameter of the remaining SiO_2 mask at the top shrunk from 82 nm to 36 nm due to mask erosion, and the shrinkage makes pillars sharper. The etching selectivity of SiO_2 to silicon was measured to be 1:86. It should be noted that the bottom parts of the pillars exhibit a crystal orientation

dependence effect. This may be due to the different reactivity of fluorine towards Si (100) and Si (111) planes at cryogenic temperatures[196].

Table 3.4 Parameters for two-step cryogenic etching process II

	Step 1	Step 2
SF_6 gas flow (sccm)	71	73
O_2 gas flow (sccm)	12	9
Pressure (mTorr)	10	10
ICP power (W)	600	600
RF bias power (W)	3	3
DC bias (V)	83	83
Duration (sec)	30	210
Temperature (°C)	-100	-100

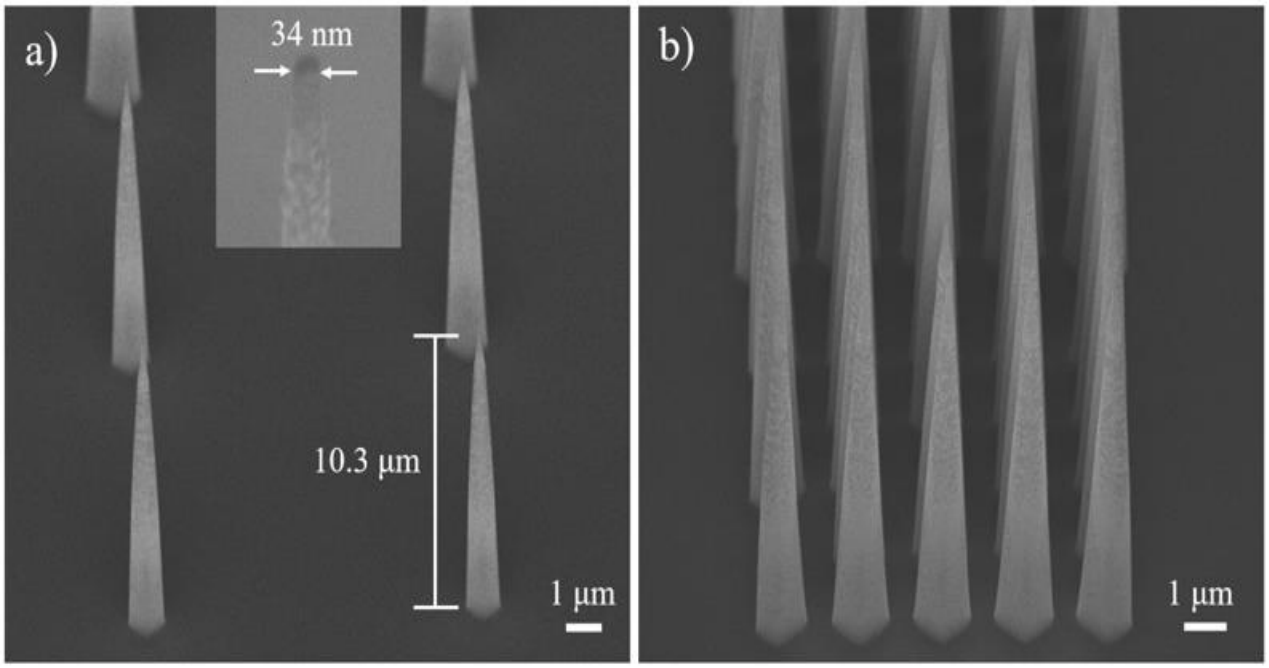


Figure 3.17 Cone-shaped silicon pillars with 10.3 µm height and different tapered parts with (a) 10 µm period and (b) 2 µm period. The embedded image depicts the top of the pillars.

In both Combination I and II, the top and bottom parts were controlled separately to have either a positive taper or a vertical profile by adjusting the gas ratio and RF bias power while fixing other parameters. When more O_2 was used, the silicon pillars were more positively tapered, while less O_2 made them vertical or less positively tapered. This is because less O_2 reduced the formation of SiO_xF_y film as a passivation layer on the plasma-exposed surface, which enhanced the lateral silicon etching and resulted in less tapered profiles[209]. In Combination II, the RF forward voltage was reduced to 83 V and the O_2 gas flow was reduced by 1 sccm, resulting in a desired taper angle of 2.2 degrees. This means that the decrease in the bombardment outweighed the reduction of SiO_xF_y film formation. By adjusting the O_2 content and RF bias voltage, it is possible to control cryogenic silicon etching and achieve precise nanostructure profiles. The resulting structures have a larger base and a smaller apex, making them more durable for various applications such as cell membrane disruption and HAR AFM probes[91,186,187].

3.3.3.4 Summary and conclusions

Si pillars with positively tapered or vertical profiles were successfully produced with excellent control by adjusting the gas ratio and RF bias voltages during the cryogenic etching process. The top and bottom profiles of the pillars were also easily controlled by changing the O_2 gas flow at different etching stages. By maintaining an SF_6 gas flow to achieve an etching rate of 2.7 μm/min, the taper angle of the Si pillars increased from 4.9° to 10° when the O_2 concentration was increased from 0.113 to 0.155. Furthermore, varying the RF forward voltages from 73 V to 119 V resulted in a change of the taper angle from 10° to 6.3° due to increased bombardment, which worsened the selectivity of the SiO_2 mask to silicon. The combination of etching steps with varied O_2 contents and RF forward voltages was utilized to produce the silicon pillars with distinct

top and bottom sections, which could be either positively tapered or vertical. The height of the silicon pillars was 10 μm and the top apex was 36 nm. These results demonstrate the ability to precisely control cryogenic silicon etching to create the desired silicon nanostructure.

3.4 Fabrication of Si Sharp Nanocones using Dry Etch with Periodic Oxygen Plasma Shrinking and Wet Etch

3.4.1 Introduction to etching recipe

Here we will first describe a fabrication process to create a silicon cone-shape structure, which has one end pointy for high resolution and the other end wide for mechanical strength. Moreover, the working principle of oxidation sharpening relies on a cone-shaped silicon structure. Cone-shape etching with a controlled sidewall taper angle is challenging because usually, anisotropic etching gives a vertical (not tapered) sidewall whereas isotropic etching gives a curved (not a straight slope) sidewall.

Since O_2 plasma etching is widely utilized for resist removal, one can use O_2 plasma etching to shrink the resist mask along with both the vertical and lateral directions. This size shrinkage is controllable due to the mature O_2 plasma etching process for polymer. The goal here is to fabricate a ~10 μm-tall tip structure with a tapered upper portion sitting on top of a cylinder-shaped (i.e. vertical sidewall) lower portion. The schematic representation for such tip profile fabrication using the Bosch etching process for the lower cylinder portion, and the pseudo-Bosch process with periodic O_2 shrinking for the upper portion, is shown in Figure 3.18 and Figure 3.19.

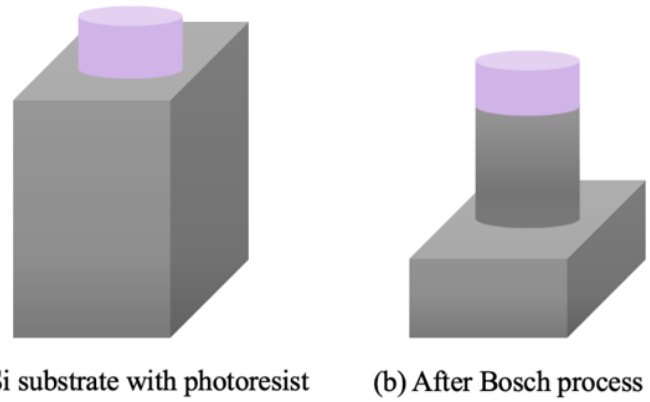


Figure 3.18 Schematic representation of Bosch etching to form a cylinder-shaped base (lower portion) in silicon.

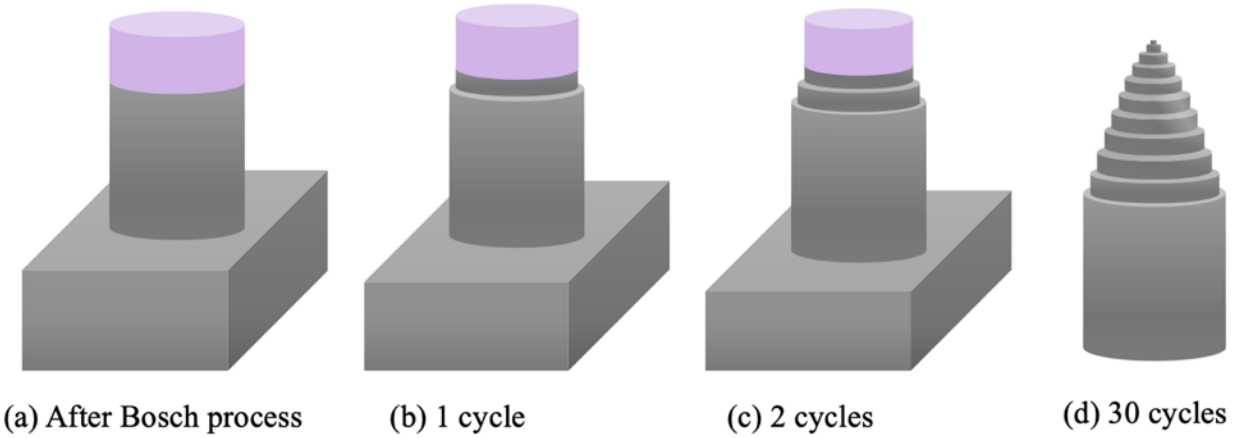


Figure 3.19 Schematic representation of pseudo-Bosch process with periodic O_2 shrinking, and the profile of etched pillar after (a) Bosch process, (b) 1 cycle of pseudo-Bosch plus O_2 shrinking of the resist, (c) 2 cycles of pseudo-Bosch plus shrinking, (d) 30 cycles of pseudo-Bosch plus shrinking (the number of steps should be 30, but here we draw fewer steps just to show the concept of the process).

3.4.2 Introduction

Si nanocone structures find diverse applications in optoelectronic devices, biological detections, and characterization tools. These applications include solar cells[210], field emission tips[211], nanoneedles[128] and nanoprobes[129]. Nanocone arrays integrated with solar cells reduce reflections and enhance antireflection characteristics[212]. In the field of emission such as X-ray imaging, optimizing tip field-induced electron emission performance is crucial. This involves

reducing the tip radius and selecting an appropriate cone height to achieve a high current under low voltage[159]. In clinical applications, Si nanoneedles with reduced tip diameters enable non-destructive cell penetration, facilitating valuable cell performance detection without cell rupture[213]. AFM is widely employed for surface measurement of insulators, semiconductors and conductors, offering atomic-scale resolution[7,214,215]. The individual probe is typically a pyramid or cone shape, with a tip diameter that can reach below 20 nm. The sharpness of the tip profile significantly impacts the scanning accuracy of AFM, and blunt tips often distort scanned images[179]. A high-precision AFM can achieve accuracies of the order of 0.1 nm horizontally and vertically.

F.Y. Zhu *et al.*[216] utilized SF_6 and C_4F_8 gases for the maskless deep reaction ion etching (DRIE) process to create a non-uniform and irregular Si nanocone forest with low reflectivity. Similarly, using the argon (Ar) ion bombardment method, S. Xue *et al.*[217] manufactured non-periodic dense Si nanocones with iron (Fe)/chromium (Cr) -enriched metal silicide apexes, demonstrating exceptional field emission properties. F. Bai *et al.*[218] performed the mask of K_2SiF_6 particles with a silver-assisted chemical etching process to generate composite structures of nanowires and nanopillars on Si substrates. To create nanocones with a specific period and regular morphology, some methods involve growing nanowires and then sharpening them through etching. A. Goryu *et al.*[219] tried VLS growth to synthesize nanowires. They spin-coated photoresist on the nanowires and then exposed the tips using O_2 plasma. The tips were sharpened in HNO_3 and HF solutions. In this method, impurities caused by the metal catalyst used in growth may impact wet etching and hinder subsequent oxidation sharpening methods[220]. H.S. Seo *et al.*[221] used electrochemical etching combined with KOH-assisted etching to fabricate nanowires. The diameter and height of the Si nanowire can be adjusted according to the current density, and the sharpness of nanocones depends on KOH etching control. In our previous work, nanowires were

fabricated by using the non-switch pseudo-Bosch process (SF_6/C_4F_8 plasma etching)[116] These nanowires were then etched into nanocones using HNO_3 and HF mixture. This process requires costly EBL and masks with small diameters. Dry etching is more efficient, has higher resolution, and is easier to control compared to wet etching. Among the common dry etching processes, the Bosch process is suitable for creating structures with high aspect ratios, but it often results in scallop sidewall[137]. The non-switch pseudo-Bosch process, which introduces etching and passivation gases simultaneously, can maintain a smooth sidewall[118].

This paper presents a novel and cost-effective approach to create a nanocone array with positively tapered profiles. The standard Bosch process was employed to form the nanopillar base. The SF_6/C_4F_8 and O_2 gases were introduced alternately to sequentially etch the nanocones and shrink the photoresist laterally. This repetitive shrinkage of the resist mask gives the tapered sidewall of the Si nanocone. The Si nanocones were subsequently sharpened through thermal oxidation followed by HF oxide removal, resulting in a final apex diameter of 20 nm.

3.4.3 Experiment

The fabrication schematic is shown in Figure 3.20. A 4-inch Si wafer was pre-cleaned by rinsing in acetone and isopropyl alcohol (IPA), and the surface was further cleaned with O_2 plasma. After spin coating 3.2 µm nLof 2035 photoresist at 3000 rpm and baking at 110 °C for 1 minute, photolithography was performed using a direct write UV lithography system (MLA150, Heidelberg Instruments) to write a dot array with a diameter of 2.5 µm and a period of 10 µm with a dose of 220 mJ/cm^2 and a 365 nm light source. The post-exposure bake is conducted at 110 °C for 1 minute. The sample was then developed in MICROPOSIT MF-319 for 1 minute.

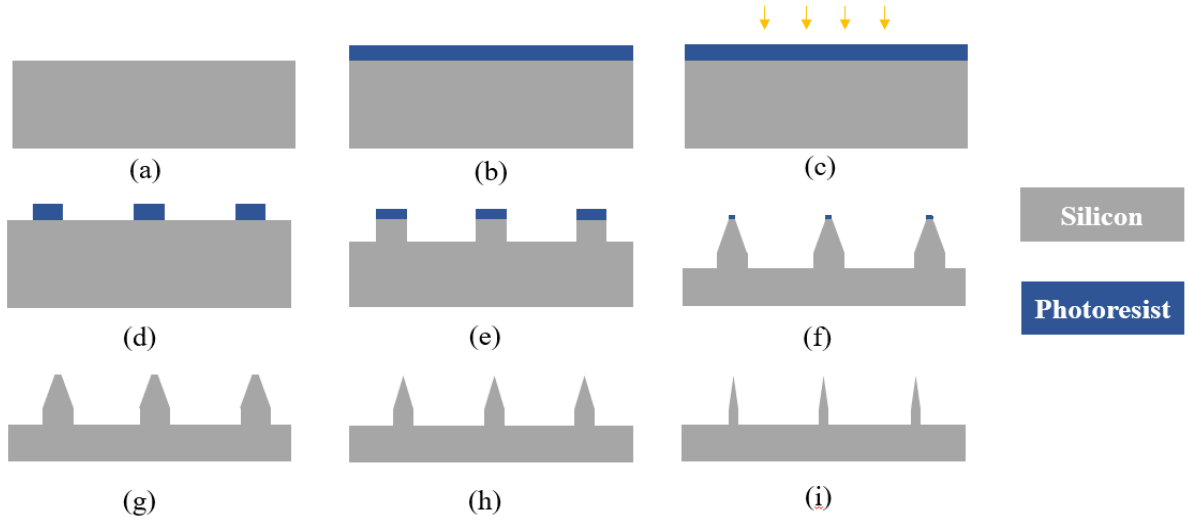


Figure 3.20 Schematic of the fabrication process for nanocones. (a) Prepare a Si wafer, (b) spin-coat nLof 2035 photoresist, (c) photolithography, (d) develop, (e) etch Si using the standard Bosch process, (f) alternatively etch Si by C_4F_8/SF_6 and shrink resist mask using O_2 plasma, (g) remove resist, (h) wet etch, (i) thermal oxidation sharpening.

After creating the mask pattern, a standard Bosch process was used to etch the cylinder base to a height of 5 µm. In the Si etching step, the conditions are 160 sccm SF_6 gas flow with 1000 W inductively coupled plasma (ICP) power and 20 W radio frequency (RF) power under 20 mTorr for 7 s. In the passivation step, the conditions of 160 sccm C_4F_8 with 1000 W ICP power and 5 W RF power under 20 mTorr for 5 s were used. After 15 cycles of standard Bosch, the non-switch pseudo-Bosch process with the O_2 plasma shrinking step was applied to etch the Si nanocone. In this cyclic etching process, SF_6 and C_4F_8 mixture (SF_6/C_4F_8 = 22/38, 1200 W ICP power, 10 W RF power,10 mTorr for 32 s) were used to etch Si, and O_2 plasma (40 sccm gas flow, 1000 W ICP power, 5 W RF power, 10 mTorr for 12 s) was utilized to shrink the photoresist mask. The total etching time of 30 cycles of the non-switch pseudo-Bosch process with the O_2 plasma shrinking step was 24 minutes.

After resist removal, HF (49%) was used to remove the surface self-growing oxide layer for 10 s. The sample was soaked in KOH (35%) with 360 W power ultrasonication at room temperature. Alternatively, we also used a solution of HNO_3 (69%): HF (49%) = 100:1 at room

temperature for etching the same sample. Finally, a sharpening process consisting of two hours of oxidation in air at 950 °C and HF (49%) wet etching was conducted to sharpen Si nanocones.

3.4.4 Results and discussion

3.4.4.1 Dry etching using the standard Bosch process and the non-switch pseudo-Bosch with oxygen plasma resist shrinking

O_2 plasma etching is widely used to remove photoresist materials. This process can also be used to reduce the size of the resist mask both vertically and laterally. The lateral etching of photoresist results in the reduction of feature size, which can help in cost-effective scaling down of resist patterns created by photolithography. A periodic O_2 plasma etching step can be inserted into the SF_6/C_4F_8 plasma Si etching step to reduce the mask size.

To fabricate a 10 μm-tall tip structure with a tapered upper portion sitting on top of a cylinder-shaped lower portion, two etching processes were conducted. Firstly, a Bosch recipe was employed to etch a vertical pillar for the bottom part. The etching rate of the Bosch process is 500 nanometers per cycle (12 sec) while the selectivity between silicon and photoresist is 40:1. In comparison, the etching rate of the pseudo-Bosch process is approximately 140 nanometers per cycle (32 sec) with a selectivity of only 6. The patterned resist dots with 3.5 μm thickness and 2.5 μm diameter were used to mask 12 cycles of the standard Bosch process, followed by 35 cycles of pseudo-Bosch with periodic O_2 shrinking. These two recipes are shown in Table 3.5 and Table 3.6. In the second etching process for the upper portion, the etching step is 32 sec and the O_2 plasma shrinking step is 12 sec. After the two etching processes, Si nanocones with a 400 nm apex and a 2.5 μm base diameter were obtained on top of a 10 μm cylinder, as shown in Fig. 3.21. The pseudo-Bosch process with periodic O_2 shrinking eliminated the sidewall scalloping effect caused by the Bosch

process. After using this recipe, the pillar apex diameter was reduced significantly from 2.5 μm to 400 nm. It can be concluded that the desired profile can be achieved by using the combination of the Bosch process and the pseudo-Bosch with periodic O_2 shrinking.

Table 3.5 Recipe of the standard Bosch process

	ICP power (W)	RF power (W)	SF_6 (SCCM)	C_4F_8 (SCCM)	Pressure (mTorr)	Time (s)
Etching	1000	20	160	0	25	7
Passivation	1000	5	0	160	20	5

Table 3.6 Recipe of the non-switch pseudo-Bosch with O_2 shrinking process

	ICP power (W)	RF power (W)	SF_6 (SCCM)	C_4F_8 (SCCM)	O_2 (SCCM)	Pressure (mTorr)	Time (s)
Etching	1200	10	38	22	0	10	32
Shrinking	1000	5	0	0	40	10	12

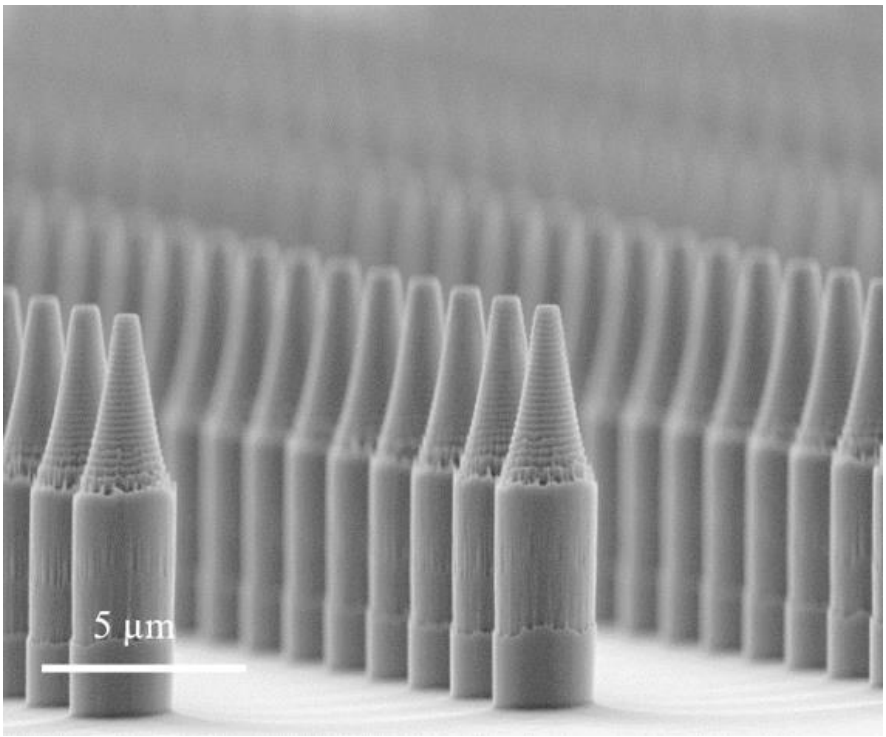


Figure 3.21 Si nanocones were created using the standard Bosch process and the non-switch pseudo-Bosch with O_2 plasma shrinking.

3.4.4.2 Anisotropic wet etching using KOH

To reduce the nanocone diameter, maskless anisotropic wet etching with KOH solutions can be employed. In an alkaline environment, hydroxide ions (OH-) oxidize Si, generating hydrogen

(H_2). The accumulation of H_2 on the surface creates a micro mask that can cause surface roughness and lower the etching rate. So we used ultrasonication to facilitate the escape of H_2 and thus improve roughness and etching rate. Moreover, the etching rate is dependent heavily on the crystal orientation of Si[222].

The pre-etched nanocones were etched in 35% KOH solution with ultrasonication at room temperature to maintain a controllable and relatively slow etching rate. As the etching proceeds, the tip apex becomes smaller. After 8 minutes of etching, the base of the cone was reduced by 350 nm horizontally and height was reduced by 700 nm. The resulting tip apex diameter reached down to 70 nm, as depicted in Figure 3.22. The profile of Si nanocones is primarily determined by the dry etching step. In KOH etching, anisotropy etching is insufficient to determine the crystal orientation of the sidewall surface. It is important to note that the "bumps" on the sidewalls may result from H_2 bubbles formed during etching even with ultrasonication.

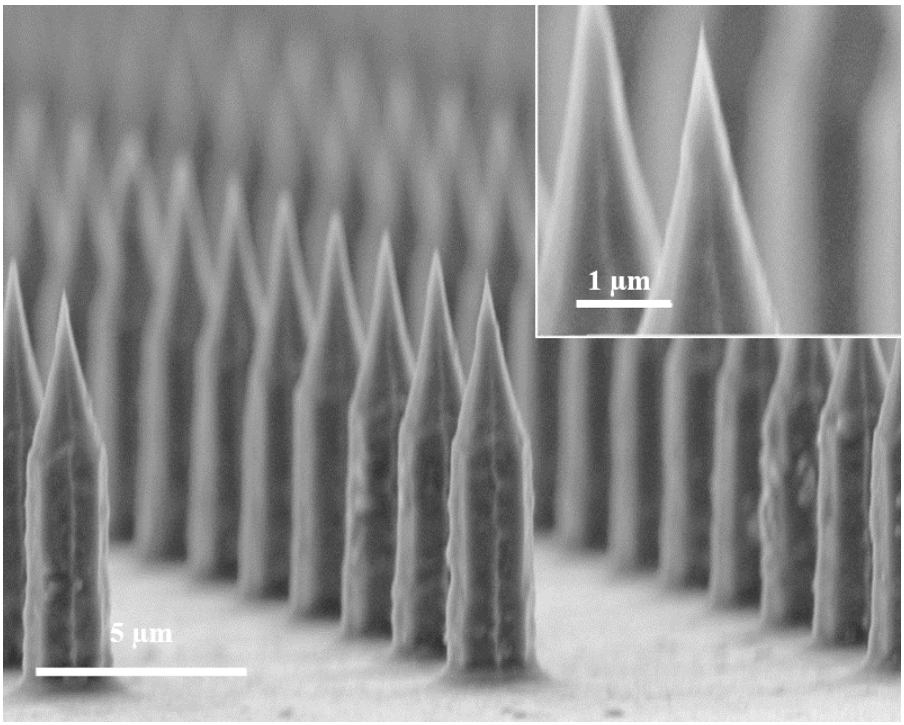


Figure 3.22 35% KOH etching at room temperature for 8 minutes with ultrasonication.

3.4.4.3 Isotropic wet etching using HNO_3 and HF

An alternative way to etch and shrink the nanocones is isotropic wet etching using HNO_3 and HF mixture. The diluents of water or acetic acid (CHCOOH) (HNA system) can be added to decrease the etching rate. In the etching process with a higher concentration of HF relative to HNO_3, the etching is driven by the oxidation of Si. HNO_2 is the etching product that also catalyzes this self-catalytic oxidation process, creating positive feedback. The presence of trace amounts of HNO_2 impurity in the HNO_3 solution introduces uncertainty in the incubation period of the reaction, resulting in a rough surface when the etching rate is limited by HNO_3[141].

To mitigate roughness and sharpen the apex of nanocones, isotropic wet etching was conducted with a very low HF concentration (100:1 HNO_3: HF ratio, etching rate limited by HF) for 3 minutes. The results are shown in Figure 3.23. The base diameter and the height of the structures were reduced by 400 nm and 300 nm respectively. The tip apex significantly decreased from 400 nm to 75 nm. Due to the isotropic etching, the Si nanocones maintained a circular shape.

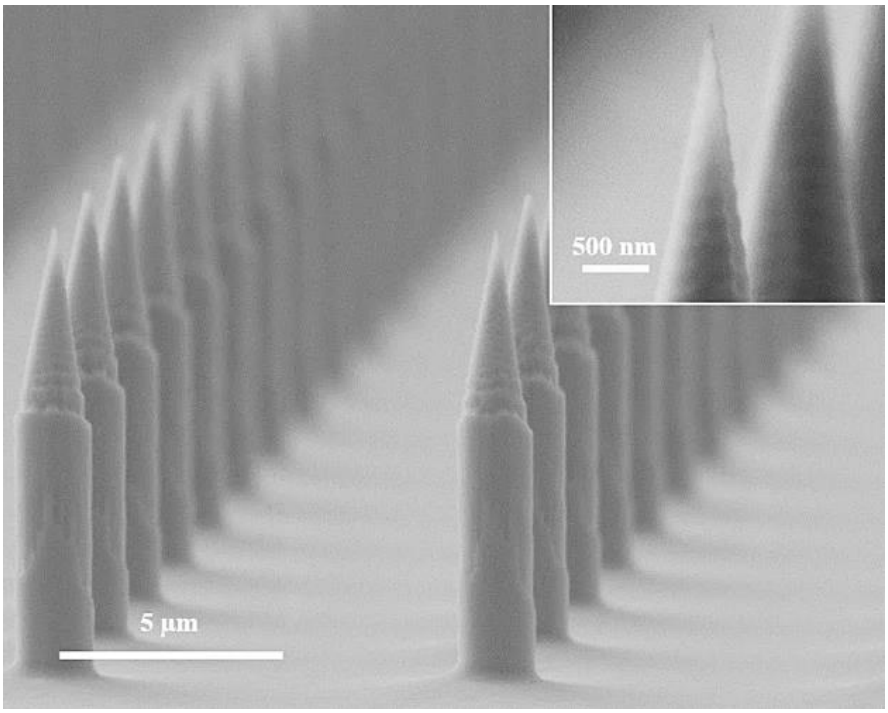


Figure 3.23 Nanocones after isotropic wet etching by 100:1 HNO_3: HF for 3 minutes.

3.4.4.4 Oxidation sharpening of Si nanocones

To further reduce the top part of Si nanocones, the oxidation and HF wet etching of the grown oxide was carried out. During thermal oxidation, the oxidation rate is slower at convex and concave corners due to stress during Si oxidation at high temperatures. Studies indicate that higher oxidation temperatures result in lower stress levels[223], and the stress distribution during cone oxidation contributes to a sharper tip apex. In the experiment, the sample was subjected to oxidation at 950 ℃ for two hours. After that, the sample was soaked in 49% HF to remove the SiO_2. The sharpened tip was ultimately reduced to 20 nm from 70-80 nm (Figure 3.24).

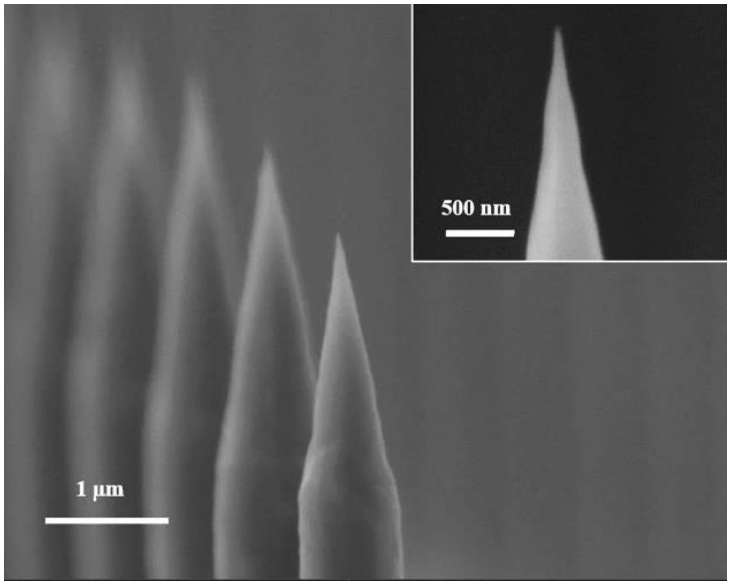


Figure 3.24 SEM image of tips after oxidation sharpening at 950 ℃ for 2 hours.

3.4.5 Summary and conclusions

To cost-effectively fabricate nanocone structures with a 20 nm apex, a hybrid approach combining dry etching and wet etching/shrinking methods is proposed in this paper. A Bosch process and a pseudo-Bosch process with periodic O_2 plasma mask shrinking are used on photolithography-defined patterns to respectively produce the base and the cone of Si structures. To preliminary sharpen the cone, anisotropic etching using KOH was performed at room

temperature. The horizontal/lateral etching rate was 44 nm/min, and the vertical etching rate was 90 nm/min. Alternatively, isotropic etching using a mixed solution of HNO_3 and HF was used, resulting in the circular shape of nanocones. The two wet etching methods can reduce the tip diameter to around 70 nm from 400 nm. The following oxidation sharpening further reduces the apex of nanocones. The final nanocones have a height of 9.5 µm, a base diameter of 2 µm and a tip apex of 20 nm. The hybrid approach enables efficient and cost-effective fabrication of nanocones using photolithography-defined patterns.

3.5 Summary

This chapter describes four methods for fabricating Si nanotip structures for AFM probes, each with distinct advantages as illustrated in Table 3.7. Selecting the most appropriate method for batch AFM probe fabrication is crucial, particularly in ensuring compatibility with Si on insulator (SOI) wafers. In this thesis, we utilize SOI wafers featuring a 10 µm thick device layer, a 2 µm buried oxide layer, and a 400 µm handle layer.

Table 3.7 Comparisons for the four methods for tip fabrication are listed above.

Methods	Fabrication process	Production difficulties	Profile	Feasibility of batch production	Cost in the lab*
Method 1 (Section 3.1)	EBL and HNA sharpening	N/A	High aspect ratio; low mechanical strength	Good	~$19.5
Method 2 (Section 3.2)	Tapered oxide patterns transferred by pseudo-Bosch	Hard to control the wet etch stop point	Extremely sharp apex	Good	~$8.5
Method 3 (Section 3.3)	EBL and Two-step cryogenic etching	Time-consuming cryogenic steps	Small taper angle	Good	~$17
Method 4 (Section 3.4)	Bosch, pseudo-Bosch with O_2 shrinking, KOH sharpening	N/A	High mechanical strength; sharp apex and small taper angle	Good	~$5.5

*Note: the cost estimation includes only the rough equipment fees for fabricating 60 tip structures, based on the industrial rates of the Quantum Nano Fabrication and Characterization Facility (QNFCF) at the University of Waterloo and nanoFAB at the University of Alberta.

Methods 1 and 3 employ EBL to pattern the tip structures. However, EBL comes with significantly higher costs than maskless optical lithography. Additionally, method 1 is rendered inapplicable as the HNA sharpening process etches the buried oxide layer as well. On the other hand, methods 2 and 4 present innovative approaches leveraging instruments initially designed for micrometer-level manufacturing to produce nano-scale components. These methods offer cost-effective solutions to achieve the desired tip profile. However, the fabrication process of method 4 is more straightforward than method 2. Consequently, we opt for method 4 for the subsequent batch fabrication of AFM probes.

Chapter 4 AFM Stair-shaped Handle Fabrication

This chapter details the fabrication of a stair-shaped Si handle. Two techniques are described: one leveraging the loading effect and RIE-lag to attain stage heights of 71 μm, 151 μm, 168 μm, and 287 μm, while the other employs pseudo-grayscale lithography with a Ti mask, yielding final stages of 52 μm, 83 μm, 161 μm, and 211 μm. Both methods are applicable for practical AFM probe fabrication without laser blocking.

4.1 Stair-shaped Handle Fabrication using RIE Loading Effect and RIE-lag

4.1.1 Introduction

In AFM imaging, the cantilever bending is sensed by a laser beam that shines on the backside of the cantilever and gets reflected to reach the photodetector. The AFM handle is a foundational support for the micro-cantilever and is typically mounted into the piezoelectric clamp holder within the AFM system, and commercially available handles often feature a cuboid profile. If the handle has a rectangular cross-section profile, as depicted in Figure 4.1 (a), the probe handle may block the laser beam, hindering accurate detection. To avoid this light-blocking, the handle should incorporate a large slope or "stairs" that mimic a slope, as illustrated in Figure 4.1 (b).

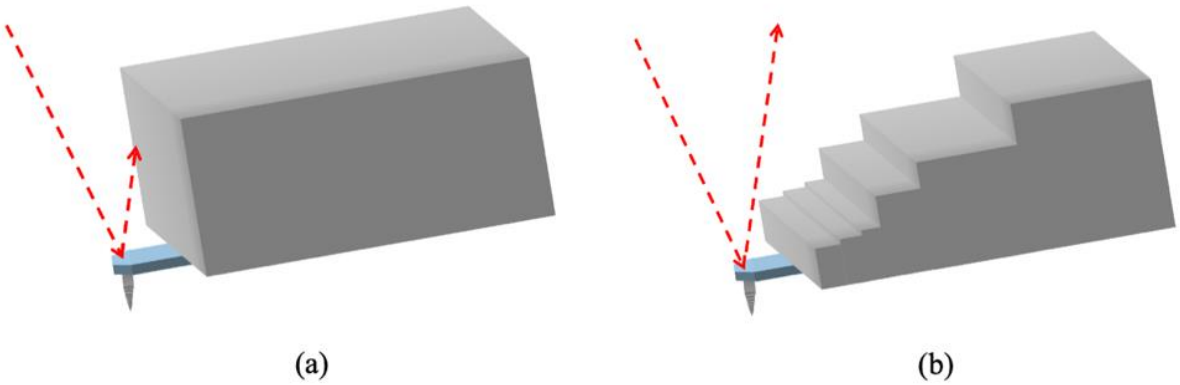


Figure 4.1 Schematic representation of tilted AFM probes with (a) rectangular cross-section handle, and (b) stair-shaped handle.

Due to the slow etching rate and challenges in controlling the morphology associated with wet etching, our focus in this section shifted primarily to dry etching techniques. DRIE relies on the supply rate of reactive species generated from a gas or gas mixture, so the etching rate decreases as the reactive species decrease. This phenomenon, known as the loading effect[224,225], occurs when the amount of material to be etched increases, while other conditions such as gas flow rate and pressure remain unchanged. The loading effect manifests in two primary forms: macro-loading and micro-loading.

Macro-loading arises when the total substrate area to be etched increases, leading to a decrease in the etch rate[226]. In specific RIE systems, a carrier wafer is required when running a recipe with small samples. The materials of carrier wafers can significantly affect the etch rate, with glass carriers typically yielding higher etch rates than Si due to macro-loading effects. However, glass carriers may not be compatible with specific equipment due to their transparency, which prevents the photodetector from detecting the carrier wafer, thus hindering operation. Micro-loading, on the other hand, arises from disparities in local pattern density[227]. For instance, densely packed features will undergo a slower etching rate than isolated features, even if they are identical. Another phenomenon, known as RIE-lag, influences the etching rate based on the width of mask openings[228–230]. Designs with varying densities and opening areas can yield distinct deep trenches.

This section explores the interplay between the micro-loading effect and RIE-lag in fabricating AFM handles, given the significant size variation among the different “stairs” in the handle part. The sample was diced into identical 5 cm × 5 cm pieces with the same pattern design, and identical 4-inch Si carrier wafers were utilized for each fabrication round.

4.1.2 Experiment

To fabricate the “stairs” with a single lithography plus etching step (instead of one lithography/etching for each stair), the consideration of the micro-loading effect and RIE-lag is utilized for advantage. The handle’s pattern design, depicted in Figure 4.2, features two dense areas comprising 10-μm side-length squares and 15-μm squares, along with four narrow lines with inter-line-spacing varying from 15 μm to 30 μm.

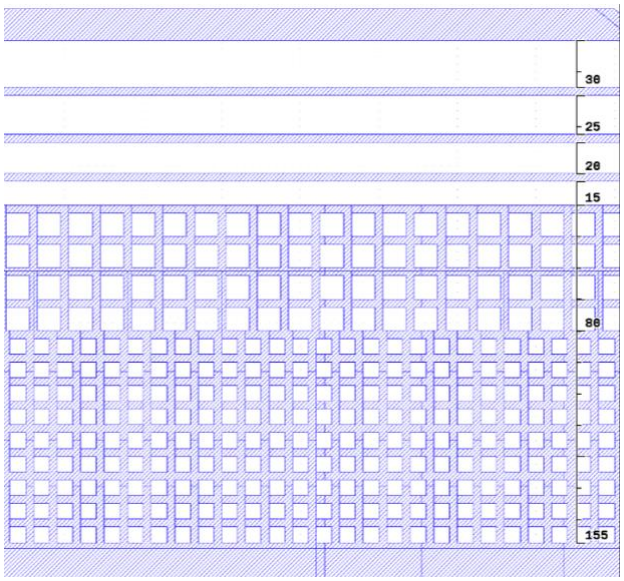


Figure 4.2 Partial CAD pattern design of the AFM handle part.

The standard Bosch process is capable of etching deep holes or trenches with varying depths, as illustrated in Figure 4.3. The hole/trench depth is maximum for the open area and decreases with decreasing open area. Additionally, the depth is smaller for holes than trenches if the diameter/side length of the holes is the same as the trench width (inter-line-spacing). For the pattern design depicted in Figure 4.2, the etching depth is expected to increase from the bottom (small square opening) to the top (large trench opening).

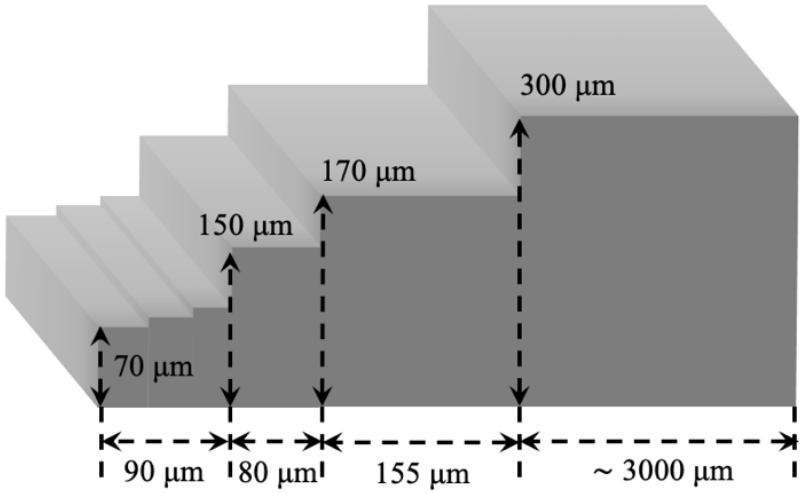


Figure 4.3 The expected 3D shape of the handle part using the CAD pattern design shown above.

In the experiment, a 5 cm × 5 cm Si piece is cleaned in acetone, IPA and 2-minute O_2 plasma. Then, a layer of positive photoresist AZ4620 is spin-coated and soft-baked at 110 ℃ for 90 seconds. The resist is exposed by MLA and then developed. Next, Si is etched by 800 cycles standard Bosch process that gives an overall etching depth of around 420 µm for an open area.

4.1.2 Results and discussion

The cross-sectional profile after 250 cycles of the standard Bosch process is depicted in Figure 4.4(a), showing varying etching depths across different areas. The vertical sidewall confirms the suitability of the Bosch recipe for this design. Subsequently, 550 additional Bosch cycles were performed, followed by a 20-minute isotropic etching using an SF_6-only recipe. This process further etched the Si down to approximately 260 µm and laterally "flattened" the steps. The final handle profile, shown in Figure 4.4 (b), reveals etched depths of 71 µm, 151 µm, 168 µm, and 287 µm for the major steps, respectively. Although the step heights are unevenly distributed, they can be effectively utilized in AFM probes to minimize the potential for laser light blocking by the final step adjacent to the cantilever.

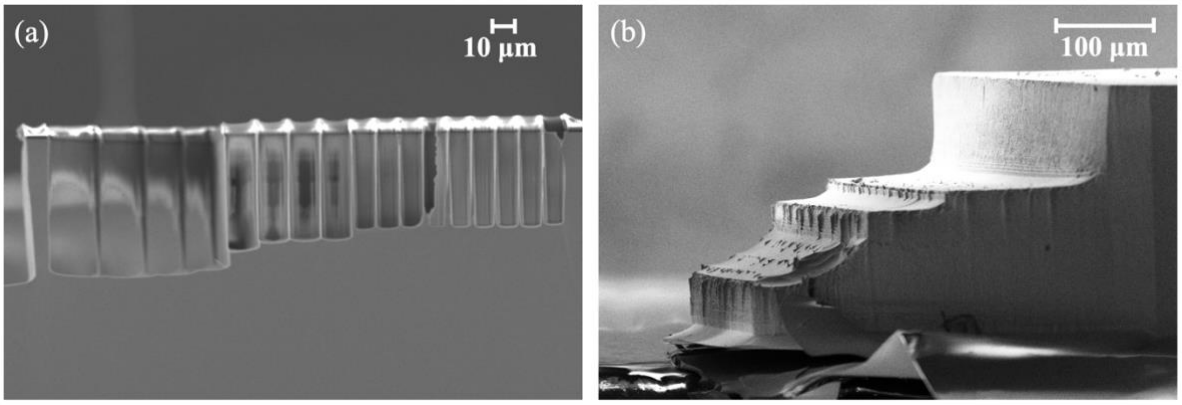


Figure 4.4 The cross-sectional profile of the handle part after (a) 250 cycles of standard anisotropic Bosch etching, (b) 550 additional cycles of standard anisotropic Bosch etching, followed by SF_6 isotropic etching and 50 more cycles of Bosch etching.

4.2 Stair-shaped Handle Fabrication by Pseudo-grayscale Lithography with a Titanium Photomask

4.2.1 Introduction

With the growing demand for 3D structure manufacturing in MEMS and NEMS devices, grayscale lithography has emerged as a versatile technique for defining such structures in photoresists with monotonously varying profiles[231]. When combined with RIE etching technologies, this method has been used in many devices such as MEMS mirrors[232], 3D passive microfluidic valves[233] and micro-machined ultrasonic transducer (CMUT) arrays[234].

Grayscale lithography employs different approaches suitable for highly complex 3D structures. One established method is direct laser writing technology, offering a lateral resolution of 300 nm and a vertical resolution of 50 nm[235,236]. However, the throughput of this method still requires improvement. Another approach involves the thermal reflow process[237] to achieve desired photoresist shapes, particularly for 3D structures in optical lens applications. By controlling baking time and temperature, the cylindrical structures transform into hemispherical structures through self-flow and surface tension of the photoresist. However, this method is limited to simpler

morphologies and has constrained accuracy[238]. High energy beam sensitive (HEBS) glass can serve as a mask for grayscale lithography, utilizing beam-induced reduction of silver ions to darken the glass without graininess, but the higher cost of HEBS masks compared to standard chromium on quartz masks impedes widespread adoption of this technique. Arranging a specific number of pixels on a mask offers another solution. This method achieves grayscale by adjusting the number and size of light transmission points on the mask[239]. The accuracy of this approach depends on the design of mask pixels, with pixel size required to be smaller than the critical resolution of the exposure machine[240–242]. Moreover, arranging pixels from the center to the surrounding areas enhances control over grayscale levels, but the simulation is complex and low-efficiency[243].

This section introduces a novel approach with titanium (Ti) metal masks for projection or contact lithography systems. This approach allows for the fabrication of multi-step photoresist structures by a single exposure, enhancing throughput compared to laser-direct writing. The Lambert-Beer law describes the relationship between the concentration of an absorbing substance in a solution and the amount of light absorbed by that solution. Ti metal exhibits a relatively low extinction coefficient and refractive index, suggesting that light can effectively penetrate masks of various thicknesses. Specifically, titanium exhibits an extinction coefficient of 1.83 and a refractive index of 1.11 under a 365 nm light source, compared to chromium (an extinction coefficient of 2.95; a refractive index of 1.12). Thus, the feasibility of this approach to fabricate stair-shaped Si AFM handles can be demonstrated.

4.2.2 Experiment

This fabrication process involves multi-step Ti photomask fabrication (Figure 4.5) and stair-shaped handle etching (Figure 4.6). For the photomask fabrication, the quartz plate is cleaned

with acetone and IPA, followed by surface treatment with O_2 plasma. Subsequently, the SUN-9i[244] is spin-coated on the quartz plate at 1400 rpm to obtain a 6 μm photoresist, with pre-and post-baking conducted at 110 ℃ for 90 seconds. Subsequently, exposure is then carried out using an MLA with 405 nm wavelength, followed by development using a 2.38% TMAH solution for 2 minutes. After development and resist removal, the sample surface undergoes treatment with O_2 plasma to ensure proper metal adhesion. The deposition rate of a 4 nm Ti layer evaporation is 1.5 Å/s, and the lift-off process is facilitated using PG remover ultrasonication at 80 ℃. This sequence is repeated four times to complete the photomask fabrication, ensuring uniformity and preventing uneven step boundaries.

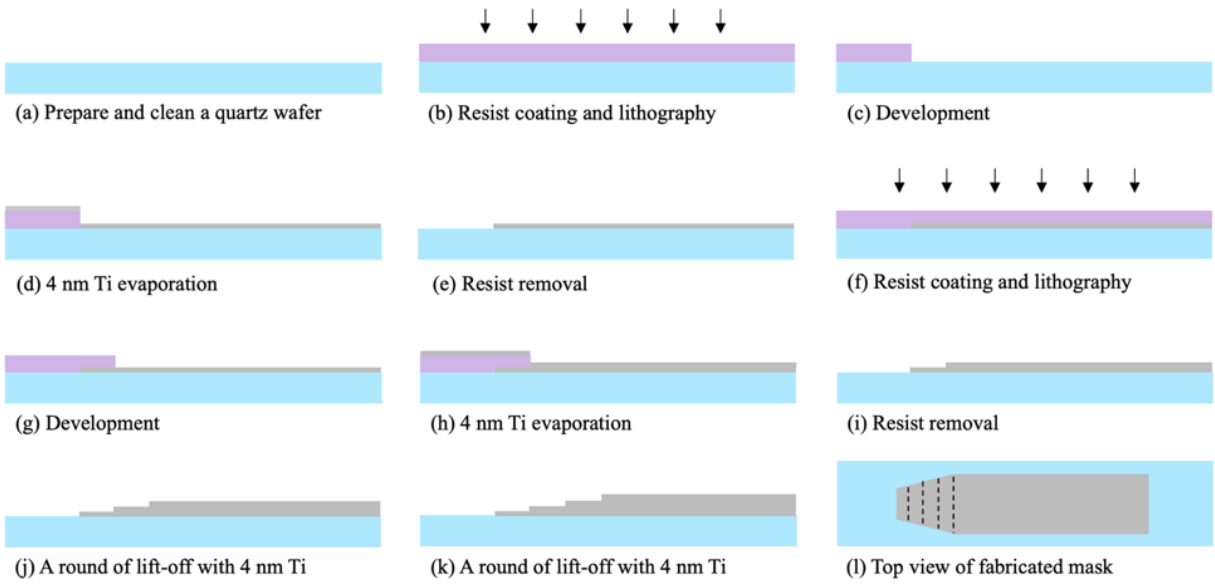


Figure 4.5 Schematic of the fabrication process for grayscale lithography mask with titanium. (a) prepare a quartz wafer, (b) photoresist coating and lithography, (c) development, (d) 4 nm Ti evaporation, (e) resist removal, (f) photoresist coating and aligned lithography, (g) development, (h) 4 nm Ti evaporation, (i) resist removal, (j) one more round of lift-off process with 4 nm Ti, (k) one more round of lift-off process with 4 nm Ti, (l) top view of fabricated grayscale mask.

Once the mask is complete, a 6 μm thick SUN-9i photoresist is spin-coated onto a cleaned Si wafer. We chose the SUSS-MA6 mask aligner to complete the lithography and then baked it at

110 ℃ for 90 seconds. After development, the multi-step photoresist is then transferred to the Si substrate by 600 cycles Bosch process.

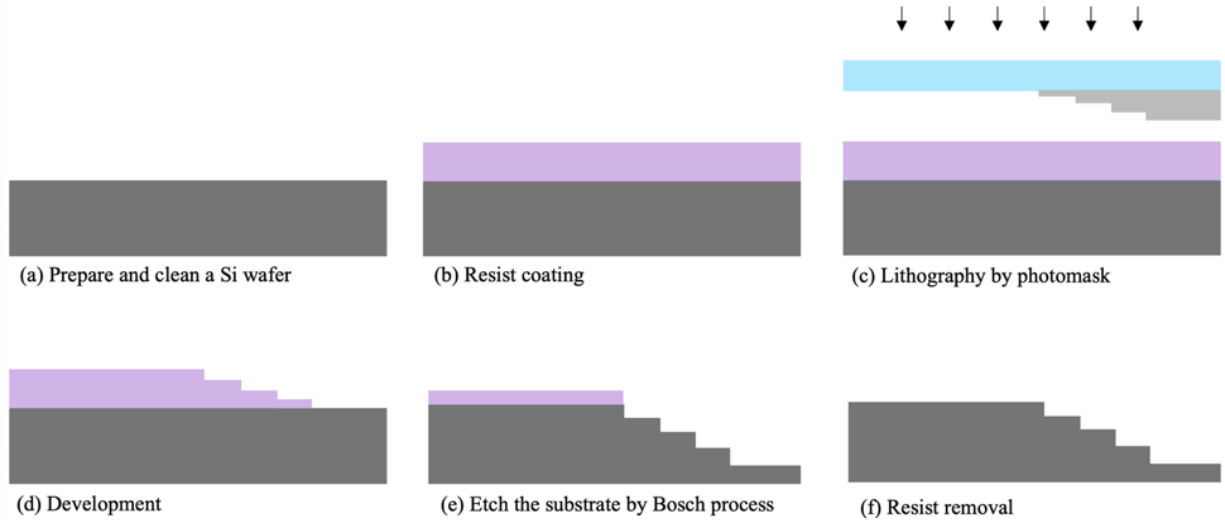


Figure 4.6 Schematic of the fabrication process for Si stair-shaped handle by the exposure with a Ti mask. (a) prepare a Si wafer, (b) photoresist coating, (c) lithography with the photomask, (d) development, (e) etch the Si substrate by Bosch process, (f) resist removal.

4.2.3 Results and discussion

Figure 4.7 (a) depicts the profile of the grayscale photomask, revealing the presence of four distinct layers of Ti metal. As a result of the varying intensity of light transmitted through the mask during photolithography, the morphology of the photoresist exhibits a stair-shaped structure in Figure 4.7 (b). The heights of these steps are measured at 1.4 μm, 1.8 μm, 2.9 μm, and 4.8 μm, respectively.

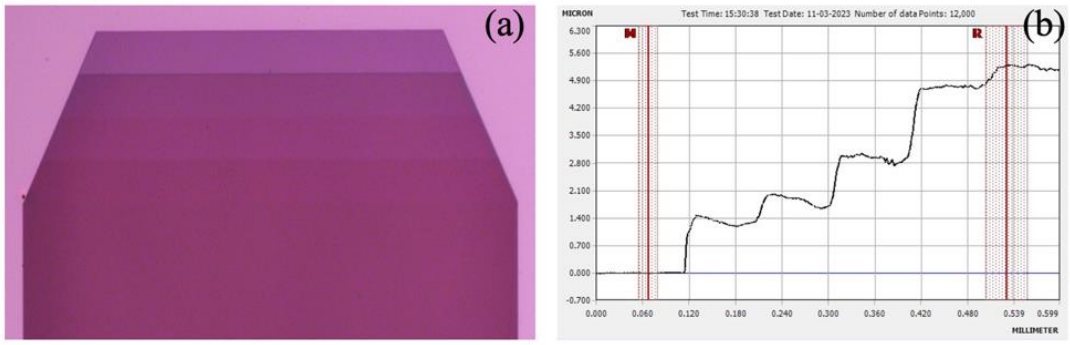


Figure 4.7 (a) the optical microscope image of the grayscale photomask, (b) the heights of resist stages after photolithography (Figure 4.6d) by using the BRUKER-Dektak XT system.

Figure 4.8 displays the cross-sectional profile following the Bosch process, revealing varying etching depths. The final handle profile exhibits etched depths corresponding to major steps of 52 μm, 83 μm, 161 μm, and 211 μm, respectively. While these step heights are not evenly distributed, they can be leveraged for AFM probes, minimizing laser light obstruction due to the last step adjacent to the cantilever.

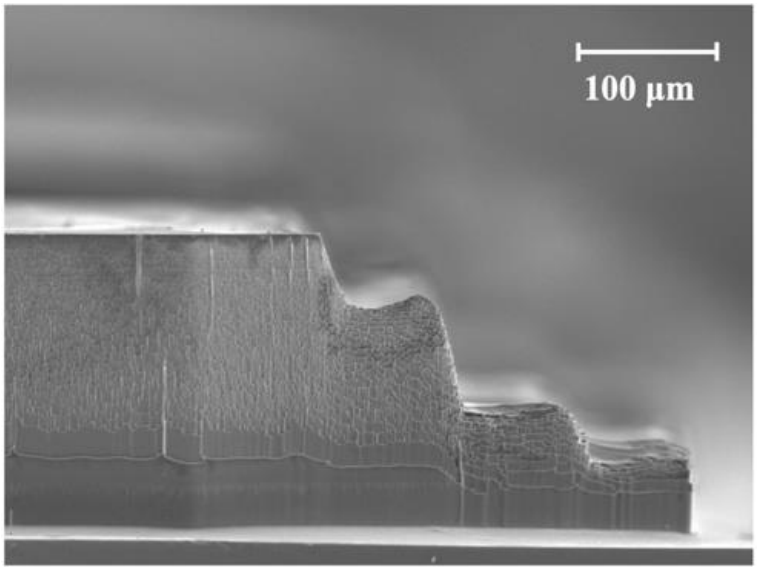


Figure 4.8 The SEM image of a fabricated stair-shaped handle.

4.3 Summary

This chapter describes two approaches for fabricating Si stair-shaped handles for AFM probes, to avoid blocking the incident of reflective laser light.

The first method involves using the RIE loading effect and RIE-lag to fabricate a complicated multi-stage structure, simplifying the fabrication process to a single round of photolithography and etching. The final structure features four progressive steps with stage heights of 71 μm, 151 μm, 168 μm, and 287 μm. The second method employs the principle of pseudo-grayscale lithography to fabricate a photomask. Although the steps to obtain a photomask are relatively complex, the photomask can be reused multiple times, greatly reducing subsequent

photolithography and etching time. The resulting structure features steps with heights of 52 μm, 83 μm, 161 μm, and 211 μm. Additionally, the step heights can be adjusted by varying the metal thickness on the photomask. The stair-shaped structures fabricated by the above two methods effectively prevent laser beam blocking. This represents an innovative advancement in AFM probe design.

Chapter 5 Cost-effective Mass Fabrication of High-performance All-Si AFM Probes with HAR Tips and Stair-shaped Handles

After comparing the advantages and disadvantages of the results in Chapter 3 and Chapter 4, we've identified the most appropriate methods for batch fabrication. This chapter explores the mass fabrication of HAR all-Si AFM probes with two different cantilever lengths, combining tips fabricated by the O_2 shrinking method with handles fabricated using the RIE loading effect and RIE-lag. The resulting probe exhibits excellent performance, boasting an optimal tip profile and extended service lifetime.

5.1 Simulation and Design

AFM probes find widespread applications across various fields, serving not only for basic surface morphology analysis and force investigation but also as pivotal tools for nano-scale manipulation and sensing tasks characterized by their sensing and manipulation characteristics. A notable advancement involves using specific materials to induce resonant frequency shifts or alter the bending properties of cantilevers, facilitating applications like molecular detection and hazardous explosives identification. In the AFM system, the tip profile directly influences scanning accuracy and image resolution. The resonant frequency of the cantilever affects scanning speed and resolution, while the spring constant determines cantilever stiffness, image quality and the force spectrum of the sample surface. Therefore, calibrating the cantilever's elastic modulus and resonant frequency is essential for studying the performance of AFM probes.

5.1.1 Direct calculation by MATLAB

Over the past two decades, V-shaped (top view) cantilevers have garnered attention in AFM probe manufacturing due to the common belief that they offer more resistance to lateral forces than rectangular cantilevers[245]. However, a study in 2021 by Feodor *et al.*[246] challenged this notion, suggesting that the findings by Sader *et al.* may not universally apply to all commercial AFM cantilevers. As a result, our experiments exclusively employed rectangular cantilevers to mitigate these uncertainties. Based on the displacement of the cantilever's unfixed end in the vertical direction for rectangular cantilevers, the spring constant (also termed as force constant) *k* and the resonance frequency *f* are calculated by the following equations:

$$k = \frac{Ewt^3}{4l^3} \tag{5.1}$$

$$f = \frac{1}{2\pi}\sqrt{\frac{k}{m_0}} = 0.162\sqrt{\frac{E}{\rho}}\frac{t}{l^2} \tag{5.2}$$

E is Young's modulus of the cantilever material, *w* is the cantilever width, *t* is the thickness, and *l* is the length. ρ is the density and m_0 is the effective mass of the cantilever. As can be seen, the resonance frequency is inversely proportional to the square of the length and proportional to thickness. An increase in length decreases the frequency very fast; therefore, the resonance frequency of the tip is mainly determined by the length. The spring constant is influenced by its width, the cube of its thickness, and is inversely proportional to the cube of its length. Given the variability in these dimensions, determining the exact spring constant values will be complex. To address this, a MATLAB 4D plot can be employed to identify a set of dimensions that yield a desired spring constant. Once appropriate dimensions are determined, the resonant frequency can be calculated using these specific values.

For Si, E is 170 GPa, and ρ is 2329 kg/m^3. Previous studies and commercially used AFM probes for tapping mode suggest that the cantilever length ranges from 80 μm to 150 μm, the width ranges from 0 μm to 40 μm, and the thickness ranges from 0.5 μm to 5 μm. Considering this analysis, a MATLAB simulation was conducted to determine the spring constants for the all-Si probe, as illustrated in Figure 5.1.

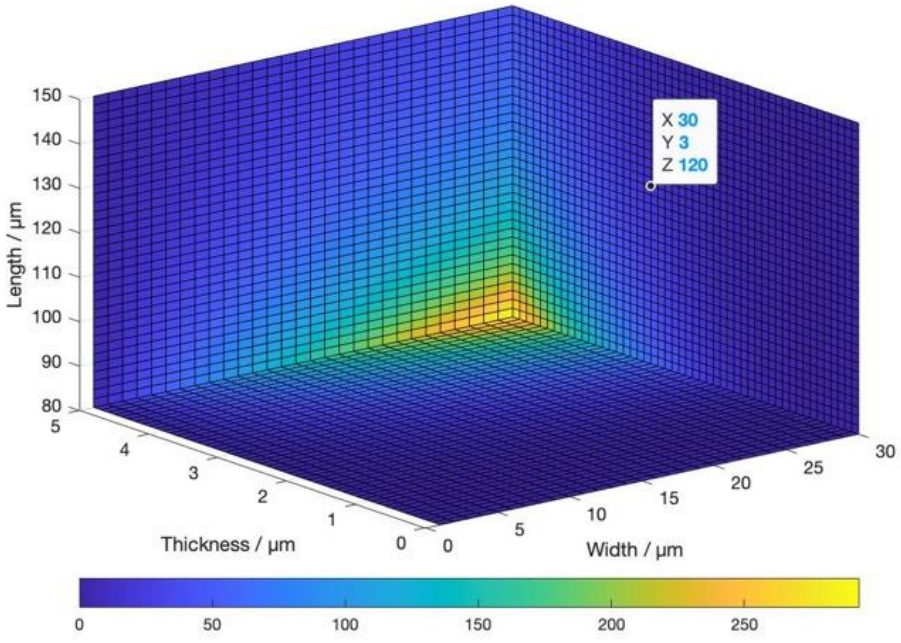


Figure 5.1 The 4D plot of spring constant k (unit N/m) and dimensions w,t,l.

As shown in the 4D slice diagrams, a thick and short cantilever exhibits a high spring constant, making it suitable for non-contact mode AFM operations (otherwise, for contact mode, it is stiff and can damage the sample). Conversely, a thin and long cantilever has a low spring constant, rendering it appropriate for contact mode AFM operations as it is soft and does less damage during scanning. Cantilevers with moderate spring constants and frequencies can be utilized for AFM tapping mode, offering a delicate balance between scanning speed and image resolution. The 4D plot theoretically allows for any combination of dimensions resulting in a

spring constant falling within the range of 0.5-50 N/m for the cantilever. However, in Si fabrication, cantilevers with a thickness below 2.5 μm may tend to curl due to stress post-release, while a width smaller than 5 μm is hard to align for photolithography and laser beam detection. Thus, an initial setting of the cantilever width at 30 μm (the width exhibits no influence on the spring constant and resonance frequency) and thickness at 3 μm is proposed. Lengths ranging from 80 to 150 μm can be achieved during the fabrication, prompting the tentative selection of two lengths: 120 μm and 140 μm. For instance, setting the dimensions as (w, t, l) = (30, 3, 120) yields a spring constant of 19.92 N/m and a resonance frequency calculated at 288.35 kHz; setting the dimensions as (w, t, l) = (30, 3, 140) yields a spring constant of 12.55 N/m and a resonance frequency calculated at 211.85 kHz.

5.1.2 Finite element simulation by COMSOL

The fundamental concept behind the finite element method involves dividing a constructed model into more minor elements and solving the resulting differential equations in the frequency domain. This method enables the creation of accurate models that can be progressively computed following arbitrary partitioning. The benefit of this approach is its ability to accurately simulate complex structures, particularly when the mesh partitioning is finely tuned. However, this precision comes due to increased computational workload and slower simulation speeds, necessitating more powerful computing resources. Consequently, the finite element method is best suited for accurately calculating moderately sized complex structures. Notably, commercial simulation software like COMSOL is built upon the principles of the finite element method.

In COMSOL Multiphysics, a geometric model of the cantilever was created with dimensions specified as follows: 120 μm in length, 30 μm in width, and 3 μm in thickness (the

overall shape of the AFM cantilever resembles an inverted T-shaped pattern with a small trapezoid on the free end). We fix one end of the cantilever beam to simulate its connection to the substrate while leaving the other end free to represent the absence of external constraints. Then we apply an external force ($F(t)=F_0 sin(\omega t)$) at the free end to obtain the vibration response of the cantilever, thereby enabling the simulation of its resonance frequency (303.75 kHz) as shown in Figure 5.2.

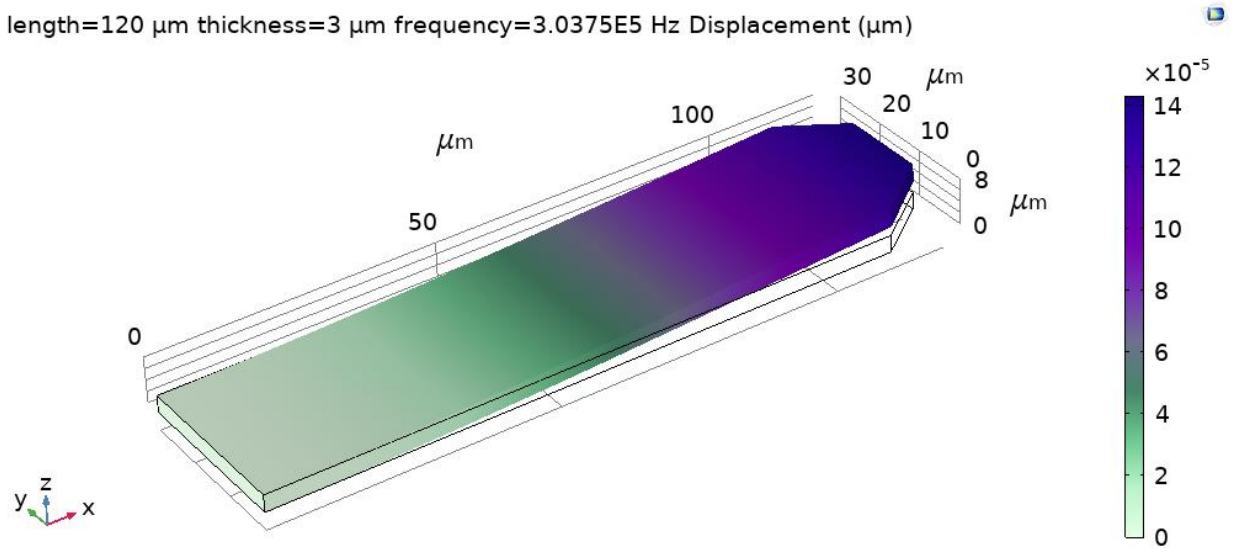


Figure 5.2 The resonance frequency was simulated for a rectangular cantilever with 30 μm in width, 3 μm in thickness and 120 μm in length.

When a constant external force is applied to the free end, the cantilever undergoes elastic deformation, with the magnitude of deflection proportional to the applied force. The spring constant describes the linear correlation between this deflection and the external force, measuring the cantilever's stiffness and elasticity properties. As illustrated in Figure 5.3, the maximum/minimum value of the applied force is 50.62/9.38 μN, and the maximum/minimum value of the cantilever's displacement is 2.52/0.42 μm. As a result, the simulated spring constant is 19.64 N/m.

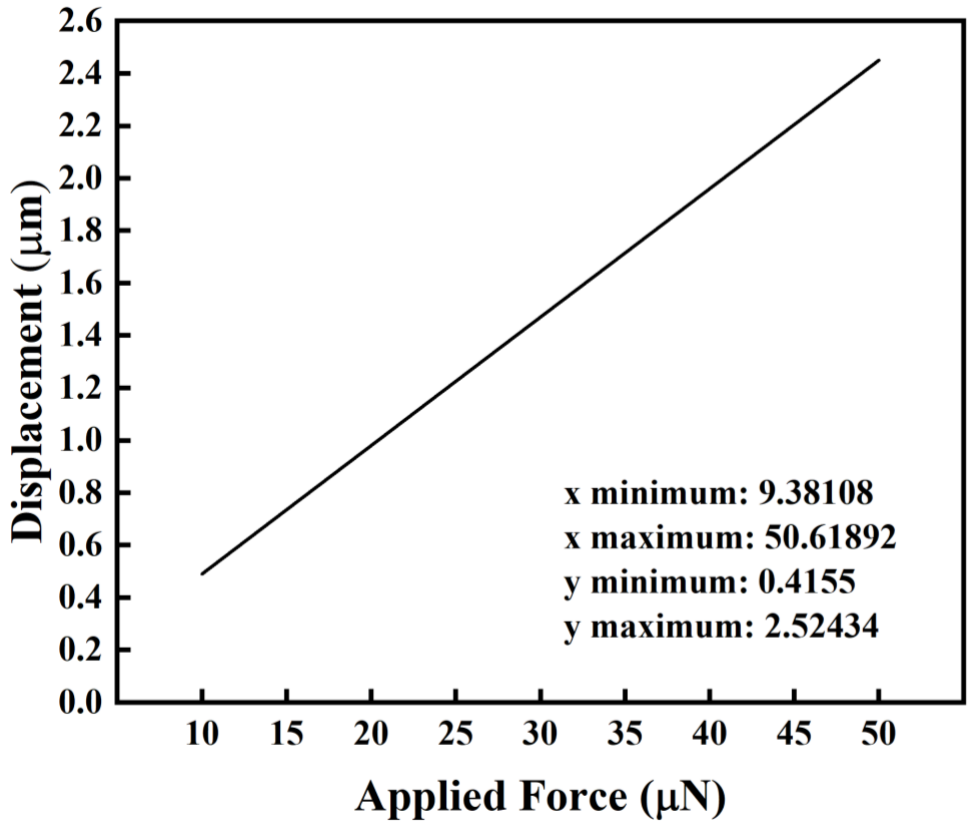


Figure 5.3 The plot of the displacement of a rectangular cantilever with 30 μm in width, 3 μm in thickness and 120 μm in length.

Similarly, a geometric model of the cantilever was created with dimensions specified as follows: 140 μm in length, 30 μm in width, and 3 μm in thickness. As shown in Figure 5.4, the simulated resonance frequency is 221.62 kHz. The maximum/minimum value of the applied force is 50.62/9.38 μN, and the maximum/minimum value of the cantilever's displacement is 4.02/0.66 μm. As a result, the simulated spring constant is 12.27 N/m.

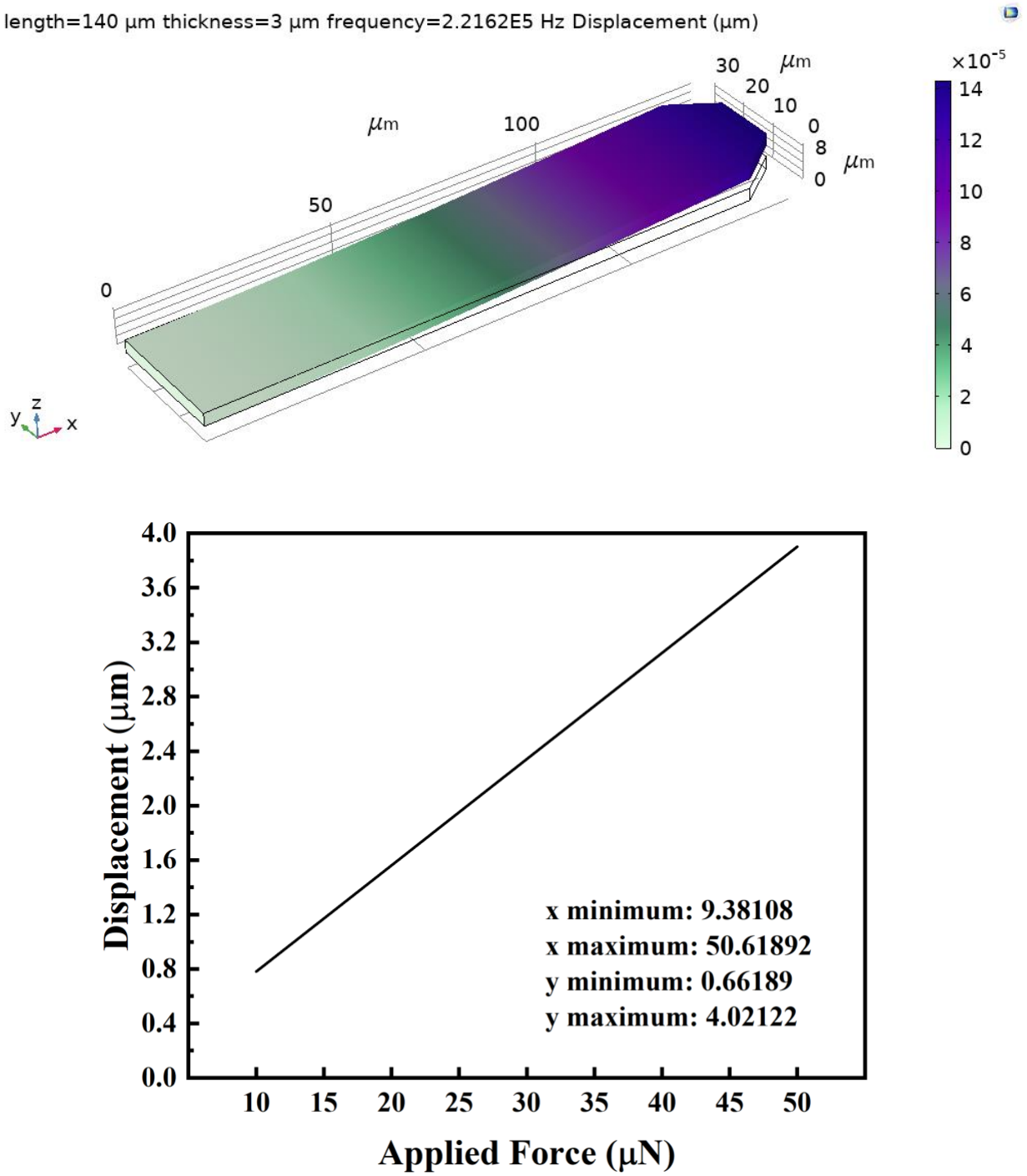


Figure 5.4 The resonance frequency and the spring constant were simulated for a rectangular cantilever with 30 μm in width, 3 μm in thickness and 140 μm in length.

5.1.3 Calculation of spring constant using Sader's method

Sader's method[247,248] analyzes the variations in the resonant frequency of a cantilever beam in the fluid. This approach considers the damping effect of the surrounding fluid, typically air, where the density and viscosity of the fluid are uniform and constant. It is assumed that the fluid provides a viscous damping force during the vibration of the cantilever, leading to a gradual reduction in its velocity over time. This method is theoretically applicable exclusively to rectangular cantilevers with an aspect ratio exceeding 3 and a Q-factor significantly greater than 1. The spring constant can be calculated by the following equations:

$$k = 7.5249\rho w^2 l\Gamma_i(R_e)Qf^2 \tag{5.3}$$

$$R_e = 1.5708\frac{\rho f w^2}{\eta} \tag{5.4}$$

Here, f represents the measured resonant frequency, while Q denotes the Q-factor, defined as $Q=f/\Delta f$ (where Δf is the full-width half maximum (FWHM) of the amplitude–driving frequency curve). Both f and Δf can be readily obtained using a standard AFM tool. This method only requires the planar dimensions of the cantilever, including the width w and the length l, which is rather convenient given the challenge associated with measuring cantilever thickness via SEM. It is important to note that cantilever thickness is not constant across a wafer or among a wafer, as it is etched back from a thick wafer when using a bare Si wafer as the starting material for tip manufacturing, or grounded and then polished back from a thick wafer during SOI wafer production when using an SOI wafer as the starting material. However, for cantilevers made out of deposited SiN_x films, the thickness is well controlled.

Γi represents the imaginary component of the hydrodynamic function, as illustrated in Figure 5.5[248]. The Reynolds number (Re) dictates the hydrodynamic function (that is dependent only on Re). Typically, the fabricated probe operates in air, where the density of the air (ρ) is 1.18

kg/m^3, and the viscosity is 1.86×10^{-5} kg/(m·s). Following the measurement of resonance frequencies of the fabricated cantilevers, their spring constant can be calculated.

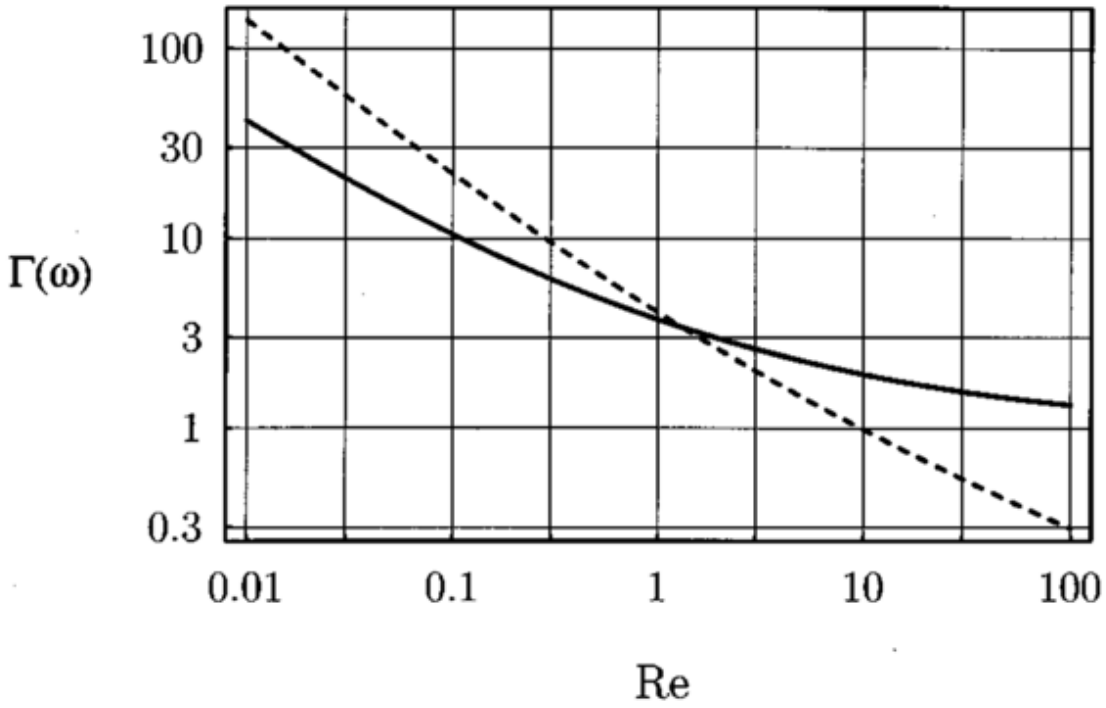


Figure 5.5 Plot of the real (solid line) and imaginary (dashed line) components of the hydrodynamic function *Γ*. (Reproduced with permission from Ref. [246]).

5.2 Fabrication Process

Fabrication of AFM probe with HAR all-Si tip includes three major parts: Si tip, Si cantilever and Si stair-shaped handle, and the proposed fabrication process on the SOI wafer is depicted in Figure 5.6.

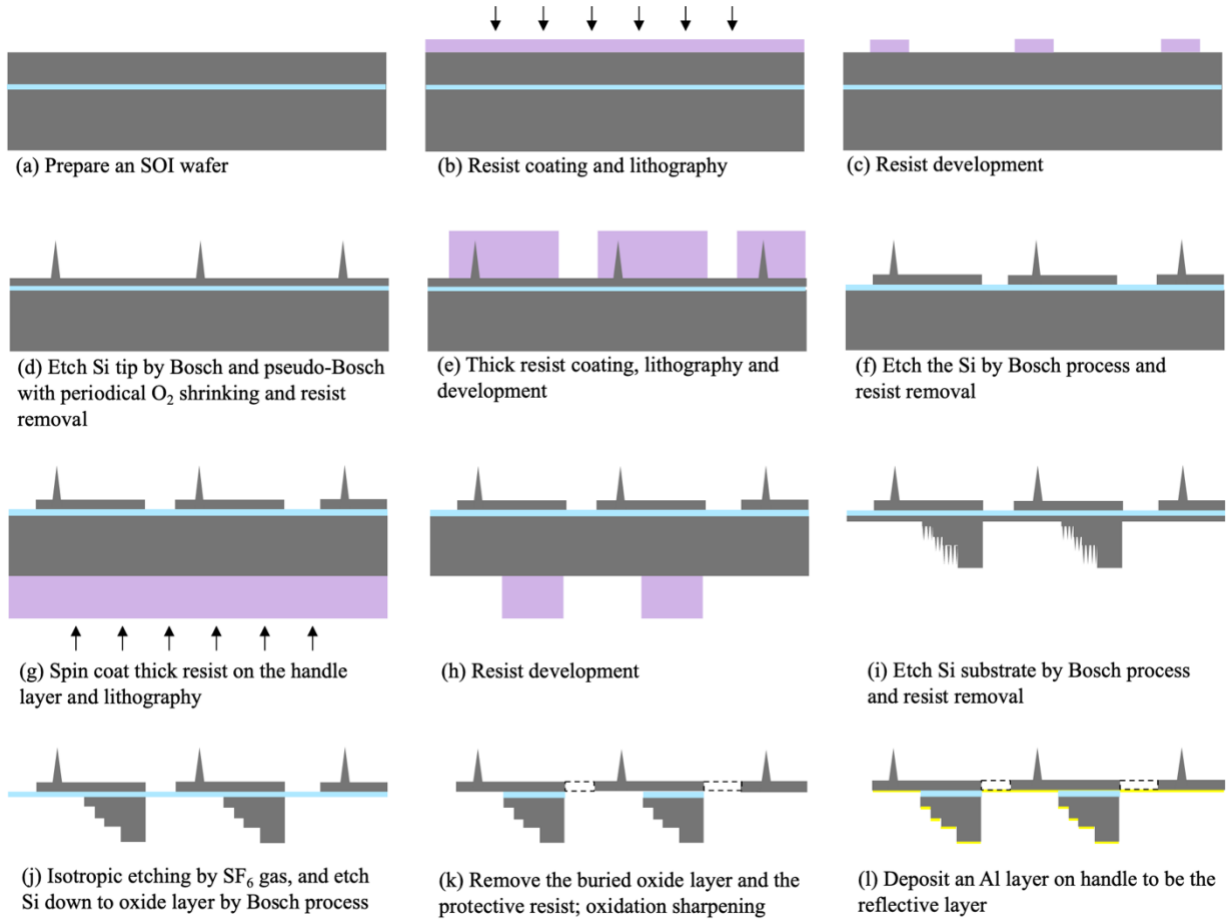


Figure 5.6 Fabrication process of all-Si AFM probes on an SOI wafer.

Here, we use an SOI wafer with a 10 µm thick device layer, 2 µm buried oxide layer and 400 µm handle layer. The process starts with rinsing with acetone and IPA and a 2-minute O_2 plasma cleaning with 20 W RF power, 20 sccm O_2 gas flow, and 20 mTorr chamber pressure. After cleaning, hexamethyldisilane (HMDS) treatment was applied to form a strong bond with the -OH group on the Si surface and leave the methyl group on the surface. Both the resist and the methyl group are hydrophobic, so the hydrophilic aqueous developer's entrance to the substrate-resist interface is avoided. This will minimize the resist structure's peeling off during the resist development process, and as such, the HMDS effectively creates a strong adhesion between the photoresist and the substrate (Figure 5.6a). Then, a layer of 3.3 µm negative resist AZ nLof 2035 is spin-coated and pre-baked at 110 ℃ for 1 minute. To pattern 3.0 µm resist pillars for defining

the tip structure along with semi-enclosed Si protective structures, standard mask-less photolithography using a direct write UV lithography system (MLA150, Heidelberg Instruments) was utilized (Figure 5.6b). After 1-minute post-exposure baking (PEB) at 110 ℃ and development (Figure 5.6c), the Bosch process followed by pseudo-Bosch with periodic O_2 shrinking (Figure 5.6d) is employed to transfer the tip pattern from the resist layer to the Si layer, and the expected tip height is 7 μm. The etching steps for tips are 4 cycles standard Bosch process plus 35 cycles of the modified resist shrinkage etching process using O_2 plasma, which is discussed in Section 3.4. The schematic structure of the HAR AFM Si tip is shown in Figure 5.7, and the overall tip height is 7 μm.

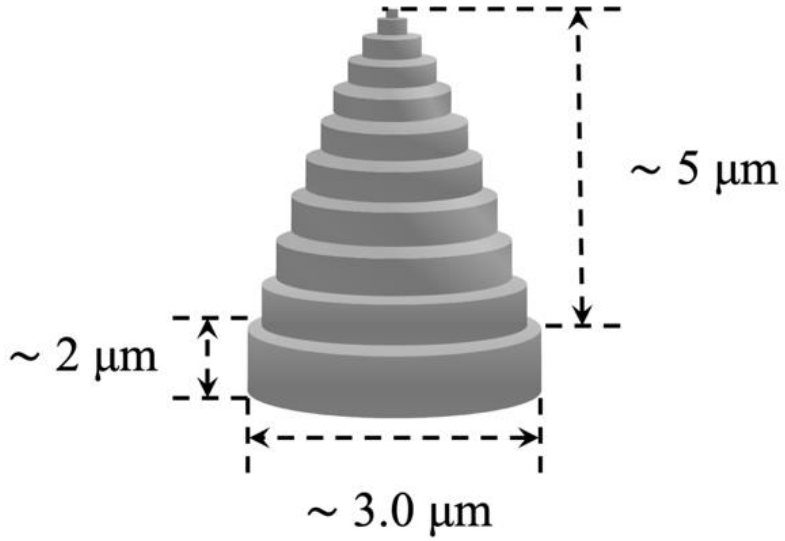


Figure 5.7 The schematic profile of HAR AFM Si tip. The formation of such a structure is explained in Section 3.4.

After determining the tip profiles, the remaining resist is removed by 2-minute O_2 plasma. First, 10 μm AZ4620 thick resist is spin-coated on the device layer to protect the fabricated tip structures and pre-baked at a temperature of 95 ℃ for 90 seconds. The lithography time of 405 nm MLA is 15 minutes, and the dose is 900 mJ/cm^2. After development (Figure 5.6e), the cantilever pattern is etched by 6 cycles of the Bosch process (Figure 5.6f), and the etching depth is 3 μm.

After resist removal, 10 μm AZ4620 resist is coated on the handle layer of the SOI wafer (Figure 5.6g), serving as the etching mask for the AFM handle patterns (Figure 5.6h). These patterns are then transferred into the Si substrate using the Bosch process, achieving an etching depth of 320 μm (Figure 5.6i). After remaining resist removal, Si isotropic etching using an SF_6 gas recipe (Figure 5.6j) is conducted to eliminate the silicon walls from lateral etching, and here the etching recipe is 160 sccm SF_6 with 20 W RF power, 1000 W ICP power, and 15 mTorr chamber pressure for 20 minutes. Once the walls are entirely removed, the Si substrate is further etched via the Bosch process until the etching ceases at the buried oxide layer (Figure 5.6k), and BOE finally removes the buried oxide layer. To enhance the optical reflectivity in the AFM imaging system, a thin layer of Al is deposited onto the backside of the cantilevers (Figure 5.6l). The final profile of the HAR AFM probe is shown in Figure 5.8.

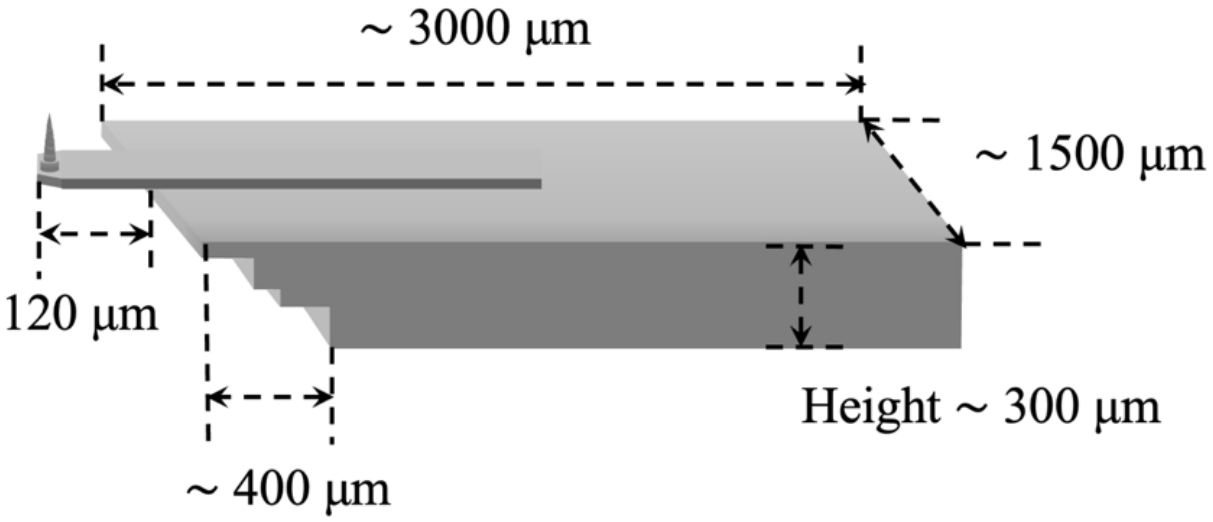


Figure 5.8 The schematic profile of HAR AFM Si probe.

5.3 Results and Discussion

5.3.1 Probes fabrication with 120 μm cantilever length

5.3.1.1 Experiment results

In the initial batch of HAR AFM probes, the cantilever length is fixed at 120 μm, based on the tapping mode requirements determined by simulation results. On the device layer of the SOI wafer, the initial step involves etching the tip, employing a designed mask diameter of 3 μm. Simultaneously, a protective structure is exposed alongside the tip, forming a semi-enclosed Si stage. This protective stage offers mechanical support to the tip, shielding it from potential damage during subsequent processes.

Figure 5.9 (a) illustrates the etched tip along with its protective stage, showcasing an etching height of 7 μm, and a magnified image of the tip is provided in Figure 5.9 (b). These figures further demonstrate that the etched tip conforms to expectations, appearing as a tapered thread at the tip. The bottom diameter of the probe remains 3 μm, while the tip diameter gradually narrows down to 200 nm. Within the overall sample area of 5 cm × 5 cm, as depicted in Figure 5.10, the sample is slightly tilted to 20°, which makes it appear less sharp than the figures in Chapter 3.4, for which the sample was mounted on a 70° tilted stub.

After completing the tip structures, we applied a thick layer of photoresist to protect them before proceeding with the cantilever etching process. The cantilever design featured a width of 30 μm and a length of 120 μm, as determined by simulation results. Considering that the Si layer on the device layer of the SOI wafer is 10 μm thick and the height of the tip is 7 μm, the predetermined thickness of the cantilever was set at 3 μm. Following the etching process down to the buried oxide, the cantilever and tip morphology are depicted in Figures 5.9 (c) and (d). It's worth noting that during the exposure of the cantilever pattern, a secondary exposure of the

protective structure is necessary. This ensures that during the etching of the cantilever, the protective structure remains intact, maintaining the same height as the probe and offering continuous mechanical support.

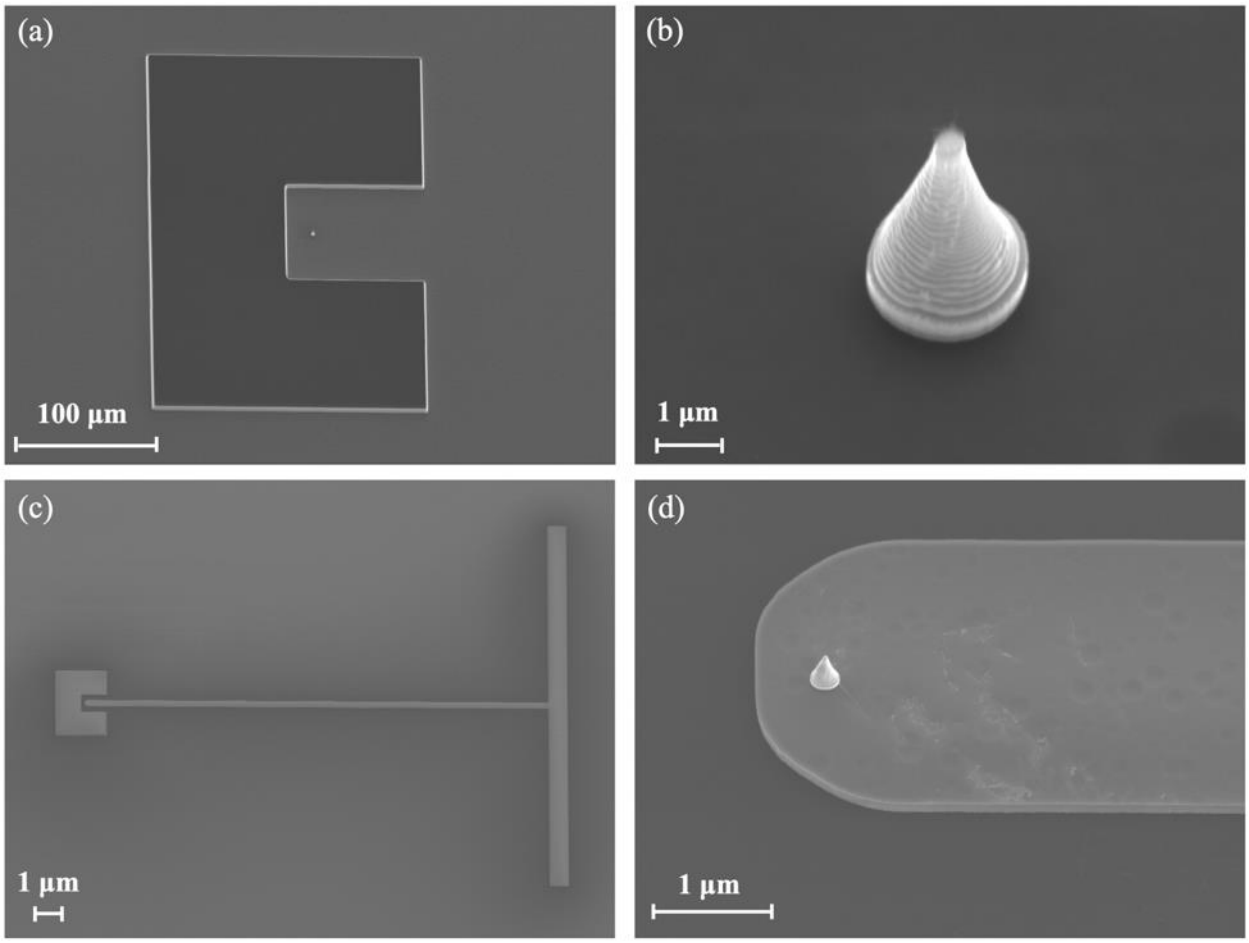


Figure 5.9 SEM images of (a) the etched tip and protective structure, (b) the enlarged view of the tip, (c) the etched tip and cantilever, and (d) the enlarged view of the tip on the cantilever. All images were captured using JOEL JSM-7200F SEM with the samples on a 20° tilted stage.

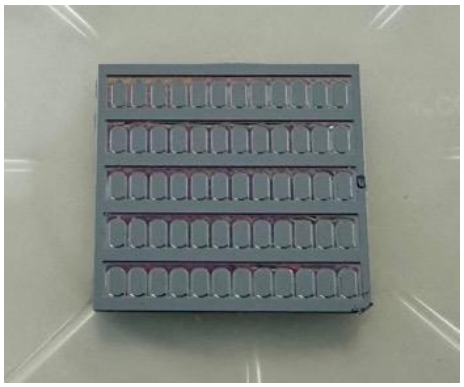


Figure 5.10 The actual product of AFM probes with dimensions of 5 cm × 5 cm.

After the tip and cantilever fabrication, alignment lithography and etching of the backside handle were completed. After removing the buried oxide, all 60 probes were extracted and individually inspected under SEM. Among these, 46 probes were determined to be intact and usable, exhibiting a probe tip height of 7 µm, a cantilever thickness of 3 µm, cantilever lengths ranging from 118 to 120 µm, and an overall handle thickness of 300 µm. This indicates a yield rate of approximately 77% for this batch of probes. An intact probe structure is shown in Figure 5.11, highlighting a tip diameter of 200 nm.

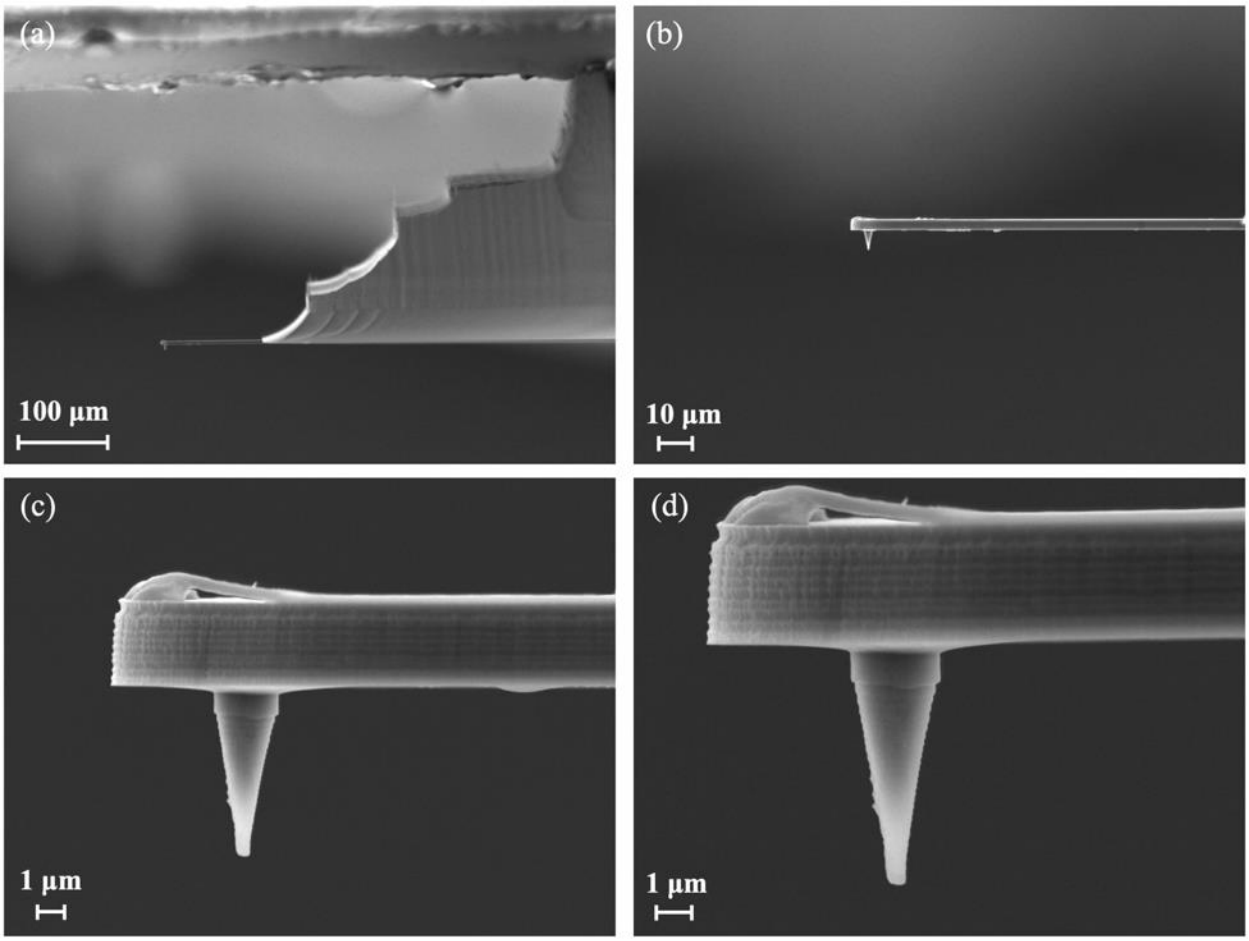


Figure 5.11 SEM images of (a) the side view of the AFM probe with the cantilever length of 120 µm, and (b-d) the enlarged view of the cantilever and the tip. All images were captured using JOEL JSM-7200F SEM with the samples mounted on a 90° tilted stage.

As outlined in Section 2.3.5, the thermal oxidation process for 3D structures experiences slower oxidation rates at concave and convex angles due to stress effects. At relatively low

temperatures (~950 ℃), thermal stress becomes more prominent, whereas temperatures exceeding 1100 ℃ tend to mitigate uneven oxidation. Considering that the etched tip apex diameter already measures only 200 nm and exhibits a preliminary conical shape, it is unnecessary to employ a KOH solution or HF/HNO3 mixture to further reduce the tip apex's size. As a result, we proceeded with thermal oxidation at 950 ℃ for 8 hours. After removing the grown SiO_2 with BOE, the final AFM probe product is presented in Figure 5.12, showcasing a final sharpened Si tip apex measuring approximately 12 nm.

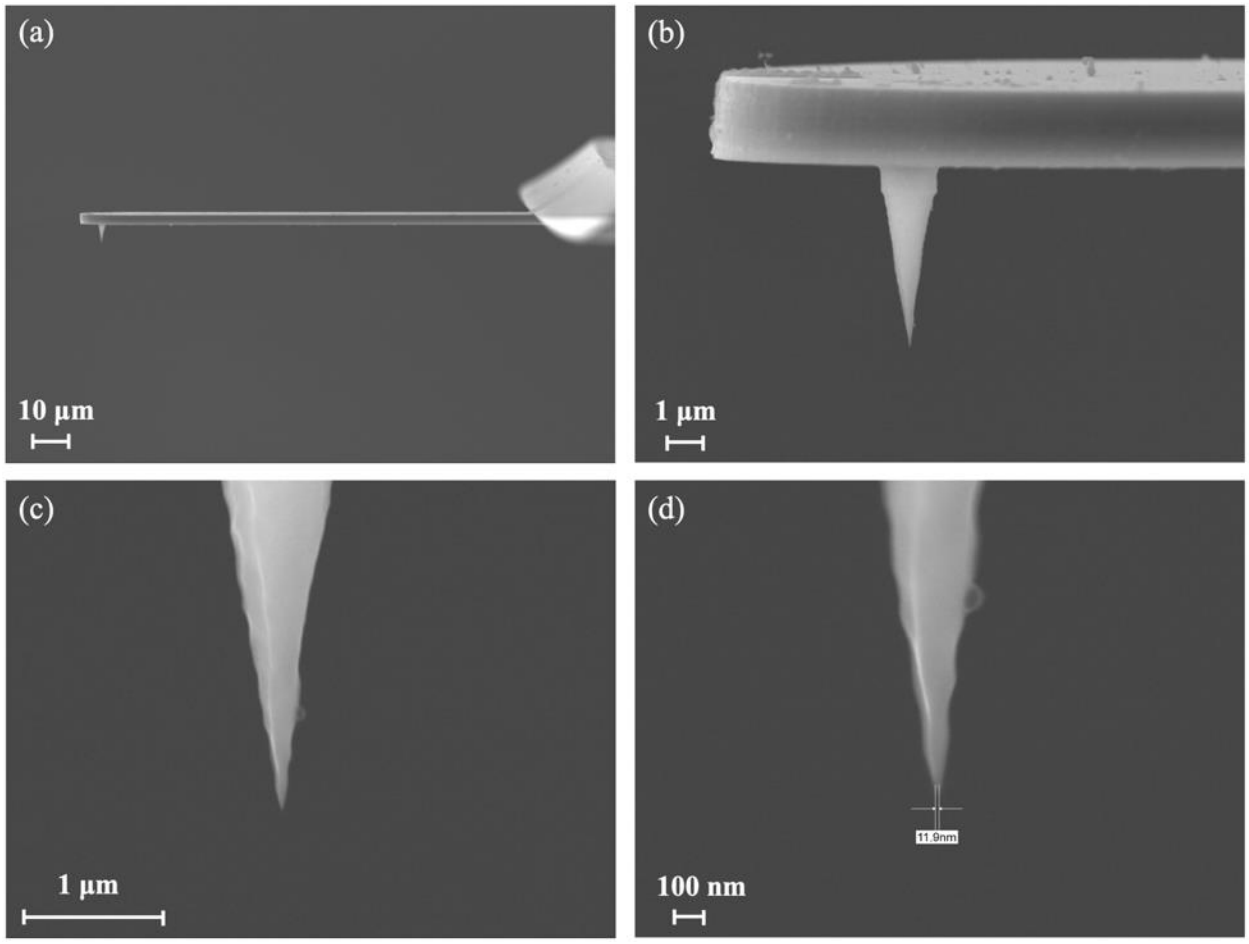


Figure 5.12 SEM images of (a) the final product of the AFM probe with 120 µm cantilever after oxidation sharpening, and (b-d) the enlarged view of the cantilever and the tip. All images were captured using JOEL JSM-7200F SEM with the samples mounted on a 90° tilted stage.

5.3.1.2 Performance test on AFM system

The all-Si AFM probe, once fabricated, was affixed onto the FM-Nanoview1000AFM, manufactured by Fisherman Company[249] (Suzhou, China), as illustrated in Figure 5.13 (a) and (b). The reflected laser energy was initially measured at 25% (2.5V) immediately following the cantilever release. However, upon depositing 30 nm of Al, the reflected laser energy increased to 38% (3.8V). The measured resonance frequency of this probe is 286.84 kHz, as depicted in Figure 5.13 (c).

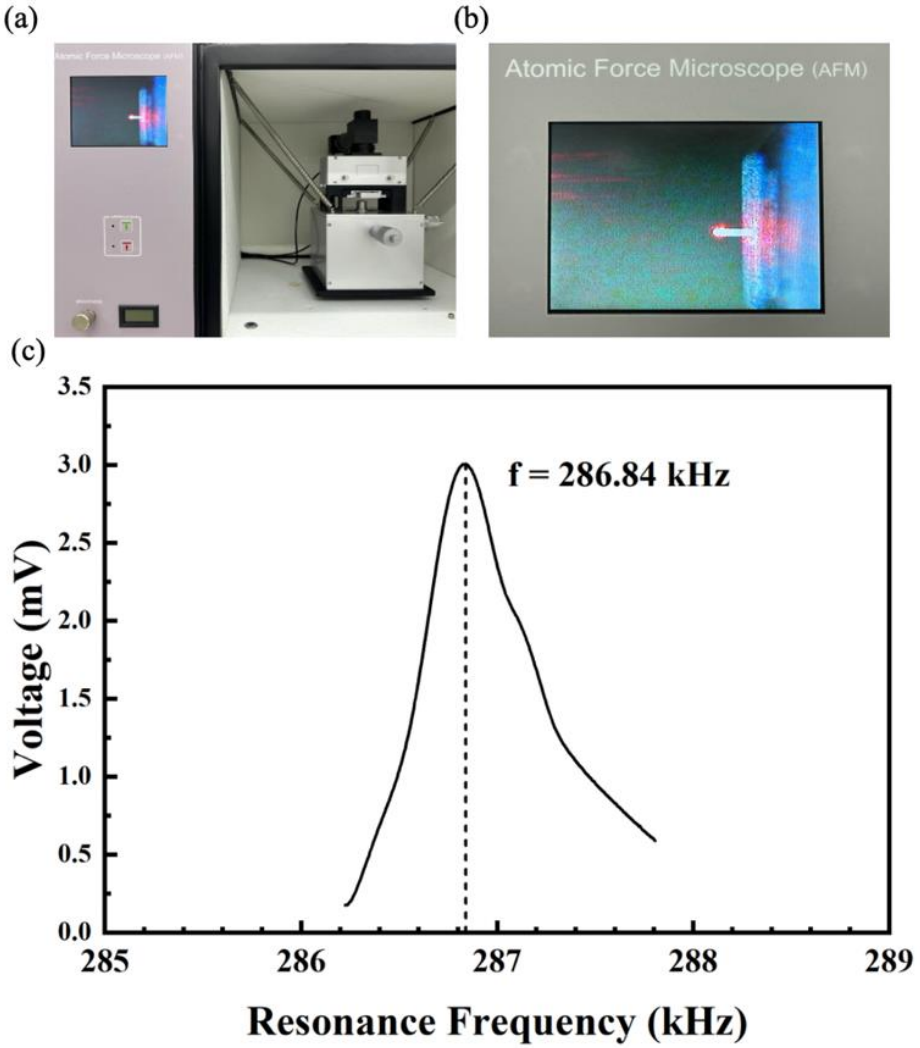


Figure 5.13 (a) the interior structure of the FM-Nanoview1000AFM model, (b) the image of a probe mounted onto the AFM system, and (c) the frequency-root mean square (f-RMS) curve of the fabricated probe.

A standard scanning sample is employed to evaluate the performance of AFM probes. This sample features a hole array with a 2.5 µm diameter, a 5 µm period, and a depth of 300 nm, as illustrated in Figure 5.14 (a). For comparison, an uncoated ACCESS-NC probe from AppNano company was purchased as the control group. As depicted in Figure 5.15, the tip apex of the AppNano probe measures approximately 47 nm, with the overall height of the tip reaching 14 µm. The probe was mounted onto the AFM system with a reflected laser energy of 15% (1.5 V). The scanning result of the standard sample using this probe is shown in Figure 5.14 (b).

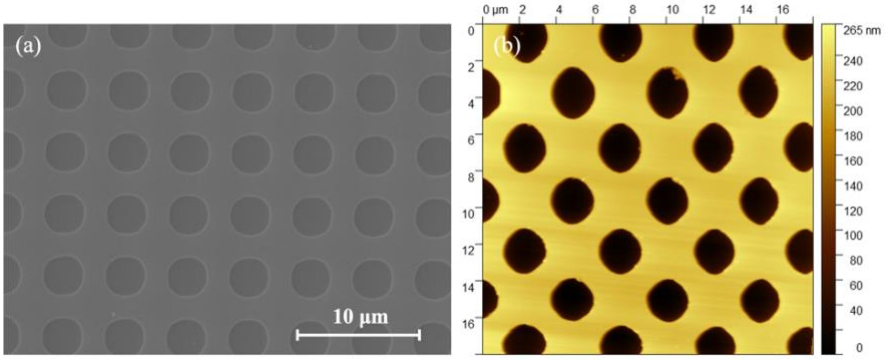


Figure 5.14 (a) The top view of the standard scanning sample, (b) the scanning result by using the commercially available Si probe bought from AppNano Company.

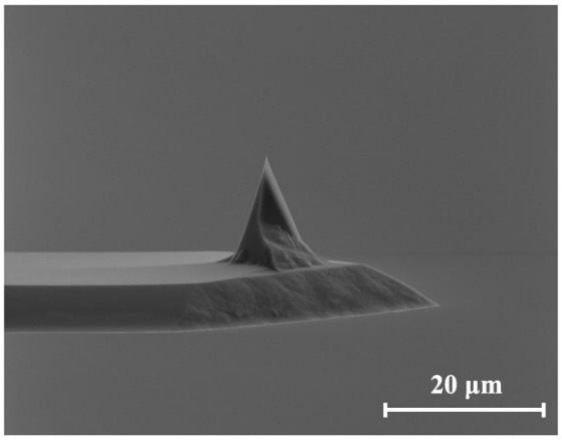


Figure 5.15 (a) The profile of an ACCESS-NC Si probe (the measured cone angle of the upper tip is 39.5°).

As shown in Figure 5.16 (a), the AFM scanning image using our probe is rather clear. The scanning rate is 0.6 Hz, and the scanned area is 18 µm with 256 pixels for each scanning line. After 2 hours of continuous scanning using the fabricated HAR probe, the image quality remains high,

as shown in Figure 5.16 (b). However, the image becomes more blurred after 3 hours of scanning as shown in Figure 5.16 (c), and the tip apex becomes blunt with a diameter of ~80 nm (Figure 5.16 (d)). For Si probes, the tip wear is mainly caused by the electrochemical corrosion of the oxide layer continuously forming on the Si surface.

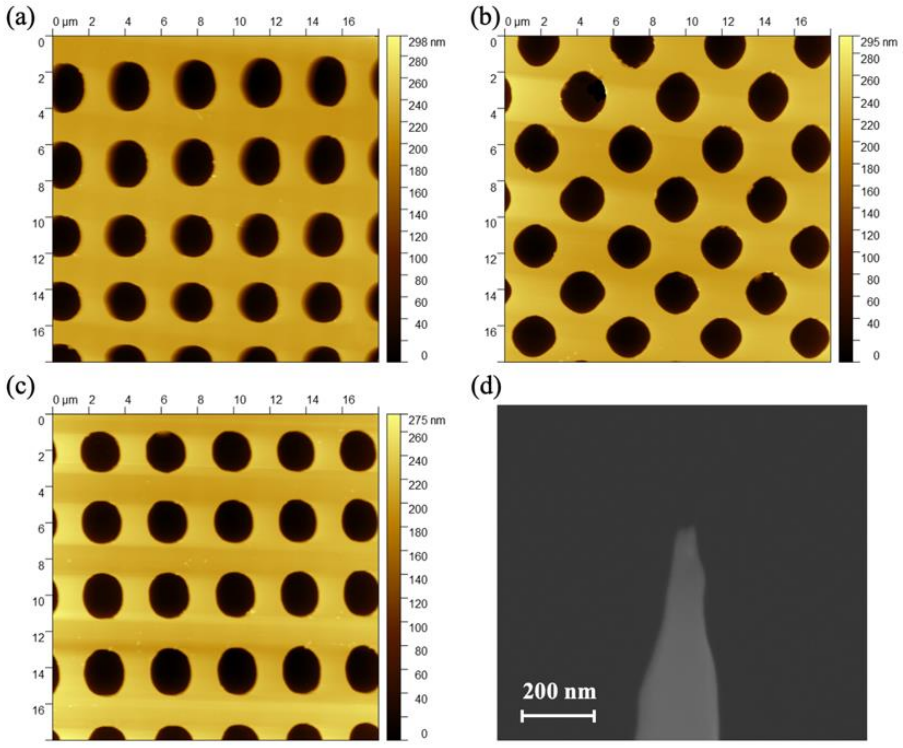


Figure 5.16 The AFM scanning image of (a) the first scan of the fabricated tip, (b) the fabricated tip used for 120 minutes, (c) the fabricated tip used for 180 minutes, (d) the SEM image of the used Si probe after 3-hour continuous scanning.

We prepared a nanoscale Si test sample with 350 nm width and 270 nm depth trenches to show the probe aspect ratio, as depicted in Figure 5.17. This sample was initially scanned using the fabricated Si probe with a 120 μm-long cantilever. The scanning results, presented in Figures 5.18 (b) and (c), indicate that the measured height corresponds to the profile observed in the SEM image. As a control, the sample was also scanned using a commercially available probe from AppNano. Although this probe can reach the bottom of the trenches, the scanning result is inaccurate (Figure 5.18 e-f). By comparing these two sets of results, it becones clear that the batch

fabrication developed in this thesis not only matches the capabilities of current commercial probes in scanning standard samples but also surpasses them in handling more challenging tasks, such as imaging high aspect ratio features.

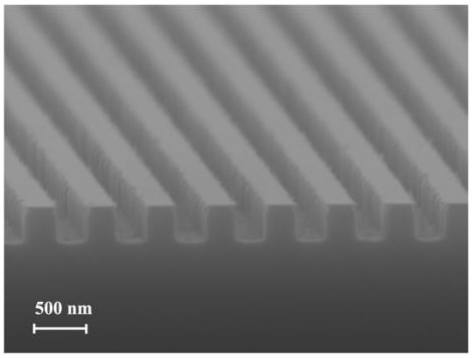


Figure 5.17 (a) The SEM image of a Si sample featuring trenches with a width of 350 nm and a depth of 270 nm.

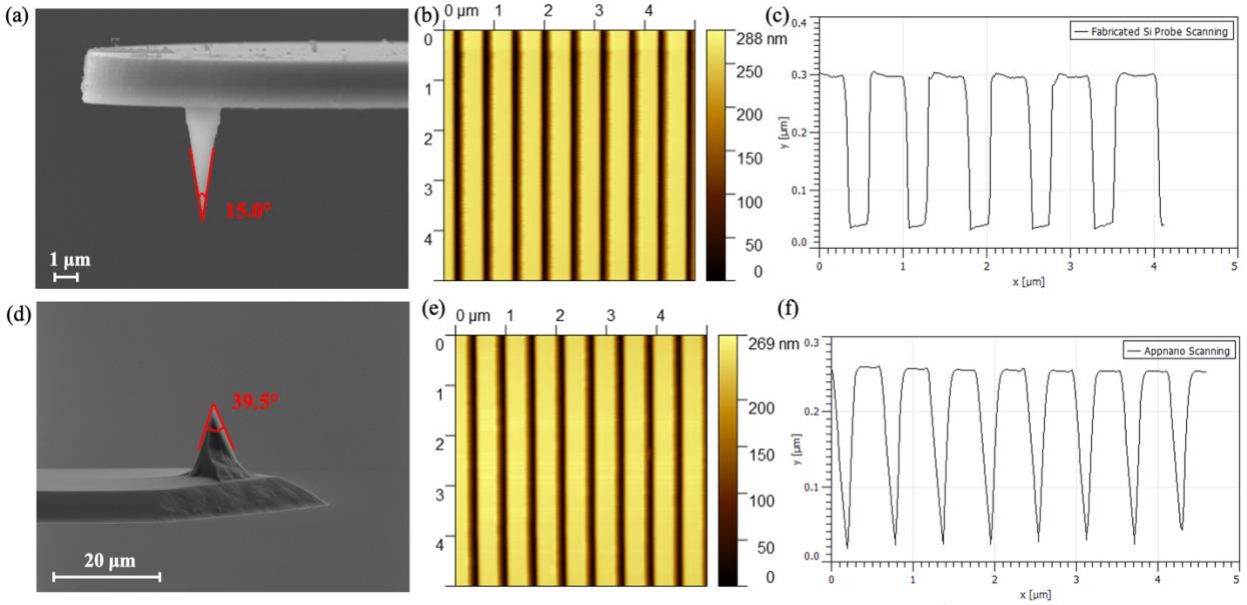


Figure 5.18 (a) The profile and cone angle of our probe, (b-c) the AFM scanning result by using our fabricated Si probe, (d) the profile and cone angle of the AppNano probe, (e-f) the AFM scanning result by using the AppNano probe.

We also prepared an optical-grade polyethylene terephthalate (PET) film to test the sharpness of our probe. Since the tip sharpened by the conventional wet etching method can also achieve a final sharpness of around 15 nm in Figure 5.19 (c), the two scanning results (Figure 5.19

b,d) are not significantly different. However, our high aspect ratio probe, with a 12 nm tip, captures more surface details, resulting in slightly better imaging outcomes.

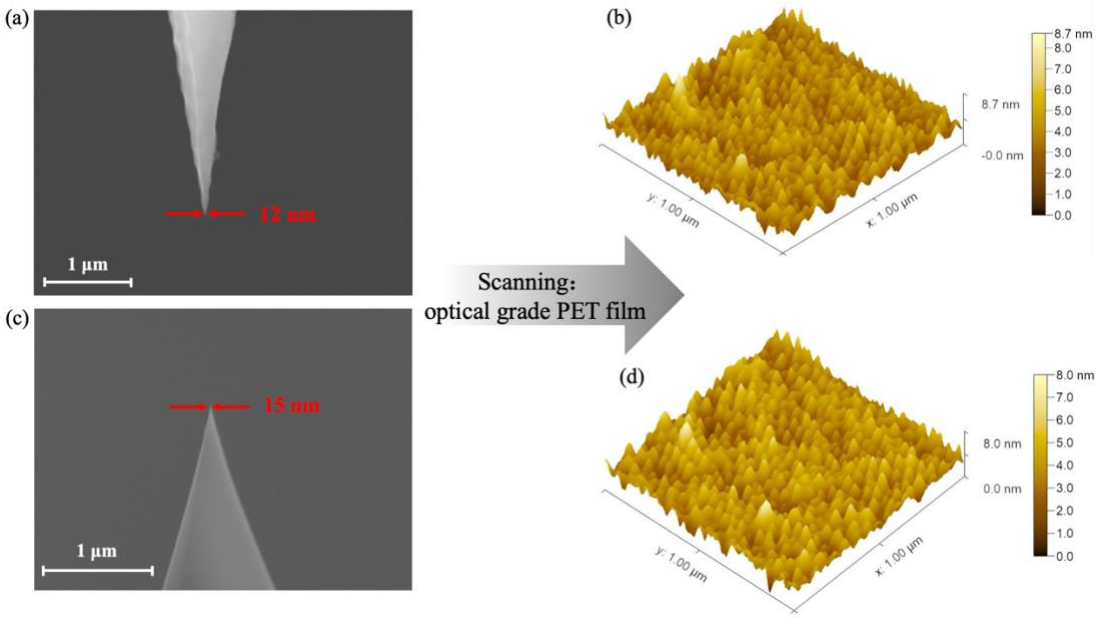


Figure 5.19 (a) The profile and apex diameter of our probe, (b) the AFM scanning result by using our fabricated Si probe, (c) the profile and apex diameter of the AppNano probe, (d) the AFM scanning result by using the AppNano probe.

5.3.2 Probes fabrication with 140 µm cantilever length

5.3.2.1 Experiment results

In the second batch of all-Si probes, the cantilever length has been adjusted to 140 µm. Based on the trends observed in spring constant and resonance frequency from simulation results, the objective of this adjustment is to fabricate a probe suitable for soft or fragile samples in the AFM tapping mode. All other experimental procedures remain consistent with those outlined in the previous section.

After removing the buried oxide, 50 probes were determined to be intact and usable, exhibiting a probe tip height of 7 µm, a cantilever thickness of 3 µm, a cantilever length of 140

μm, and an overall handle thickness of 300 μm. This indicates a yield rate of approximately 83% for this batch of probes. An intact probe structure is shown in Figure 5.20 (a) and (b), highlighting a tip diameter of 170 nm.

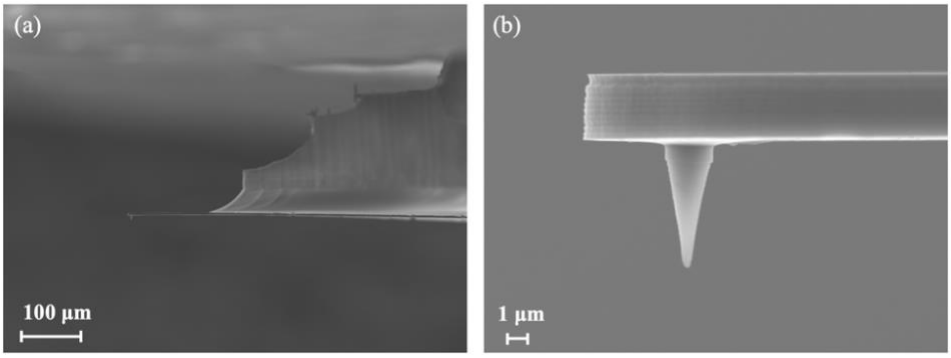


Figure 5.20 SEM images of (a) the side view of the AFM probe with the cantilever length of 140 μm, and (b) the enlarged view of the cantilever and the tip before oxidation sharpening. All images were captured using JOEL JSM-7200F SEM with the samples mounted on a 90° tilted stage.

After the thermal oxidation at 950 ℃ for 8 hours and the grown SiO_2 removal with BOE, the final AFM probe product is presented in Figure 5.21, showcasing a final sharpened Si tip apex measuring approximately 20 nm.

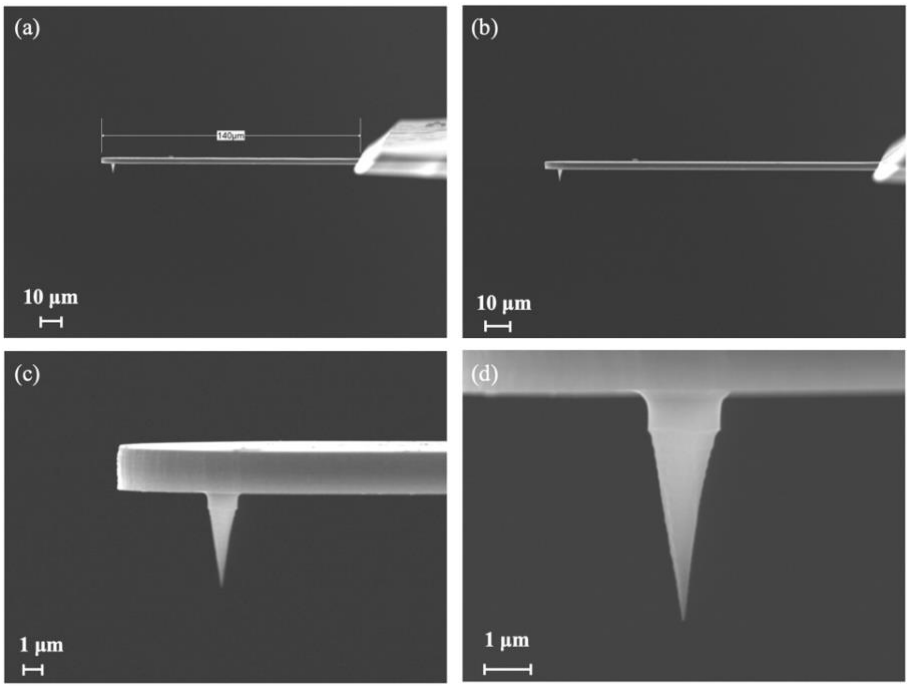


Figure 5.21 SEM images of (a) the final product of the AFM probe with 140 μm cantilever after oxidation sharpening, and (b-d) the enlarged view of the cantilever and the tip. All images were captured using JOEL JSM-7200F SEM with the samples mounted on a 90° tilted stage.

5.3.2.2 Performance test on AFM system

The fabricated AFM probe was installed on the Aist-NT SmartSPM 1000 in AFM tapping mode, demonstrating that our probes can mounted on various AFM models to showcase their versatility. The resonance frequency of this probe was measured to be 227.26 kHz, as displayed in Figure 5.22.

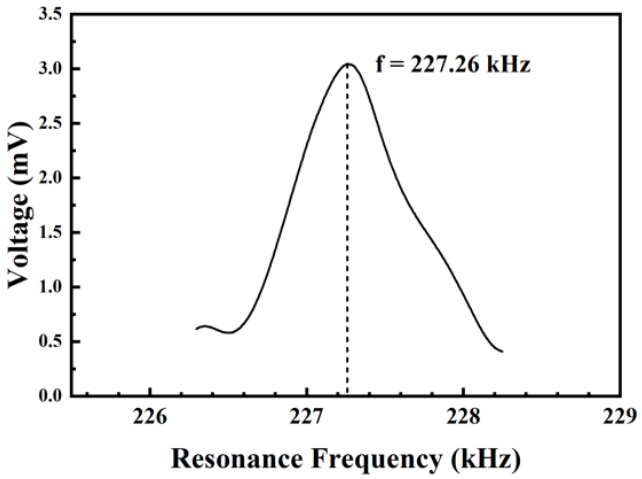


Figure 5.22 The resonance frequency curve of the fabricated probe, which was mounted on the Aist-NT SmartSPM 1000 in AFM mode.

Here, a soft sample with a photoresist pattern was prepared. Initially, a layer of positive resist AZ3330[250] was spin-coated onto a bare Si wafer. Subsequently, a line array with a width of 2.5 μm and a period of 5 μm was exposed using an MLA. After development, the final depth reached 3.2 μm, and the profile of the resist line exhibited a positive taper. The resulting scanning image is depicted in Figure 5.23 (a) and (b), with a scan rate of 0.5 Hz (2 μm/s tip velocity). Notably, the final height precisely matches the patterned dimensions. However, when attempting to use the commercial AppNano probe to scan this sample, issues arose because the sample was coated with AZ4620 photoresist, which is highly adhesive. This resulted in the commercial probe experiencing varying degrees of sticking and tip immersion during scanning, preventing the acquisition of usable scanning results.

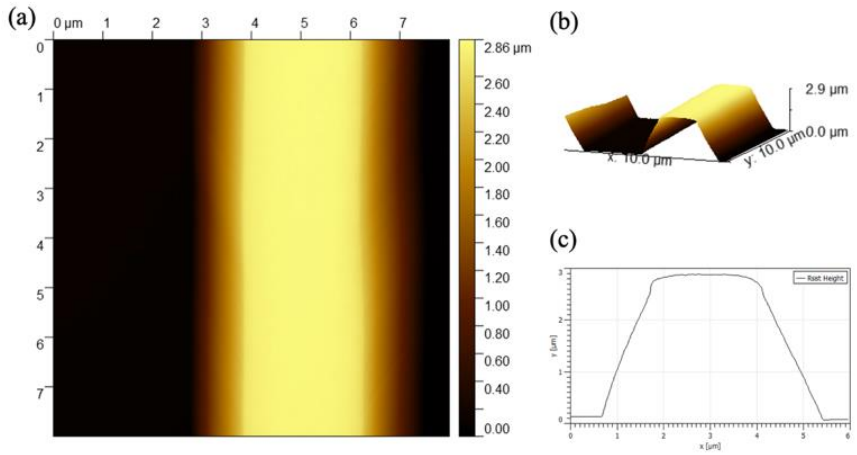


Figure 5.23 (a) The AFM scanning image of the photoresist AZ3330 lines with positively tapered sidewall, (b) the 3D view image, and (c) the cross-sectional view.

5.4 Summary

In this chapter, we investigated the mass production of all-Si AFM probes, featuring HAR tips fabricated via the O_2 shrinking method, Si cantilevers, and stair-shaped handles using the RIE loading effect and RIE-lag.

The first batch exhibited a tip height of 7 µm, an apex diameter ranging from 10 to 15 nm, a cantilever thickness of 3 µm, cantilever lengths ranging from 118 to 120 µm, and an overall handle thickness of 300 µm. When a randomly selected probe from this batch was mounted onto the AFM system, it showed an initial reflected laser signal of 25%, significantly higher than the ~15% typically observed in commercial uncoated AFM probes. The measured resonance frequency was 286.84 kHz, and the spring constant, calculated using Sader's method, was 18.65 N/m. The variances of the resonance frequency were 0.5% (compared to the calculated value in Section 5.1.1) and 5.9% (compared to the simulated value in Section 5.1.2), and the variances of the spring constant were 6.8% and 5.3%, indicating that the fabricated dimensions of this probe closely matched the model specifications. Furthermore, continuous scanning tests demonstrated that the service lifetime of this probe extends to at least 2 hours.

The second batch of probes had their cantilever lengths adjusted to 140 μm. When a randomly selected probe from this batch was mounted onto the AFM system, the measured resonance frequency was 227.26 kHz, and the spring constant, calculated using Sader's method, was 16.98 N/m. The variances of the resonance frequency were 6.7% compared to the calculated value and 2.4% compared to the simulated value. The variances of the spring constant can be attributed to the actual dimensions of the cantilever and the higher Q-factor due to different working conditions on specific AFM models.

Overall, both types of all-Si probes exhibit excellent tip profiles and are highly compatible with the tapping mode imaging of various AFM systems. Based on the scanning results, these HAR probes are capable of scanning structures with an aspect ratio greater than 1. Furthermore, they benefit from short fabrication cycles, low production costs, and high yield rates, broadening the range of applications for AFM probes.

Chapter 6 Mass Fabrication of Low-spring-constant AFM Probes with HAR Si Tips, SiN_x Cantilevers and Stair-shaped Handles

This chapter explores the adoption of LPCVD SiN_x as an alternative to Si for cantilevers. This nitride cantilever offers benefits such as low spring constants and precise deposition control, resulting in thin and low-spring constant cantilevers. The fabricated probe with a Si tip and a SiN_x cantilever minimizes damage to both the sample and tip, making it ideal for fragile samples with higher-resolution scanning results.

6.1 Simulation and Design

6.1.1 Direct calculation by MATLAB

After deposition, thin film cantilevers typically experience a certain internal stress level, resulting in cantilever deformation. Thus, low-stress nitride is employed; the stochastic Si_3N_4 exhibits very high tensile stress, and the low-stress nitride is silicon-rich, with an approximate Si and N ratio of 1:1. This is achieved by significantly increasing the gas flow ratio of SiH_2Cl_2 to NH_3 during LPCVD growth.

For SiN_x, E is 250 GPa, and ρ is 3100 kg/m^3. As described in Chapter 5.1, for simulation, the cantilever length ranges from 80 μm to 150 μm, while the width ranges from 0 μm to 30 μm. To achieve a low spring constant, the thickness was set between 0 μm and 2 μm. A MATLAB simulation was carried out to determine the spring constants for the probe with nitride cantilever, as illustrated in Figure 6.1.

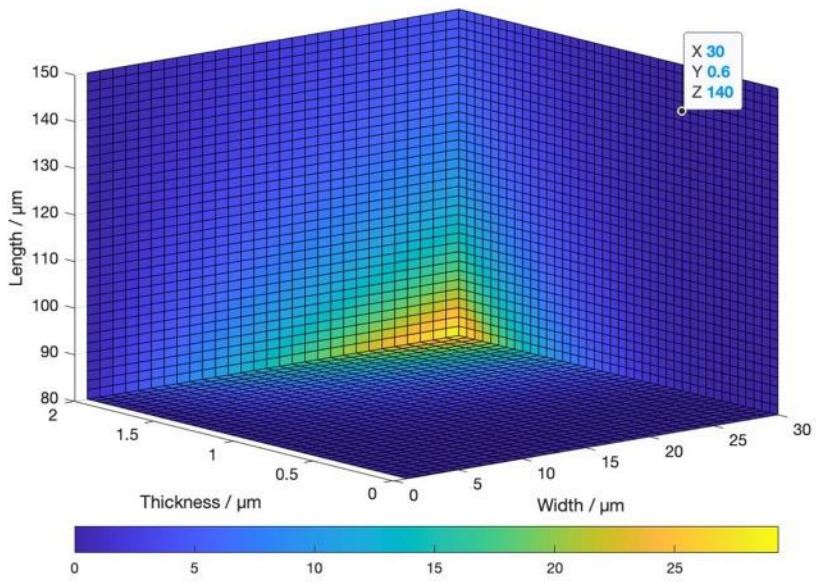


Figure 6.1 The 4D plot of spring constant k (unit N/m) and dimensions w,t,l.

We conducted stress measurements on our LPCVD SiNx films with thicknesses of 600 nm and 800 nm, revealing tensile stress levels of 90 MPa and 120 MPa, respectively. However, the stress measurement is generally just a guideline with low accuracy. In our experiment, we opted for the 600 nm thickness. In Figure 6.1, the simulated spring constant is found as 0.15 N/m when the dimensions (w, t, l) are set as (30, 0.6, 140), with a corresponding resonance frequency of 44.53 kHz.

6.1.2 Finite element simulation by COMSOL

Similar to the simulation in Section 5.1.2, a geometric model of the cantilever was created with dimensions specified as follows: 140 µm in length, 30 µm in width, and 600 nm in thickness. As shown in Figure 6.2, the simulated resonance frequency is 46.37 kHz. The maximum/minimum value of the applied force is 0.51/0.09 µN, and the maximum/minimum value of the cantilever's displacement is 3.44/0.57 m. As a result, the simulated spring constant is 0.14 N/m.

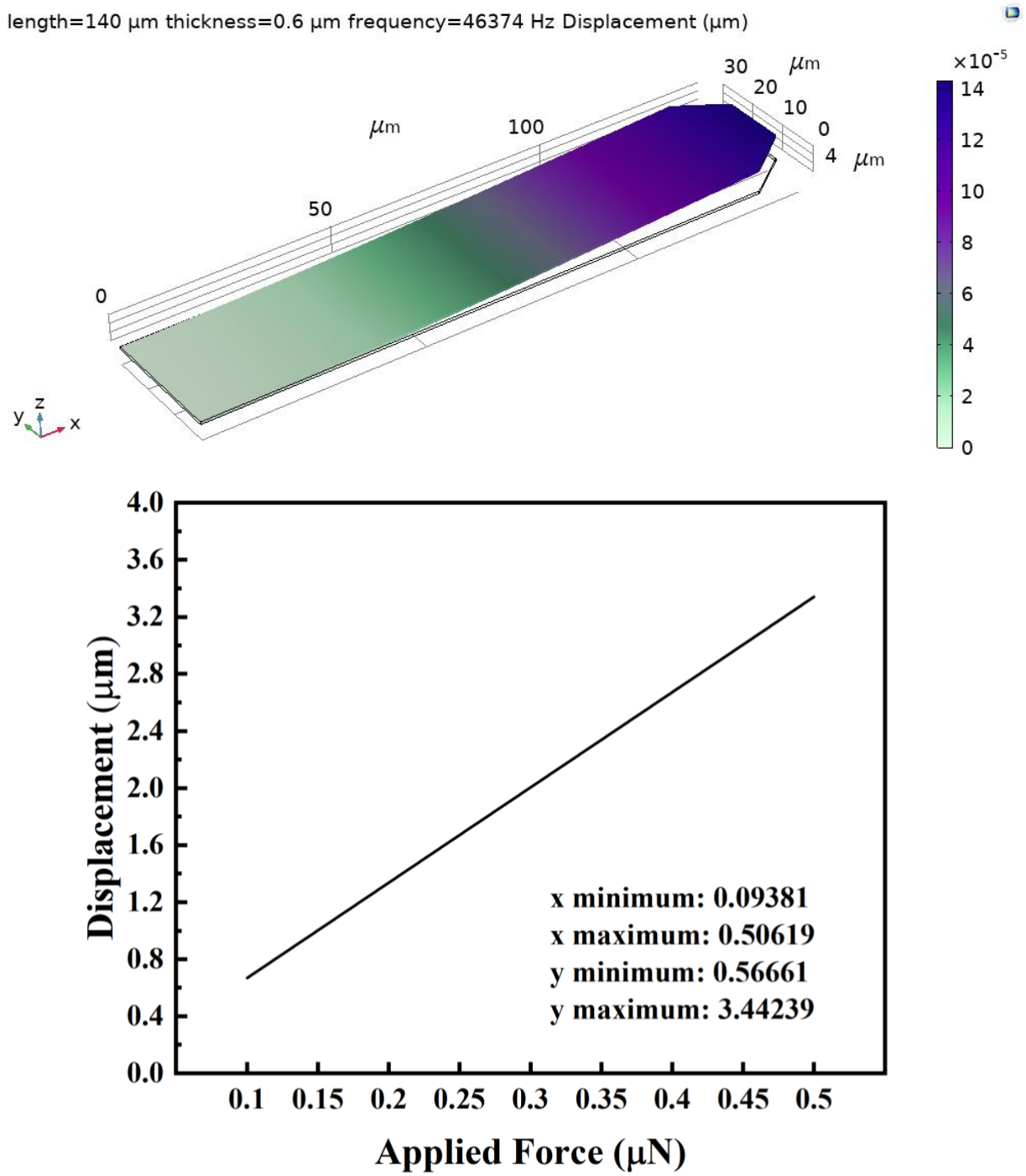


Figure 6.2 The resonance frequency and the spring constant were simulated for a rectangular nitride cantilever with 30 µm in width, 600 nm in thickness and 140 µm in length.

6.2 Fabrication Process

Fabrication of specific AFM probe with Si tip and nitride cantilever includes the Si tip, SiN_x cantilever and Si stair-shaped handle. The proposed fabrication process on the SOI wafer for the AFM probe with SiN_x cantilever is depicted in Figure 6.3.

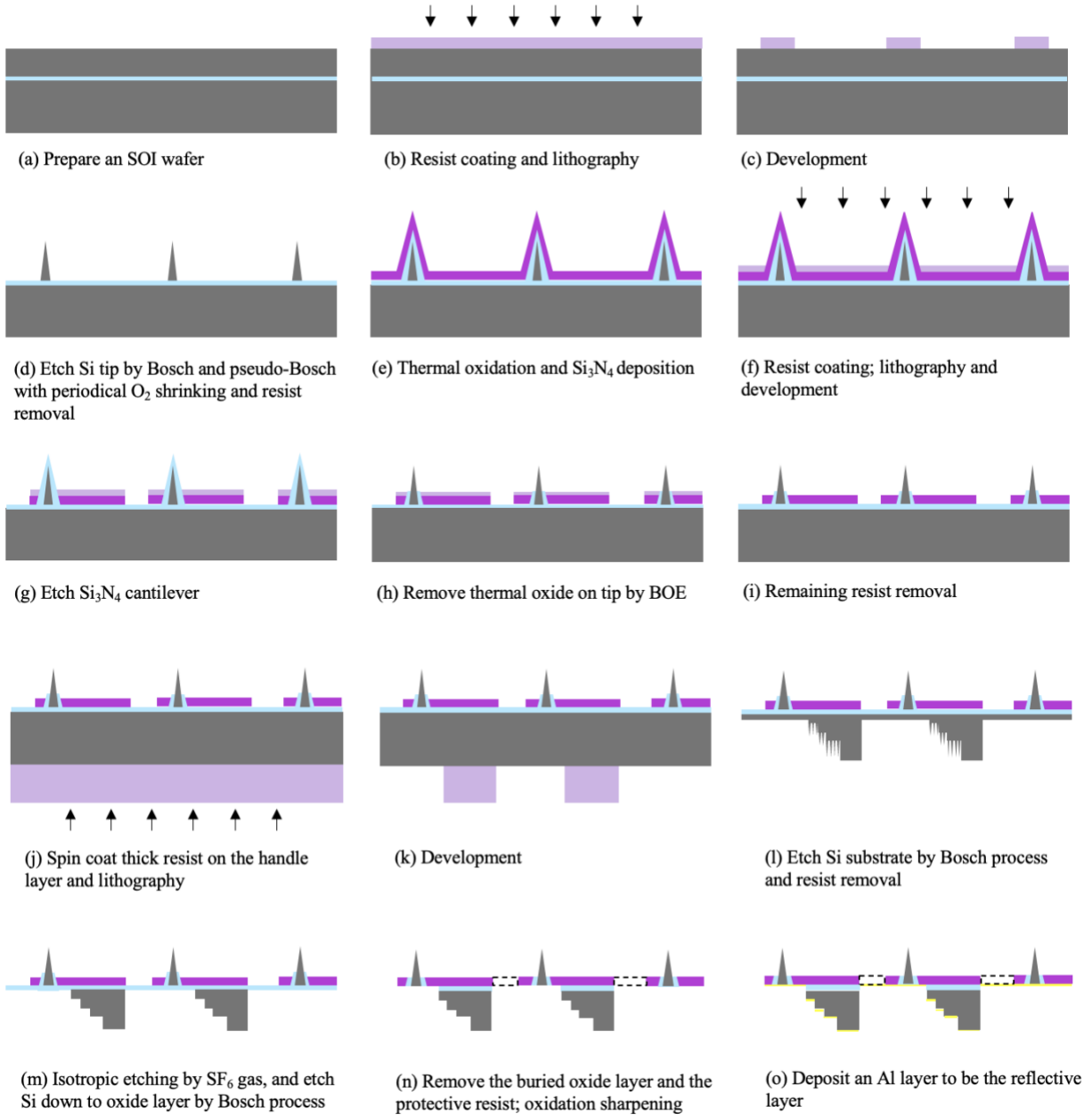


Figure 6.3 Fabrication of AFM probe with SiN_x cantilever and stair-shaped handle.

The tip etching process follows the same procedure outlined in Chapter 5.2, except for the final target height, set as 10 µm. This involves initially etching by using the standard Bosch process for 12 cycles, followed by 35 cycles of the modified resist shrinkage etching process using O_2 plasma (Figure 6.3a-d). The next step is thermal oxidation under atmospheric conditions at 950℃ for 2 hours to protect as well as sharpen the tip after the eventual oxide removal. On top of the oxide layer, a 600 nm low-stress amorphous SiN_x layer is coated by LPCVD (Figure 6.3e). A round of AZ nLof 2035 resist coating, lithography and development are carried out for the cantilever structure (Figure 6.3f). The etching recipe for SiN_x (Figure 6.3g) is 45 sccm SF_6, 50 W RF power and 2000 W ICP power under 10 mTorr chamber pressure for 3 minutes. When applying the nitride etching recipe, the layer of SiN_x on tips would also be removed (Figure 6.3h), allowing for subsequent removal of the thermal oxide layer on tips using BOE (Figure 6.3i). Fabrication of the Si tip and nitride cantilever on the device layer is completed after the remaining resist removal, and the fabrication process for the stair-shaped handle follows the same steps outlined in Chapter 5.2. After completing the handle fabrication, the final profile of the HAR AFM probe is shown in Figure 6.4.

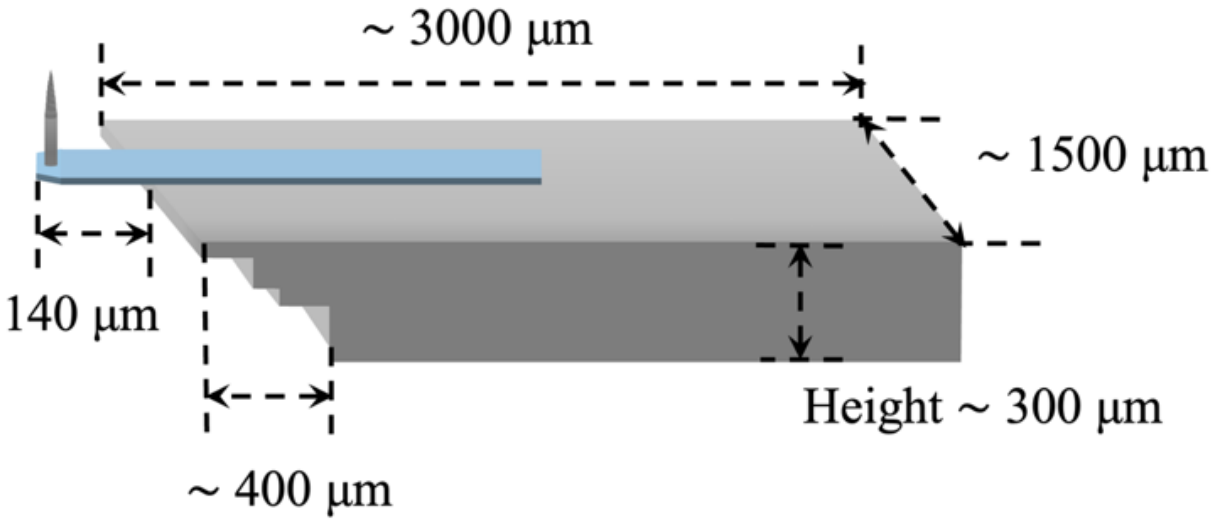


Figure 6.4 The schematic structure of the AFM probe with a handle has several steps.

6.3 Results and Discussion

The initial step involves conducting an etching test of the nitride layer. For this purpose, a 600 nm SiN_x layer is deposited by LPCVD. LPCVD is chosen due to its capability to coat a low-stress amorphous nitride layer, which prevents curling after the cantilever is released. As the Si tip structures are already on the sample, removing the nitride deposited on the upper part of the tip is challenging, and it relies on lateral etching with the oxide as the etching stop layer.

The first task is to develop a nitride etching recipe that gives significant lateral etching to remove the nitride coating on the sidewall of the Si tip without etching away all the nitride and oxide on the top surface of the Si tip. To achieve this, a test sample with 600 nm SiN_x by LPCVD is prepared. This sample is spin-coated with a bilayer of PMGI and S1805 photoresist for liftoff. Following photolithography, 100 nm Cr is evaporated and then lifted off to create a metal mask for etching. After etching for 1 min by recipe with 45 sccm SF_6, 50 W RF power, 2000 W ICP power, and 10 mTorr, the etched test sample is shown in Figure 6.5.

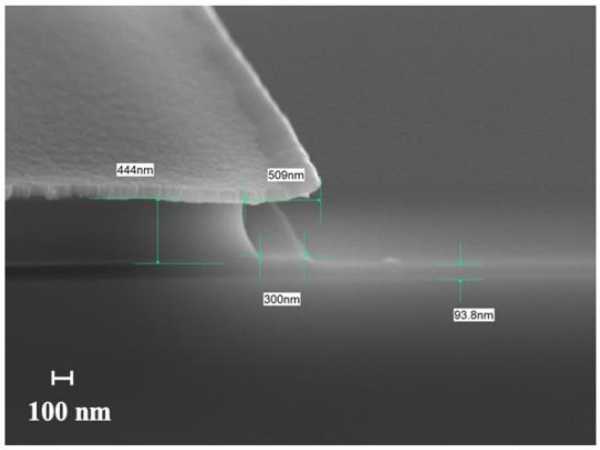


Figure 6.5 The lateral and vertical etching of the nitride layer using Cr as a mask for the test sample.

The nitride etching rate along the vertical direction is 444 nm/min, and that along the lateral direction is 509 nm/min (the number should be lower since the Cr is curved up at the edge after liftoff; a more reasonable number should be 300 nm lateral etching). Therefore, this recipe provides

considerable nitride lateral etching, just like the isotropic etching of Si using SF_6 gas, and it is suitable for nitride etching in the AFM cantilever fabrication process.

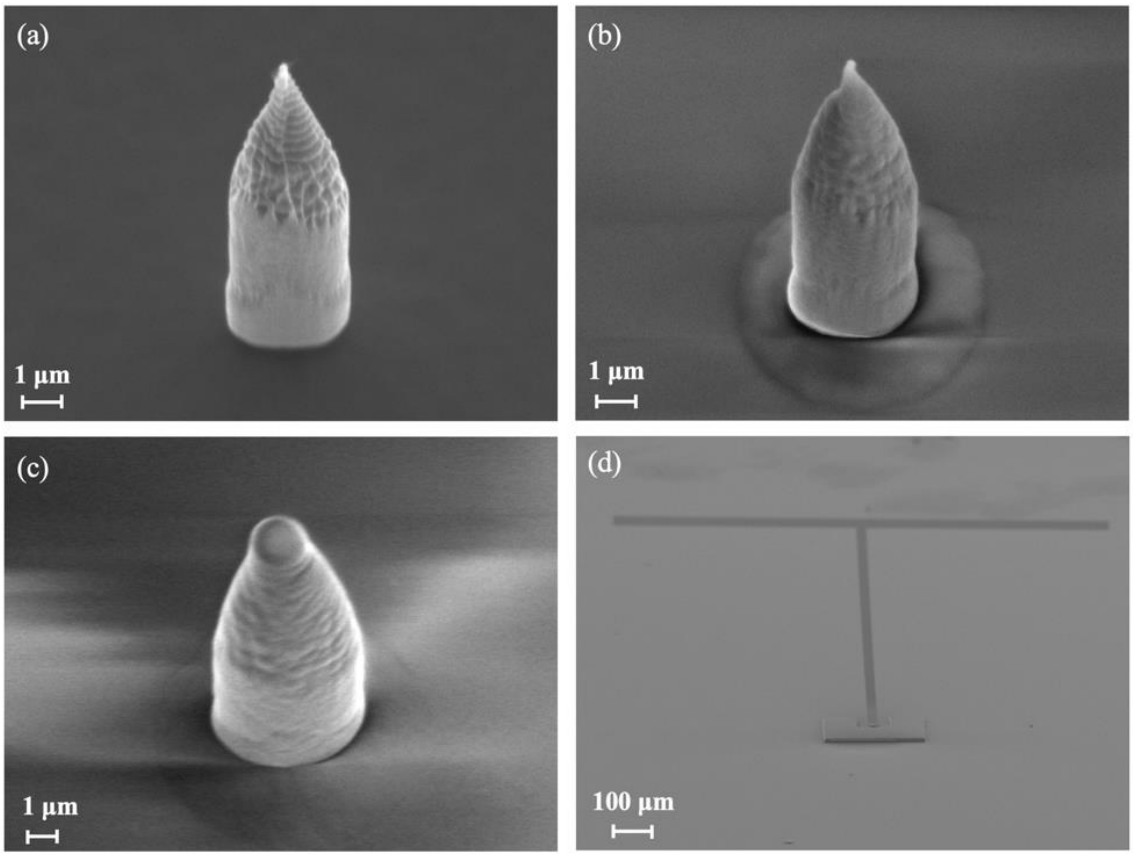


Figure 6.6 SEM image of (a) the etched tip before oxidation, (b) the tip profile after thermal oxidation at 950°C for 2 hours, (c) the tip after 600 nm LPCVD nitride deposition, (d) the overview of the tip and the cantilever. All images were captured using JOEL JSM-7200F SEM with the samples mounted on a 20° tilted stage.

Starting with an SOI wafer, the Si tip is fabricated with a designed resist mask diameter of 3.0 µm using the process above. As depicted in Figure 6.6 (a), the Si tip shows the sample tilted by 20°. The apex diameter of the etched tip measures 0.6 µm, while the base diameter is 3 µm. Following thermal oxidation at 950°C for 2 hours, as shown in Figure 6.6 (b), and 600 nm LPCVD nitride deposition, as depicted in Figure 6.6 (c), the SiN_x cantilever wraps around the lower/base part of the Si tip to hold it. This differs from the configuration where it sits below the Si tip, which already rests on the oxide layer of the SOI wafer, as shown in Figure 6.6 (d).

After the handle fabrication, the exposed buried oxide is removed by BOE wet etching. Out of the total 60 probes fabricated, 56 probes were found to be intact and usable, indicating an impressive yield rate of approximately 93% for this batch of probes. An intact probe with a Si tip and nitride cantilever is shown in Figure 6.7 (a) and (b).

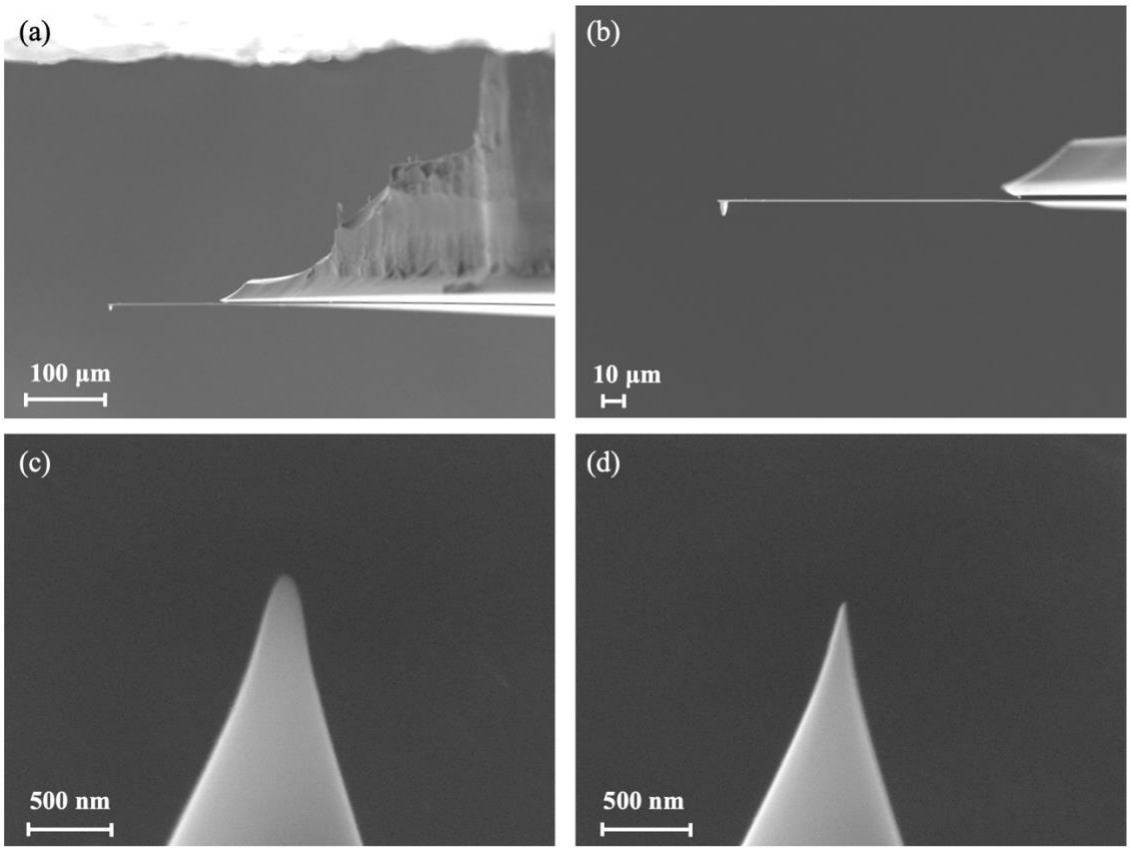


Figure 6.7 (a) Overview SEM image of nitride probe, (b) the enlarged profile of the thin cantilever, (c) the tip profile before thermal oxidation sharpening, (d) the tip profile after thermal oxidation sharpening. All images were captured using JOEL JSM-7200F SEM with the samples mounted on a 90° tilted stage.

The tip height measures 9.2 µm (which should be reduced by approximately 0.6 µm, the cantilever thickness, as the nitride surrounds this bottom portion of the tip). The apex diameter is 0.8 µm, indicating the need for an additional round of oxidation sharpening. After 2 rounds of thermal oxidation at 950 ℃ for 8 hours and the grown SiO_2 removal with BOE, the final AFM probe product is presented in Figure 6.7 (d), showcasing a final sharpened Si tip apex measuring approximately 15 nm. Additionally, the SiN_x cantilever exhibited a thickness of 600 nm and a

length of 145 μm. This deviation was primarily due to a slight misalignment during the photolithography step and the over-etch during the handle etching step of the handle fabrication.

6.4 Performance Test of Fabricated AFM Probe

Currently, AFM systems are predominantly operated in tapping mode, while contact mode is less common[19,251]. The fabricated AFM, featuring a Si tip and SiN_x cantilever, was integrated into the tapping mode of the FM-Nanoview1000AFM by Fisherman Company since this AFM model doesn't support contact mode imaging. The reflected laser signal was measured as 32.9% (3.29V) after depositing 30 nm Al on the cantilever backside, and the measured resonance frequency of the cantilever is 35.36 kHz.

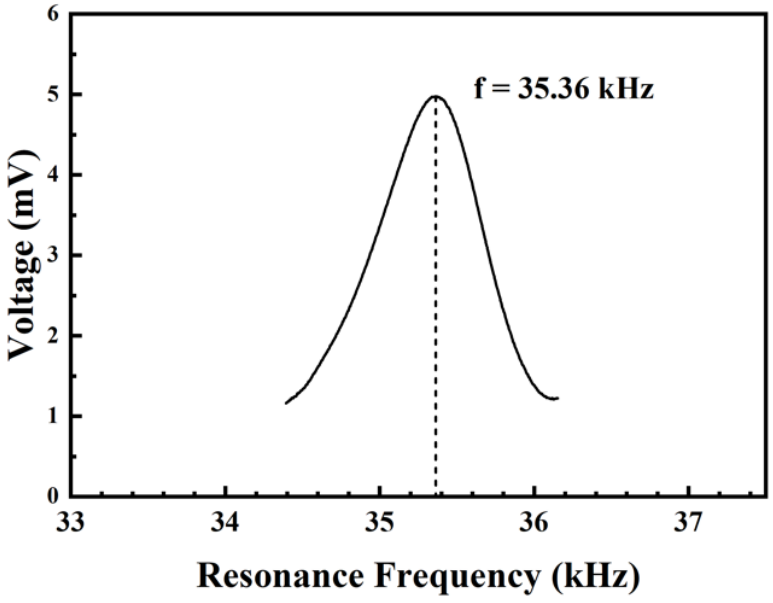


Figure 6.8 The measured resonance frequency of fabricated AFM probe after metal (30 nm Al) deposition on the cantilever backside.

To test the probe performance for imaging high aspect ratio soft structures, a new photoresist sample featuring trenches with a bottom width of 400 nm and a depth of 700 nm is prepared with slightly positive tapered sidewalls, as depicted in Figure 6.9 (a). This sample was initially scanned using the fabricated Si probe with a 145 μm-long nitride cantilever. The scanning

results, presented in Figures 6.9 (b) and (c), demonstrate that the measured height aligns with the profile observed in the SEM image. As a control, the sample was also scanned using a commercially available Si probe from AppNano. However, this probe was unable to reach the bottom of the trenches.

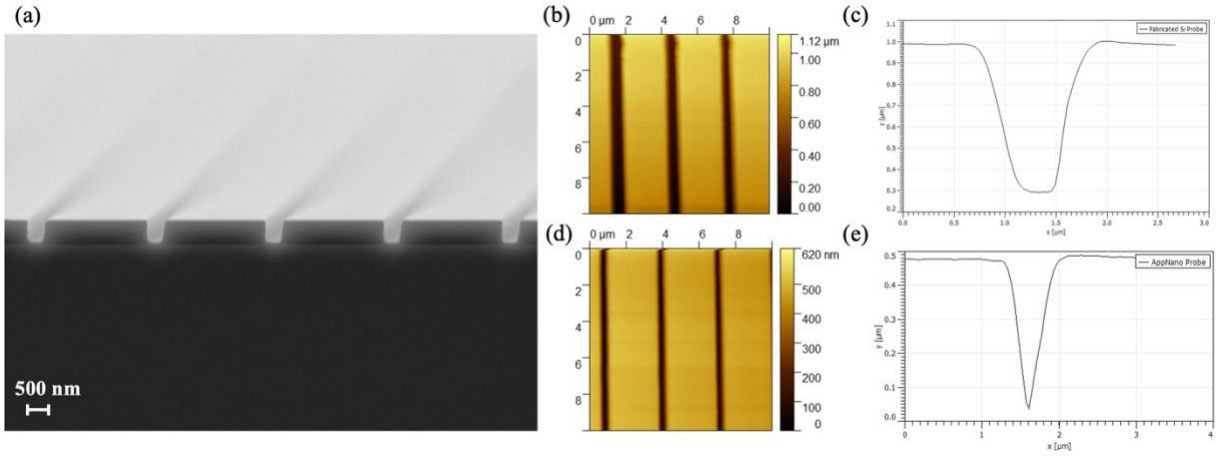


Figure 6.9 (a) The SEM image of the new photoresist sample featuring trenches with a trench bottom width of 400 nm and a depth of 700 nm, (b-c) the AFM scanning result by using our fabricated probe with nitride cantilever, (d-e) the AFM scanning result by using the AppNano probe.

6.5 Summary

In this chapter, we explored the mass fabrication of low-spring constant AFM probes suitable for imaging soft biological samples, featuring HAR tips fabricated by the O_2 shrinking, SiN_x cantilevers, and stair-shaped handles using the RIE loading effect and RIE-lag. The fabricated batch features SiN_x cantilevers with lengths of 145 µm and thicknesses of 600 nm, and tips with heights of 9 µm and apex diameters ranging from 15 to 20 nm. For a randomly selected probe, the measured resonance frequency was 35.36 kHz, while the spring constant, calculated using Sader's method, was 0.14 N/m. The observed variances in resonance frequency and spring constant compared to the calculated value in Section 5.1.1 and the simulated value in Section 5.1.2 can be attributed to the 5 µm variance in the final fabricated cantilever length.

These probes are versatile, offering enhanced performance in tapping mode imaging. The low spring constant and resonance frequency can minimize the risk of damage to both the sample and tip, making them particularly suitable for fragile/soft samples and subtle surface imaging.

Chapter 7 Conclusions and Future Work

This thesis presents systematic studies on the fabrication of HAR AFM probes. The main results are summarized as follows:

1. HAR Si nanocones are applicable to numerous potential applications, and their profiles perfectly match the requirements for AFM tip structures. Four distinct methods for tip fabrication are proposed, each offering unique benefits. Method 1 in Section 3.1 achieves an exceptional aspect ratio of 1:135 by using the EBL and the non-switching pseudo-Bosch etching with wet sharpening techniques. Method 2 in Section 3.2 employs an innovative tapered oxide mask profile transfer, yielding an apex diameter of 3.54 nm, significantly below the 20 nm typical value for AFM tips. Method 3 in Section 3.3 utilizes a two-step cryogenic etching, producing a slight taper angle of 2.2°, optimal for scanning deep holes and trenches. Method 4 integrates the standard Bosch process with the non-switching pseudo-Bosch process, incorporating periodic O_2 shrinking steps to achieve a tip apex sharpness of 20 nm. Method 4 is chosen for final probe fabrication due to its simplicity, cost-effectiveness and uniformity.
2. To mitigate laser beam blocking, we proposed the stair-shaped AFM handle structures which are not currently available in the market, and two distinct fabrication methods are explored in this thesis. Method 1 in Section 4.1 utilizes the RIE loading effect and RIE-lag, and optimizes the pattern design to grid structures intelligently, thus simplifying the fabrication to a single round of photolithography and etching. The resulting stair-shaped handle features four steps with stage heights of 71 μm, 151 μm, 168 μm, and 287 μm. The second method employs the pseudo-grayscale lithography on a photomask combined with DRIE, and the resulting stair-shaped handle features steps with heights of 52 μm, 83 μm, 161 μm, and 211 μm. Method 1 is selected for final probe fabrication due to its relative simplicity.

3. The fabrication and performance evaluation of two AFM probes including all-Si HAR AFM probes optimized for tapping mode, and low-spring constant HAR probes featuring a Si tip and silicon nitride cantilever suitable for surface morphology scanning of soft/fragile samples. Table 7.1 is a summary of the parameters of the fabricated probes, compared with three commercially available Si probes from Nanoworld, Bruker, and AppNano. As shown in the table, the resonant frequency and force constant of the probes closely match the simulated values. Our probes not only exhibit a high aspect ratio but also are more cost-effective than standard probes fabricated by current methods (such as wet etching). Additionally, the continuous scanning lifespan of our fabricated probes extends up to three hours, making them suitable for in-line inspection in the semiconductor manufacturing industry.

Table 7.1 A summary of the parameters of the fabricated probes and three commercially available Si probes from Nanoworld, Bruker, and AppNano.

Parameters		Si Probe 1	Si Probe 2	Nitride Probe	NanoWorld Si Probe	Bruker Si Probe	AppNano Si Probe
Length (μm)		120	140	145	225	100	150
Width (μm)		30	30	30	33	30	54
Thickness (μm)		3	3	0.6	5	5	5
Frequency (kHz)	Calculated	288.35	211.85	44.53	-	-	-
	COMSOL	303.75	221.62	46.37	-	-	-
	Measured	286.84	227.26	35.36	130	320	200-400
Spring Constant (N/m)	Calculated	19.92	12.55	0.15	-	-	-
	COMSOL	19.64	12.27	0.14	-	-	-
	Sader's Calibration	18.65	16.98	0.14	15	37	32-169

In the future, using a probe test sample with suitable dimensions is crucial to demonstrate the optimal performance of our fabricated AFM probe. Extensive performance tests on various samples with our fabricated tip are required in the next stage. Additionally, exploring cryogenic etching for tip fabrication and pseudo-grayscale lithography for handle fabrication could be beneficial to ensure scalability for mass production.

Overall, the thesis represents a significant academic contribution to Si nanocone and handle fabrication, showcasing a systematic research approach and experimental validation, which could advance both academic and industrial AFM probe production.

References

1. Mait, J. N. A History of imaging: revisiting the past to chart the future. *Opt Photonics News* **17**, 22–27 (2006).

2. Broglie, L. de. A tentative theory of light quanta. *The London, Edinburgh, and Dublin Philosophical Magazine and Journal of Science* **47**, 446–458 (1924).

3. Ruska, E. & Elektronenmikroskopie, A. The development of the electron microscope and of electron microscopy. *Rev Mod Phys* **59**, 627 (1987).

4. Zhou, W., Apkarian, R. P., Lin Wang, Z. & Joy, D. Fundamentals of scanning electron microscopy. in *Scanning microscopy for nanotechnology: techniques and applications* vol. 1 1–40 (2007).

5. Binning, G., Rohrer, H., Gerber, C. & Weibel, E. Surface studies by scanning tunneling microscopy. *Phys Rev Lett* **49**, 6196 (1975).

6. Hansma, P. K. & Tersoff, J. Scanning tunneling microscopy. in *Journal of Applied Physics* vol. 61 1–24 (1987).

7. Binnig, G., Quate, C. F., Gi, E. L. & Gerber, C. Atomic force microscope. *Phys Rev Lett* **56**, 930 (1986).

8. Giessibl, F. J. Advances in atomic force microscopy. *Rev Mod Phys* **75**, 949 (2003).

9. Seo, Y. & Jhe, W. Atomic force microscopy and spectroscopy. *Reports on Progress in Physics* **71**, (2008).

10. Butt, H. J., Cappella, B. & Kappl, M. Force measurements with the atomic force microscope: technique, interpretation and applications. *Surf Sci Rep* **59**, 1–152 (2005).

11. Jalili, N. & Laxminarayana, K. A review of atomic force microscopy imaging systems: Application to molecular metrology and biological sciences. *Mechatronics* **14**, 907–945 (2004).

12. Ahia, C. C. & Meyer, E. L. Advances in the use of atomic force microscopy as a diagnostic tool for solar cells characterization: from material design to device applications. *Physica Status Solidi (A) Applications and Materials Science* **221**, (2024).

13. Maghsoudy-Louyeh, S., Kropf, M. & Tittmann, B. R. Review of progress in atomic force microscopy. *Open Neuroimag J* **12**, 86–104 (2019).

14. Voigtlander, B. Tip-sample forces. in *Atomic Force Microscope* 161–164 (2019).

15. Xu, S. & Arnsdorf, M. F. *Electrostatic Force Microscope for Probing Surface Charges in Aqueous Solutions*. *Biophysics* vol. 92 (1995).

16. Wang, Y. J. Constant force feedback controller design using PID-like fuzzy technique for tapping mode atomic force microscopes. *Intelligent Control and Automation* **04**, 263–279 (2013).

17. Gotsmann, B., Seidel, C., Anczykowski, B. & Fuchs, H. Conservative and dissipative tip-sample interaction forces probed with dynamic AFM. *Phys Rev B* **60**, (1999).

18. Simpson, G. J., Sedin, D. L. & Rowlen, K. L. Surface roughness by contact versus tapping mode atomic force microscopy. *Langmuir* **15**, 1429–1434 (1999).

19. Geerlings, J. *et al.* Design and fabrication of in-plane AFM probes with sharp silicon nitride tips based on refilling of anisotropically etched silicon moulds. *Journal of Micromechanics and Microengineering* **24**, (2014).

20. Saadi, M. A. S. R., Uluutku, B., Parvini, C. H. & Solares, S. D. Soft sample deformation, damage and induced electromechanical property changes in contact and tapping-mode atomic force microscopy. *Surf Topogr* **8**, (2020).

21. James, P. J. *et al.* Interpretation of contrast in tapping mode AFM and shear force microscopy. *Langmuir* **17**, 349–360 (2001).

22. Kuwahara, Y. Muscovite surface structure imaged by fluid contact mode AFM. *Phys Chem Minerals* **26**, 198–205 (1999).

23. Akiyama, K. *et al.* Development of a metal-tip cantilever for noncontact atomic force microscopy. *Review of Scientific Instruments* **76**, (2005).

24. Altman, E. I., Baykara, M. Z. & Schwarz, U. D. Noncontact atomic force microscopy: an emerging tool for fundamental catalysis research. *Acc Chem Res* **48**, 2640–2648 (2015).

25. Ueyama, H., Sugawara, Y. & Morita, S. Stable operation mode for dynamic noncontact atomic force microscopy. *Appl Phys A Mater Sci Process* **66**, (1998).

26. Yang, C. W., Hwang, I. S., Chen, Y. F., Chang, C. S. & Tsai, D. P. Imaging of soft matter with tapping-mode atomic force microscopy and non-contact-mode atomic force microscopy. in *Nanotechnology* vol. 18 (2007).

27. Cleveland, J. P., Anczykowski, B., Schmid, A. E. & Elings, V. B. Energy dissipation in tapping-mode atomic force microscopy. *Appl Phys Lett* **72**, 2613–2615 (1998).

28. Schmitz, I., Schreiner, M., Friedbacher, G. & Grasserbauer, M. Tapping-mode AFM in comparison to contact-mode AFM as a tool for in situ investigations of surface reactions with reference to glass corrosion. *Anal Chem* **69**, 1012–1018 (1997).

29. Putman, A. J. *et al.* Tapping mode atomic force microscopy in liquid. *Appl Phys Lett* **64**, 2454–2456 (1994).

30. Abbas, Y., Rezk, A., Saadat, I., Nayfeh, A. & Rezeq, M. Photodetection characteristics of gold coated AFM tips and n-silicon substrate nano-Schottky interfaces. *Sci Rep* **9**, (2019).

31. Amelio, S. *et al.* Measurements of elastic properties of ultra-thin diamond-like carbon coatings using atomic force acoustic microscopy. *Thin Solid Films* **392**, 7584 (2001).

32. Phillips, G. N., Siekman, M., Abelmann, L. & Lodder, J. C. High resolution magnetic force microscopy using focused ion beam modified tips. *Appl Phys Lett* **81**, 865–867 (2002).

33. NanoSensors. Point probe plus AFM probes. *NanoSensors Company* 1 Preprint at (2024).

34. NanoSensors. Diamond coated point probe plus silicon SPM probes. *NanoSensors Company* 1 Preprint at (2024).

35. NanoSensors. Magnetic force microscopy silicon MFM probes. *NanoSensors Company* 1 Preprint at (2024).

36. NanoSensors. Tilt compensated high aspect ratio silicon probes. *NanoSensors Company* 1 Preprint at www.nanosensors.com (2024).

37. Verbiest, G. J. & Rost, M. J. Resonance frequencies of AFM cantilevers in contact with a surface. *Ultramicroscopy* **171**, 70–76 (2016).

38. Raman, A., Melcher, J. & Tung, R. Cantilever dynamics in atomic force microscopy. *Nano Today* **3**, 20–27 (2008).

39. Rabe, U., Turner, J. & Arnold, W. Analysis of the high-frequency response of atomic force microscope cantilevers. *Appl Phys A Mater Sci Process* **66**, (1998).

40. Mendels, D. A. *et al.* Dynamic properties of AFM cantilevers and the calibration of their spring constants. *Journal of Micromechanics and Microengineering* **16**, 1720–1733 (2006).

41. Walters, D. A. *et al.* Short cantilevers for atomic force microscopy. *Review of Scientific Instruments* **67**, 3583–3590 (1996).

42. Wei, Z., Liu, J., Zheng, X., Sun, Y. & Wei, R. Influence of squeeze film damping on quality factor in tapping mode atomic force microscope. *J Sound Vib* **491**, (2021).

43. Tamayo, J., Humphris, A. D. L., Owen, R. J. & Miles, M. J. High-Q dynamic force microscopy in liquid and its application to living cells. *Biophys J* **81**, 526–537 (2001).

44. Bruker. Introduction to Bruker's ScanAsyst and peak force tapping atomic force microscopy technology. *Bruker Company* 1 Preprint at (2009).

45. Alsteens, D. *et al.* High-resolution imaging of chemical and biological sites on living cells using peak force tapping atomic force microscopy. *Langmuir* **28**, 16738–16744 (2012).

46. Li, M., Xi, N. & Liu, L. Peak force tapping atomic force microscopy for advancing cell and molecular biology. *Nanoscale* **13**, 8358–8375 (2021).

47. Xu, K. *et al.* Recent development of PeakForce Tapping mode atomic force microscopy and its applications on nanoscience. *Nanotechnol Rev* **7**, 605–621 (2018).

48. Schillers, H., Medalsy, I., Hu, S., Slade, A. L. & Shaw, J. E. PeakForce tapping resolves individual microvilli on living cells. *Journal of Molecular Recognition* **29**, 95–101 (2016).

49. Voss, A., Dietz, C., Stocker, A. & Stark, R. W. Quantitative measurement of the mechanical properties of human antibodies with sub-10-nm resolution in a liquid environment. *Nano Res* **8**, 1987–1996 (2015).

50. Pyne, A., Thompson, R., Leung, C., Roy, D. & Hoogenboom, B. W. Single-molecule reconstruction of oligonucleotide secondary structure by atomic force microscopy. *Small* **10**, 3257–3261 (2014).

51. Fakhrullina, G., Akhatova, F., Kibardina, M., Fokin, D. & Fakhrullin, R. Nanoscale imaging and characterization of Caenorhabditis elegans epicuticle using atomic force microscopy. *Nanomedicine* **13**, 483–491 (2017).

52. Trtik, P., Kaufmann, J. & Volz, U. On the use of peak-force tapping atomic force microscopy for quantification of the local elastic modulus in hardened cement paste. *Cem Concr Res* **42**, 215–221 (2012).

53. Sadeghian, H. *et al.* Parallel, miniaturized scanning probe microscope for defect inspection and review. in *Metrology, Inspection, and Process Control for Microlithography XXVIII* vol. 9050 90501B (SPIE, 2014).

54. Sarov, Y. *et al.* Realization of cantilever arrays for parallel proximity imaging. in *Journal of Physics: Conference Series* vol. 253 (Institute of Physics Publishing, 2010).

55. Satoh, N. *et al.* Multi-probe atomic force microscopy using piezoelectric cantilevers. *Japanese Journal of Applied Physics, Part 1: Regular Papers and Short Notes and Review Papers* **46**, 5543–5547 (2007).

56. Tsunemi, E. *et al.* Multi-probe atomic force microscopy with optical beam deflection method. *Japanese Journal of Applied Physics, Part 1: Regular Papers and Short Notes and Review Papers* **46**, 5636–5638 (2007).

57. Cinar, E., Sahin, F. & Yablon, D. Development of a novel nanoindentation technique by utilizing a dual-probe AFM system. *Beilstein Journal of Nanotechnology* **6**, 2015–2027 (2015).

58. E. Cinar, and F. S. A new approach for nanoindentation using multiprobe AFM system. *IEEE International Conference on Nanotechnology* 1059 (2014).

59. Ando, T., Uchihashi, T. & Fukuma, T. High-speed atomic force microscopy for nano-visualization of dynamic biomolecular processes. *Prog Surf Sci* **83**, 337–437 (2008).

60. Adams, J. D. *et al.* Harnessing the damping properties of materials for high-speed atomic force microscopy. *Nat Nanotechnol* **11**, 147–151 (2016).

61. Ando, T. *et al.* A high-speed atomic force microscope for studying biological macromolecules. *Proceedings of the National Academy of Sciences* **98**, 12468–12472 (2001).

62. Schitter, G., Thurner, P. J. & Hansma, P. K. Design and input-shaping control of a novel scanner for high-speed atomic force microscopy. *Mechatronics* **18**, 282–288 (2008).

63. Ando, T., Uchihashi, T. & Kodera, N. High-speed AFM and applications to biomolecular systems. *Annu Rev Biophys* **42**, 393–414 (2013).

64. Payton, O. D., Picco, L. & Scott, T. B. High-speed atomic force microscopy for materials science. *International Materials Reviews* **61**, 473–494 (2016).

65. Uchihashi, T., Watanabe, H., Fukuda, S., Shibata, M. & Ando, T. Functional extension of high-speed AFM for wider biological applications. *Ultramicroscopy* vol. 160 182–196 Preprint at https://doi.org/10.1016/j.ultramic.2015.10.017 (2016).

66. Orji, N. G. & Dixson, R. G. 3D-AFM measurements for semiconductor structures and devices. *Metrology and Diagnostic Techniques for Nanoelectronics* **109**, (2017).

67. Dai, G. *et al.* Development of a 3D-AFM for true 3D measurements of nanostructures. *Meas Sci Technol* **22**, (2011).

68. Bruker. Innovation with integrity AFM probes. 28 Preprint at www.brukerAFMprobes.com (2013).

69. Infinitesima. *Metron 3D Brochure*. (2022).

70. Business Research Insights. AFM probe market size: forecast from 2024-2032. 1 (2024).

71. Xing, S., Zhou, J., Zhang, X., Elliott, S. & Sun, Z. Theory, properties and engineering of 2D magnetic materials. *Prog Mater Sci* **132**, (2023).

72. Deng, X. *et al.* Application of atomic force microscopy in cancer research. *J Nanobiotechnology* **16**, V (2018).

73. Efremov, Y. M. *et al.* Anisotropy vs isotropy in living cell indentation with AFM. *Sci Rep* **9**, (2019).

74. Yvanoff, C. & Willaert, R. G. Development of bone cell microarrays in microfluidic chips for studying osteocyte-osteoblast communication under fluid flow mechanical loading. *Biofabrication* **14**, (2022).

75. ITRS. *The International Semiconductor Technology Roadmap*. (2015).

76. Semiconductor Industry Association. *State of the U.S. Semiconductor Industry*. (2023).

77. Lee, M.-K. *et al.* Applications of AFM in semiconductor R&D and manufacturing at 45 nm technology node and beyond. in *Metrology, Inspection, and Process Control for Microlithography XXIII* vol. 7272 72722R (SPIE, 2009).

78. van der Heide, P. A. W. *et al.* Surface analysis in the semiconductor industry: present use and future possibilities. in *Surface and Interface Analysis* vol. 52 786–791 (John Wiley and Sons Ltd, 2020).

79. van Reijzen, M., Boerema, M., Kalinin, A., Sadeghian, H. & Bozdog, C. Recent advancements in atomic force microscopy. in *Metrology, Inspection, and Process Control for Semiconductor Manufacturing* 121 (SPIE-Intl Soc Optical Eng, 2021). doi:10.1117/12.2595426.

80. Foucher, J. *et al.* Paving the way for multiple applications for the 3D-AFM technique in the semiconductor industry. *Metrology, Inspection, and Process Control for Microlithography* 158–166 (2008) doi:10.1117/12.772675ï.

81. Murugesan, M., Ohara, Y., Fukushima, T., Tanaka, T. & Koyanagi, M. Low-resistance Cu-Sn electroplated-evaporated microbumps for 3D chip stacking. *J Electron Mater* **41**, 720–729 (2012).

82. Ma, Y. *et al.* The micro-fabrication and performance analysis of non-magnetic heating chip for miniaturized SERF atomic magnetometer. *J Magn Magn Mater* **557**, (2022).

83. Russell, P. & Krause, O. *AFM Probe Manufacturing*. *NanoWorld Innovative Technologies* (2008).

84. NanoWorld. NCL-NanoWorld. *NanoWorld Innovative Technologies* Preprint at (2024).

85. NanoWorld. PNP-DB-NanoWorld. *NanoWorld Innovative Technologies* Preprint at (2024).

86. Zaluzec, N. J. Microscopy society of America. *Microscopy and Microanalysis* **17**, 40–48 (2011).

87. FEI Company. Industry news. *Microscopy Today* vol. 25 50–51 Preprint at https://doi.org/10.1017/s1551929516001012 (2017).

88. Vasile, M. J., Grigg, D., Griffith, J. E., Fitzgerald, E. & Russell, P. E. Scanning probe tip geometry optimized for metrology by focused ion beam ion milling. *Journal of Vacuum Science & Technology B: Microelectronics and Nanometer Structures Processing, Measurement, and Phenomena* **9**, 3569–3572 (1991).

89. Rodriguez, D. J. *et al.* Fabrication of probe tips via the FIB method for nanodiagnostics of the surface of solids by atomic force microscopy. in *Journal of Physics: Conference Series* vol. 2086 (IOP Publishing Ltd, 2021).

90. Samaan, M. *et al.* Fabrication of high aspect ratio atomic force microscope probes using focused ion beam milled etch mask. *Microelectron Eng* **267–268**, (2023).

91. Tan, S. C., Zhao, H. & Thompson, C. V. Fabrication of high aspect ratio AFM probes with different materials inspired by TEM “lift-out” method. *Journal of Vacuum Science & Technology B, Nanotechnology and Microelectronics: Materials, Processing, Measurement, and Phenomena* **34**, (2016).

92. Fu, Y. Geometrical characterization issues of plasmonic nanostructures with depth-tuned grooves for beam shaping. *Optical Engineering* **45**, 108001 (2006).

93. Keller, D. J. & Chih-Chung, C. *Imaging Steep, High Structures by Scanning Force Microscopy with Electron Beam Deposited Tips*. *Surface Science* vol. 268 (1992).

94. Brown, J. *et al.* Electrically conducting, ultra-sharp, high aspect-ratio probes for AFM fabricated by electron-beam-induced deposition of platinum. *Ultramicroscopy* **133**, 62–66 (2013).

95. Nanda, G., van Veldhoven, E., Maas, D., Sadeghian, H. & Alkemade, P. F. A. Helium ion beam induced growth of hammerhead AFM probes. *Journal of Vacuum Science & Technology B, Nanotechnology and Microelectronics: Materials, Processing, Measurement, and Phenomena* **33**, (2015).

96. Lijima Sumio. Helical microtubules of graphitic carbon. *Nature* **354**, (1991).

97. Engstrom, D. S. *et al.* High throughput nanofabrication of silicon nanowire and carbon nanotube tips on AFM probes by stencil-deposited catalysts. *Nano Lett* **11**, 1568–1574 (2011).

98. Yazdanpanah, M. M. *et al.* Micro-wilhelmy and related liquid property measurements using constant-diameter nanoneedle-tipped atomic force microscope probes. *Langmuir* **24**, 13753–13764 (2008).

99. Yazdanpanah, M. M. Starting from scratch. *Phys. World* **25**, 60 (2012).

100. B. E. Deal, M. S. A. S. G. and E. H. S. Characteristics of the surface-state charge (Qss) of thermally oxidized silicon. *J. Electrochem. Soc.* **114**, (1967).

101. Han, X. L., Larrieu, G. & Krzeminski, C. Modelling and engineering of stress based controlled oxidation effects for silicon nanostructure patterning. *Nanotechnology* **24**, (2013).

102. Dey, R. K., Shen, J. & Cui, B. Oxidation sharpening of silicon tips in the atmospheric environment. *Journal of Vacuum Science & Technology B, Nanotechnology and Microelectronics: Materials, Processing, Measurement, and Phenomena* **35**, (2017).

103. Hong, C. Y. & Akinwande, A. I. Oxidation sharpening mechanism for silicon tip formation. *Electrochemical and Solid-State Letters* **8**, (2005).

104. ThermoFisher Scientific. *PMMA SDS*. (2024).

105. Zeon Chemicals L. P. *ZEP520A SDS*. (2024).

106. Holloway, G. *Raith Electron Beam Lithography*. https://fab.qnc.uwaterloo.ca/equip/ebl-30kv/authorized-materials (2024).

107. Kayaku Advanced Materials. *LOR and PMGI SDS*. (2024).

108. Karouta, F. A practical approach to reactive ion etching. *J Phys D Appl Phys* **47**, (2014).

109. Donnelly, V. M. & Kornblit, A. Plasma etching: Yesterday, today, and tomorrow. *Journal of Vacuum Science & Technology A: Vacuum, Surfaces, and Films* **31**, (2013).

110. Jansen, H., Gardeniers, H., De Boer, M., Elwenspoek, M. & Fluitman, J. A survey on the reactive ion etching of silicon in microtechnology. *J. Micromech. Microeng* **6**, 14–28 (1996).

111. Goodyear, A. L., Mackenzie, S., Olynick, D. L. & Anderson, E. H. High resolution inductively coupled plasma etching of 30 nm lines and spaces in tungsten and silicon. *Journal of Vacuum Science & Technology B: Microelectronics and Nanometer Structures Processing, Measurement, and Phenomena* **18**, 3471–3475 (2000).

112. Laermer, F. & Urban, A. Milestones in deep reactive ion etching. *Actuators and Microsystems* **2**, 1118–1121 (2005).

113. Ayón, A. A., Bayt, R. L. & Breuer, K. S. Deep reactive ion etching: a promising technology for micro-and nanosatellites. *Smart Mater. Struct.* **10**, 1135 (2001).

114. Fu, Y. Q. *et al.* Deep reactive ion etching as a tool for nanostructure fabrication. *Journal of Vacuum Science & Technology B: Microelectronics and Nanometer Structures Processing, Measurement, and Phenomena* **27**, 1520–1526 (2009).

115. Laermer, F. & Urban, A. Challenges, developments and applications of silicon deep reactive ion etching. in *Microelectronic Engineering* vols 67–68 349–355 (2003).

116. Pan, A., Samaan, M., Yan, Z., Hu, W. & Cui, B. Fabrication of ultrahigh aspect ratio Si nanopillar and nanocone arrays. *Journal of Vacuum Science & Technology B* **41**, (2023).

117. Aydinoglu, F., Pan, A., Zhu, C. & Cui, B. Effect of oxygen plasma cleaning on nonswitching pseudo-Bosch etching of high aspect ratio silicon pillars. *Journal of Vacuum Science & Technology B, Nanotechnology and Microelectronics: Materials, Processing, Measurement, and Phenomena* **38**, (2020).

118. Saffih, F., Con, C., Alshammari, A., Yavuz, M. & Cui, B. Fabrication of silicon nanostructures with large taper angle by reactive ion etching. *Journal of Vacuum Science & Technology B, Nanotechnology and Microelectronics: Materials, Processing, Measurement, and Phenomena* **32**, (2014).

119. Ayari-Kanoun, A., Aydinoglu, F., Cui, B. & Saffih, F. Silicon nanostructures with very large negatively tapered profile by inductively coupled plasma-RIE. *Journal of Vacuum Science & Technology B, Nanotechnology and Microelectronics: Materials, Processing, Measurement, and Phenomena* **34**, (2016).

120. Refino, A. D. *et al.* Versatilely tuned vertical silicon nanowire arrays by cryogenic reactive ion etching as a lithium-ion battery anode. *Sci Rep* **11**, (2021).

121. Zhu, X., Pan, A., Shokouhi, B. & Cui, B. Cryogenic etching of positively tapered silicon pillars with controllable profiles. *Journal of Vacuum Science & Technology B* **42**, (2024).

122. Pan, A. *et al.* Fabrication of the highly ordered silicon nanocone array with sub-5 nm tip apex by tapered silicon oxide mask. *IEEE Transactions on Semiconductor Manufacturing* (2024).

123. Kang, R., Pan, A. & Cui, B. Fabrication of silicon sharp nanocones using dry etch with periodic oxygen plasma shrinking and wet etch. *Journal of Vacuum Science & Technology B* **42**, (2024).

124. Song, Y. *et al.* Ultra-High Aspect Ratio InP Junctionless FinFETs by a Novel Wet Etching Method. *IEEE Electron Device Letters* **37**, 970–973 (2016).

125. Hashem, I. E., Zachary Carlin, C., Hagar, B. G., Colter, P. C. & Bedair, S. M. InGaP-based quantum well solar cells: Growth, structural design, and photovoltaic properties. *J Appl Phys* **119**, (2016).

126. Sharma, A. *et al.* Large area, patterned growth of 2D MoS2 and lateral MoS2-WS2 heterostructures for nano-and opto-electronic applications. *Nanotechnology* **31**, (2020).

127. Teng, Q., Wang, K., Zhang, L. & He, J. The Layer-Wise Training Convolutional Neural Networks Using Local Loss for Sensor-Based Human Activity Recognition. *IEEE Sens J* **20**, 7265–7274 (2020).

128. Han, S. W., Nakamura, C., Obataya, I., Nakamura, N. & Miyake, J. A molecular delivery system by using AFM and nanoneedle. in *Biosensors and Bioelectronics* vol. 20 2120–2125 (Elsevier Ltd, 2005).

129. Obataya, I., Nakamura, C., Han, S., Nakamura, N. & Miyake, J. Nanoscale operation of a living cell using an atomic force microscope with a nanoneedle. *Nano Lett* **5**, 27–30 (2005).

130. Matsumoto, D. *et al.* Oscillating high-aspect-ratio monolithic silicon nanoneedle array enables efficient delivery of functional bio-macromolecules into living cells. *Sci Rep* **5**, (2015).

131. Lombardo, D., Kiselev, M. A. & Caccamo, M. T. Smart Nanoparticles for Drug Delivery Application: Development of Versatile Nanocarrier Platforms in Biotechnology and Nanomedicine. *J Nanomater* **2019**, (2019).

132. Bhavana, V., Thakor, P., Singh, S. B. & Mehra, N. K. COVID-19: Pathophysiology, treatment options, nanotechnology approaches, and research agenda to combating the SARS-CoV2 pandemic. *Life Sciences* vol. 261 Preprint at https://doi.org/10.1016/j.lfs.2020.118336 (2020).

133. He, G. *et al.* Hollow Nanoneedle-Electroporation System to Extract Intracellular Protein Repetitively and Nondestructively. *ACS Sens* **3**, 1675–1682 (2018).

134. Wagner, R. S. & Ellis, W. C. Vapor-liquid-solid mechanism of single crystal growth. *Appl Phys Lett* **4**, 89–90 (1964).

135. Li, M. *et al.* Metal-assisted chemical etching for designable monocrystalline silicon nanostructure. *Materials Research Bulletin* vol. 76 436–449 Preprint at https://doi.org/10.1016/j.materresbull.2016.01.006 (2016).

136. Li, K. *et al.* Fabrication of hard x-ray zone plates with high aspect ratio using metal-assisted chemical etching. *Journal of Vacuum Science & Technology B, Nanotechnology and Microelectronics: Materials, Processing, Measurement, and Phenomena* **35**, (2017).

137. Wu, B., Kumar, A. & Pamarthy, S. High aspect ratio silicon etch: A review. *Journal of Applied Physics* vol. 108 Preprint at https://doi.org/10.1063/1.3474652 (2010).

138. Morton, K. J., Nieberg, G., Bai, S. & Chou, S. Y. Wafer-scale patterning of sub-40 nm diameter and high aspect ratio (>50:1) silicon pillar arrays by nanoimprint and etching. *Nanotechnology* **19**, (2008).

139. Mukherjee, P., Kang, M.-G., Zurbuchen, T. H., Guo, L. J. & Herrero, F. A. Fabrication of high aspect ratio Si nanogratings with smooth sidewalls for a deep UV-blocking particle filter. *Journal of Vacuum Science & Technology B: Microelectronics and Nanometer Structures Processing, Measurement, and Phenomena* **25**, 2645–2648 (2007).

140. Con, C., Zhang, J. & Cui, B. Nanofabrication of high aspect ratio structures using an evaporated resist containing metal. *Nanotechnology* **25**, (2014).

141. Schwartz, B. & Robbins, H. Chemical Etching of Silicon IV. Etching Technology. *J. Electrochem. Soc.* **123**, 1903 (1976).

142. Marcus, R. B. & Sheng, T. T. The Oxidation of Shaped Silicon Surfaces. *J. Electrochem. Soc.* **129**, 1278 (1982).

143. Wang, B., Dong, X., Wang, Z., Wang, Y. & Hou, Z. The Humidity-Induced Sensitivity Amplification Effect in an Ionization Gas Sensor with Silicon Nanostructures. *IEEE Electron Device Letters* **41**, 908–911 (2020).

144. Midahuen, R. *et al.* Wafer-scale fabrication of biologically sensitive Si nanowire FET: From pH sensing to electrical detection of DNA hybridization. in *European Solid-State Device Research Conference* vols 2021-September 175–178 (Editions Frontieres, 2021).

145. Del Alamo, J. A. Nanometre-scale electronics with III-V compound semiconductors. *Nature* vol. 479 317–323 Preprint at https://doi.org/10.1038/nature10677 (2011).

146. Luo, R. *et al.* Fabrication and Characterization of a Low Parasitic Capacitance and Low-Stress Si Interposer for 2.5-D Integration. *IEEE Transactions on Semiconductor Manufacturing* **31**, 521–527 (2018).

147. Miwa, K., Inokuchi, T., Takahashi, T., Oikawa, A. & Imaoka, K. Reduction of depth variation in an Si etching process by applying an optimized run-to-run control system. in *IEEE Transactions on Semiconductor Manufacturing* vol. 18 517–521 (2005).

148. Glagolev, P. Y., Demin, G. D., Djuzhev, N. A., Evsikov, I. D. & Filippov, N. A. Analysis of the Field Emission Current from an Array of Silicon Field Nanoemitters for Portable X-Ray Systems. in *2021 34th International Vacuum Nanoelectronics Conference, IVNC 2021* (Institute of Electrical and Electronics Engineers Inc., 2021). doi:10.1109/IVNC52431.2021.9600758.

149. Hsu, C. M. *et al.* High-efficiency amorphous silicon solar cell on a periodic nanocone back reflector. *Adv Energy Mater* **2**, 628–633 (2012).

150. Jeong, S., McGehee, M. D. & Cui, Y. All-back-contact ultra-thin silicon nanocone solar cells with 13.7% power conversion efficiency. *Nat Commun* **4**, (2013).

151. Liu, W. *et al.* Flexible solar cells based on foldable silicon wafers with blunted edges. *Nature* **617**, 717–723 (2023).

152. Magdi, S., El-Rifai, J. & Swillam, M. A. One step fabrication of Silicon nanocones with wide-angle enhanced light absorption. *Sci Rep* **8**, (2018).

153. Park, W. *et al. Biodegradable Silicon Nanoneedles for Ocular Drug Delivery*. *Sci. Adv* vol. 8 https://www.science.org (2022).

154. Elnathan, R. *et al.* Biointerface design for vertical nanoprobes. *Nature Reviews Materials* vol. 7 953–973 Preprint at https://doi.org/10.1038/s41578-022-00464-7 (2022).

155. Jiang, R. *et al.* A Miniaturized Single-Wall Carbon Nanotubes Field Emission Cathode with RF Excited by Coaxial Resonant Cavity. *IEEE Trans Electron Devices* **68**, 4681–4686 (2021).

156. Lee, J. *et al.* High-performance field emission from a carbon nanotube carpet. *Carbon N Y* **50**, 3889–3896 (2012).

157. Bocharov, G. S. & Eletskii, A. V. Theory of carbon nanotube (Cnt)-based electron field emitters. *Nanomaterials* vol. 3 393–442 Preprint at https://doi.org/10.3390/nano3030393 (2013).

158. Cheng, Y. & Zhou, O. Electron field emission from carbon nanotubes. *Comptes Rendus Physique* vol. 4 1021–1033 Preprint at https://doi.org/10.1016/S1631-0705(03)00103-8 (2003).

159. Basu, A., Swanwick, M. E., Fomani, A. A. & Velásquez-García, L. F. A portable x-ray source with a nanostructured Pt-coated silicon field emission cathode for absorption imaging of low-Z materials. *J Phys D Appl Phys* **48**, (2015).

160. Owen K J, V. B. P. R. L. High aspect ratio deep silicon etching. *IEEE 25th International Conference on Micro Electro Mechanical Systems* 251–254 (2012).

161. Sistani, M., Staudinger, P. & Lugstein, A. Polarity Control in Ge Nanowires by Electronic Surface Doping. *Journal of Physical Chemistry C* **124**, 19858–19863 (2020).

162. Balaghi, L. *et al.* High electron mobility in strained GaAs nanowires. *Nat Commun* **12**, (2021).

163. Huang, Q. & Zhu, Y. Patterning of Metal Nanowire Networks: Methods and Applications. *ACS Applied Materials and Interfaces* vol. 13 60736–60762 Preprint at https://doi.org/10.1021/acsami.1c14816 (2021).

164. Chang, S., Lee, G. J. & Song, Y. M. Recent advances in vertically aligned nanowires for photonics applications. *Micromachines* vol. 11 Preprint at https://doi.org/10.3390/MI11080726 (2020).

165. Walavalkar, S. S., Homyk, A. P., Henry, M. D. & Scherer, A. Three-dimensional etching of silicon for the fabrication of low-dimensional and suspended devices. *Nanoscale* **5**, 927–931 (2013).

166. Cui, Z. *Nanofabrication: Principles, Capabilities and Limits*. *Nanofabrication: Principles, Capabilities and Limits* (Springer US, 2009). doi:10.1007/978-0-387-75577-9.

167. Kumar, A., Lee, W. H. & Wang, Y. L. Optimizing the Isotropic Etching Nature and Etch Profile of Si, Ge and Si0.8Ge0.2by Controlling CF4Atmosphere with Ar and O2Additives in ICP. *IEEE Transactions on Semiconductor Manufacturing* **34**, 177–184 (2021).

168. Limanond, S., Si, J. & Tseng, Y.-L. *Production Data Based Optimal Etch Time Control Design for a Reactive Ion Etching Process*. *IEEE TRANSACTIONS ON SEMICONDUCTOR MANUFACTURING* vol. 12 (1999).

169. Parasuraman, J. *et al.* Deep reactive ion etching of sub-micrometer trenches with ultra high aspect ratio. *Microelectron Eng* **113**, 35–39 (2014).

170. Jonker, D. *et al.* Large Dense Periodic Arrays of Vertically Aligned Sharp Silicon Nanocones. *Nanoscale Res Lett* **17**, (2022).

171. Hung, Y. J., Lee, S. L., Thibeault, B. J. & Coldren, L. A. Fabrication of highly ordered silicon nanowire arrays with controllable sidewall profiles for achieving low-surface reflection. *IEEE Journal on Selected Topics in Quantum Electronics* **17**, 869–877 (2011).

172. Refino, A. D. *et al.* Versatilely tuned vertical silicon nanowire arrays by cryogenic reactive ion etching as a lithium-ion battery anode. *Sci Rep* **11**, (2021).

173. Hsu, C. M., Connor, S. T., Tang, M. X. & Cui, Y. Wafer-scale silicon nanopillars and nanocones by Langmuir-Blodgett assembly and etching. *Appl Phys Lett* **93**, (2008).

174. Wang, Q. *et al.* Field emission properties of carbon coated Si nanocone arrays on porous silicon. *Nanotechnology* **16**, 2919–2922 (2005).

175. Pisco, M. *et al.* Nanosphere lithography for optical fiber tip nanoprobes. *Light Sci Appl* **6**, (2017).

176. Colson, P., Henrist, C. & Cloots, R. Nanosphere lithography: A powerful method for the controlled manufacturing of nanomaterials. *Journal of Nanomaterials* vol. 2013 Preprint at https://doi.org/10.1155/2013/948510 (2013).

177. Obataya, I., Nakamura, C., Han, S. W., Nakamura, N. & Miyake, J. Mechanical sensing of the penetration of various nanoneedles into a living cell using atomic force microscopy. in *Biosensors and Bioelectronics* vol. 20 1652–1655 (Elsevier Ltd, 2005).

178. Penedo, M. *et al.* Cell penetration efficiency analysis of different atomic force microscopy nanoneedles into living cells. *Sci Rep* **11**, (2021).

179. Rangelow, I. W. Sharp silicon tips for AFM and field emission. *Microelectron Eng* **23**, 369–372 (1994).

180. Bagur Rudrappa, D. *et al.* A Simple Method for Fabrication of Self-sharpened Silicon Tips for Atomic Force Microscopy Applications. *Crystal Research and Technology* **57**, (2022).

181. Chen, Z., Luo, J., Doudevski, I., Erten, S. & Kim, S. H. Atomic Force Microscopy (AFM) Analysis of an Object Larger and Sharper than the AFM Tip. *Microscopy and Microanalysis* **25**, 1106–1111 (2019).

182. Nguyen, Q. D. & Chung, K. H. Effect of tip shape on nanomechanical properties measurements using AFM. *Ultramicroscopy* **202**, 1–9 (2019).

183. Fan, Z. *et al.* Challenges and prospects of nanopillar-based solar cells. *Nano Research* vol. 2 829–843 Preprint at https://doi.org/10.1007/s12274-009-9091-y (2009).

184. Chen, W. T., Zhu, A. Y. & Capasso, F. Flat optics with dispersion-engineered metasurfaces. *Nature Reviews Materials* vol. 5 604–620 Preprint at https://doi.org/10.1038/s41578-020-0203-3 (2020).

185. Choudhury, B. D. *et al.* Silicon nanopillar arrays with SiO2 overlayer for biosensing application. *Opt Mater Express* **4**, 1345 (2014).

186. Capozza, R. *et al.* Cell Membrane Disruption by Vertical Micro-/Nanopillars: Role of Membrane Bending and Traction Forces. *ACS Appl Mater Interfaces* **10**, 29107–29114 (2018).

187. Velásquez-García, L. F. & Akinwande, A. I. Fabrication of large arrays of high-aspect-ratio single-crystal silicon columns with isolated vertically aligned multi-walled carbon nanotube tips. *Nanotechnology* **19**, (2008).

188. Laermer, F. & Urban, A. MEMS at Bosch – Si plasma etch success story, history, applications, and products. *Plasma Processes and Polymers* vol. 16 Preprint at https://doi.org/10.1002/ppap.201800207 (2019).

189. Ouyang, Z., Ruzic, D. N., Kiehlbauch, M., Schrinsky, A. & Torek, K. Etching mechanism of the single-step through-silicon-via dry etch using SF6/C4F8 chemistry. *Journal of Vacuum Science & Technology A: Vacuum, Surfaces, and Films* **32**, (2014).

190. Tachi, S., Tsujimoto, K. & Okudaira, S. Low-temperature reactive ion etching and microwave plasma etching of silicon. *Appl Phys Lett* **52**, 616–618 (1988).

191. Dussart, R., Tillocher, T., Lefaucheux, P. & Boufnichel, M. Plasma cryogenic etching of silicon: From the early days to today's advanced technologies. *Journal of Physics D: Applied Physics* vol. 47 Preprint at https://doi.org/10.1088/0022-3727/47/12/123001 (2014).

192. Pruessner, M. W., Rabinovich, W. S., Stievater, T. H., Park, D. & Baldwin, J. W. Cryogenic etch process development for profile control of high aspect-ratio submicron silicon trenches. *Journal of Vacuum Science & Technology B: Microelectronics and Nanometer Structures Processing, Measurement, and Phenomena* **25**, 21–28 (2007).

193. Miao, H., Chen, L., Mirzaeimoghri, M., Kasica, R. & Wen, H. Cryogenic Etching of High Aspect Ratio 400-nm Pitch Silicon Gratings. *Journal of Microelectromechanical Systems* **25**, 963–967 (2016).

194. Jansen, H., De Boer, M., Wensink, H., Kloeck, B. & Elwenspoek, M. The black silicon method. VIII. A study of the performance of etching silicon using SF6/O2-based chemistry with cryogenical wafer cooling and a high density ICP source. *Microelectronics J* **32**, 769–777 (2001).

195. Jansen, H. V., De Boer, M. J., Unnikrishnan, S., Louwerse, M. C. & Elwenspoek, M. C. Black silicon method X: A review on high speed and selective plasma etching of silicon with profile control: An in-depth comparison between Bosch and cryostat DRIE processes as a roadmap to next generation equipment. *Journal of Micromechanics and Microengineering* **19**, (2009).

196. Blauw, M. A., Zijlstra, T., Bakker, R. A. & van der Drift, E. Kinetics and crystal orientation dependence in high aspect ratio silicon dry etching. *Journal of Vacuum Science &*

Technology B: Microelectronics and Nanometer Structures Processing, Measurement, and Phenomena **18**, 3453–3461 (2000).

197. Wells, T., El-Gomati, M. M., Wood, J. & Johnson, S. Low temperature reactive ion etching of silicon with SF6/O2 plasmas. in *Proceedings of the IEEE International Vacuum Microelectronics Conference, IVMC* 349–353 (IEEE, 1996). doi:10.1116/1.589333.

198. Zhang, M., Li, J. Z., Adesida, I. & Wolf, E. D. Reactive ion etching for submicron structures of refractory metal silicides and polycides. in *Journal of Vacuum Science and Technology B: Microelectronics and Nanometer Structures* vol. 1 1037–1042 (1983).

199. Nguyen, V. T. H. *et al.* Ultrahigh aspect ratio etching of silicon in SF6-O2 plasma: The clear-oxidize-remove-etch (CORE) sequence and chromium mask. *Journal of Vacuum Science & Technology A: Vacuum, Surfaces, and Films* **38**, (2020).

200. Aachboun, S. & Ranson, P. Deep anisotropic etching of silicon. *Journal of Vacuum Science & Technology A: Vacuum, Surfaces, and Films* **17**, 2270–2273 (1999).

201. Weidenfeller, L. *et al.* Cryogenic etching for pattern transfer into silicon of Mix-and-Match structured resist layers. *Microelectron Eng* **227**, (2020).

202. Dussart, R. *et al.* Passivation mechanisms in cryogenic SF6/O2 etching process. *Journal of Micromechanics and Microengineering* **14**, 190–196 (2004).

203. Bartha, J. W., Greschner, J., Puech, M. & Maquin, P. *Low Temperature Etching of Si in High Density Plasma Using SF6/O2*. *Microelectronic Engineering* vol. 27 (1995).

204. Oehrlein, G. S. & Kurogi, Y. Sidewall surface chemistry in directional etching processes. *Materials Science and Engineering* **24**, 153–183 (1998).

205. Zarowi, C. B. & Horwath, R. S. *Control of Plasma Etch Profiles with Plasma Sheath Electric Field and RF Power Density*. *The Electrochemical Society Softbound Proceedings Series* vol. 129 (1973).

206. Ishchuk, V., Olynick, D. L., Liu, Z. & Rangelow, I. W. Profile simulation model for sub-50 nm cryogenic etching of silicon using SF6/O2 inductively coupled plasma. *J Appl Phys* **118**, (2015).

207. Henry, M. D., Welch, C. & Scherer, A. Techniques of cryogenic reactive ion etching in silicon for fabrication of sensors. *Journal of Vacuum Science & Technology A: Vacuum, Surfaces, and Films* **27**, 1211–1216 (2009).

208. Zhang, Y. *et al.* Control of ion energy and angular distributions in dual-frequency capacitively coupled plasmas through power ratios and phase: Consequences on etch profiles. *Journal of Vacuum Science & Technology A: Vacuum, Surfaces, and Films* **33**, (2015).

209. Pereira, J. *et al.* In situ x-ray photoelectron spectroscopy analysis of SiOxFy passivation layer obtained in a SF6/ O2 cryoetching process. *Appl Phys Lett* **94**, (2009).

210. Pei, Z. *et al.* An amorphous silicon random nanocone/polymer hybrid solar cell. *Solar Energy Materials and Solar Cells* **95**, 2431–2436 (2011).

211. Le Shim, E. *et al.* Facile fabrication of scalable patterned nickel nanocone arrays for field emission applications. *Journal of Vacuum Science & Technology B, Nanotechnology and Microelectronics: Materials, Processing, Measurement, and Phenomena* **31**, (2013).

212. Stelzner, T. *et al.* Silicon nanowire-based solar cells. *Nanotechnology* **19**, (2008).

213. Kihara, T. *et al.* Development of a method to evaluate caspase-3 activity in a single cell using a nanoneedle and a fluorescent probe. *Biosens Bioelectron* **25**, 22–27 (2009).

214. Gao, W., Aoki, J., Ju, B. F. & Kiyono, S. Surface profile measurement of a sinusoidal grid using an atomic force microscope on a diamond turning machine. *Precis Eng* **31**, 304–309 (2007).

215. Takahashi, H., Ando, K. & Shirakawabe, Y. *Self-Sensing Piezoresistive Cantilever and Its Magnetic Force Microscopy Applications*. *Ultramicroscopy* vol. 91 (2002).

216. Zhu, F. Y., Zhang, X. S. & Zhang, H. X. Formation mechanism of multi-functional black silicon based on optimized deep reactive ion etching technique with SF6/C4F8. *Sci China Technol Sci* **58**, 381–389 (2015).

217. Xue, S., Wu, S., Qiu, Y. & Lu, M. Stable field emission ofion-sputtering-induced Si nanocone arrays. *Chinese Optics Letters* **11**, 111601 (2013).

218. Bai, F. *et al.* Template-free fabrication of silicon micropillar/ nanowire composite structure by one-step etching. *Nanoscale Res Lett* **7**, 1–5 (2012).

219. Goryu, A., Ikedo, A., Ishida, M. & Kawano, T. Nanoscale sharpening tips of vapor-liquid-solid grown silicon microwire arrays. *Nanotechnology* **21**, (2010).

220. Wang, Y., Bauer, J., Senz, S., Breitenstein, O. & Gösele, U. Aluminum-enhanced sharpening of silicon nanocones. *Appl Phys A Mater Sci Process* **99**, 705–709 (2010).

221. Seo, H. S. *et al.* Fabrication of precisely controlled silicon wire and cone arrays by electrochemical etching. *Mater Lett* **63**, 2567–2569 (2009).

222. Zubel, I. & Kramkowska, M. Etch rates and morphology of silicon (h k l) surfaces etched in KOH and KOH saturated with isopropanol solutions. in *Sensors and Actuators, A: Physical* vol. 115 549–556 (2004).

223. Kobeda, E. & Irene, E. A. SiO2 film stress distribution during thermal oxidation of Si. *Journal of Vacuum Science & Technology B: Microelectronics Processing and Phenomena* **6**, 574–578 (1988).

224. Karttunen, J., Kiihamäki, J. & Franssila, S. Loading effects in deep silicon etching. *Micromachining and microfabrication process technology VI. SPIE* **4174**, 90–97 (2000).

225. Mogab C J. The loading effect in plasma etching. *J Electrochem Soc* **124**, 1262 (1977).

226. Stoltz, A. J. *et al.* Macro-loading effects of electron-cyclotron resonance etched II-VI materials. *J Electron Mater* **33**, (2004).

227. Hedlund, C., Blom, H.-O. & Berg, S. Microloading effect in reactive ion etching. *Journal of Vacuum Science & Technology A: Vacuum, Surfaces, and Films* **12**, 1962–1965 (1994).

228. Gerlt, M. S., Läubli, N. F., Manser, M., Nelson, B. J. & Dual, J. Reduced etch lag and high aspect ratios by deep reactive ion etching (DRIE). *Micromachines (Basel)* **12**, (2021).

229. Chou TKA, N. K. Fabrication of out-of-plane curved surfaces in Si by utilizing RIE lag. *MEMS 2002 IEEE International Conference. Fifteenth IEEE International Conference on Micro Electro Mechanical Systems* 145–148 (2002).

230. Ohara, J., Asami, K., Takeuchi, Y. & Sato, K. Development of RIE-lag reduction technique for Si deep etching using double protection layer method. *IEEJ Transactions on Electrical and Electronic Engineering* **5**, 125–130 (2010).

231. Cunha, J. *et al.* Assessing tolerances in direct write laser grayscale lithography and reactive ion etching pattern transfer for fabrication of 2.5D Si master molds. *Micro and Nano Engineering* **19**, (2023).

232. Garcia, I. S. *et al.* Fabrication of a MEMS Micromirror Based on Bulk Silicon Micromachining Combined with Grayscale Lithography. *Journal of Microelectromechanical Systems* **29**, 734–740 (2020).

233. Phi, H. B., Bohm, S., Runge, E., Dittrich, L. & Strehle, S. 3D passive microfluidic valves in silicon and glass using grayscale lithography and reactive ion etching transfer. *Microfluid Nanofluidics* **27**, (2023).

234. Ge, C. & Cretu, E. Design and fabrication of SU-8 CMUT arrays through grayscale lithography. *Sens Actuators A Phys* **280**, 368–375 (2018).

235. Grushina, A. Direct-write grayscale lithography. *Advanced Optical Technologies* **8**, 163–169 (2019).

236. Mckenna, C., Walsh, K., Crain, M. & Lake, J. Maskless direct write grayscale lithography for MEMS applications. *18th Biennial University/Government/Industry Micro/Nano Symposium* 1–4 (2010).

237. Tseng, J. K., Chen, Y. J., Pan, C. T., Wu, T. T. & Chung, M. H. Application of optical film with micro-lens array on a solar concentrator. *Solar Energy* **85**, 2167–2178 (2011).

238. O'neill, F. T. & Sheridan, J. T. Photoresist reflow method of microlens production Part I: Background and experiments. *Optik (Stuttg)* **113**, 391–404 (2002).

239. Daschnen W, Long, P., Stein, R., Wu, C. & Lee, S. H. Cost-effective mass fabrication of multilevel diffractive optical elements by use of a single optical exposure with a gray-scale mask on high-energy beam-sensitive glass. *Appl Opt* **36**, 4675–4680 (1997).

240. Martinez, P., Dorrer, C. & Kasper, M. Simulation and process design of gray-tone lithography for the fabrication of arbitrarily shaped surfaces. *Jpn J Appl Phys* **33**, 6809 (1994).

241. Su, J. *et al.* New method to design halftone mask for the fabrication of continuous microrelief structure. *Design, Test, and Microfabrication of MEMS and MOEMS* **3680**, 879–886 (1999).

242. Zhang, J. *et al.* Micro-optical elements fabricated by metal-transparent-metallic-oxides grayscale photomasks. *Appl Opt* **51**, 6606–6611 (2012).

243. Cui, Z., Du, J. & Guo, Y. Overview of grey-scale photolithography for micro-optical elements fabrication. *Micromachining technology for micro-optics and nano-optics* **4984**, 111–117 (2003).

244. Suntific Company. SUN-9i(500cp). (2024).

245. Sader, J. E. & Sader, R. C. Susceptibility of atomic force microscope cantilevers to lateral forces: Experimental verification. *Appl Phys Lett* **83**, 3195–3197 (2003).

246. Borodich, F. M., Al-Musawi, R. S., Brousseau, E. B. & Evans, S. L. Comparison between torsional spring constants of rectangular and V-Shaped AFM cantilevers. *IEEE Trans Nanotechnol* **20**, 168–176 (2021).

247. Sader, J. E., Larson, I., Mulvaney, P. & White, L. R. Method for the calibration of atomic force microscope cantilevers. *Review of scientific instruments* **66**, 3789–3798 (1995).

248. Sader, J. E., Chon, J. W. M. & Mulvaney, P. Calibration of rectangular atomic force microscope cantilevers. *Review of scientific instruments* **70**, 3967–3969 (1999).

249. AZoNetwork. *Aist-NT Smart SPM 1000*. https://www.azonano.com/equipment-details.aspx?EquipID=169 (2024).

250. AZ Electronic Materials. *AZ 3300 Series Crossover Photoresists*. (2024).

251. Kitazawa, M., Shiotani, K. & Toda, A. Batch fabrication of sharpened silicon nitride tips. *Japanese Journal of Applied Physics, Part 1: Regular Papers and Short Notes and Review Papers* **42**, 4844–4847 (2003).

Appendix: Supplementary Information for Chapter 3.2

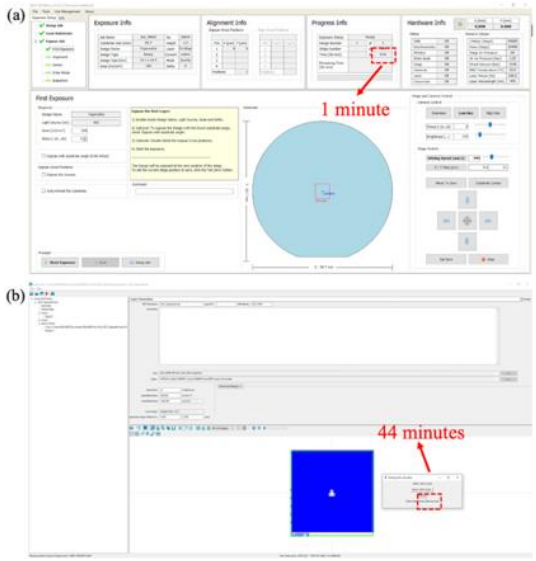


Fig. SI-1. (a) The simulation result of 1cm × 1 cm pattern design on the direct write UV lithography system (MLA150, Heidelberg Instruments) with a 405 nm light source and 100 mJ/cm^2, and the exposure time is 1 minute (b) The simulation result of 1 cm × 1 cm pattern design on BEAMER for the JEOL JBX-6300FS EBL system with 200 μC/cm^2, and the exposure time is 44 minutes.

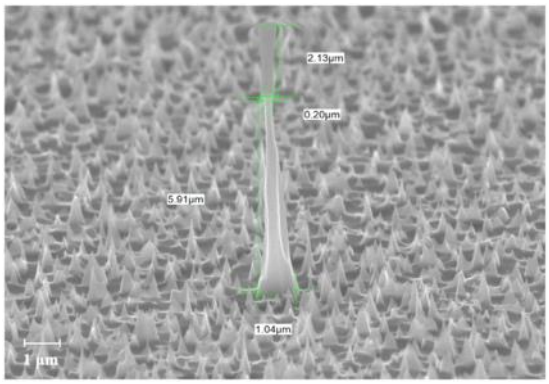


Fig. SI-2. The black silicon on the sample surface when the ratio of C_4F_8 and SF_6 was adjusted to 45:15. The experiment with a p-type (boron dopant, 0.01 Ω·cm) prime Si wafer with <100> surface orientation. After the identical cleaning process in the manuscript, a layer of 3 μm photoresist nLof 2035 was spin-coated on the wafer. Standard mask-less photolithography using a direct write UV lithography system (MLA150, Heidelberg Instruments) was utilized with a 375 nm light source and 200 mJ/cm^2 to write identical dots with 1 μm dot diameter. After development, the etching recipe is the non-switching pseudo-Bosch process with a 15/45 gas flow ratio of SF_6 over C_4F_8, 1200 W ICP power, 20 W RF power, 10 mTorr for 30 minutes by using the Oxford PlasmaLab 100 ICP 380 DRIE Si etcher system. The formation of black silicon was observed, as shown in Fig. SI-2, when a C_4F_8 gas flow larger than 45 sccm was applied.

Table SI-1. The dimensions of 9 Si nanocones in the Si array with 1.1 μm design after 10 min etching using Recipe 1 as shown in Fig. 4 (a). Note: The radius is 63 ± 3.12 nm, and the height is 4.03 ± 0.04 μm.

Si nanocone #	1	2	3	4	5	6	7	8	9

Radius (nm)	60	68	65	62	64	60	67	61	60
Height (μm)	4.02	4.08	4.00	4.01	4.00	4.10	4.01	4.05	4.00

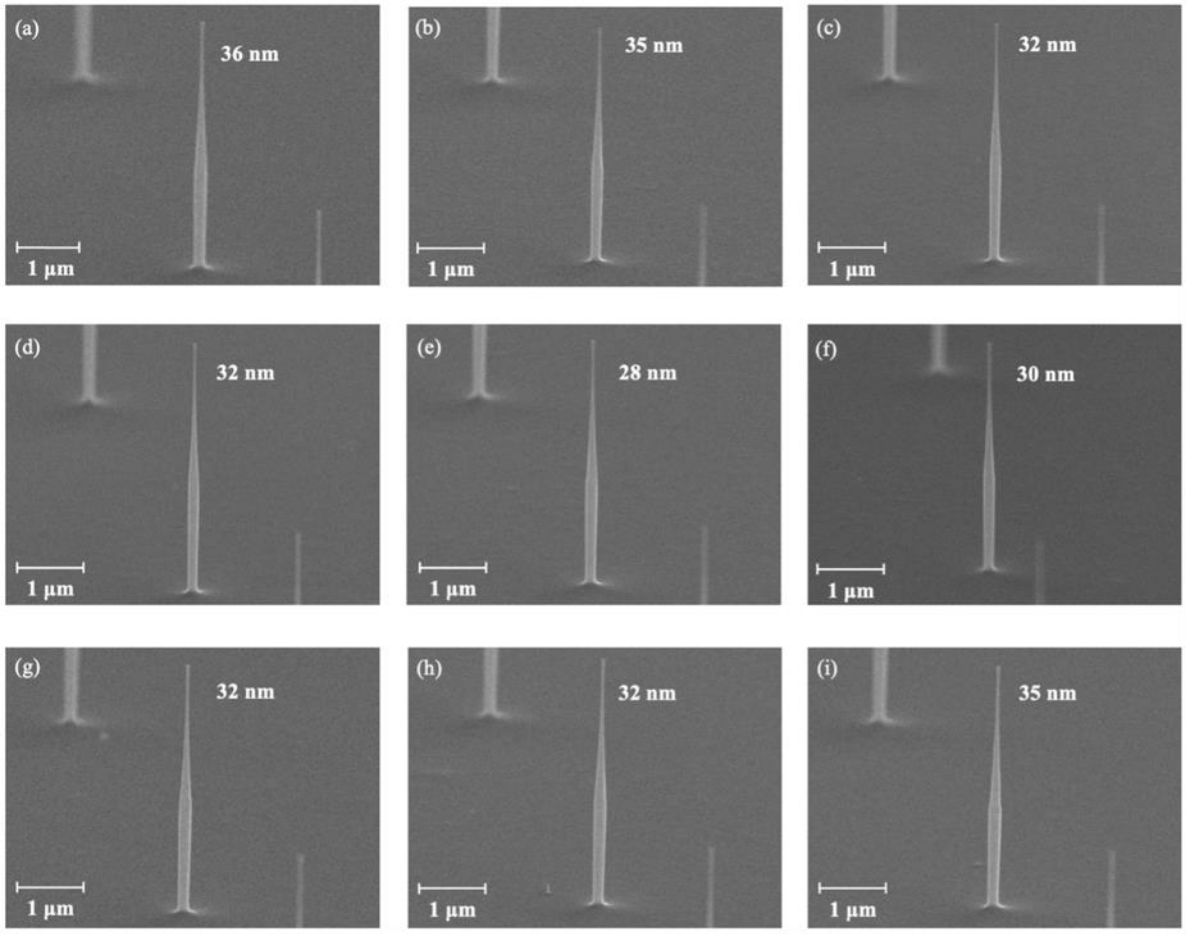


Fig. SI-3. (a) The SEM image of cylindrical Si nanocone which is the same image as Fig. 4 (b) (b)-(i) Additional SEM images of the Si cylindrical nanocones at various locations in the Si array after the oxidation sharpening process.

Table SI-2. The dimensions of 9 Si nanocones in the Si array with 1.1 μm design after oxidation sharpening process as shown in Fig. 4 (b). Note: The radius is 32.44 ± 2.55 nm, and the height is 4.01 ± 0.02 μm.

Si nanocone #	1	2	3	4	5	6	7	8	9
Radius (nm)	36	35	32	32	28	30	32	32	35
Height (μm)	4.00	4.02	4.01	4.00	4.00	4.05	4.02	4.00	4.03

Table SI-3. The dimensions of 9 Si nanocones in the Si array with 1.0 μm design after 5-minute etching as shown in Fig. 5 (a) and (b). Note: The radius is 27.11 ± 1.17 nm, and the height is 2.04 ± 0.03 μm.

Si nanocone #	1	2	3	4	5	6	7	8	9
Radius (nm)	28	26	27	28	26	29	26	26	28
Height (μm)	2.00	2.05	2.04	2.00	2.05	2.10	2.05	2.01	2.05

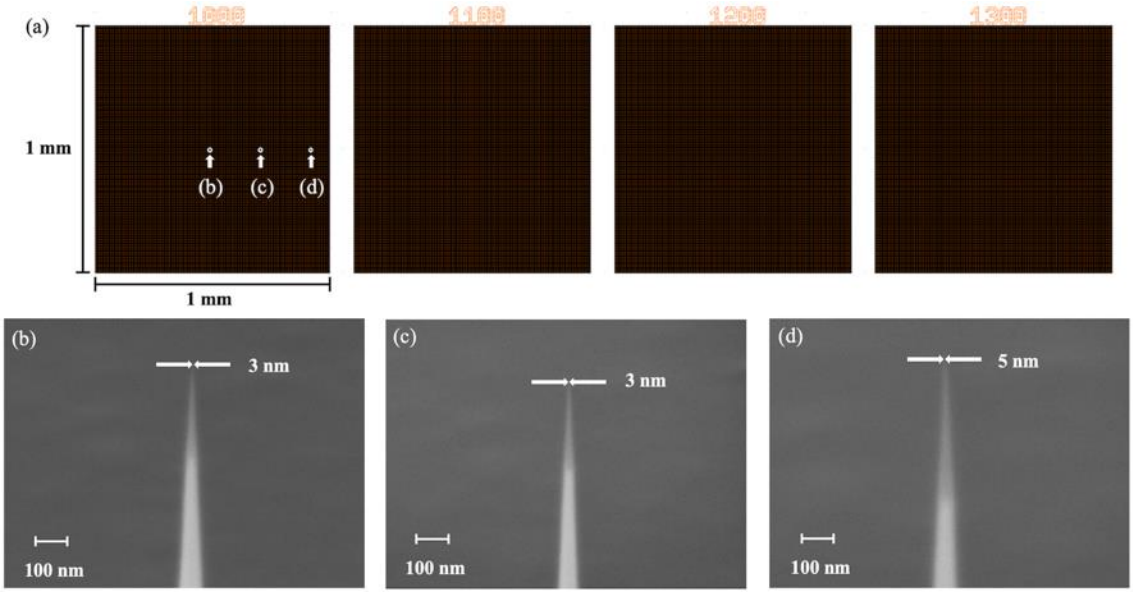


Fig. SI-4. (a) The pattern design utilized for the initial experiment (3 rounds in total), featuring four distinct diameters (b)-(d) SEM images of the Si nanocones at various locations (b, c, d) after the oxidation sharpening process.

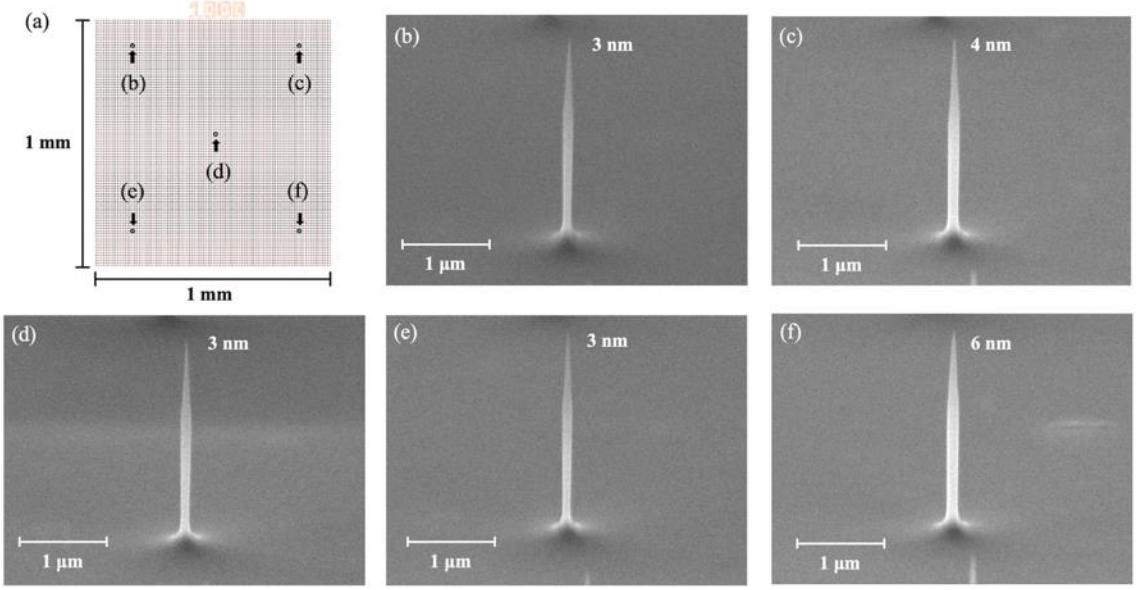


Fig. SI-5. (a) The pattern design utilized in the second-round experiment (3 rounds in total) employed features a 1.0 μm diameter (b)-(f) SEM images of the Si nanocones at various locations (b, c, d, e, f) after the oxidation sharpening process.